

Patient-Specific Mathematical Modelling of
the Hybrid Procedure in the Treatment of
Hypoplastic Left Heart Syndrome

Andrew G. Young

Department of Biomedical Engineering

University of Strathclyde

This thesis is submitted in partial fulfilment for the degree of

Doctor of Engineering

2014

This thesis is the result of the author's original research. It has been composed by the author and has not been previously submitted for examination which has led to the award of a degree.

The copyright of this thesis belongs to the author under the terms of the United Kingdom Copyright Acts as qualified by University of Strathclyde Regulation 3.50. Due acknowledgement must always be made of the use of any material contained in, or derived from, this thesis.

Signed:

Date:

Acknowledgements

For from Him and through Him and to Him are all things. To Him be glory for ever. Amen.

Romans 11:36

I would like to thank the many people who helped and contributed to the completion of this thesis. Firstly, I would like to express my gratitude to my three supervisors: Thanks to Mr. Mark Danton for his time and efforts throughout the project ensuring clinical focus and relevance. Thank you to Prof. Sean McKee for being there to bounce ideas off of and for encouraging a high standard of writing. Finally to Prof. Terry Gourlay, thanks for overseeing the whole project and for the inspirational visits to Govan.

I would also like to express my gratitude to Dr. Ruth Allen, whose assistance in obtaining anonymous patient images and validating the constructed 3D geometry was invaluable. Also my sincere appreciation to all the staff at the Cardiology Department at the Royal Hospital for Sick Children, Glasgow.

My humble thanks to the Engineering and Physical Sciences Research Council for their funding of the EngD in Medical Devices and the Departments of Biomedical Engineering and Mathematics & Statistics for the opportunity to study and complete this thesis.

Finally, this thesis would not have been possible without the encouragement and support of friends and family. The list is too long to thank everyone personally, however know that I am grateful to you all: Thanks to my course mates, it has been a pleasure; To my parents, Monica and David, thank you for believing in me and putting up with the phone calls and moods; To my siblings, Angela (and Steven and my beautiful niece Jessica), Ian and Karen you are all the best; to Claire for being there for me and helping me get over the finishing line; And to Nana (and Granda) who is joyfully numbered in the myriads of myriads at the Great Gathering.

Abstract

Hypoplastic Left Heart Syndrome (HLHS) is a rare congenital heart disease characterised by the underdevelopment of the left sided structures of the heart, compromising systemic blood supply. The Hybrid Procedure is a palliative repair that delays cardiopulmonary bypass surgery and allows the opportunity for left ventricular growth and biventricular repair. The ductus arteriosus is stented open via catheter, which allows the right ventricle to supply the systemic circulation. In order to balance the pulmonary-systemic flow ratio, branch pulmonary arterial bands are surgically placed. Currently, banding (and stent) dimensions are based on surgical experience, intuition and limited Doppler measurements. In mathematically modelling the Hybrid Procedure, it is possible to optimise the dimensions based on haemodynamic and ventricular data. These simulated results are often difficult and invasive to measure clinically. Due to the broad spectrum of abnormalities observed in HLHS, creating patient-specific models is an area for development. Therefore a thorough investigation of routinely collected clinical data was undertaken, assessing the potential collaboration between biomedical engineering and clinical protocols. A lumped circulation model of the post-Hybrid circulation was produced and clinically validated following novel investigation. An external band diameter of 3 mm was optimal, with 3.5 mm appropriate for larger patients. A patient-specific three-dimensional geometry was constructed and virtual surgery performed for a range of band diameters for steady state analysis. Boundary conditions were determined using matching patient-specific and literature data. This model was coupled to the lumped circulation model in a multiscale model. This highlighted the conflict of definition between internal and external diameter band dimensions. It was shown that the 2 mm internal band diameter was optimal. Regarding patient-specificity, it was demonstrated that current clinical practices are not conducive to mathematical modelling with many steps required in the processing of data. The quality of the data is suboptimal and will require multidisciplinary cooperation for future improvement. Due to the incompleteness of the data sets and the inconsistent data collection, full patient-specificity and predictive modelling was not achieved.

Contents

List of Figures	vi
List of Tables	x
List of Abbreviations	xii
1 Objectives and Outline of Thesis	1
1.1 Objectives	1
1.2 Thesis Outline	2
2 Hypoplastic Left Heart: Anatomy and Treatment	4
2.1 Hypoplastic Left Heart Syndrome	4
2.1.1 What is Hypoplastic Left Heart Syndrome?	5
2.2 Current Treatment	9
2.2.1 Transplantation	11
2.2.2 Norwood Procedure	11
2.2.3 Sano Repair	12
2.2.4 Sano vs. Modified Blalock-Taußig	13
2.3 Hybrid Procedure	15
3 Cardiovascular Modelling	20
3.1 One Dimensional Modelling	21
3.2 Lumped Circulation Modelling	23
3.2.1 Modelling Experience	26
3.3 Three Dimensional Modelling	32
3.3.1 Introduction	32
3.3.2 Published 3D Models	35
3.4 Multiscale Modelling	36

3.5	Modelling: The Future and Beyond This Study	40
4	Processing Clinical Data	43
4.1	Ethical Approval	43
4.2	Acquisition of Clinical Data	43
4.2.1	Further Considerations Regarding the Flow Rate Profiles	45
4.3	Format of Raw Clinical Data	48
4.4	Digitisation	50
4.4.1	Step 1	50
4.4.2	Step 2	51
4.4.3	Step 3	53
4.4.4	Step 4	56
4.5	Selection of Profiles From Clinical Data	58
4.5.1	Comparing Clinical Profiles	59
4.6	Outcome of Ensemble Averaging	63
4.6.1	Scaled vs. Absolute Time	64
4.7	Geometrical Data	68
4.8	Concluding Remarks on Clinical Data	69
4.8.1	Superfluous Digitisation	69
4.8.2	Coordination of Data	70
5	Lumped Circulation Model	72
5.1	Introduction	72
5.2	Methods	75
5.2.1	General Descriptions	75
5.2.2	Specific Sub-Models	78
5.2.3	Implementation and Protocols	81
5.2.4	Numerical Time Integration	82
5.2.5	Model Protocols	84
5.2.6	Calculation of Arterial and Venous Saturation and Oxygen Delivery	85
5.2.7	Circulatory Parameters	88

5.3	Outcomes	88
5.3.1	Norwood Circulation	88
5.3.2	Hybrid Circulation	93
5.3.3	Hybrid vs. Norwood Comparison	108
5.4	Summary and Conclusions	113
6	Patient-Specific Three Dimensional Modelling	116
6.1	Available Patient Data	116
6.2	Construction of Patient-Specific Geometry	119
6.3	Patient-Specific Geometry to Computational Fluid Dynamics . .	124
6.4	Simulating “ <i>Virtual Surgeries</i> ”	127
6.5	Steady State Computational Fluid Dynamics	130
6.5.1	Mean Pressure Drop from Specified Flows	131
6.5.2	Flow Rates from Clinically Derived Pressures	135
6.5.3	Comments on Transient Simulations, Desired Outcomes and Appropriate Boundary Conditions	138
6.6	Summary of Three Dimensional Approach	139
7	Coupled Multiscale Modelling	142
7.1	Introduction	142
7.2	Methods	143
7.2.1	Alteration of Valve Model	146
7.2.2	Adjustment of Pulmonary Branch of Lumped Circula- tion Model	150
7.2.3	Cardiac Cycle Repetition	153
7.2.4	Protocols	155
7.3	Outcomes	156
7.3.1	Varying Band Diameter	157
7.3.2	Varying Total Stressed Blood Volume	177
7.3.3	Zero Dimensional vs. Multiscale Modelling	182
7.4	Patient-Specific vs. Generalised Geometry	185
7.4.1	Comparison of Geometrical Data	185

7.4.2	Comparison of Methodologies	188
7.4.3	Stroke Work Discrepancy	189
7.5	Summary	192
8	Discussion, Limitations and Future Work	195
8.1	Clinical Data and Patient-Specific Modelling	195
8.2	Reproduction of Literature Models and Creation of Hybrid Model	198
8.3	Fully Patient-Specific Models	200
8.4	Predictive Modelling	202
8.5	Key Outcomes	202
A	Additional Mathematical Comments	204
A.1	One Dimensional Models	204
B	Caldicott Guardian Approval	208
C	Fluent Coupling Code	212
D	Matlab *.m files	221
E	Patient-Specific Catheterisation Data	229
	References	235

List of Figures

2.1	Anatomical representation normal heart vs. hypoplastic left heart	5
2.2	Atrial septal defects	7
2.3	Illustrations of surgical procedures used in conventional staged palliation of HLHS	9
2.4	Flow diagram of post-surgery circulations	10
2.5	Illustration of aortic arch reconstruction as part of the Norwood Procedure	12
2.6	Illustration of Hybrid Procedure	17
3.1	Illustration of mesh definitions	34
3.2	Multiscale modelling concept: Coupling of varying degrees of dimensionality as published by Van de Vosse	38
4.1	Clinical example of Doppler echocardiogram (with ‘ghosting’) .	47
4.2	Illustration of the doppler angular correction procedure	48
4.3	Examples of images available from raw clinical data of catheterisation and CT investigation	49
4.4	Screenshot of GetData software used in digitising image files in to usable data	51
4.5	The effect of using the re-organised data for both <i>spline</i> and <i>pchip</i> functions	56
4.6	Results of using linear, cubic splines and piecewise continuous cubic Hermite polynomials for interpolation of a clinical waveform from paired data points	57
4.7	Multiple pressure profiles available for the descending aorta, main pulmonary artery and ventricle from clinical data set . . .	58
4.8	Pressure differences of available profile families for stent flow . .	60
4.9	Alternative flow profiles based on selected MPA and available ventricular pressure profiles	61
4.10	Ensemble wave produced from eight original velocity profiles from Doppler echo of a branch pulmonary artery banding site .	62
4.11	Averaged waveform with varying number of data points	63

4.12	All clinically acquired profiles coloured by heart rate	66
4.13	All families of ventricular and main pulmonary artery pressures with scaled velocity marking the ejection phase from the ventricle	67
4.14	All clinical pressure profiles directly comparing Normalised and Absolute time scaling methods	68
5.1	Analagous electrical circuit of the post-Norwood Procedure circulations	73
5.2	Analagous electrical circuit of the circulation post-Hybrid Procedure for HLHS	74
5.3	Time step process to determine numerical solution	83
5.4	Hemodynamical profiles and pressure-volume loop of simulation with 8 mm ductal stent diameter	94
5.5	Hemodynamical outcomes versus pulmonary band diameter	98
5.6	Hemodynamical outcomes versus ductal stent diameter	101
5.7	Hemodynamical outcomes versus cardiac output	103
5.8	Haemodynamical outcomes with physiological reference regions as cardiac output is increased for different banding diameters	105
5.9	Fixed stressed blood volume in comparison to varied stressed blood volume as published by Shimizu <i>et al.</i> model	109
5.10	Pressure-Volume loops of the optimal Hybrid configuration and optimal configurations of the Norwood procedure	112
6.1	Summary flow chart of three dimensional patient-specific modelling	117
6.2	Identification of patient used in patient-specific analysis	120
6.3	Screenshot of MIMICS interface with 4 window setup	121
6.4	Manually constructed patient-specific geometry before manual correction and smoothing	122
6.5	Manually constructed patient-specific geometry	123
6.6	Patient-Specific geometry captured by angiogram	125
6.7	Surface mesh produced for patient-specific geometry	127
6.8	Virtual surgery	129
6.9	Pulmonary pressure drop versus band diameter for defined range of cardiac outputs	134
6.10	Steady state analysis of fixed pressure configurations for varying band diameter	137

7.1	Explicit coupling of the 0D and 3D models as reproduced reproduced from Janela, Moura and Sequeira	143
7.2	Circuit diagram representing the removal of 0D components which is replaced by the 3D submodel in the multiscale model. .	145
7.3	$\Delta t = 1 \times 10^{-4}$ versus $\Delta t = 1 \times 10^{-5}$ time steps for pressures, valvular flows, and systemic and pulmonary flows	148
7.4	Linear valve model versus quadratic valve model for pressures, valvular flows, and systemic and pulmonary flows	149
7.5	Continuous and beat-by-beat profiles of MPA pressure, stent flow, right PA pressure, systemic perfusion, systemic venous pressure for the coupled multi-scale model	154
7.6	Flow profiles as 3D geometry is varied	159
7.7	Pressure profiles as 3D geometry is varied	161
7.8	Internal pulmonary artery banding diameter versus cardiac output, pulmonary-to-systemic flow ratio, systemic flow, systemic oxygen delivery, stroke work	162
7.9	Pressure-volume loops for varying internal pulmonary band diameter	163
7.10	Absorption of reflection oscillations	166
7.11	Visualisation of default internal band geometry results	170
7.12	Visualisation of 1.5 mm internal band geometry results	171
7.13	Visualisation of 2 mm internal band geometry results	172
7.14	Visualisation of 2.5 mm internal band geometry results	173
7.15	Visualisation of 3 mm internal band geometry results	174
7.16	Visualisation of 3.5 mm internal band geometry results	175
7.17	Visualisation of 4 mm internal band geometry results	176
7.18	Analysis of linearity of haemodynamical outcomes as total stressed blood volume is varied	179
7.19	Pressure-Volume loops for varying total stressed blood volume with 2 mm geometry	181
7.20	Comparison of generic and patient-specific Hybrid geometries .	186
7.21	Figure 3 from Hsia <i>et al.</i> showing pressure-volume loop for BT shunt (BTS), Sano shunt (RVS) and Hybrid (HYB) repairs	190
7.22	Systolic systemic pressure data from the literature	191

8.1 Flow chart outlining the work undertaken throughout the investigation of mathematical modelling of the Hybrid Procedure for the treatment of hypoplastic left heart syndrome 196

List of Tables

3.1	Electric-Hydraulic analogy	24
5.1	Parameters used in modelling the Hybrid and Norwood repairs for HLHS	75
5.2	Direct comparison between reproduction of and published results of Shimizu <i>et al.</i>	90
5.3	Comparison between adapted Norwood model and reproduced results of Shimizu <i>et al.</i>	91
5.4	Hemodynamical data for Hybrid Circulation with varying pulmonary arterial banding	95
5.5	Normalised systemic oxygen delivery	97
5.6	Hemodynamical data for Hybrid Circulation with varying ductal stent diameter	100
5.7	Hemodynamical data for Hybrid Circulation with varying cardiac output	106
5.8	Hemodynamical data of the Hybrid Procedure varying total stressed blood volume	107
5.9	Hemodynamical data comparing the optimal Hybrid configuration versus optimal configurations of the Norwood Procedure	110
6.1	Summary of meshes generated for banding diameters simulated	130
6.2	Steady state analysis of pressure drops for fixed cardiac output	133
6.3	Mean pressure values derived from patient-specific catheterisation procedure for appropriately labeled clinical profiles	134
6.4	Pressure configurations used for steady state analysis of cardiac output and flow distribution of patient-specific geometries	135
6.5	Steady state analysis of cardiac output and flow distribution for varying band diameter geometries	136
7.1	Haemodynamical results of linear and quadratic/oriface valve models for $\Delta t = 1 \times 10^{-4}$ and 1×10^{-5} s	151
7.2	Parameter values of pulmonary components used in the stand alone lumped circulation model versus altered coupled lumped circulation model	153

7.3	Multiscale model results varying internal PAB diameter	158
7.4	Multiscale model haemodynamical results varying total stressed blood volume	178
7.5	Analysis of linearity of outcomes with respect to total stressed blood volume	180
7.6	Matching internal and external band diameters using lumped circulation model	182
7.7	Haemodynamical results of coupled Hybrid model versus the matched lumped circulation model	184
7.8	Comparison of band diameter variation for idealised and patient- specific geometry	187
7.9	Comparison of MOCHA 2 mm idealised geometry and 2 mm patient-specific geometry for varying total stressed blood volumes	188
7.10	Review of clinical publications presenting systolic systemic pres- sures for Hybrid patients	191

List of Abbreviations

<i>A</i>	Diastolic Elastance Scaling Factor
<i>B</i>	Diastolic Elastance Exponent
<i>C</i>	Compliance
<i>D</i>	Shunt or Stent Diameter
<i>E</i>	Elastance
<i>P</i>	Pressure
<i>Q</i>	Flow
<i>R</i>	Resistance
<i>V</i>	Volume
V_T	Total Stressed Blood Volume
$a(t)$	Cardiac Activation Function
<i>d</i>	Pulmonary Band Diameter
<i>n</i>	Iteration
<i>t</i>	Time
0D	Zero Dimensional
1D	One Dimensional
1VR	Single Ventricle Repair
2VR	Bi-Ventricular Repair

3D Three Dimensional

AAR Aortic Arch Reconstruction

ASD Atrial Septal Defect

AVSD Atrialventricular Septal Defect

BCs Boundary Conditions

BSA Body Surface Area

CT Computed Tomography

CVS Cardiovascular System

FSI Fluid-Structure Interaction

HLHS Hypoplastic Left Heart Syndrome

LCM Lumped Circulation Model

LPM Lumped Parameter Model

mBT shunt modified Blalock-Taussig shunt

mmHg Millimetres of Mercury

MPA Main Pulmonary Artery

MRI Magnetic Resonance Imaging

P-V Pressure-Volume

PA Pulmonary Artery

PAB Pulmonary Arterial Banding

PDA Patent Ductus Arteriosus

PVA Pressure-Volume Area

RV Right Ventricle

RVEDV Right Ventricular End Diastolic Volume

s.s.e. Sum of Squared Error

SA Systemic Artery

VSD Ventricular Septal Defect

Chapter 1

Objectives and Outline of Thesis

1.1 Objectives

This thesis discusses the development of a patient-specific predictive mathematical modelling tool to help guide cardiac surgeons to administer the optimal configuration of the Hybrid Procedure for the treatment of Hypoplastic Left Heart Syndrome (and related abnormalities) with the aim of achieving long-term survival and enhanced quality of life. A strong motivation throughout this study has been to apply existing technology and methodologies to non-generalised cases by utilising routinely gathered clinical data and demonstrate how this could lead to optimised procedures.

The objectives at the beginning of this project were as follows:

- Assess the available clinical data and its applicability for use in patient-specific modelling of the Hybrid Procedure.
- Reproduce relevant mathematical models from the literature and construct equivalent models for the Hybrid Procedure.
- Implement full patient specificity for all aspects of mathematical models produced (lumped parameters and geometrical representation of the surgical region).

- Assess the predictive capabilities of patient-specific modelling by comparing the predictions of the modelled post-surgical data built from pre-surgical data, with the actually observed clinical outcomes.

1.2 Thesis Outline

Chapter 2 defines Hypoplastic Left Heart Syndrome and introduces the current treatment options available to congenital cardiac treatment teams in a review of the medical literature. The Hybrid Procedure is described in detail with the benefits of this procedure providing motivation for modelling that can lead to optimisation of the configuration of the surgery for a specific patient.

In Chapter 3 the various approaches to cardiovascular modelling are introduced, reviewing the historical literature as well as the relevant recent developments in the field.

The fourth chapter outlines the type of raw clinical data routinely collected with which patient specificity could be implemented. The laborious nature of digitising the raw data is an often neglected topic and is highlighted here to reinforce the fact that with the standard technology used today, this is an unnecessary complication. Also, it is not as straightforward as might be initially thought, since data from different sources (e.g. pressure data from catheterisation and velocity data from echocardiogram) and different time periods need to be employed: this data is unlikely to be self-consistent given the current data capture process.

Following on from the review in Chapter 3, a generalised lumped circulation model for the Hybrid Procedure is presented in Chapter 5. This follows the successful reproduction of a similar model for various forms of the alternative surgical option, The Norwood Procedure. A full analysis of the Hybrid circulation model is presented including a direct comparison to the Norwood Circulation.

Further processing of clinical data, specifically for the purpose of generating a three dimensional geometry, is detailed in Chapter 6. In addition to the considerations of generating a geometry that can be used for computational fluid dynamic modelling, the results of averaged, steady-state analysis is presented.

The two distinct models, the three dimensional and the lumped circulation model, are then combined to provide adaptable boundary conditions in a coupled multiscale model, one of the leading approaches to surgical repair modelling in this research area. The methods and results are presented in the penultimate chapter of this thesis, which is the culmination of the research project.

The entire research project is summarised and the implications of the findings and future developments are discussed in the final chapter. This includes a review of the initial objectives outlined at the beginning of this chapter.

Chapter 2

Hypoplastic Left Heart: Anatomy and Treatment

2.1 Hypoplastic Left Heart Syndrome

Hypoplastic left heart syndrome (HLHS) is one of the most lethal congenital heart diseases (CHDs) and despite improvements in the treatment options available, the associated morbidity (as well as mortality) rates are still some of the greatest recorded [1]. To put CHD into perspective, it is more prevalent than childhood cancer [2]. 600 out of every 100,000 live births suffer from moderate to severe CHD [3], with HLHS and its variants considered a severe diagnosis. Elsewhere it has been reported that HLHS occurs between 16 to 36 out of every 100,000 live births [4] while it accounts for approximately 8% of all structural CHD [5]. It is also more common in males who contribute to up to 70% of cases [6].

HLHS is one of the most challenging and costly CHDs to treat as well as suffering from high mortality rates [7, 8]. It has also been described as “*the most serious congenital cardiac anomaly*” [1]. The challenge of treatment, utilising all major disciplines and teams involved in the treatment plan (surgical, cardiology, anaesthetics to name but a few), justifies its use as a marker for a cardiac centre’s performance. To fully appreciate the complexities involved in the treatment, HLHS must be defined and explained, including the the com-

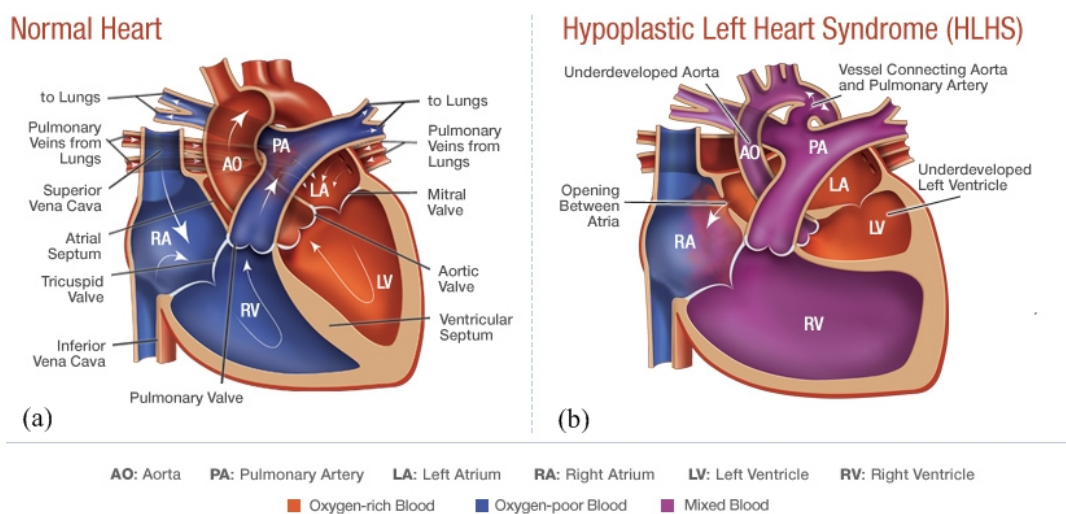


FIGURE 2.1: Anatomical representation of: (a) Normal heart; (b) Hypoplastic left heart. Figures from Cardiac Centre at The Children’s Hospital of Philadelphia.

plexities and intricacies of the condition which is addressed in the following section.

2.1.1 What is Hypoplastic Left Heart Syndrome?

Hypoplastic Left Heart Syndrome is the diagnosis given to a collection of concurrent lesions present in a newborn with underdevelopment of the left sided structures of the heart. It affects the heart’s ability to supply blood to the body (the systemic flow) with the body’s natural response to HLHS being to maintain the patency of the ductus arteriosus, and foetal-like circulation. The patent (open) ductus arteriosus (PDA) is one of the methods the foetal circulation employs to divert blood flow from the unopened lungs (pulmonary flow) to the systemic circulation and is located between the aortic arch in the systemic system and the pulmonary artery (PA) in the pulmonary circulation. It is effectively a natural occurring shunt that should close primarily in the first 24 hours of life with complete closure in the first few months. For HLHS survival the ductus has to remain patent as outlined above. A hole called the foramen ovale, in the atrial septum (wall dividing the left and right atria) is also essential. As blood returns from the lungs to the left atria, in order for

the oxygenated blood from the lungs to reach the body, it must enter the right atria through this hole allowing it to reach the body via the right ventricle (RV) and PDA.

The term “Hypoplastic Left Heart Syndrome” is one that has had widespread and varying use [9]. Tchervenkov *et al.* as part of a Nomenclature Work Group, discuss the history of the terms used to refer to the many complex lesions, as well as the use of the term HLHS, in great detail. The final definition of HLHS (synonymous with “Hypoplasia of the Left Heart”) is given as: “*a spectrum of cardiac malformation characterised by the underdevelopment of the left heart with significant hypoplasia of the left ventricle including atresia, stenosis, or hypoplasia of the aortic or mitral valve, or both valves, and hypoplasia of the ascending aorta and aortic arch.*” On viewing an illustrative representation of the anatomy of this complex collection of lesions, the problem is better understood and can be seen in Figure 2.1 contrasted with a fully functional “normal” heart. Atresia was defined as “*the congenital absence or closure of a normal body orifice or tubular organ*” while stenosis is a narrowing of a duct or canal.

In a PubMed Medline Search the phrase “Hypoplastic Left Heart Syndrome” resulted in 2314 articles from November 1958 through May 2013, emphasizing its use and this was one of the reasons the term was not disbanded by the Work Group. Previous to the publication of the Work Group, Tchervenkov *et al.* also coined the phrase “Hypoplastic Left Heart Complex” (HLHC) which refers to newborns with the lesions as in HLHS without intrinsic stenosis of the aortic or mitral valves. A patient diagnosed with HLHC would be a candidate for the treatment plans discussed in this thesis. A recently introduced term for related conditions is “hypoplastic left heart physiology” defined as “*the inability of the left heart to sustain adequate cardiac output following birth because of underdevelopment of one or more left heart structures despite surgical or medical intervention*” [10]. It is a specific subset of this cohort of patients that was the motivation in this study.

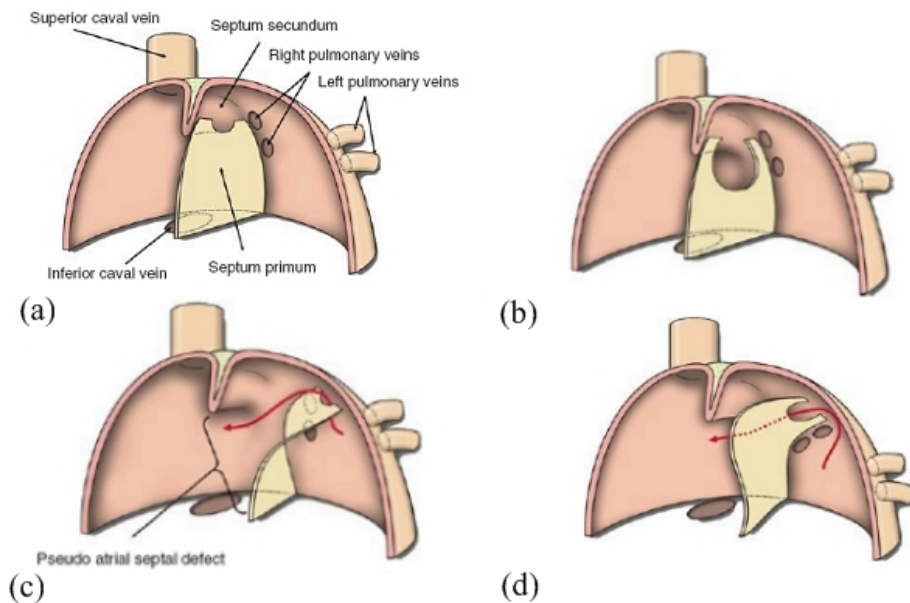


FIGURE 2.2: Atrial septal defects: (a) Normal Atrial Septum (b) ASD: Stretched Foramen Ovale (c) ASD: Leftward displacement of Primary Septum, bracket represents large pseudo-defect (d) Bulging of left displaced Primary Septum with Foramen Ovale partially obstructed, red arrows show flow of blood. Original figure from [9].

Septal Defects

Defects in the septum dividing the left and right ventricles (ventricular septal defect - VSD) and atria (atrial septal defect - ASD) are common complications seen with HLHS. Defects of the septum dividing the atria and the ventricle (atrioventricular septal defect - AVSD) are also found, although less common. VSDs (AVSDs) are simplistically described as leaks between the two ventricles (ventricle and atria), that cause a host of haemodynamical issues affecting the pressures, direction of flow and the uncoordinated mixing of oxygen-rich (from the lungs to be sent to the body) and oxygen-deprived (from the body to be sent to the lungs) blood.

More specifically, and perhaps counter-intuitively, an ASD can be the lack of the hole (foramen ovale) mentioned previously. The atrial septum is composed of a fixed secondary septum (Septum Secundum) with the flap valve, the Primary Septum or Septum Primum, having the crescent foramen ovale at its superior end. Again, it is best described visually, with Figure 2.2 illus-

trating additional malformations found in ASDs: Stretched foramen ovale as found with increased pulmonary venous return with correct Primary Septum attachment (Figure 2.2 (b)); A pseudo-ASD where there appears to be no septum at all due to the primary septum attaching to the wrong place (Figure 2.2 (c)); and a stretched pseudo-ASD (Figure 2.2 (d)).

What is important in Hypoplastic Left Heart Syndrome, is that there is direct communication between the left and right atrium so that oxygen rich blood can return from the lungs to the right ventricle to be delivered to the body. Therefore, to ensure unrestricted flow from the left to right atria, a balloon septostomy is often performed in the Hybrid Procedure, which is detailed following an outline of the other available treatment options for HLHS.

Aortic Arch

The size of the aortic arch is also critical in Hypoplastic Left Heart Syndrome, and is of particular importance when aortic atresia is present. In aortic atresia, there is no forward flow in the ascending aortic arch, therefore, due to where the ductus arteriosus meets the aortic arch, cerebral and coronary perfusion is entirely dependent on retrograde flow.

This can be critical in the Hybrid Procedure as improper placement of the stent can impair this crucial retrograde flow. This can occur when the stent is over extended into the aortic arch directly restricting the flow into the ascending aortic arch, or by failing to cover the length of the ductus with a stenosis formed at the proximal end as it attempts to naturally close. The Hybrid Procedure is detailed below in Section 2.3.

Tricuspid Regurgitation

Tricuspid regurgitation, blood that leaks back across the tricuspid valve, is a common complication observed with HLHS. In a study of 100 HLHS patients by Barber *et al.* 37 patients suffered from mild tricuspid regurgitation with a

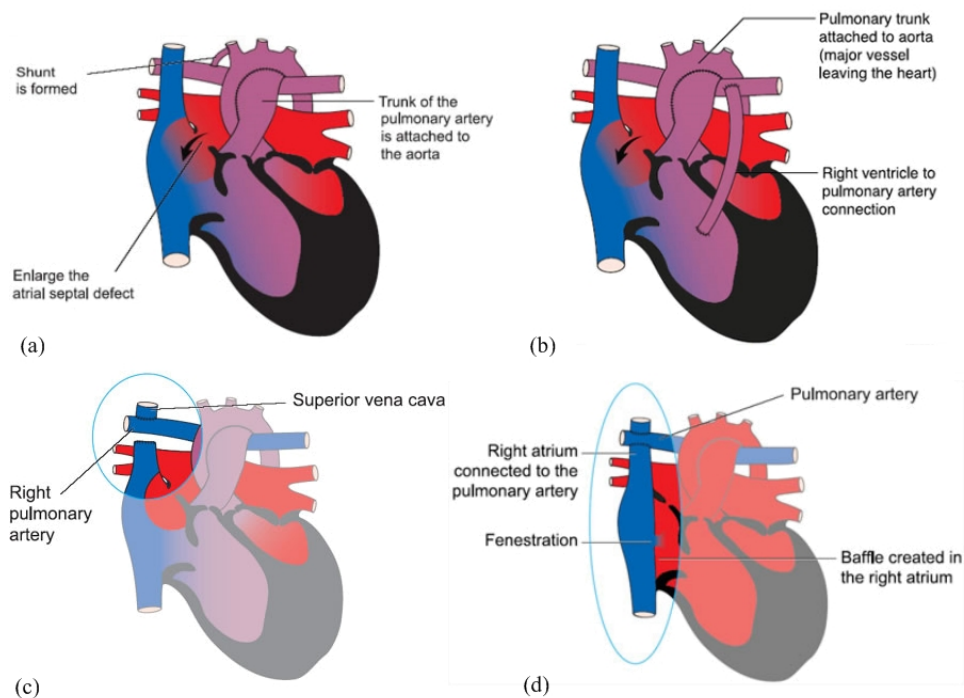


FIGURE 2.3: Illustrations of surgical procedures used in conventional staged palliation of HLHS: (a) Classical Norwood Repair (b) Sano Repair (c) Glenn Procedure (d) Fontan Procedure. Figures from www.lhm.org.uk.

further 13 and 3 suffering moderate and severe regurgitation respectively [11]. It was also observed that tricuspid valve competence was significant factor in the long-term outcome of treatment.

An additional consequence of tricuspid regurgitation is that any attempts to estimate volumetric indices and myocardial performance can be skewed.

2.2 Current Treatment

Without surgical intervention, newborns will not survive past the first few months of life [12], and before the 1980s the only option available for parents of Hypoplastic Left Heart children was comfort care [1]. In the mid 1980s two surgical options became available: transplantation; and a staged procedure resulting in a single ventricle anatomy, where the right heart pumps blood directly to the body where it then passively drains to the lungs (bypassing the conventional right heart). Blood is then pumped to the body again via the

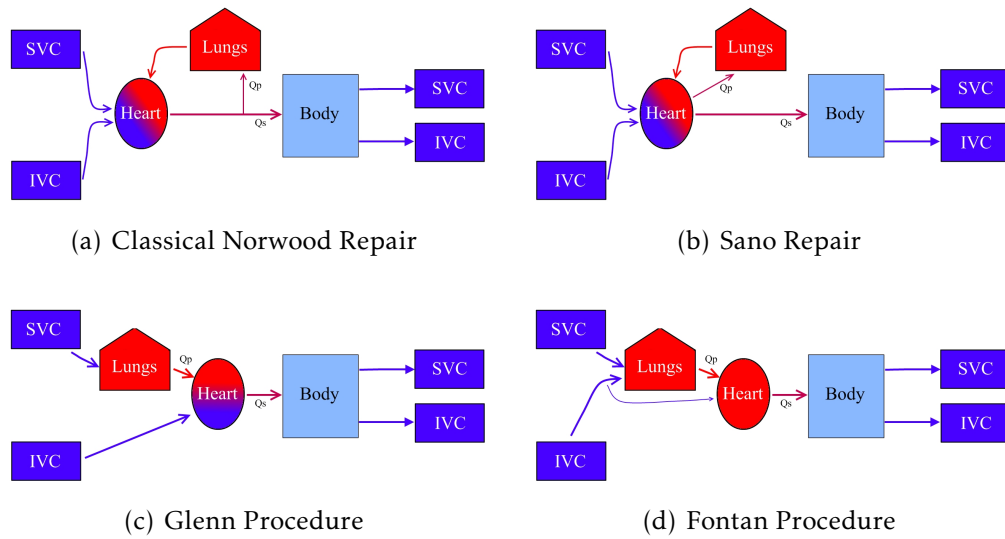


FIGURE 2.4: Flow diagram of post-surgery circulations. Red: oxygenated blood; Blue: de-oxygenated blood; IVC: inferior vena cavae; Q_p : pulmonary flow; Q_s : systemic flow; SVC: superior vena cavae. Figures adapted from Alsoufi *et al.* [13]

right heart. This results in what is known as a Fontan circulation, where both the inferior (IVC) and superior (SVC) venae cavae are anastomosed (attached) directly to the PA as shown in Figure 2.3. Stage I is referred to as the Norwood Procedure (Figure 2.3 (a)), and has been adapted into what is now called the Sano Procedure (Figure 2.3 (b)) both of which are undertaken in the early postnatal period. Stage II, which involves feeding just the SVC directly into the PA, is referred to as a Glenn Procedure or a Bidirectional Cavopulmonary Connection (BDCPC), see Figure 2.3 (c), and is done at approximately 4 to 6 months depending on urgency. A cavo-pulmonary connection is a union of the venae cavae (inferior, superior or both) and the pulmonary artery. The Fontan Procedure (Stage III) is carried out at 2 to 4 years of age (Figure 2.3 (d)). Figure 2.4 depicts the path of blood flow (appropriately) in flow chart fashion for the two Stage I repairs in addition to Stages II and III.

The latest technique to start on the path to Fontan circulation is the catheter and surgical based Hybrid Procedure; however this does not necessarily result in a traditional single ventricle repair (1VR). The Hybrid Procedure allows the possibility of a biventricular repair (2VR) and it is the modelling of this repair with the potential to determine appropriate candidates for 2VR that was

a motivating factor of this research. As a consequence of when these treatments became available, along with the associated learning curves, adaptations, improvements and varying concomitant treatment, long-term information on prognosis, survival and quality of life is still limited [4].

2.2.1 Transplantation

Although transplantation is not extensively reviewed, it is necessary to acknowledge it. Paediatric heart transplant is the preferred surgical intervention of some cardiac centres. The first successful heart transplant for HLHS was carried out at the Loma Linda International Heart Institute in 1985, where they built up a reputation for the procedure, and by 1993 were reporting a 5-year actuarial survival rate of 82% [14]. The main drawback of this option is the availability of suitable donors, and maintaining systemic flow until the operation, both of which contribute between 10 to 25% of waiting list deaths [14]. The Hybrid Procedure studied in this thesis can also be a course of treatment adopted as a bridge to transplantation while awaiting a donor, which is subject to availability. Transplantation has the additional drawback of the patient requiring immunosuppressants for the remainder of their life, as well as the life-threatening uncertain wait for a donor.

2.2.2 Norwood Procedure

The first successful palliative surgery for HLHS was reported by Norwood *et al.*[16]. This was achieved by remodelling the anatomy of the great arteries (PA and hypoplastic aorta) resulting in a drastically altered physiology. The PA is detached near the end of the main pulmonary artery (MPA) before it splits into its left (LPA) and right (RPA) branches, and the ductus is removed from between the transverse and descending aorta. The hypoplastic aorta is cut and anastomosed to the MPA and descending aorta, possibly with the use of a curved homograft patch, as shown in Figure 2.5 [12, 15] thus completing aortic arch reconstruction (AAR). Then to provide blood to the pulmonary

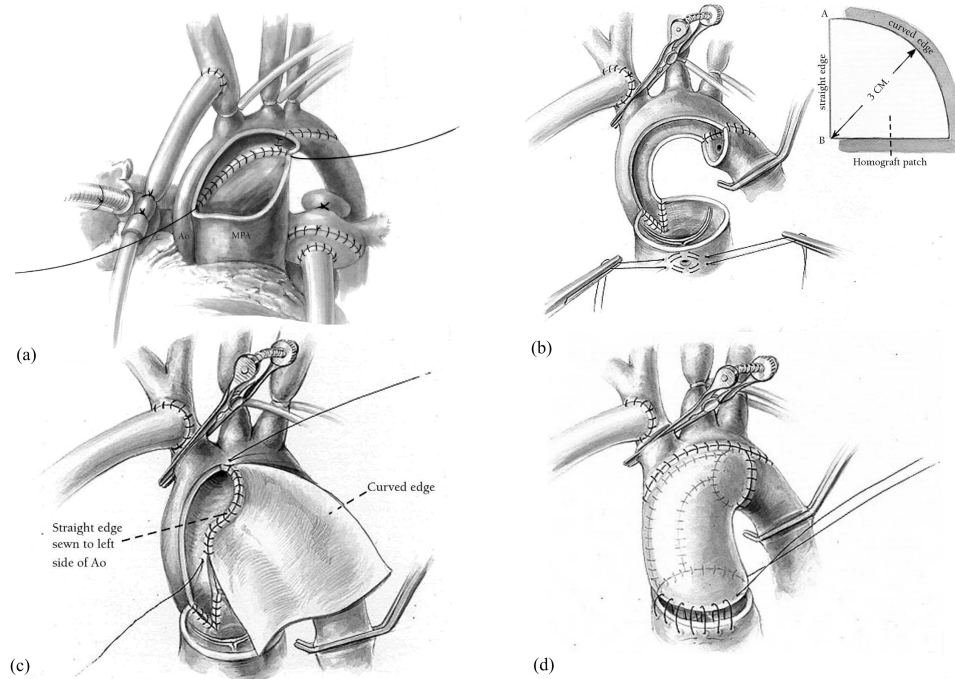


FIGURE 2.5: Illustration of aortic arch reconstruction as part of the Norwood Procedure. Illustration taken from [15].

system, a systemic-to-pulmonary shunt is placed between either the innominate artery or the ascending aorta and the RPA (although variations in the site of anastomosis exist). This shunt is referred to in the literature as a modified Blalock-Taußig (mBT) Shunt. This new anatomical set up is illustrated in Figure 2.3 (a). Excellent graphics are found in “The Norwood Procedure with an Innominate Artery-to-Pulmonary Artery Shunt” by Tweddell and is recommended to assist in visualisation of the full procedure. It also shows the removal of the atrial septum (septectomy), thus providing a single atria for this 1VR [15].

2.2.3 Sano Repair

The blood supply to the cardiac tissues is from the coronary arteries which are located near the base of the ascending aorta. Most of the perfusion, 70% to 80% [2], is during diastole (when the heart is resting and refilling) partly due to the contraction of the heart during systole constricting its flow. The shunt used in the classical Norwood Repair suffers from diastolic run off. This

means that a significant portion of the forward flow of (mixed) oxygenated blood during diastole is diverted into the PA, unlike in normal physiology, resulting in less oxygen-rich blood in the aorta (or in this case neoaorta) to supply the heart. This phenomenon is known as “coronary steal”. It is this issue which motivated the modification of the classical Norwood Procedure that uses the modified BT shunt.

In February 1998, Sano and his team performed the first fully successful “Sano Repair”. Instead of the systemic-to-pulmonary shunt, they resurrected the idea of using a right ventricle-pulmonary artery shunt (see Figure 2.3) first attempted by Norwood’s team [12, 16]. The techniques of the neoaortic reconstruction of the Classical Norwood Repair were unchanged (see Figure 2.5). The ratio of pulmonary flow to systemic flow was too great to maintain viable circulation with shunts of 8 mm and 12 mm diameter as used by Norwood, while Sano’s smaller 4 mm to 6 mm diameter conduits were successful. The size of the shunt resulted in higher diastolic pulmonary pressures, hence less diastolic run-off preventing the impaired coronary supply. Another reason for the successful second attempt at the RV-PA conduit is the comparatively small ventriculotomy (cutting a hole in the ventricle wall). A small incision appears to have no significant impact on contractility, where the larger incision impaired the function of the RV [12]. The Sano shunt results in a more natural pulsatile supply to both the systemic and pulmonary circulations. As with the Norwood Repair, the Sano Repair involves an atrial septectomy.

2.2.4 Sano vs. Modified Blalock-Taussig

The choice of which treatment method to use is highly dependent upon factors such as the cardiac centre’s facilities and experience. The skill and experience of the operating surgeon and treatment teams also contributes to the decision. As with most surgical procedures there will be learning curves associated with the implementation of a new technique, and this evidence can be found in the

literature [1, 14] where there are obvious improvements in surgical survival with time.

Both the Glenn and Fontan Procedures are relatively well tolerated [13] and it is Stage I palliation that results in the greatest mortality rate [1]. Too many centres have published a wide variety of results which to mention specifically, however the two Norwood based procedures currently yield similar results of between 70% to up as high as 90% survival. These results often exclude high risk factors such as low-birth weight, non-cardiac complications as well as additional contraindicators to the surgical repair (like right ventricle dysfunction). Therefore, these results tend to be skewed in comparison to the results for the Hybrid Procedure as many centres use the Hybrid Procedure for high-risk patients only, which will be discussed in the subsequent section.

Fuller *et al.* published a review of the current Norwood Stage I methodologies including descriptions of pre- and post-operative management techniques of both the modified BT and Sano shunts [17]. They do not, however, review the outcomes of the two approaches. Following a substantial review of what publications were available, Ohye *et al.* in 2007 concluded that “*The current literature is contradictory, retrospective, and predominantly historically controlled.*” [2] It was therefore deemed necessary to implement a randomised controlled clinical trial to answer this question. Sponsored by the Pediatric Heart Network and incorporating 15 centres across North America, a study recruiting 555 eligible patient between May 2005 and July 2008 was carried out and consequently published [7].

The Primary outcome was death or cardiac transplant at 12 months following randomisation while the secondary outcomes included unplanned interventions and ventricular function. Despite more unintended interventions (92 vs 70 per 100 infants $P = 0.003$) and complications (5.3 vs 4.7 $P = 0.002$) from randomisation to 12 months for the the Sano shunt, it performed significantly better than the modified BT shunt in the primary outcome. Transplantation free survival at 12 months following randomisation was 74% for the

Sano shunt versus 64% for the modified BT shunt ($P = 0.01$). However, following the 12 month window, the data available showed no significant differences between the two methods. Data did show that the greater the volume of single right ventricle infants seen per year at a specific centre, the better the survival rate seen in the Sano shunt [7].

As stated earlier, long-term information on prognosis, survival and quality of life is still limited [4]. Only in the Classical Norwood Procedure are survival rates published for 15 years, with 10 year rates available for the Sano variation [13]. The 5, 10 and 15 year survival for the classical Norwood published by Mahle *et al.* and Tibballs *et al.* were 40%, 39%, 39% and 38%, 38%, 25% respectively [18, 19].

2.3 Hybrid Procedure

The Hybrid Procedure is the focus of this research, therefore is presented distinctly from the other available treatments in this section.

Unacceptable donor waiting length time, and high Stage I and inter-stage mortality rates with the Norwood/Sano Repair, led to the introduction of The Hybrid Procedure [14]. First used as a palliative stage towards Fontan circulation for HLHS by Gibbs *et al.* [20], it utilises the patency of the ductus arteriosus mentioned previously. Through a catheterisation procedure (thin tools being deployed through the vascular system), a stent is placed to maintain the patency of the PDA which can alternatively be achieved with the use of pharmacological agents such as Prostaglandin E2. A surgical procedure is then carried out to increase the resistance to blood flow in the PA, which if left unaltered would result in a high $Q_P : Q_S$ ratio observed in the pre-surgical condition. Intuitively blood will follow the path of least resistance, which is found in the pulmonary circulation as the systemic resistance is far greater following the drop in pulmonary vascular resistance in the first few weeks of life.

The increase in resistance is achieved by placing bands around the branch PAs following a sternotomy. Currently the band diameter is relatively arbitrary selected, with protocols not well defined and based predominantly on the surgeon's experience and intuition. Most newborns under the weight of 2.5 Kg receive bands of 3.0 mm external diameter, while those above receive 3.5 mm bands. Most centres vary the tightness of the band according to the Doppler velocity from an echocardiogram investigation [21] while one centre in Tokyo used the formula of band circumference of 7 and 7.5 mm plus an additional millimetre for each kilogram of birth weight (rounded to the nearest half Kg) for the left and right pulmonary arteries respectively [22]. The circumferences of a 3.0 mm and 3.5 mm diameter band are approximately 9.4 mm and 11.0 mm respectively.

There has also been an adjustable banding brought to market (FloWatch[®]) which is wireless, battery free and allows the band to be loosened as well as tightened, all without the need for surgical re-intervention. This so far has led to a reduction in mortality and morbidity associated with the fixed MPA banding, significantly reducing the length of intensive care unit and hospital stay [23]. However, this technology has yet to be scaled for use on the bilateral branch pulmonary arteries. With greater understanding of the optimal band diameter throughout the development of a child undergoing the Hybrid Procedure, the technology, if scalable, may not be far away to implement any proposed protocols of vary band diameter that may come about through future research.

Not only is the choice of banding size not well established, neither is the diameter of the stent which is normally maintained at the native size of the PDA. For example, see the patient descriptions found in [24].

The final element of the Hybrid Procedure is to ensure unrestricted atrial communication, often by performing a balloon atrial septostomy (BAS) as stated previously. Figure 2.6 (a) depicts the outcome of the (Stage 1) Hybrid Procedure.

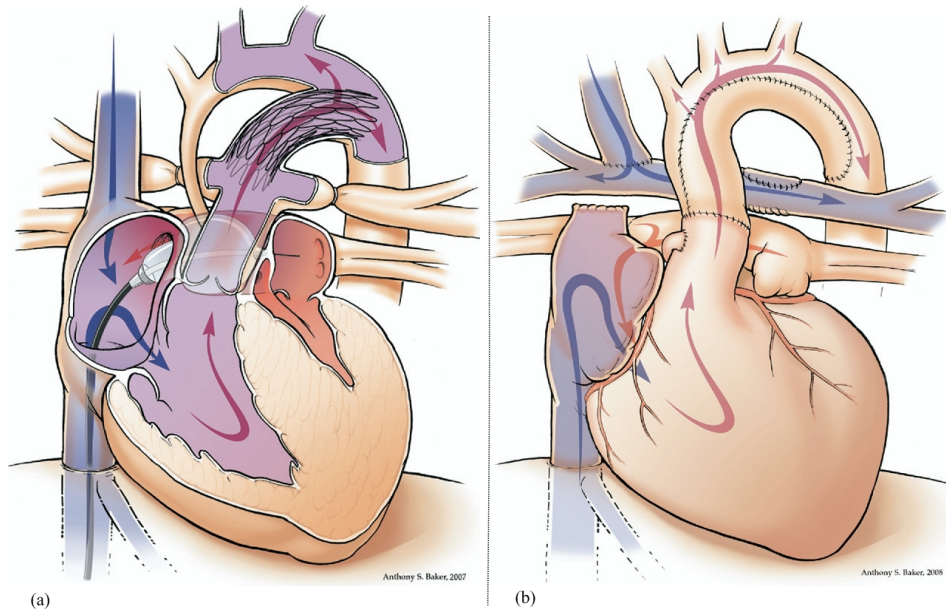


FIGURE 2.6: Illustration of Hybrid Procedure (a) Stage 1 consisting of Ductal Stenting, Pulmonary Artery Banding and Balloon Atrial Septostomy (b) Stage 2 comprehensive Glenn shunt physiology. Figure from Galantowicz *et al.* with permission[25]

The avoidance of a ventriculotomy, a cutting into the ventricle in the placement of the Sano shunt, (with only a sternotomy - cutting open of the chest - to enable the placement of branch PA bands) and the avoidance of cardiopulmonary bypass until later in life is one of the many advantages of this procedure. This removes the exposure to extracorporeal circulation in an already demanding procedure. Stage II of the Hybrid Procedure along the Fontan path incorporates Stages I and II from the traditional Norwood based methods (Figure 2.6 (a)). At around 4 to 6 months (as is the timing for Norwood/Sano Procedures) Hybrid Stage II consists of AAR, as outlined above (see Section 2.2.2), as well as the BDCPC/Glenn Procedure while the pulmonary banding is removed. The Fontan operation then completes the 1VR palliation process if this route is pursued.

As Apitz *et al.* comment: “Preoperative assessment of whether the left ventricle is adequate to sustain systemic circulation and allow biventricular repair can be extremely difficult in patients with left ventricle structures of borderline size” [26]. By choosing the Hybrid Repair for Stage I palliation, specifically for cases of borderline HLHS, it provides the opportunity for the left ventricle to develop

before a decision is made. It also stabilises patients on heart transplant waiting lists. What makes the initial assessment even more difficult is the possibility of underestimating the left ventricular size due to an overloaded right ventricle distending and impinging on the left as seen by echocardiogram. One study showed that Echo grossly underestimates the left ventricular end-diastolic volume by almost 100%, and claims the average potential increase in its volume is 23% for HLHS patients [27]. This potentially leads to the unfair exclusion of patients from the 2VR, who are left with little alternative than to attempt the non-physiological 1VR.

The Geißen centre, one of the pioneering centres for the Hybrid Procedure, have recently published their results following initial palliation outlining the versatility of this option for HLHS and related left heart obstructive lesions [24]. Of the 20 patients noted in the study: two patients received a heart transplant with two deaths occurring while on the waiting list for transplantation; two deaths occurred following the Hybrid Procedure; two patients successfully underwent a successful 2VR with an additional patient awaiting 2VR surgery; ten patients underwent the Hybrid Stage II with one death and the final patient awaiting a Stage II repair.

As this study demonstrates, the Hybrid Procedure, which is often only used in high risk patients by some centres, delays the decision between a 1VR or 2VR repair, allowing the left heart structures time to grow. Assisting the surgical decision making process choosing between single and bi-ventricular repairs is a strong motivation for the improvement of patient-specific modelling. Once modelling of the Hybrid Procedure is developed to a suitably robust standard, incorporating patient-specific definitions of anatomy, circulatory and ventricular components, it may assist in this difficult decision making process. This was a key motivation in the need to develop patient specific modelling of the Hybrid Procedure further.

The later publication of Akintürk reported on their experience from Geißen, Germany on using the Hybrid Procedure as a basis for 1VR or 2VR [28]. The

decision of repair was based on pathological results e.g. RV and atrio-ventricular valve dysfunction, left ventricle growth and, most essentially, parental consent. Of the 18 patients who received a 2VR there were no deaths, with one patient later listed for a heart transplant. The overall survival rate for the Hybrid in all second stage repairs was 89%. This demonstrates the success and versatility of the procedure.

Alsoufi *et al.* look at the limited published results available for transplants and the Hybrid [13]. It is worth noting that the patients providing the data for these statistics are from surgeries at the start of the learning curve, and so the outcomes may improve with time.

With published hospital survival rates of between 82.5% and 90% [1, 25] with scope to improve after the learning curve [14], the Hybrid Procedure cannot be discounted as a primary treatment course as opposed to some centres using it predominantly for high-risk patients. Regarding the evidence of which method is superior when considering the Norwood or the Hybrid Procedures, there have been many publications [29–33]. All studies show no significant difference between the methods, with minor differences noted: inferior cardiac output and pulmonary supply in the early post-operative results following the Hybrid [32]; and reduced length of intubation time and both intensive care unit and overall hospital stay time [30]. As stated by many, a randomised controlled clinical trial similar to that for the modified BT versus Sano shunts in the Norwood Procedure is one way to determine any differences [7].

With this evidence, the benefits of the Hybrid Procedure, including the potential for 2VR, provide a strong motivation for further understanding and optimisation of the Hybrid Procedure through mathematical modelling. By producing patient-specific modelling (based on clinically appropriate data) to assist the decision making process for clinicians, the survival and long term health of a HLHS child may be improved.

Chapter 3

Cardiovascular Modelling

Mathematical models help understand function by simplifying real systems. Mathematical modelling became an important aspect of understanding science and physics ever since Isaac Newton first published *Mathematical Principles of Natural Philosophy*. Newton's approach of using mathematical equations to describe the relationships between variables based on experimental evidence is still the fundamental focus of scientific research.

Despite being difficult to obtain experimental evidence for medical science due to the invasive nature of data acquisition, cardiovascular modelling has a rich history. In 1735 Hales was the first to measure blood pressure in the arterial system observing that it varied over a cardiac cycle. Hales hypothesised that this was related to the elasticity of the large arteries [34]. Almost a century later, Weber was one of the first to make a critical observation: The systemic arterial system resembles the old-fashioned hand-pumped fire engines. These fire engines pumped water into an air chamber which provided a continuous outflow of water. Windkessel, German for "air chamber", models were born.

It was Otto Frank, in 1899, who quantitatively defined the Windkessel model in terms of a systemic peripheral resistance, and total arterial compliance [35]. Now referred to as the two element Windkessel model, this was the first class of lumped parameter or lumped circulation models (LPM/LCM), distributing the properties of the arterial system into discrete components re-

moving any spatial dependence. They are often referred to as zero dimensional (0D) models and can be considered analogous to an electrical circuit.

In this chapter, we introduce the various forms of mathematical models that have developed since the introduction of 0D models. This will focus particularly on the evolution of lumped parameter and the development of three-dimensional (3D) models as they are the basis for the research presented in this thesis. One dimensional models, although not utilised in this project, will briefly be discussed preceding a review of 0D and 3D models, which more recently have been coupled (also with 1D models) to address the issue of boundary conditions related to 3D modelling. This is referred to in the literature as multiscale modelling. The scope of mathematical models that describe various elements of the cardiovascular system (CVS) is far too broad to comprehensively review, therefore in this chapter, the relevant model types adopted in this research will be focussed on. Where the scope within the specific subsections addressed is great, publications focussed on congenital analysis will be prioritised.

3.1 One Dimensional Modelling

The motion of all fluid flow can be described by the Navier-Stokes equations, using conservation of momentum and mass, and certain specified conditions (boundary values, initial values, incompressibility of fluid) to construct the governing equations. One dimensional haemodynamic modelling can be derived from the axisymmetric (1D) form of the Navier-Stokes equations coupled with equations of equilibrium for the forces acting on the vessel wall. Often in the literature these equations are linearised to simplify the complex calculation of the solution [36]. These are often considered as analogous to the telegraph equations, again allowing the electric analogy [37].

The outcome variables for one dimensional modelling, include the radius of a vessel (often considered as area given the axisymmetric definition) as well as the fundamental pressure and flow solutions of the fluid. The study of 1D

models is predominantly focussed on pulse wave transmission throughout the arterial vascular network. By using branched networks to represent the structure of the cardiovascular tree, and the physical properties of each segment to derive the electrical equivalence of resistance, compliance, etc. the entire arterial system can be modelled. This uses information such as the natural or unstressed radius, length of a vessel, vessel wall thickness and Young's modulus.

By changing certain parameters (e.g. increasing Young's modulus, or decreasing radius) disease states such as stenosis [38, 39], or deployment of grafts [40, 41] or stents [42–44] can be assessed, and have been utilised in the context of clinical diagnosis analysing conditions such as hypertension and atherosclerosis.

A recent development in this field is the study of the wave intensity analysis proposed by Parker and Jonas [45]. This uses the product of pressure and velocity changes over a small interval as a metric for the rate of energy flux per unit area. This has already been used to analyse the pulse wave transmission in the left ventricle, coronary vessels, systemic arteries and pulmonary arteries (as cited in [36]). Regarding the appropriateness of 1D modelling, it has been shown numerically that by linearising around a steady state, 1D modelling matches the non-linear system in a very appropriate manner, even for very realistic test cases [43].

Investigations of 1D modelling for congenital networks are limited. This was one of the key reason for not investigating the multiple branched network models (based on reference diameters/areas and lengths of vessels to determine parameter values) for use in this research. Also, the additional difficulty in assigning physical parameters (e.g. dimensions, stiffness, etc.) for a neonate, particularly in a diseased state, resulted in a focus on the established LCMs already published. In the following section a succinct review of 0D, or lumped circulation models is presented.

Appendix A discusses mathematical models of the cardiovascular system from the full Navier-Stokes equations, to 1D modelling and then lumped modelling. Also included are comments on length scales of modelling, the discretisation of the Navier-Stokes equations, and choice of numerical integration with respect to time. These comments are in addition to the narrative of the research presented in the main body of this thesis.

3.2 Lumped Circulation Modelling

One dimensional (1D) and lumped circulation/parameter models (0D) are closely linked. Milisic and Quarteroni [46] have offered a formal proof that 0D models for the vessel network can be regarded as first order discretisations of one dimensional linear systems.

The cardiovascular system can be modelled as a closed hydraulic network acted upon by a pulsatile pump. Given this description, the hydraulic electric analogy is now presented. The two outcome variables of significance, pressure and flow, are analogous to voltage and current respectively. The resistance to flow (due to viscous dissipation inside the vessel) is well thought of as electrical resistance which restricts the flow of electrons. Capacitors represent the compliant chambers of the CVS included in any model (whether one or multiple) while the volume of blood stored in each chamber is analogous to charge. Another electrical element often used in cardiovascular modelling, predominantly in the larger vessels if at all, is the inductor where electrical inductance is equivalent to the inertia of the blood. A summary of the comparison is given in Table 3.1.

Using the hydraulic equivalent of Ohm's Law for resistance, introducing the complex inductance element results in Equation (3.1):

$$\Delta P = R \cdot Q + L \cdot \frac{dQ}{dt} \quad (3.1)$$

TABLE 3.1: Analogous terms used for hydraulic/haemodynamic problem approached from an electrical circuit analogy

Hydraulic Term	Electrical Term
Pressure (P)	Voltage (V)
Rate of Flow (Q)	Current (I)
Resistance to flow (R)	Electrical Resistance (R)
Blood Inertia (L)	Inductance (L)
Vessel Wall Compliance (C)	Capacitance (C)
Volume (V)	Charge (q)
Ohm's Law	Conservation of Momentum
Kirchoff's Law	Conservation of Mass

which when the inductance is neglected ($L = 0$) simplifies to the original Ohm's law adopted in Chapter 5:

$$\Delta P = R \cdot Q \quad (3.2)$$

The conservation of mass, comparable to Kirchoff's Law, dictates that the change in volume (charge) of a compliant chamber (stored in a capacitor) must equal the flow of blood (current) into and out of the chamber:

$$\frac{dV}{dt} = \sum Q_{in} - \sum Q_{out} \quad (3.3)$$

thus supplying a set of ordinary differential equations which can then be easily solved, in contrast to the partial differential equations found in 1D models.

It is on these principles that the lumped parameter Windkessel models are founded. They can be combined in multiple compartments (representing specific segments of the circulation) or used in isolation. Often the two or three

element Windkessel models are now used for impedance matching boundary conditions in multi-dimensional modelling, which will be addressed later in this chapter. The simplicity of the two element is its greatest strength, providing a simple way of reproducing the diastolic pressure decay in the aorta. It is used clinically to estimate total arterial compliance when combined with the aortic pressure pulse waveform and peripheral vascular resistance [47, 48].

In comparing a three element (RCR) Windkessel model (sometimes referred to as the Westkessel model following substantial study by Westerhof and co-workers [49]) to haemodynamics taken from anaesthetised open-chested dogs, Burkhoff *et al.* analysed the performance of lumped models. Regarding predicting stroke volume, stroke work, systolic and diastolic aortic pressure and oxygen consumption, the RCR model provides a good representation of the after-load. However, the peak aortic flow is significantly underestimated, while it slightly underestimates the mean arterial pressure and does not provide realistic aortic pressure and flow waveforms [50].

As more elements are added to the Windkessel models, the better the representation of the character of the vascular impedance data. This is effectively adopting the multi-compartmental approach where the identification of parameters through non-linear regression analysis becomes difficult. The authors opinion, based upon personal study and use of multi-compartmental models, matches that of Shi *et al.*: “... *there is a danger in the adoption of these more complex descriptions that, although in principle they can represent the system more accurately, in practice it is often very difficult to estimate appropriate values for many of the model parameters*”. The more parameters that need to be estimated, the greater the number of (often invasive) measurements are required, while the solution of the inverse problem of determining the parameter values is often non-trivial. This topic will be addressed again, when discussing in greater detail, the reproduction and verification of published models which enhanced the authors understanding greatly of the issues around multiscale modelling.

As is evident in the entirety of the literature regarding mathematical modelling of the CVS, including its specific subsections, the modelling methodology depends on the focus of the research. Not only regarding dimensionality, but also the degree of detail adopted within models of the same dimension. Specific 0D models are available looking at the heart [51–59], heart valves [53, 54, 60, 61], neuro-regulation [62–67], auto-regulation [68–71], venous circulation [66, 72–77] and pressure-dependent vascular properties, which is considered important in the coronary vessels and the veins [56, 62, 70, 71, 73, 78–80]. A comprehensive review and the references therein (many cited above) by Shi, Lawford and Hose [36] is recommended for a more detailed analysis of the literature pertaining to both 0D and 1D modelling. They also publish tables exposing the wide range of parameter values used in comparative models (Tables 4 and 5); and the variation in 0D models used, based on its clinical application (Table 6).

3.2.1 Modelling Experience

“What we have to learn to do, we learn by doing.”

Aristotle (384 - 322 BC)

The words spoken by Aristotle echo throughout this research project. In trying to decide what method of model to apply to the modelling of the Hybrid Procedure, the most productive way of following the literature was indeed to *‘learn by doing’*.

The ultimate goal of the research was to perform a ‘virtual Hybrid surgery’ on a purely patient-specific multiscale model, building on the generalised example from Laganà, Migliavacca *et al.* and the Modelling of Congenital Hearts Alliance (MOCHA) research group [81–84]. Thus certain models, all of which were supported by and developed in other publications, were studied initially in an attempt to reproduce their published results, and learn about lumped parameter modelling by *‘doing’* [85–87].

It was deemed important, with the prospect of applying the model to patient-specific data, to have as few compliant chambers as possible to reduce the number of parameters introduced. The first attempt was chosen for its applicability to the Hybrid Procedure, being a fully lumped model of the Norwood Circulation, the predominant surgical option for HLHS [85]. Additionally, this model later formed the coupled LCM providing boundary conditions for future multiscale modelling. Despite failing to reproduce the results quantitatively in the beginning of the project, qualitatively similar results were obtained, and the knowledge and experience gained in producing 0D models was essential. The adult model published by the New Zealand based group [87] provided greater clarity and was successfully reproduced. In the parameter identification methods described, they explicitly include the defining of initial conditions. The vital distinction was by reintroducing the volume/charge variable, where the Politecnico di Milano group had substituted it out in most compartments to only include pressure and flow highlighting that no indication of initial conditions were published. The work by the New Zealand based group then went on to approach the problem of parameter identification for patient-specific data. Despite this adult model being incompatible with the neonatal, hybrid data available it has great potential, and will be discussed briefly in Section 5.1.

By having difficulties in reproducing the original Norwood circulation lumped parameter model, and subsequently trying to simplify or adapt the model, certain specific problems were identified. This included the number of compartments to include in any model, balancing adequate description of the circulation with simplicity and reduction of parameters. The more compartments, the more parameters needed defining, hence concluding the same as Shi *et al* (see above). The original lumped circulation paper by Migliavacca *et al.* [85] was later simplified, by amalgamating compartments and altering certain aspects (e.g. fixing heart rate, linearising valve model, see section 3.2.1, neglecting inertia by omitted the inductor component) by Shimizu *et al.* and will be presented fully in Chapter 5.

The problems that arose, even after consulting models of the comparable circulations and methodologies cited [88, 89] (univentricular circulation for Glenn’s Procedure and full-term foetal circulation respectively) concerns developed with the justification for certain aspects of the methodology and can be presented in the follow distinct sections:

Heart Model

There are multiple forms of pressure-volume functions of ventricles (predominantly based on the left ventricle) in the literature. They range from basic linear elastance models, to exponential models, to those that include activation functions (which again have many different implementation). All model parameters (obviously depending on the model used) are fitted to best describe known pressure and volume tracings of the ventricle against time and as such makes it difficult to justify using different models over their alternatives, save for ease of use, provided it matches the data sufficiently. This is best seen in a review of 6 pressure-volume functions describing the left ventricle by Lankhaar *et al.* who concluded that a linear model suffices for realistic simulations of the instantaneous pressure-volume relation [90]. The six models reviewed were:

1. Linear Model with Fixed Intercept:

$$P(t) = E(t)[V(t) - V_0]$$

2. Linear Model with Free Intercept:

$$P(t) = E(t)[V(t) - V_0(t)]$$

3. Langewouters Model:

$$P(t) = P_0(t) + P_1(t) \tan \left(\frac{\pi \left(V(t) - \frac{1}{2} V_m \right)}{V_m} \right)$$

4. Sigmoidal Model:

$$P(t) = A(t) \frac{[V(t)/V_{ref}(t)]^{\alpha(t)}}{1 + [V(t)/V_{ref}(t)]^{\alpha(t)}} + B(t)$$

5. Shroff Model:

$$P(t) = E(t)[V(t) - V_0][1 - \rho \dot{V}(t)]$$

6. Burkhoff Model:

$$P(V, t) = \alpha(t)[E_{max}(V - V_0)] + [(1 - \alpha(t))[A(\exp B(V - V_0) - 1)]$$

Their conclusion was reached based on the fit to the data tested and the number of parameters that needed identifying. In fact, the Migliavacca model, and its predecessors from the Politecnico di Milano group, used the Burkhoff model with a further term to account for the viscous properties of the myocardial tissue. This was dependent on the rate of change of volume of the ventricle, therefore introducing an additional differential equation which complicates the solution. Negligible difference was observed in the initial attempts at validating the Norwood circulation model by removing this term, and it appears to have been removed by other groups that have developed the original model [86, 91]. Thus, as this model of the pressure-volume relationship of the ventricle was the most intuitive and was readily implemented, the viscous properties were neglected in our lumped circulation model of the Hybrid circulation (see Chapter 5).

The appeal of the linear model with fixed intercept was its use of physiological data. The original work of Suga *et al.* [51] and the use of a Fourier summation description of a normalised elastance, calculated from single heart beats from a range of health conditions, [52] was strongly considered for future use. The applicability to a single ventricle neonatal heart was uncertain, particularly in a patient-specific context and so this was not adopted for the work of modelling the Hybrid Procedure.

Regarding patient-specific heart modelling, although not fully implemented in this research due to lack of time and sufficient clinical data, worthy of specific mention (in the context of patient-specific irregular heart configurations) is the work by the New Zealand cardiovascular modelling group [92]. This proposes a method of identifying a patient-specific cardiac driving function (combined activation function and varying elastance value) based on the aor-

tic pressure waveform. This is where the future of modelling has to head. Not generalised models to give indicative results of the circulation, but patient-specific models, particular to each patient to assist in individual clinical care.

Valve Model

As discussed by Shi, Lawford and Hose, the simplest and most commonly adopted valvular model is treating it as an ideal diode [88, 93–95]. Two diode models have been used by the Politecnico Milano group. In all cases the pressure drops across the outflow valve from a ventricle are described by the non-linear expression:

$$\Delta P(t) = K \cdot Q(t)^2 \quad (3.4)$$

while in the model of the foetal circulation [89] the atrioventricular valves have an additional inertial component:

$$\Delta P(t) = K \cdot Q(t)^2 + L \cdot \frac{dQ(t)}{dt} \quad (3.5)$$

With the inclusion of the inertial term $\left(L \cdot \frac{dQ(t)}{dt}\right)$ the equation has changed from an algebraic to a differential equation and therefore changes the method and order in which all variables are solved. There was no justification given in the later papers [85, 88] for why this inertial term was discounted, nor was there satisfactory reference provided for (3.5), with the citation of Yellin *et al.* [96] not justifying the quadratic Poiseuille resistance expression as in the other non-linear equations found in the paper as suggested.

Shimizu *et al.* later implement a linear valve model, using the same numerical value for the resistance:

$$\Delta P(t) = R \cdot Q(t) \quad (3.6)$$

Until later on in the project, the distinction between the linear and quadratic diode model was unclear, particularly in using the same numerical value for the resistance. This was later clarified in the process of implementing the full coupled model and will be presented in Section 7.2.1.

Atria Model

Compared with the equations used to model the atria, the valve models used in the literature seem consistent. Of the three models produced by the Politecnico Milano group (Norwood, Univentricular Glenn and Foetal Circulations) a different one was adopted in each. The three atria models used are as follows:

1. Constant Compliance:

$$Q_{\text{in}} - Q_{\text{out}} = C_a \frac{dP_a}{dt} \quad [88]$$

2. Constant Compliance with Activated Contractile Term:

$$Q_{\text{in}} - Q_{\text{out}} = C_a \frac{dP}{dt} + A_a(t) \cdot U_{a0} \quad [89]$$

3. Pressure-Volume Function:

$$P_a = P_0 \left(e^{K_E(V_a - V_0)} - 1 \right) + A_a(t) \left[E_i^*(V_a - V_0) \right] \quad [85]$$

where the Constant Compliance model treats the atria as any other Windkessel compartment, the addition of the Activated Contractile Term represents the systolic-diastolic cycle of the atria, and the Pressure-Volume Function describes the beating atria in the same manner as the ventricle.

In all three papers, no justification or validation is done of the method chosen to represent the atria, and no reasoning given for the increased complexity compared with that used in the previously published similar circulation model. However, an investigation by Korakianitis and Shi investigate the effect of including the atrial contraction model. The more complex atrial description helps capture such clinical phenomenon as a-wave (local peaks in the atrial pressure response at the end of diastole) and both A and E velocities (the two local peaks in transvalvular flow) and validate that atrial contraction

accounts for 25% of the stroke volume [61]. The alternative argument is that the simpler the model of the atria, the easier it is to implement and the fewer physiological parameters needed to characterise the model, assuming that an appropriate value fits the test data. Following the publication by Shimizu *et al.* [86] the Pressure-Volume Function method was adopted in this research.

Initial Conditions

When solving time dependent differential equations, initial state conditions are essential. In trying to reproduce the Migliavacca Norwood LCM results, no indication of initial conditions was supplied. The dependence of the final periodically steady solution upon the initial conditions was not fully appreciated by the author until the published adaptation of this work by Shimizu *et al.* was reviewed. Although the initial conditions in terms of the distribution of the blood volume is ‘forgotten’ in the cyclic nature of the solution, the total stressed blood volume dictates the output of the model [86]. Thus in attempting to supply initial pressure values for the system, without considering the total volume of stressed blood, the final results can vary significantly. This issue will be addressed specifically within Chapter 5 and considered again in Chapter 7.

3.3 Three Dimensional Modelling

3.3.1 Introduction

The equations describing the mass and momentum conservation of all fluid motion, as stated earlier is the Navier-Stokes (N-S) equation:

$$\begin{cases} \rho \frac{\partial \mathbf{u}}{\partial t} + \rho (\mathbf{u} \cdot \nabla) \mathbf{u} - \mu \nabla^2 \mathbf{u} + \nabla P = 0 \\ \nabla \cdot \mathbf{u} = 0 \end{cases} \quad (3.7)$$

where ρ is the density of blood, \mathbf{u} is the velocity field and μ is the dynamic viscosity of blood. In this study, blood is considered a Newtonian fluid. This is a widely used simplification in biological computational fluid dynamics (CFD) studies. Blood, of course, is not Newtonian as the viscosity, μ , varies with wall shear rate [97]. This can be due to the complex constitution of blood with red blood cells being suspended (in addition to other elements) in plasma, with phenomenon such as the aggregation of the red blood cells resulting in non-Newtonian behaviour.

The N-S equations can be solved over a defined region of interest following several processes. First the region of interest (in our case a defined vascular region) has to be discretised into sufficiently small control-volumes. The governing equations given in Equation (3.7) are then integrated to obtain algebraic equations for the variables of interest (pressure, velocity). These equations are then approximated over the control-volumes and iterative techniques are used to obtain a solution. As well as spatial discretisation, the equations can be discretised temporally so transient problems can be solved.

The process of spatially discretising the region of interest is known as “*meshing*”, and requires defining points in space (nodes) throughout the region, which get linked together to form edges, with a group of edges making a face, and a group of faces defining a cell (see Figure 3.1).

In order to solve the equations, certain information must be defined at certain locations, or *boundaries* of the region, in addition to initial conditions if solving for unsteady flow. This invokes Newton’s Laws where forces must be equal and opposite. The simplest boundary conditions for any walls in any CFD simulation, is that of rigid walls and a non-slipping condition. The rigidity of the wall means that its motion, and hence velocity is zero. The non-slipping condition requires that the velocity of the fluid adjacent to the wall is equal to the velocity of the wall (zero). More complex force balances are possible, and is currently being explored by the leading research groups in the cardiovascular field. It is known as Fluid-Structure Interaction (FSI) mod-

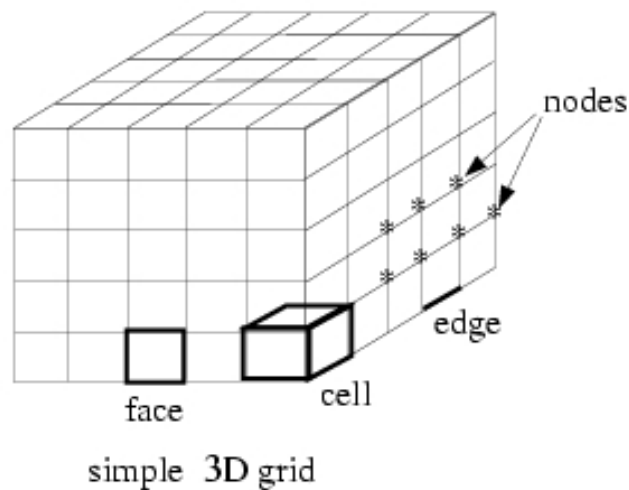


FIGURE 3.1: Illustration of mesh definitions

elling and is the current state of the art in modelling methodologies which has been made possible by the increased availability of appropriate computing power. This will be discussed below in reviewing the 3D CFD available in the literature.

The remaining boundaries must now be defined so that the solution can be fully determined. This involves specifying one of the dependent variables (pressure profile, velocity/flow profile) over the inlet and outlets, so that all other dependent variables are calculated. With regard to cardiovascular modelling, this takes the form of specifying the pressure distribution at the open orifices or alternatively some form of flow/velocity distribution.

It is possible to discretise and linearise the Navier-Stokes equations using established numerical methods for solution of spatial and temporal equations oneself in writing one's own numerical code. This gives greater control on possible inaccuracies, or scenarios in which the assumptions used are inappropriate. Knowing the specific problem being solved, the code can be streamlined to suit. However, as CFD is such a widely adopted approach, for all forms of fluid flow, commercial software is available. This allows timely implementation of rigorously tested code for many forms of fluid flow.

3.3.2 Published 3D Models

Computational Fluid Dynamics first emerged as a tool for investigating local haemodynamics for vascular flow in the mid 1980's when bifurcations were analysed [98]. Perktold was an early pioneer of 3D CFD in the late 1980's and 1990's [99–102]. By the mid 1990's CFD was being integrated with medical imaging linking local haemodynamics with vascular dysfunction [103, 104].

Initially generalised or idealised geometries were adopted for specific research questions, similar to what dictated the model adopted for lumped parameter modelling. Among the topics analysed were large artery anatomic variations, wall compliances, rheology of blood (Newtonian vs. non-Newtonian), mass transport (drug delivery) and exercise. The relationship between low wall shear stress and vessel wall remodelling is validated by CFD. Computational Fluid Dynamics has been used to simulate a wide range of cardiovascular research topics. For a brief overview of the development of this field, please refer to the review by Steinman and Taylor [105] and the references therein. There are many distinct sub-groups, which have been reviewed elsewhere, that are related but are too numerous to explore given our applications in the context of congenital heart repair. These include areas such as stent design (see [106]), ventricular assist devices (see [107]) and even FSI studies looking at the flow through the cardiac chambers and valves (see [108, 109]).

The main limitations of most published 3D CFD analysis is the assumptions of rigid walls, Newtonian fluids, fully developed boundary conditions and laminar flows. This is beginning to be challenged with the advancement in fluid-structure interactions.

Specifically of interest within this investigation, is the 3D CFD studies of congenital heart repairs. This has analysed the use of different systemic-pulmonary artery shunts used in the Norwood Procedure [5, 110], and the different grafts available for the Fontan Procedure [111–113]. A comprehensive review of studies modelling the Fontan circulation up to 2008 was carried

out by DeGroff highlighting the limitations indicated in this chapter [114]. It highlights the under-utilised resource of mathematical modelling and encourages the developments seen in the most recent literature and in this thesis.

In the past decade, CFD has become relatively easy to simulate, and as a result studies with imposed boundary conditions have been superseded by multi-scale modelling. This is the leading technique in boundary condition specification, and is being adopted by an increasing number of research groups.

3.4 Multiscale Modelling

Boundary conditions of 3D models is very much a current, crucial issue [115]. Before the introduction of multiscale modelling, boundary conditions at inlets and outlets were either prescribed profiles, or fixed pressure/flow values [116] (and references therein). A study by Pekkan *et al.* applied steady state conditions to the Fontan anatomy, which is an acceptable approximation due to the low pulsatility in the pulmonary circulation. The numerical results were validated against an *in vitro* model based on MRI data [117].

The problem with this approach, is that what is of interest is how a change in the local anatomy affects the global haemodynamics. By prescribing what is happening at the inlets and outlets, the upstream and downstream pressures and flow rates/distributions are already defined. In changing the anatomy, through surgery, it should effect the global haemodynamics. The outcomes that contribute to the understanding of whichever surgery is under investigation (e.g. the Fontan Procedure) pertain to the results *within* the geometry. This is of course still significant, when testing configurations that involve fixed flow rates, or pressures, or investigating prescribed conditions for example, of ventricular assist devices or (drug eluting) stent design. What is now of interest is optimising the anatomical configuration of the surgical region (i.e. performing *virtual surgeries*) with respect to the global haemodynamics and ventricular workload. This is where the adaptable boundary conditions from

multiscale modelling has been developed from the original publication by Laganà *et al*[118].

The theoretical definition and exploration of coupling models of various dimensionality is available in the literature [119–122] which has recently been improved upon to be more versatile in boundary coupling types, and allow implicit time integration techniques [123]. In the cited papers’ test cases of interest, such as two dimensional coronary artery bypasses (original artery being fully and partially occluded) and simple one dimensional examples are given, with investigations of specific anatomical variations and surgeries published shortly after. An evolution of 3D applications were presented where a straight pipe in a simple hydraulic network, then straight pipe of the scale of a coronary artery in a cardiovascular network were tested, followed by a simplified 3D systemic-pulmonary shunt [118]. This validated the approach of determining boundary values from the 3D region to input to the lumped model which in turn would supply updated boundary conditions for the 3D region for the next time integration step.

This fully explicit approach is adopted in this research and is presented in Chapter 7. The simplified shunt was then replaced with a more comprehensive 3D model of the great arteries of an idealised/generic HLHS patient and various dimensions of B-T and Sano shunts simulated [81, 82, 124]. These studies highlighted the issue of coronary supply, with a central shunt resulting in a reduction in blood supply to the heart. When considering the cardiac output, a larger shunt diameter is necessary for a Sano shunt versus a B-T shunt. They also demonstrated good correlation with clinical results. Kim *et al.* apply similar 0D-3D coupling, involving a model describing the time varying elastance properties of the ventricle, although not a closed loop circuit, providing physiologically realistic flow and pressure waveforms under rest and exercise conditions for a patient-specific adult thoracic aorta (including simulation of a coarctation) [125].

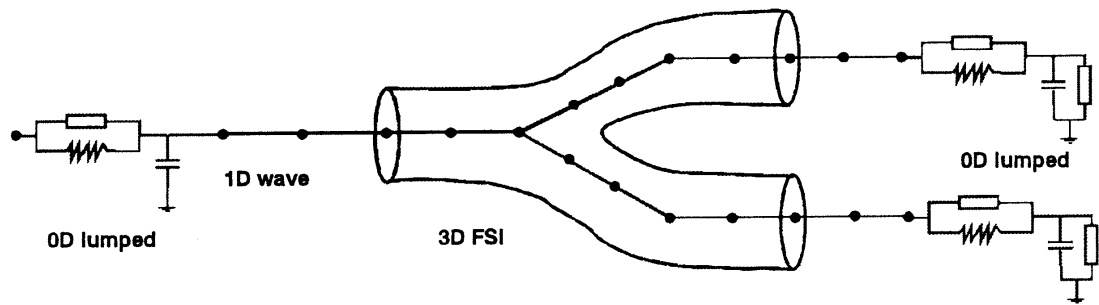


FIGURE 3.2: Multiscale modelling concept: Coupling of varying degrees of dimensionality as published by Van de Vosse [126]

Figure 3.2 taken from the introduction to the special issue of the Journal of Engineering Mathematics (Volume 47/3-4, 2003) on the mathematical modelling of the cardiovascular system [126] surmises the multiscale concept. The less detailed model can determine the pressure/flow at an interface which can be passed on (given certain assumptions and interface conditions) to a model of greater specificity. This can also be reversed with the output of a model of greater detail being simplified to pass on information to a model of lower dimensionality. This means that certain regions, where the local haemodynamics are of critical importance, or under greater scrutiny, can be analysed at an appropriate level, while still accounting for lumped upstream and/or downstream effects. For mathematical description of the different network coupling approaches (whether pressure or flows are specified for the higher dimensional region) see [121].

It was this work and similar works of this nature, that motivated the research presented in this thesis with specific focus on how to implement and integrate this technology within a clinical setting, for the Hybrid Procedure. Given the massive patient-to-patient variation patient specificity was essential. With this motivation, it was hypothesized it would be possible to either (a) optimise the Hybrid Procedure for a specific patient, or (b) identify which patients of borderline left ventricle size would be strong candidates for biven-tricular repair. During the course of this research project, the same group later published a idealised model of the Hybrid circulation [83], adapting the idealised geometry from the Norwood studies [81, 82, 124]. The three variations

of surgical protocol for Hypoplastic Left Heart Syndrome were then compared [127].

The Norwood studies showed higher diastolic pressure, decreased pulmonary artery pressure, lower $Q_p : Q_s$ ratio, and higher coronary perfusion pressure for the Sano shunt with minimal regurgitant flow (despite the lack of a valve as modelled in 0D in [86]) [82, 124]. The Hybrid study concluded that the diameter of the stent (7 mm vs 8 mm) has no significant influence, while the diameter of the pulmonary banding is critical for haemodynamics and oxygen delivery in particular [83]. The optimal band diameter proposed by the study was 2 mm, however it must be emphasised that this is the *internal* luminal diameter, and not the *external* band diameter applied. This is a key clinical distinction which could potentially result in the mistrust of mathematical modelling from experienced surgeons, who would be well aware that a 2 mm band is potentially lethally tight. The comparison between the three alternative protocols demonstrated that compared with either of the Norwood configurations, the Hybrid palliation had higher $Q_p : Q_s$ ratio and lower cardiac output. The total systemic oxygen delivery in the Hybrid was also inferior. Cerebral oxygen delivery, modelled by separating the upper and lower body in the LCM, was also lower in the Hybrid [127].

The studies of the idealised Hybrid geometry, adapted from previously investigated idealised Norwood geometries, were published during the course of this research project. This thesis presents, in parts, similar work with a key distinction made regarding the integration of clinical data, attempting to apply this methodology to specific patients using historically collected data without additional invasive procedures. The findings from the culmination of the research will illuminate how these results were obtained, and advise exercising caution when interpreting these results due to methodological ambiguity found in the literature.

3.5 Modelling: The Future and Beyond This Study

A review in 2010 by Pennati *et al.* [128] focus specifically on the challenges being faced in the single ventricle circulation. The references therein (many of which have been cited above) compare the limited publications on the shunt-type circulations (Norwood, Hybrid, HLH) in contrast to the vast number of publications studying the Fontan or Glenn circulations. They highlight the lack of clinical data available to date, mainly as a consequence of the rarity of data, the limited time frame for data collection and the young age of the patients undergoing this course of treatment. This is something this research has attempted to address, by determining what data that is routinely collected as current protocol which can be used with mathematical modelling in mind (see Chapter 4).

Six key topics to be addressed are identified by Pennati *et al.* The first two pertain to patient specificity as outlined in [129], and although patient-specific parameters are discussed in this thesis, attempts at parameter identification for a fully patient-specific lumped circulation model were unsuccessful. The use of a clinically captured 3D region, instead of an idealised geometry, however, has been. Regarding patient-specific parameters for the coupled 0D/1D models, they must be identified and determined within physiological remits unlike the concept of *tuning* the parameters as in [130] which alters the parameters of the circulation model to obtain a targeted output from the 3D simulation.

Other key topics identified by Pennati *et al.* were the need to model the effect of both the global circulatory responses and the local vessel structure/remodelling in the short, medium and long-term. For example, the global haemodynamics would influence the contractility of the heart, particularly in a single ventricle circulation. Caution must be exercised when considering predictive patient-specific modelling, particularly what medium term effects on the lumped circulation any geometrical changes can have. This is highlighted in

[115], where pre-and post-surgery simulations and clinical data are combined. The most significant remarks warn against the difficulties in accurately predicting the post-operative results. Attempting to reproduce the post-operative anatomy from the pre-operative anatomy is difficult due to geometrical differences, probably due to vessel distortion and synthetic conduit attachment. It also raised concerns over the applicability of downstream lumped parameter values, as the pre-operative resistances are not compatible with the clinical data, suggesting that the pulmonary vascular resistances change individually dependent on the post-surgery haemodynamics.

The final key topic from Pennati *et al.* requiring further research was the assumption of rigid walls. This is acknowledged as one of the major limitation of this study. It was shown that in shunt-type systemic geometries, the lack of fluid-structure interaction is more significant than in the lower and less pulsatile pressures found in the cavopulmonary anastomosis [128]. Due to the limited resources and the development of the model starting afresh, rigid walls were considered out with the scope of this study.

One future avenue of research in this topic of interest that explores both the above issues is that discussed in [131] which presents a new computational framework combining the developments of until recently separate fields. Biological solid and fluid mechanics and exploitation of new information on the biology of vascular growth and/or remodelling can help simulate vessel adaptations, disease progression and clinical intervention (e.g. pharmacological agents, or growth of structures with fixed shunts attached). This of course requires great advances in the knowledge of how vessel growth and disease respond to different haemodynamical, biomechanical and biochemical changes. Again, this was beyond the scope of this research.

The effect of respiration is thought to play an influential role in pulmonary haemodynamics. The Modelling Of Congenital Hearts Alliance, a collaboration with its core base from the Politecnico di Milano group, have recently published a model that implemented the effect of respiration on the Fontan

circulation [132]. Although they found no significant differences by including respiration, the physiological waveforms have visibly improved. This offers the potential for more accurate parameter identification through improved averaging techniques if the respiration effect is accounted for in the averaging process.

The MOCHA collaboration group have also utilised the theory presented by Marsden *et al.* [133] of geometrical optimisation based on a prespecified (clinically relevant) measure of performance. Building on the 2D, simplified cases presented in the original work, an optimisation of Norwood (BT) shunt placement is investigated [134]. Results showed that a smaller shunt diameter with a distal shunt-brachiocephalic anastomosis is optimal for systemic oxygen delivery, whereas a more proximal anastomosis is optimal for coronary oxygen delivery and a shunt between these two anatomies is optimal for both systemic and coronary oxygen deliveries.

An attempt at incorporating patient-specific lumped parameter model has recently been published by MOCHA [135, 136]. This is a positive step towards reaching the goal of patient-specific LCMs, however their methods would be best described as *patient-specific scaling* of the previously adopted generic lumped values. Clinical validation is not yet forthcoming.

Chapter 4

Processing Clinical Data

4.1 Ethical Approval

Access to anonymised patient records for clinically selected appropriate patients was approved by the Caldicott Guardian. This permitted access to all data that had potential use in generating a patient-specific model prior to any potential clinical study based on this model being proposed. A copy of the approved request is supplied in Appendix B.

4.2 Acquisition of Clinical Data

In order to implement truly patient-specific modelling, it is vital that actual clinical data is used to enable the derivation of the parameters used in a Multiple Windkessel model. Work on an adult physiology for identification of certain cardiovascular events has been carried out by [87]. This is in contrast to the conventional selecting of parameters to produce clinically appropriate output from sample data [85, 137, 138]. The methods used to gather the relevant clinical data needed to derive Lumped Circulation Model (LCM) parameters are described presently.

Data was available in historical pictorial form only. This meant that all data had to be manually digitised and then processed appropriately for further use. The clinically available data for potential LCM parameter identification

came from two sources: Continuous Wave Doppler (CWD) velocity profiles; and pressure profiles from an invasive catheterisation procedure. The velocity profiles were intended as a precursor for volumetric flow data, which can be determined using Equation (4.1) where v is the time dependent velocity normal (perpendicular) to the cross-sectional area of the vessel A . The start of a cardiac cycle is denoted t_0 , while the period of the heart beat is denoted by T . Periodicity of $v(t)$ is assumed. This is necessary to be able to converge to a periodic solution in any intended final model.

$$Q = A \int_{t_0}^{T+t_0} v(t) dt \quad (4.1)$$

Equation (4.1) is based on a number of assumptions:

1. equal velocity across a constant cross-section (alternatively a mean velocity \bar{v} is provided)
2. that the velocity is measured at the same location as the measured cross-sectional area
3. that the measured velocity is normal to A

This is dependent on the original capture of the Doppler velocity profile by the clinician, and was out with the control of this project, due to the nature of using routine, historical data. Corrections are possible by studying how CWD is determined, but difficult to apply retrospectively due to the unavailability of all the required data to apply these corrections satisfactorily.

4.2.1 Further Considerations Regarding the Flow Rate Profiles

The methodology applied to the processing of pressure profiles was also used for the flow profiles; this is reinforced by many of the figures used to demonstrate the methods originating from flow orientated data. Flow data was used to present the issues below as they were more pronounced. The flow data is produced originally from velocity profile data (with respect to time) using Equation (4.1).

In the clinical setting it can often be difficult to capture the normal velocity exactly, especially when spatial accuracy is required. This is further complicated in this study by the many extremely irregular anatomies found in Hypoplastic Left Heart Syndrome. Therefore the data captured was *entirely dependent* on the expert echocardiogram user's interpretation, which was specifically undertaken for *clinical diagnostic purposes* and not optimised for this research. This means that, particularly in early available cases, not all profiles were available from the same physiological conditions, with some profiles not captured at all.

This project has been highly focused on utilising data acquired from routine clinical procedures for the use in patient-specific modelling, aiming to determine what can be achieved without exposing these very ill children to traumatic and potentially unnecessarily risky procedures such as the general anaesthetic needed for an MRI scan. This creates many problems with the acquired clinical data as some compromises are inevitable, but this is one of the pertinent questions raised by this research. What modelling can be achieved without additional, invasive procedures? What data can be used as a surrogate for the missing data so that the hypothesised methodology can be assessed? What justification can modelling give to either justify or alter clinically invasive protocols?

With the clinical motivation in mind, when undertaking an echo scan, the patients are not anaesthetised and therefore it is potentially difficult for the operator if the child is perhaps struggling. It may also be awkward to position the probe at a specific angle. In short, clinicians do the best they can to get what they need for diagnostic purposes and anything else, for now, is a bonus. Therefore views such as cross-sections of valves, or of banding locations or stents are not commonly carried out resulting in approximations based on the cross-sectional area A being circular and measuring the maximum diameter (D):

$$A = \pi \frac{D^2}{4} \quad (4.2)$$

Due to the unconventional layout of the structures of the heart in HLHS, and their spatial proximity to each other, it can be difficult to capture the exact perpendicular velocity at the precise location required. In fact, in some scans, e.g. through the pulmonary valve, through the right pulmonary band and down the stent, they are so close that one may see multiple profiles on the output. It is almost a ‘ghosting’ effect with this phenomenon illustrated in Figure 4.1. Also these vessels are not straight, and when curvature is involved, it creates even more uncertainty as to determining the correct velocity magnitude normal to the cross-section under consideration. This is almost impossible to quantify precisely but qualitatively is considered adequate for diagnostic purposes. The velocity profile output from *Royal Hospital for Sick Children (Yorkhill)*, unlike some Doppler ultrasound, is not corrected for angle.

Angle correction is necessary because the Doppler techniques gives the velocity profile along the direction of the probe. If it is not in line, i.e. an angle of 0° , then the output is the velocity component in the direction of the probe (both positive and negative depending on the Doppler frequency shift). So if the direction of flow is at an angle θ from the direction of the probe, using simple trigonometry, the magnitude of the desired velocity measurement can be determined by dividing the measured magnitude by the cosine of the angle. For clarity, if u is the measured velocity magnitude, and θ is the offset

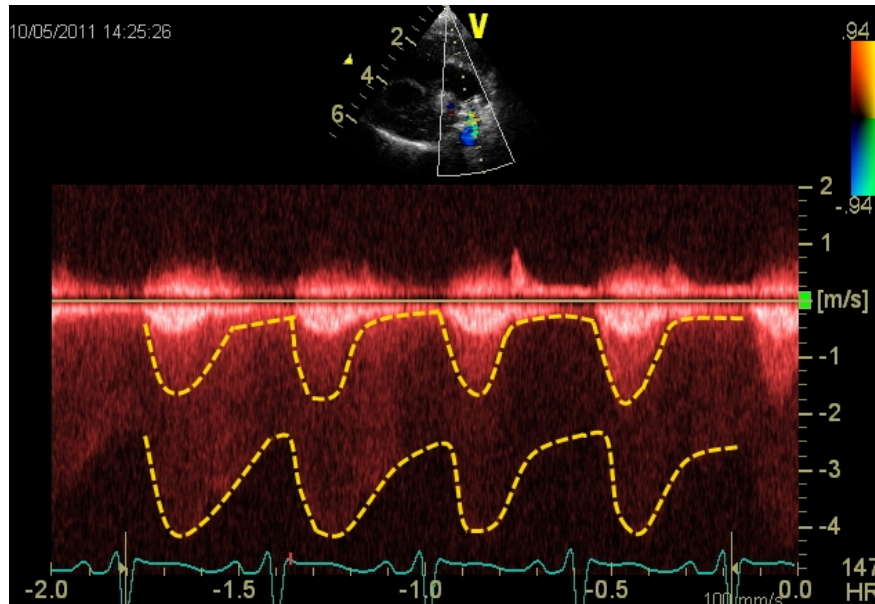


FIGURE 4.1: A Doppler echocardiogram showing the ‘ghosting’ of multiple velocity profiles from a single observation. The flow through the pulmonary valve is most prominent, then the flow through the stent can be seen behind with the profile of the right pulmonary band faintly visible around 4ms^{-1}

angle of the flow and the investigating signal, the true velocity magnitude v is determined by:

$$v = \frac{u}{\cos \theta} \quad (4.3)$$

which of course means that $v \geq u$ as $\cos \theta \leq 1$ for appropriate angles. As long as the angular offset is within 30° the error is approximately less than 15%, with 30° being a significant angle that an experienced operator would easily correct for. Figure 4.2 illustrates the concept of angle correction. There are other concerns regarding what plane of the vessel the measurement is made as all measurements are captured from a 2D slice which of course can be angled. As stated earlier, the velocities captured by the echocardiograph experts is assumed correct. Using their experience, θ is corrected for by the echocardiographer, and all limitations are fully acknowledged hence the predominant use of this form of data being diagnostic.

In summary, there are multiple factors that can lead to errors and difficulty in obtaining quantitatively accurate flow data from CWD. This format of data

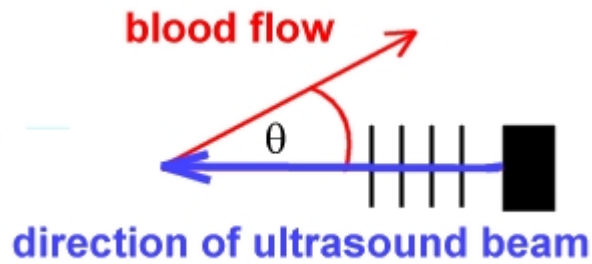
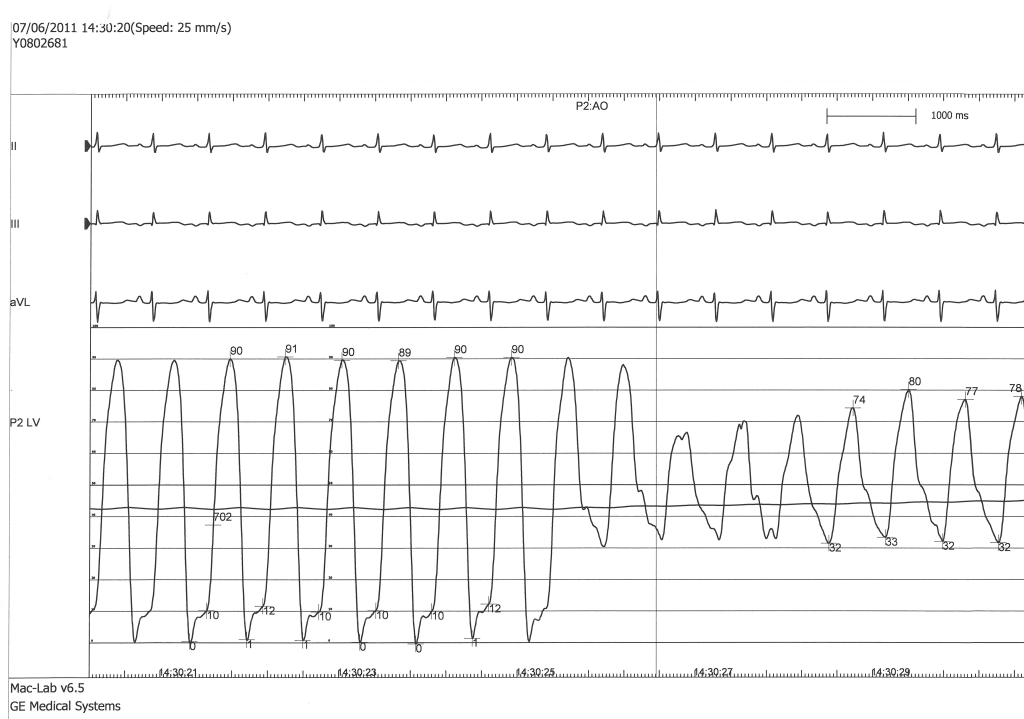


FIGURE 4.2: Illustration of the doppler angular correction procedure

has fantastic clinical diagnostic and qualitative qualities, but presents multiple opportunities for the introduction of quantitative errors. There was little justification at this stage to alter the current clinical practice regarding the capture of ultrasound data. It is best used in conjunction with other clinical data such as other imaging (where flow data can be obtained from magnetic resonance imaging) and catheterisation data. Alternatively, flow profiles can be measured more accurately with specialised flow meters, however this would require invasive investigations. However, it is worth proposing a clinical investigation that would compare a set of velocity/volumetric flow measurement protocols with currently accepted clinical standards, due to the non-invasive nature of data acquisition.

4.3 Format of Raw Clinical Data

Anonymised images of clinically stored velocity profiles were saved in jpeg format directly from the onsite EchoPAC software (GE Healthcare, Milwaukee, WI). As outlined above, interpreting the velocity profile required user knowledge and experience to interpret the variable intensity of the CDW output as already seen in Figure 4.1. Also seen in Figure 4.1 is the simultaneous Electrocardiogram (ECG) which was used to identify the peak of the R-wave, the most prominent feature of an ECG, in systole. The timing of the R-wave was used as the start of each heart cycle ($t_0 = t_R$).



(a) Pressure profile



(b) CT slice

FIGURE 4.3: Examples of images available from raw clinical data of catheterisation and CT investigation

For the pressure profiles, anonymised hard-copy printouts were obtained from the catheterisation procedure. These were then electronically scanned and also saved in jpeg format. Figure 4.3(a) is a sample of the available image. As with the velocity profiles, the ECG was visible and used as an isochronal time point to synchronise all data.

4.4 Digitisation

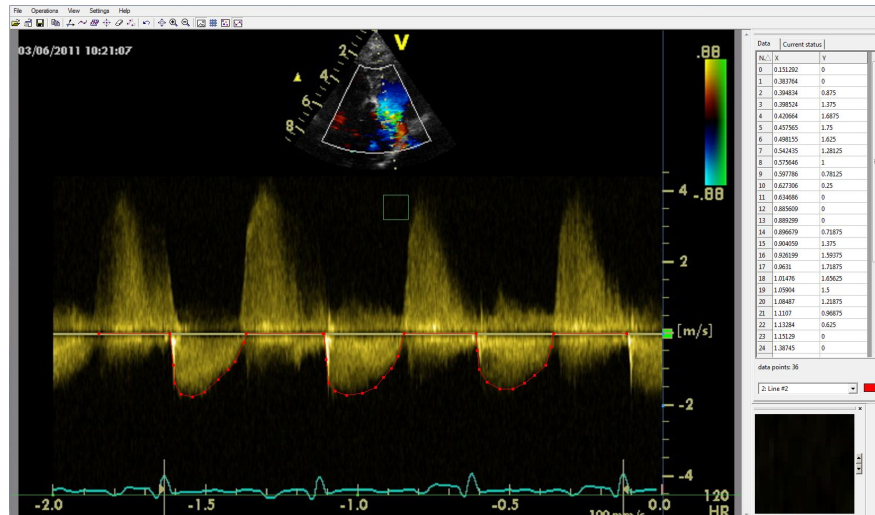
The digitisation process of converting the jpeg image files into usable numerical data sets consisted of four steps:

1. Manually selecting data points from the raw image file
2. Grouping the continuous data into individual beat data sets for each family of profiles
3. Interpolation of each data set
4. Generating an ensemble average profile for each distinct family of profiles

4.4.1 Step 1

The software package GetData Graph Digitizer (Sergei Fedorov, Moscow, Russia) was used to manually select a sufficient number of points of paired (t, x) data from the print out to describe the wave profile. The t values denote time, while x denotes the general form of either velocity or pressure. By marking the t and x axis scales (found on the jpeg), each value could then be scaled and calculated by the software. Additionally the t_R values of the peak of the R-wave were noted to distinguish a consistent time point for each beat, with the magnitude of the ECG signal unnecessary.

Figure 4.4 shows screenshots of the manually captured profiles. This process introduced errors due to unavoidable manual processing of the raw data.



(a) Doppler velocity data from echo



(b) Pressure data from catheterisation

FIGURE 4.4: Screenshot of GetData software used in digitising image files in to usable data

An ensemble averaging process was undertaken to counteract this issue. The data was then exported automatically into a spreadsheet for use in Excel 2007 (Microsoft, Redmond, WA) for Step 2.

4.4.2 Step 2

A custom Macro was written to process the raw continuous data into data sets of individual beats using Excel (Microsoft, Redmond, WA). Two variations of processing was implemented. The first normalising the time values by the the

period (T), the second using absolute time, with each having its own advantages and disadvantages. A comparison will be presented following a description of each respective methodology.

The list of t_R points were used to identify which time points in the full continuous data set of (t, x) data corresponded to the reference start point of each beat. For cases when there was no exact match, a linear interpolation of the paired data either side of the ECG time point (t_R) was used. Where (t_-, x_-) and (t_+, x_+) are the paired data points either side of t_R , the corresponding x_R was calculated as:

$$x_R = x_- + \frac{(t_R - t_-)(x_+ - x_-)}{t_+ - t_-} \quad (4.4)$$

This was necessary for both processing methods, with the location of the data pair at the peak R-wave of a heart beat noted for the ordering process. It was at this stage that the time processing methodologies diverged. In both cases each t_R was used to separate the continuous (t, x) data in to individual beat groupings. Multiple smaller data sets (t', x') were produced where the time component (t') was adjusted with the starting value of each set, t_R , zeroed.

Normalised

For the normalised time processing, the time values were divided by the period of each beat $t_R^{(n+1)} - t_R^{(n)}$. Therefore all time points (t) in the list between the noted t_R values were determined by:

$$t' = \frac{t - t_R^{(n)}}{t_R^{(n+1)} - t_R^{(n)}} \quad (4.5)$$

with all corresponding x data unchanged.

Absolute Time

For the absolute time method each beat's data set started from the (t, x) point before the $t_R^{(n)}$ denoting zero, and five data points succeeding $t_R^{(n+1)}$ were used to ensure enough forward data was available to allow "clipping", a process used to ensure uniformity of period which is guaranteed in the normalised approach. This was necessary as the data had varying heart rates for individual profiles (beat-to-beat) *as well as* between profile families (continuous data from different locations in the vascular tree). This will be discussed in Section 4.6.1. Therefore t' was defined as:

$$t' = t - t_R^{(n)} \quad (4.6)$$

where t runs from the data point before $t_R^{(n)}$ to the fifth time point following $t_R^{(n+1)}$. The additional negative timepoint in the beat dataset was necessary for the interpolation of $x_R^{(n)}$ in the absolute time processing, which will be discussed in the Section 4.4.3.

4.4.3 Step 3

It was necessary to interpolate the values of the (t, x) data in equally spaced time points, and in fine resolution or at a specific spacing, for future use in any parameter identification for a patient-specific lumped circulation model. Using Matlab (The Mathworks Inc., Natick, MA) for the generation of the equally spaced data points there were several possible built-in interpolation functions available. This was necessary so that all collected patient profiles were available in a uniform format. A short discussion of the interpolation methods are now presented:

Linear Interpolation

The simplest interpolation method, as defined in (4.4), is linear interpolation. It employs the gradient between the two points and determines the x

value based on where the given t point lies on the connecting straight line. This was deemed appropriate for the insertion of one point within a suitable range. However, it was not appropriate for determining multiple inter-lying points, particularly with the clearly visible curved waves found in clinical data (see Figures 4.3(a) and 4.1). Linear interpolation simply inserts points on the straight line between the manually captured digitised data points and so by definition fails to incorporate any complex profiles. Figure 4.6 shows the result of simple linear interpolation: a piecewise linear profile. Periodicity was enforced by a method that will be discussed in the following section.

Cubic Interpolation

It was therefore necessary to use one of the other built-in interpolation techniques. The next most commonly used technique in the arsenal of numerical interpolation methods is cubic splines. Cubic splining uses a piecewise-cubic function that is continuous at orders 0,1 and 2. This means that that at each data point used, the two cubic functions used to describe the profile either side are: equally valued (continuous); the derivatives are equal (same slope); and the second derivatives are equal (same curvature). So, if f_L (f_R) is the cubic function to the left (right) of the data point, and t_i is the data point the cubic is defined using the following conditions:

$$f_L(t_i) = f_R(t_i)$$

$$f'_L(t_i) = f'_R(t_i)$$

$$f''_L(t_i) = f''_R(t_i)$$

Normalised: If there are say, N data points t_i , $i = \{1, 2, \dots, N\}$ in a cycle set, there is a problem of determining the coefficients of the first and last cubic function as there is no f_L and f_R for points t_1 and t_N respectively. In this case the predefined Matlab function *spline* uses the “not-a-knot” convention for boundary conditions where $f'''(t_1) = f'''(t_N)$. On using this condition, and the

fact that it is an interpolating polynomial (i.e. it must pass through the points used), it results in some extra, unnecessary curvature. By assuming periodicity it allows the addition of points to the set of (t_i, x_i) . The additional points are therefore located at (t_0, x_0) and (t_{N+1}, x_{N+1}) with $x_0 = x_{N-1}$ and $x_{N+1} = x_2$. Therefore to ensure periodicity as in the linear case, the value at the end points over which the interpolation is carried out, x_1 and x_N must be equal so that the new data points are (t_1, x^*) and (t_N, x^*) where the average value x^* is defined as:

$$x^* = \frac{x_1 + x_N}{2} = \frac{x_R^{(n)} + x_R^{(n+1)}}{2}$$

A separate function for reordering the data was written and used. The difference in generating the interpolated points with the original data and the reorganised data can be seen in Figure 4.5. This shows the extra curvature (not present in the clinical graphs) in the interpolated values between the first two data points. A similar phenomenon was found between the last two data points. In some cases the effect was not as pronounced, but the reorganisation resulted in a uniformly repetitive heart beat, therefore the re-organisation was justified as well as easily implemented.

Absolute Time: Regarding the absolute time approach, as periodicity could not be forced, and the additional data pair preceding (t_1, x_1) was already determined (Section 4.4.2), and the initial data set had already been extended, the additional curvature at the end of the profile was superfluous.

Piecewise Cubic Hermite Interpolating Splines

On visual inspection of the original scans, the graphs produced from using the *spline* function were still prone to overshoots, a result of the nature of fitting smooth cubic functions between the points. Matlab contained an alternative built in function named *pchip* which overcame this. The *pchip* function uses piecewise cubic Hermite interpolating polynomials (PCHIP). It is similar to cubic splines, but utilises differing conditions at the data points. It is less smooth as it is not continuous at the second derivative level, but is shape

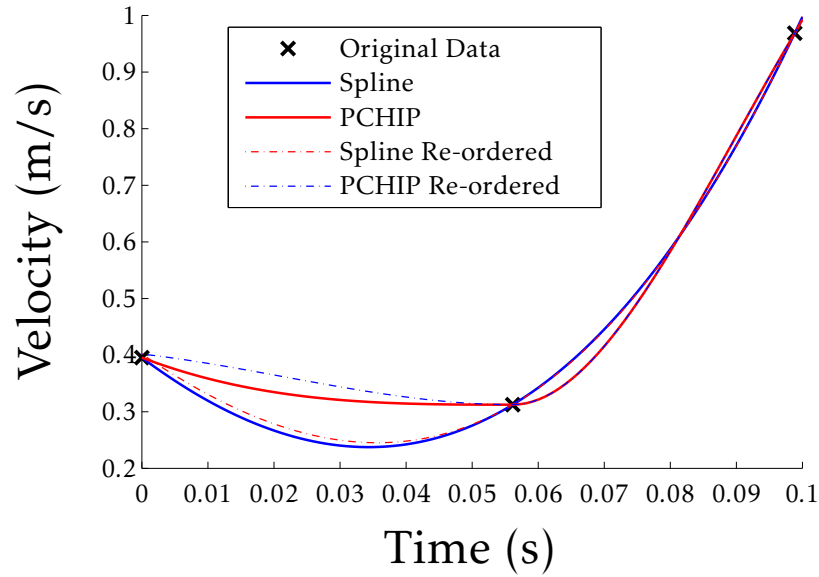


FIGURE 4.5: The effect of using the re-organised data for both *spline* and *pchip* functions with original data points

preserving and maintains monotonicity i.e. is monotonic on intervals when the data is monotonic (always either increasing or decreasing) and includes turning points where monotonicity is broken. Both functions are used identically, and so, after the visual inspection it was clear that the data was not smooth enough to use traditional cubic splines, and so the PCHIP approach was adopted. This was due to the fact that PCHIP is less prone to overshooting and oscillation from non-smooth data. The effect of the three interpolation approaches are illustrated in Figure 4.6 at equally spaced points of 0.001 with the PCHIP method visually the best approach. A close up of the initial overshoot can be found in Figure 4.5. The results are illustrated from the normalised approach, but are equally applicable to the absolute approach.

4.4.4 Step 4

The averaging process mentioned in Step 1 is now discussed. An ensemble average was carried out to produce a typical profile for each family of profiles specific to the test patient. The averaging process was intended to remove any beat-to-beat variation and the possibility of selecting inconsistent individual profiles. A family of profiles is considered as the collection of all individual

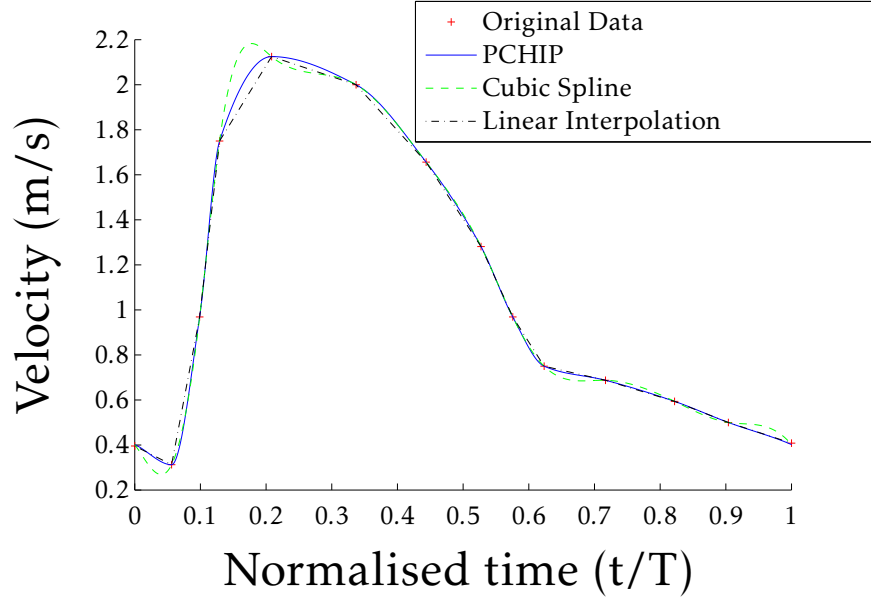


FIGURE 4.6: Results of using linear, cubic splines and piecewise continuous cubic Hermite polynomials for interpolation of a clinical waveform from paired data points. The data used is from a velocity profile at a branch pulmonary banding site.

beat profiles from the same location in the cardiovascular tree, and therefore consistent in magnitude and timings. These families were determined from the clinically labeled locations from the catheter and echo data.

If all data was equally spaced, and there were M data sets (M profiles from M beats), it would have been easy to determine the average value of each data point x_i^* for $i = \{1, 2, \dots, N\}$ as $x_i^* = (1/M) \sum_{m=1}^M x_i^{(m)}$. This would then provide a single, equally spaced data set from which interpolation on the averaged points could be carried out. However, due to the nature of the initial step in the digitisation process, it was virtually impossible to ensure uniformly spaced t_i , especially when normalised by heart cycle period. To overcome this issue, interpolation (using the process described above) at fine resolution (0.001) was performed on each separate data set of the clinical profile. Then a sufficiently high number of equally spaced time points ($t_k, k = 1, 2, \dots, K$), where $K > N$, and $t_1 \leq t_k \leq t_N$ were used to determine the corresponding average x component x_k^* . The interpolant of the (t_k, x_k^*) data was used to produce averaged profile at the same resolution at timesteps of 0.001. The PCHIP interpolation

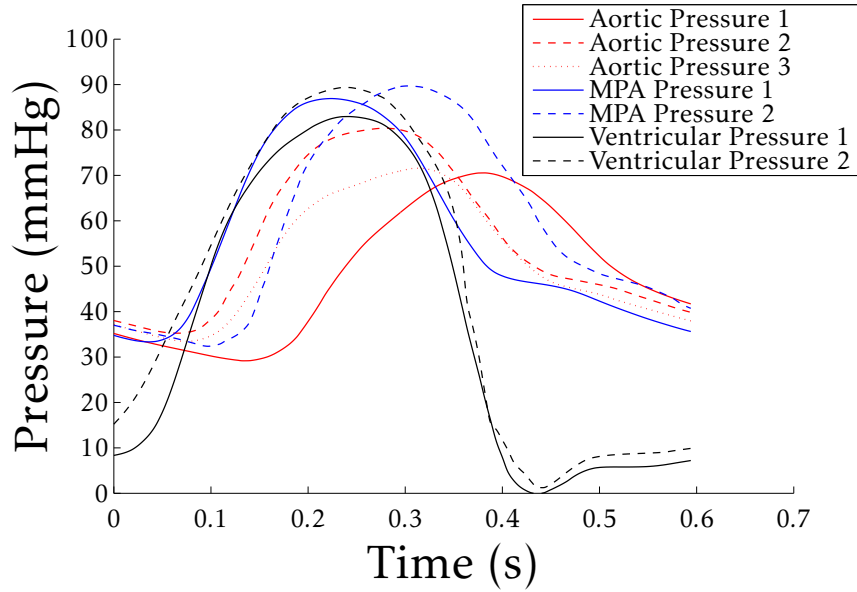


FIGURE 4.7: Multiple pressure profiles available for the descending aorta, main pulmonary artery and ventricle from clinical data set

method described in Section 4.4.3 was used here in both the normalised and absolute time approaches.

4.5 Selection of Profiles From Clinical Data

When reviewing the pressure data from the catheterisation procedure (see Appendix E), an unforeseen complication arose. Some of the medically labelled profiles resulted in several families of waves being present at some locations. The single ventricle, and the main pulmonary artery both had two distinct families of profile, with the descending aorta having three. After grouping the profiles for each compartment into their respective families, an ensemble average for each family was generated. The resulting profiles are shown in Figure 4.7.

Particularly in the three descending aortic profile families, the effect of wave propagation is clearly visible. Wave propagation through the cardiovascular tree is in itself a large area of research, and a phenomenon that many groups have tried modelling in an attempt to better understand its significance, particularly with reference to identifying disease. See [139, 140] for

further consideration. It is this phenomenon that is captured by 1D mathematical modelling and is not described by the lumped circulation models.

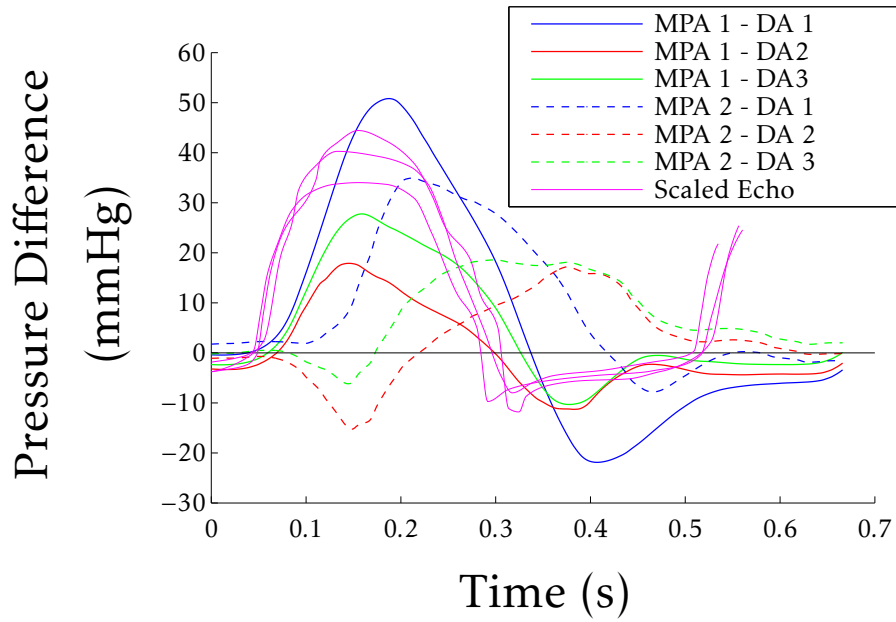
What is observed in clinical investigation (and successfully modelled in 1D mathematical representations) is the effect of wave reflections. The pressure wave can be observed to reflect and propagate in the opposite direction of the flow of blood e.g. at a branch or bifurcation point. Therefore, it is supposed that differing spatially-specific locations within the clinical labelled areas which are affected by different phase shifts of forward and reflected waves that have differing cancellation and reinforcing effects. This can be observed in a pressure recovery phenomenon seen in clinical investigation, and the propagative effect is visible in the aortic profiles presented.

4.5.1 Comparing Clinical Profiles

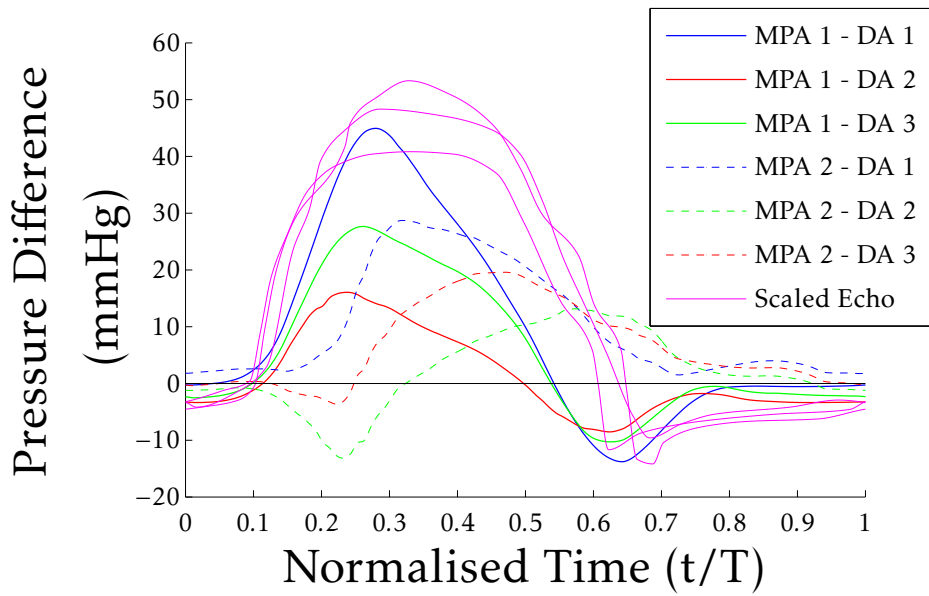
To compare all available profiles generated from the difference between all of the pressure profiles gathered were checked against a scaled version of the velocity profile for the relevant pressure drop. The first difference considered was from the main pulmonary artery to the descending aorta ($P_{mpa} - P_{sys}$) and this was compared with the velocity profile across the stented patent ductus arteriosus.

This resulted in excluding one of the two main pulmonary artery profiles, as the only profile that resulted in a remotely similar shape failed to capture the necessary backflow component in diastole. Of the three descending aortic profiles, the second one was prioritised as it matched the timing of flow reversal best. This can be seen visually in Figures 4.8 and 4.9.

The choice of ventricular families was again relatively straight forward owing to the fact that the first of the ventricular profiles was physiologically inconsistent with the main pulmonary artery pressure profiles as it did not result in a positive pressure gradient through the valve permitting forward flow out



(a) Absolute Time



(b) Normalised Time

FIGURE 4.8: Pressure differences of available profile families for stent flow, with appropriately scaled stent flow in dotted line. Both scaled and absolute time profiles are shown

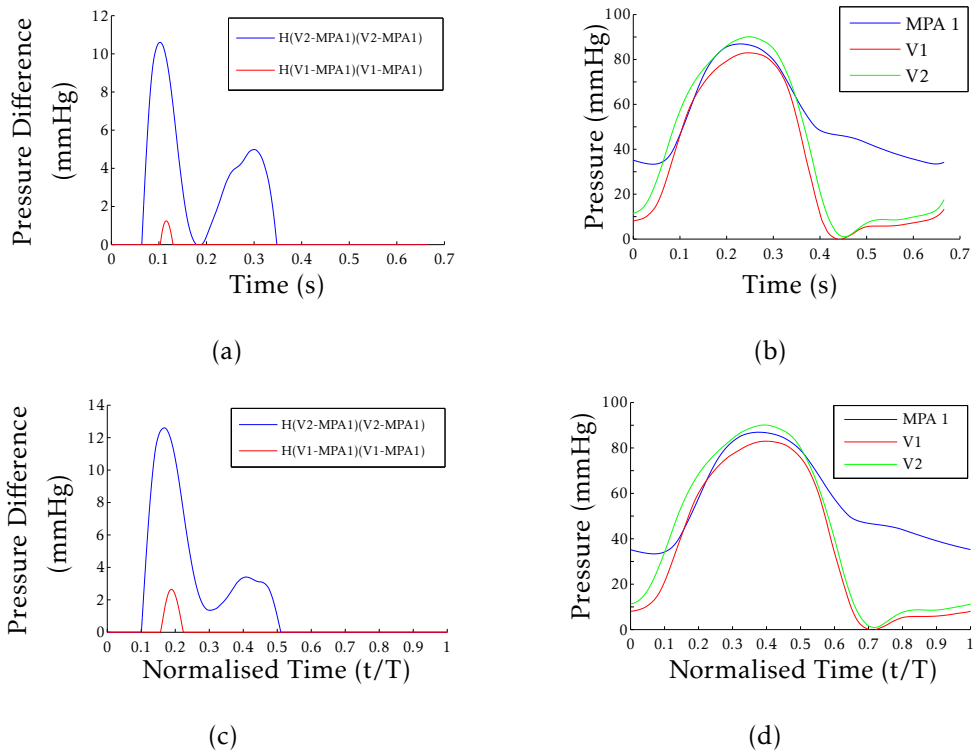
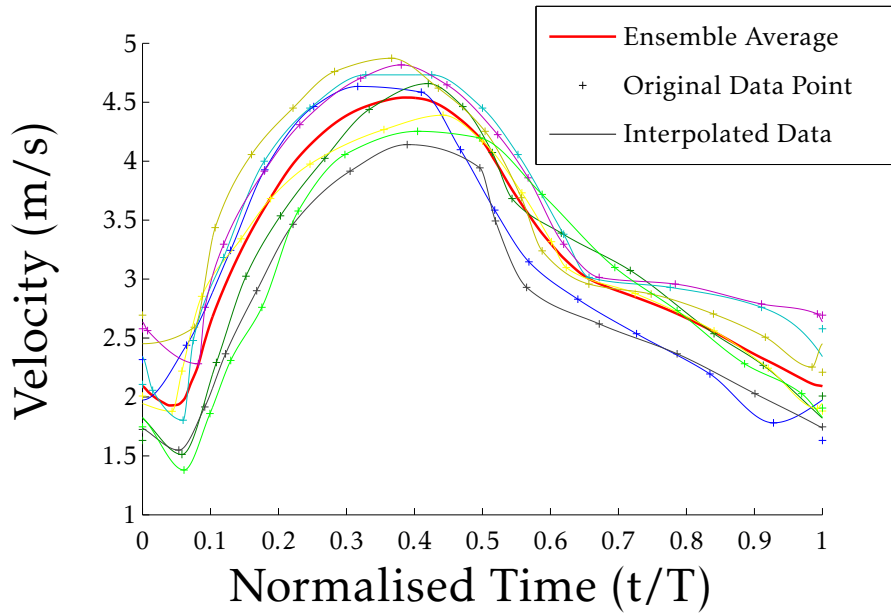


FIGURE 4.9: Alternative flow profiles (left) based on selected MPA and available ventricular pressure profiles (right). Both absolute (top) and scaled (bottom) are shown

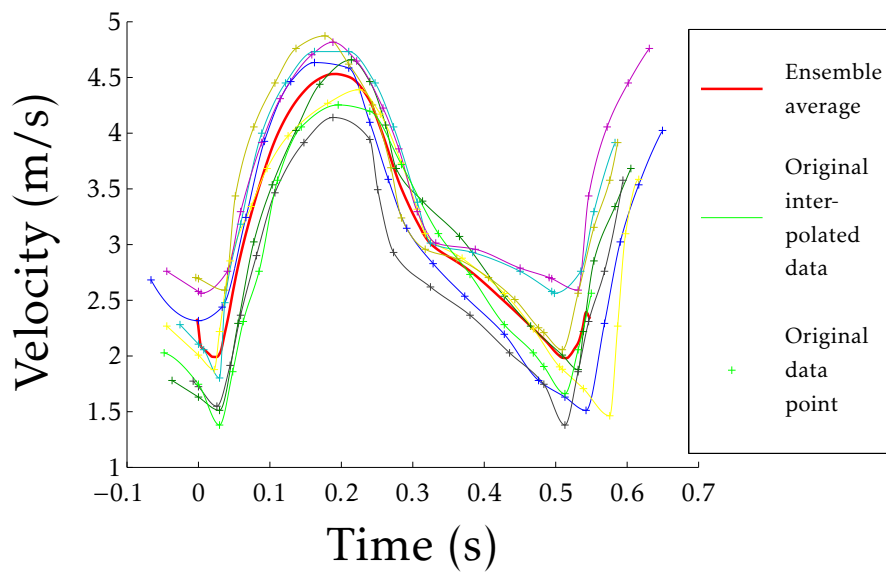
of the ventricle. Again, this could be as a result of errors associated with the invasive catheterisation measurement or patient movement.

The remaining profile however, highlighted a concern with the averaging process. The shapes, which should be similar, differ in the sense that there appears to be a shouldering on the ventricular profile that is not present in the MPA profile.

When viewing the graph of the positive difference across the valve there appears to be two pulses, which is physiologically inaccurate. It is suggested that this difference is possibly a consequence of the averaging process. A direct comparison with Doppler velocity profile for the pulmonary valve flow was dismissed due to the timing mismatch which will be detailed in Section 4.6.1.



(a) Normalised time with enforced periodicity



(b) Absolute time with enforced periodicity

FIGURE 4.10: Ensemble wave (red) produced from eight original velocity profiles from Doppler echo of a branch pulmonary artery banding site. The original data points are marked with a '+' and are clearly unequally spaced. The fine resolution interpolation of each profile is seen with the solid lines.

4.6 Outcome of Ensemble Averaging

Figure 4.10 shows the output of the averaged waveform with $K = 100$ for eight velocity profiles taken from Doppler echo of a branch pulmonary artery banding site. Each original velocity profile is seen with the original data points used for interpolation marked with a '+', which are clearly unequally spaced. The ensemble averaged profile visibly captures the characteristic shape. Figure 4.11 shows the effect of taking an insufficient quantity of data points to average over, in this case for $K = 5, 10$ and 20 using a different profile set from Figure 4.10. All clearly miss the initial profile shape. $K = 100$ was deemed an appropriate sampling rate to capture an average profile representative of the available data.

Figure 4.10(b) clearly demonstrates that it is inappropriate to enforce periodicity in the ensemble average produced from the absolute time data. Once this was established, periodicity was not enforced, but is included here for illustrative purposes. The general shapes of the averages for both absolute (excluding end points) and normalised time do not appear to distort significantly and this highlights the difficulty in selecting one method over the other.

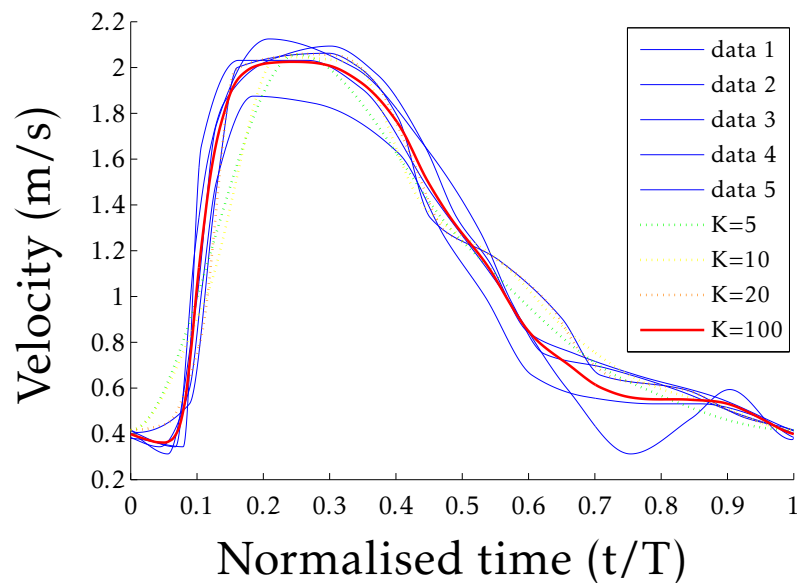


FIGURE 4.11: Results of averaged waveform profile by varying the number of data points K taken. The data used is from a velocity profile at a branch pulmonary banding site.

4.6.1 Scaled vs. Absolute Time

As stated previously, it was unclear as to which method was best to use for the time domain: Scale the time values by the heart beat period for each individual beat; or maintain absolute time.

Both approaches could be justified from different perspectives. The advantage of normalising the period meant that each profile from each location of the cardiovascular tree could be directly compared and periodicity could be enforced. The problem with scaling the time is that physiologically, the timings of the heart beat are not scaled linearly. A heart beat consists of two distinct phases (although definitive definitions of these is still debated): systole, the active phase; and diastole, the relaxation phase. Therefore the period T is the sum of the length of systole T_s and diastole T_d :

$$T = T_s + T_d$$

The problem is when scaling the period by, say α is that they are not scaled linearly:

$$\alpha T \neq \alpha T_s + \alpha T_d$$

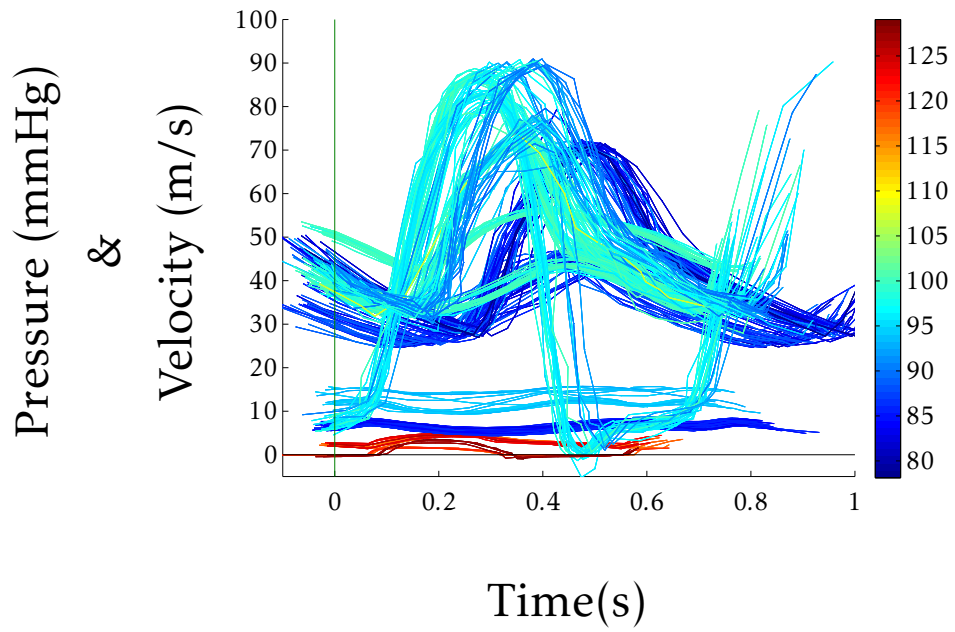
In other words, the ratio of length of systole to length of diastole T_s/T_d is not fixed, and varies with heart rate. For example a conventional heart, when the heart rate is increased (and heart period decreased), the length of systole remains similar while the relaxation phase is reduced to facilitate the change. Recently in the literature groups have been investigating this relationship in both healthy [141] and HLHS patients [142]. The aim of the investigation however, has been to determine if the ratio can be used as a marker for performance of a ventricle, not to determine a relationship between T_s/T_d and the length of a heart beat T . Again, it needs to be reiterated that due to the complexity of the condition there is no conventional “normal” and therefore would be difficult

to use a standard relationship to infer some proportional scaling method for an individual patient with varying heart rate.

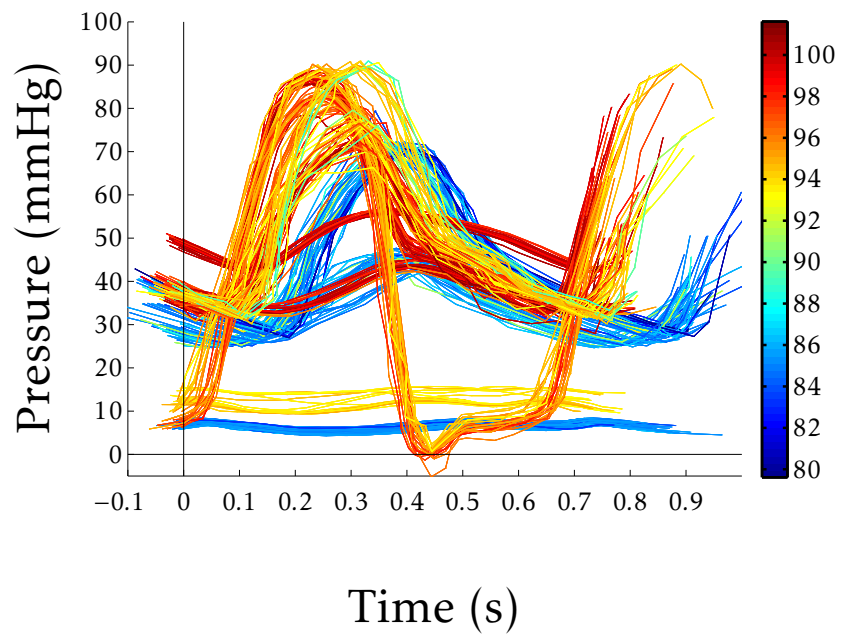
The biggest mismatch in heart rate from the sample patient came from comparing the Doppler velocity profiles and the catheterised pressure data. Pressure data was at a heart rate around 95 beats per minute (bpm), while the echos were of the order of 120 bpm. These were taken 3 days apart and under different physiological conditions, therefore the difference is not unexpected. There was nothing within the study's control that could be done to alter this historical data, however this issue has been raised with our clinical partners and, with no additional risk to the patient, simultaneous (or immediately prior to or following) echo investigation is now under consideration when undergoing a catheterisation procedure.

Figure 4.12(a) shows the absolute time data for all available profiles. The families of profiles can clearly be identified with each individual profile coloured by heart rate. It is obvious that the echo data is substantially different, yet there is still a degree of variation between the pressure profiles within the one catheterisation procedure as illustrated in Figure 4.12(b).

Additional advice was sought from Michael F. O'Rourke, co-author of the latest editions of the renowned textbook 'McDonalds Blood Flow in Arteries' [143]. O'Rourke backed the absolute time method, which involves extending the profile past the next R-wave for all data so that the wave can then be clipped at the period corresponding to the desired heart rate, but recognised that this was a simple approach to the problem and could be inappropriate in some cases. The main issue with this approach for this research is that each profile is not periodic, and one is limited in the maximum heart rate one can model by the shortest beat recorded. It is possible to consider non-periodic profiles for data fitting, but by the nature of the modelling methodologies outlined in the forthcoming chapters the modelled output profiles are periodic. Therefore, until parameter fitting is further investigated, ensuring periodicity was deemed the most appropriate way of processing the profile data.



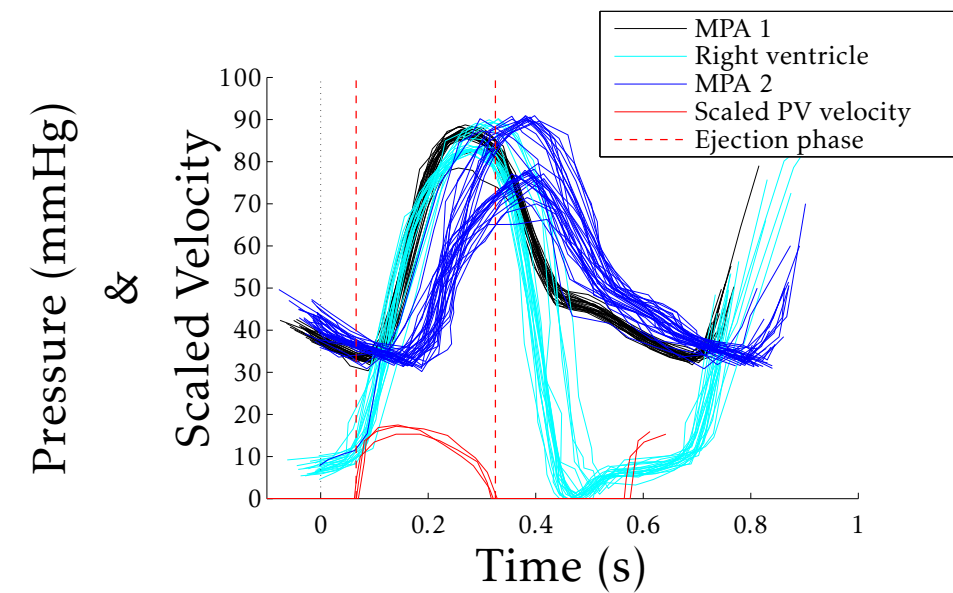
(a) Pressure and Velocity profile data



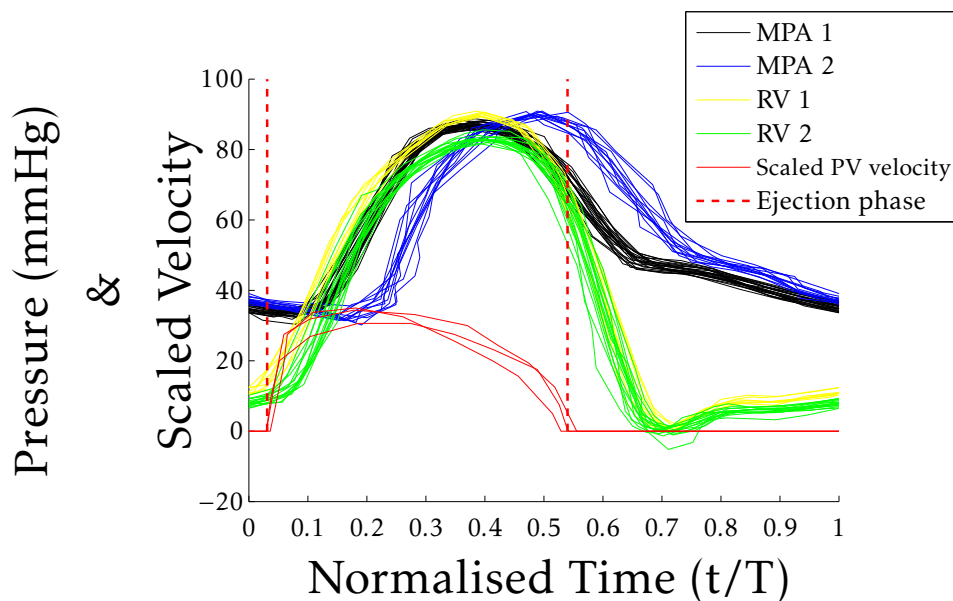
(b) Pressure only data

FIGURE 4.12: All clinically acquired profiles coloured by heart rate. Pressure profiles only given in (b)

The incompatibility of the Doppler velocity profiles at the faster heart rates is emphasized in Figure 4.13. Despite a seemingly good match for the closing of the valve, the opening of the valve was timed poorly when comparing the available pressure and Doppler velocity data.



(a) Absolute time



(b) Normalised time

FIGURE 4.13: All families of ventricular and main pulmonary artery pressures with scaled velocity marked in red showing the ejection phase from the ventricle

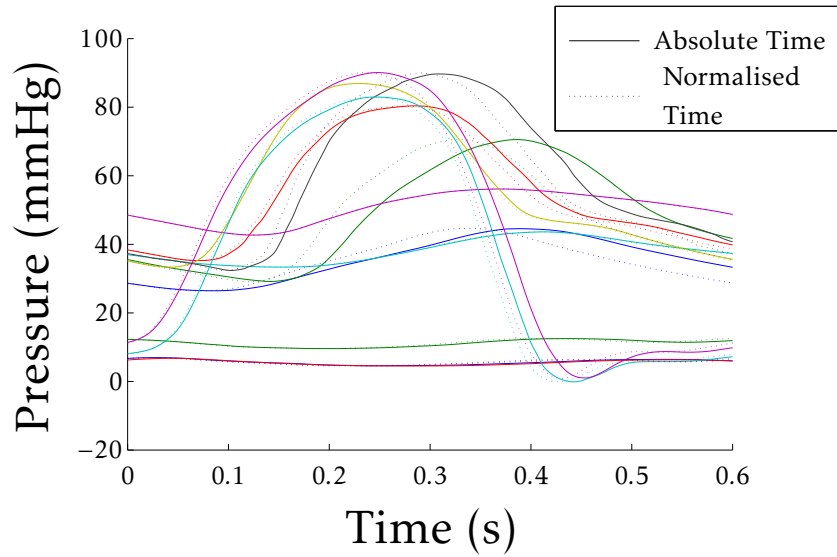


FIGURE 4.14: All clinical pressure profiles directly comparing Normalised and Absolute time scaling methods

Figure 4.14 shows the change in profile shape by using scaled (dotted) vs. absolute time (solid line) for each individual ensemble averaged profile for each available pressure location. The scaled data was rescaled so that the period matched that when the absolute time data was clipped. This was at a period of 0.6s or heart rate of 100 bpm. Currently, the choice of methodology is not resolved. Analysis of the simultaneous pressure and velocity data is needed to shed light on this area as well as to inspire a more consistent approach.

4.7 Geometrical Data

Two available forms of clinical data were available regarding construction of a digitised three dimensional geometry: Magnetic Resonance Imaging (MRI); and Computed Tomography (CT).

Both were available in their raw DICOM format which contains multiple stacked grayscale images that can be manipulated using specialised software. The processing of the geometrical data will be discussed fully in Chapter 6, along with experimental results from the consequential modelling. As the

MRI and CT data was amongst the available clinical data, it was necessary to raise awareness of its forthcoming discussion in its own relevant section. A jpeg image of a slice CT is provided in Figure 4.3(b) alongside the other raw data formats.

4.8 Concluding Remarks on Clinical Data

In conclusion of this chapter, the implications of the above processing of clinical data is discussed alongside where the clinic and modelling dichotomies actually can overlap and improve to each others benefit.

4.8.1 Superfluous Digitisation

Given the current technologies deployed in healthcare, the use of digitised measurement is the prevalent form of data capture. With this in mind, the retrospective processing of the data manually seems superfluous. Section 4.4 outlines the necessary steps to manipulate data, formerly digitised (by definition being originally available and stored on computers), from the analogue pictorial form. It is the author's belief that with minor adaptations to current technology, that the waveforms required for the use in model verification/parameter identification discussed in this thesis could be readily exported in a more accurate format. Thus removing the manual processing and interpretive errors introduced with the current methodology.

Depending on the sample rate of any waveform data (pressure or velocity/flow profiles) the influence of the interpolation methods discussed will diminish. Regarding the generation and use of an ensemble average, this could either be generated within the suggested improved export from the recording source, or creates the opportunity for product development. This product would be an interface, whether purely software, or including hardware enabling direct connection with the original source data, that could record and swiftly produce ensemble waves once families are identified.

An automated profile analyser would require greater understanding of the distinction between the two methods of processing the temporal element of the data, and the associated strengths and weaknesses of the respective methodologies. Until this understanding is developed, as may be the conclusion from any investigative study (deemed out with the remit of this present investigation), both the absolute time (clipping) and normalisation approaches should be included.

4.8.2 Coordination of Data

The ideal data set for patient-specific modelling would be taken from as consistent haemodynamical circumstances as possible. This would include the slice imaging data, where MRI provides the greatest potential with the removal of exposure to X-rays and also having the capability to measure flow data. If the flow/velocity, pressure and geometrical data was all measured as close to simultaneously as possible, it would overcome many of the compatibility issues related to the consistency of data.

Currently, no accurate flow data is measured, and although the velocity data from echo cardiograms could be used, there is too much uncertainty in the results to acquire a quantitatively accurate profile. This is in part due to the lack of explicit quantification of the cross sectional area of the lumen where the velocity is measured, as well as the issues outlined previously.

Additionally the available measurements are predominantly taken at different times. It would be strongly recommended, particularly in such uncertain circumstances as a single ventricle neonatal circulation, that when collating the available patient-specific data for the purposes of modelling it is recorded simultaneously from a consistent haemodynamical state. Of course this is clinically very difficult, but it should be possible, without any additional constrain on the patient, to manage the timings of the procedure such that echo and catheterisation procedures were done within the same investigation. If this were to be scheduled to coincide with medical imaging (leading

to the production of a three dimensional geometric reconstruction) under the same physiological conditions, a fully consistent data set would be produced. By achieving a consistent data set, it reduces the risk of identifying parameters based on disjointed data set and coupling those with an inconsistent geometry.

This approach should be adopted for both pre and post procedure until a correlation between the two, if it exists has been established. The data gathering outlined above is relevant to a consistent haemodynamical state; the comparison of pre and post operative lumped circulation parameters would require further investigation. This would be a critical step in the development of predictive mathematical modelling, but currently consistent data sets for multiple patients is lacking.

Another improvement would be to have a more precise labelling of the locations of the pressure profiles from catheterisation procedures. This would permit more meaningful lumped circulation models, where each tracing location would correspond to a compliant component. Currently all compartments are generically and arbitrarily located. Ensuring the accurate definition of the spatial location of profile data from within the cardiovascular tree will remove the uncertainty in selecting between the families of profiles (e.g. for the descending aorta) and could lead to clearer clinical interpretation of Windkessel compartments or chambers which will be discussed in the following chapter.

Chapter 5

Lumped Circulation Model

5.1 Introduction

A multi-compartmental Windkessel model was adapted from published models of the post-Norwood circulation and native HLHS circulations [85, 86, 91]. The analogous electrical circuit of the circulations simulated are given in Figures 5.1 and 5.2. In essence, the differences in this Hybrid circulation model from the published Norwood variations are that the pulmonary resistance is dependent on the external diameter of the PAB, and the systemic supply is via the stented PDA. The stented PDA can be considered as a naturally occurring PA-to-SA shunt. An equation describing the relationship between flow through and pressure drop across the stent is adapted from a SA-to-PA shunt published in the literature [5].

This chapter presents the implementation of a subtly altered version of the post-Norwood circulation study by Shimizu *et al.* which is later adapted to simulate the post-Hybrid circulation. A condensed version of this work has already been published in the medical literature [144]. Shimizu *et al.* successfully reproduced and adapted the original model of a mBT shunt Norwood circulation presented by Migliavacca *et al.* [85], while providing greater transparency in their methodological approach. The specific protocols adopted by Shimizu *et al.* provides better clinical interpretation of the results, while also clarifying the limitations of the results and subsequent comparisons of model

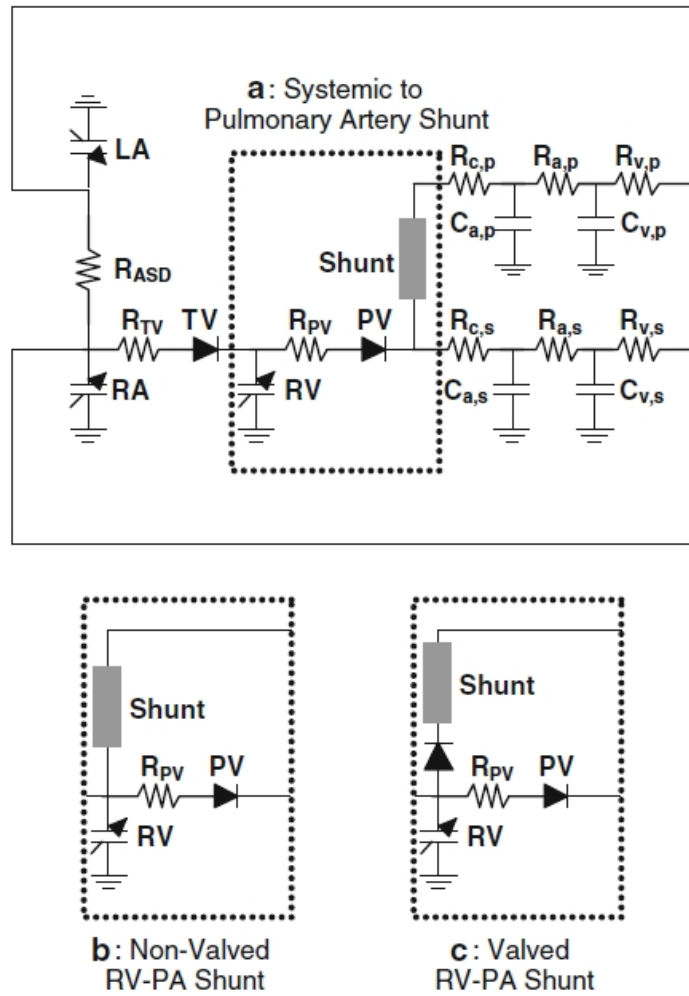


FIGURE 5.1: Analogous electrical circuit of the post-Norwood Procedure circulations as originally published by Shimizu *et al.* [86]

variations [86]. Their methodology is adapted to allow an equally valid clinical comparison based on the same principles (see Section 5.3.1). This essential step regarding the initial conditions/methodologies is often neglected in publications in this field, potentially raising concerns over mathematical models from clinical partners, rather than encouraging their adoption and utilisation.

Although the specific methodology and results will not be presented here, a multi-compartmental adult model published from an independent group was successfully reproduced as a basis for our own patient-specific investigations [137]. This work evolved to look into the inverse problem of identifying patient specific parameters for both the circulatory constants [87], and those

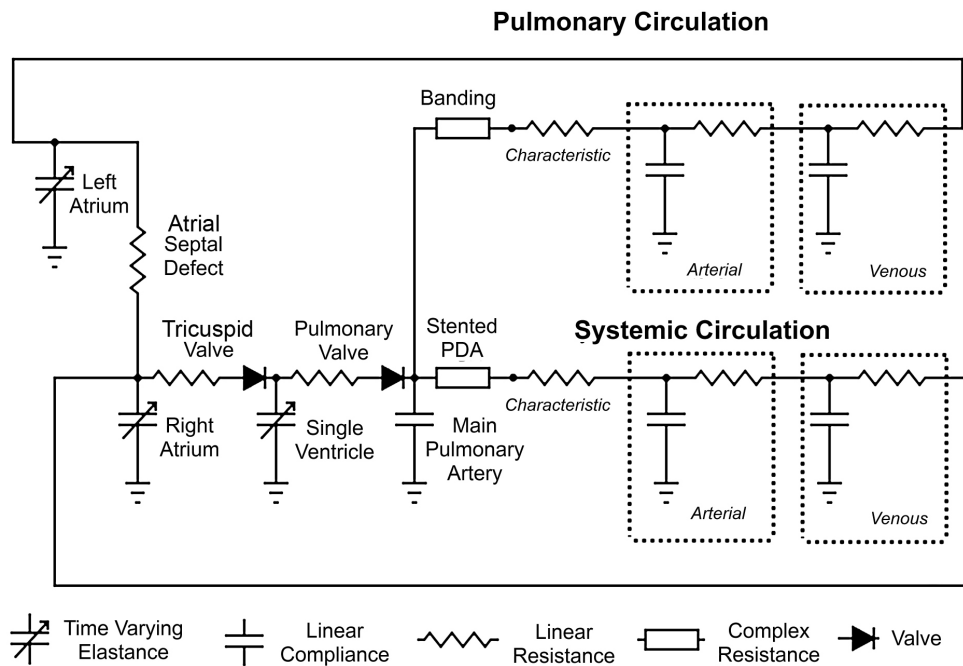


FIGURE 5.2: Analogous electrical circuit of the circulation post-Hybrid Procedure for HLHS

describing the heart [92]. This is a vital step in the future direction of mathematical modelling of the CVS.

The general equations of the heart model adopted and a reiteration of the equations describing the state variables of pressure, flow and volume for each cardiac chamber will be presented in this chapter. This is followed by the specific descriptions of the differences between model configurations. The successful reproduction and subsequent adaptation of the original Norwood circulations are briefly validated before a full analysis of the novel Hybrid circulation model is presented, focusing on clinical relevance. The optimal Hybrid configuration is then compared to the best performing Norwood configurations before discussing patient-specific lumped parameter modelling.

TABLE 5.1: Parameters used in modelling the Hybrid and Norwood repairs for HLHS as adapted from Shimizu *et al.* [86]

Heart Rate (beats/min)	160		
Period of cardiac cycle, T_c (s)	0.375		
	<i>Right Ventricle</i>	<i>Left Atrium</i>	<i>Right Atrium</i>
End Systolic Time, T_{es} (s)	0.136	0.056	0.056
End Systolic Elastance, E_{es} (mmHg/ml)	8.5	7.35	7.35
End Diastolic Pressure Volume Relation Scaling Factor, A (mmHg)	0.9	0.17	0.17
End Diastolic Pressure Volume Relation Exponent, B (ml⁻¹)	0.062	0.484	0.484
End Diastolic Volume, V_0 (ml)	4	1	1
	<i>Pulmonary Valve</i>	<i>Tricuspid Valve</i>	<i>ASD</i>
Cardiac Resistances, R (mmHg)	4×10^{-4}	4×10^{-5}	0.001
	<i>Characteristic</i>	<i>Arterial</i>	<i>Venous</i>
Systemic Resistance, R (mmHg · s/ml)	0.20	3.83	0.083
Systemic Capacitance, C (ml/mmHg)		0.44	4.39
Pulmonary Resistance, R (mmHg · s/ml)	0.028	0.63	0.011
Pulmonary Capacitance, C (ml/mmHg)	0.061	0.31	0.89
Index of Pure Viscous Effects, k_1 (mmHg · mm⁴ · s/ml)	57.6		
Index of Convective Acceleration, k_2 (mmHg · mm⁴ · s²/ml²)	18.7		

5.2 Methods

5.2.1 General Descriptions

Heart

The three chambers of the hypoplastic left heart (right atrium, left atrium and single ventricle) were modelled with a time varying elastance. This well established approach [63, 85, 145] uses a separate pressure-volume (P-V) relationship for systole and diastole and an activation function to switch between the two in a cyclic manner.

In the present study we described the cardiac chambers of the heart using: a linear systolic P-V relationship (5.1); an exponential pressure increase dur-

ing the diastolic filling phase (5.2); and a squared sine wave as the activation function (5.3); which are combined to give the full P-V relationship (5.4):

$$P_{\text{sys}} = E \cdot (V - V_0) \quad (5.1)$$

$$P_{\text{dia}} = A \left(e^{B(V-V_0)} - 1 \right) \quad (5.2)$$

$$a(t) = \begin{cases} \frac{1}{2} \left(1 - \cos \left(\frac{t\pi}{T_{\text{ps}}} \right) \right) & 0 < t \leq 2 T_{\text{ps}} \\ 0 & 2 T_{\text{ps}} < t \leq T_c \end{cases} \quad (5.3)$$

$$P = a(t) \cdot P_{\text{sys}} + [1 - a(t)] \cdot P_{\text{dia}} \quad (5.4)$$

where all parameters symbols and values for each cardiac chamber are defined in Table 5.1. The parameter values for the left and right atria are assumed identical. Different values for T_{ps} , the time to peak systole, account for the difference in duration of ventricular and atrial systole. The delay in onset of systole between the atria and ventricle was achieved by a temporal translation of the activation function (5.3), by ΔT .

In this research, the cardiac timings ($T_c, T_{\text{ps}}, \Delta T$) were not varied. The nature of mathematical modelling means that vast amounts of data can be produced and so caution must be exercised in focusing on the primary questions addressed by each individual study. The variation of heart-rate, although considered by Migliavacca *et al.* [85], has not been simulated by Shimizu *et al.* [86] or in the present study. Heart-rate responds to physiological stimuli and unless a feedback loop is designed for future studies, analysis of heart-rate variation would overwhelm the study of how varying the geometry affects the circulation. Additionally, the ratio of systole to diastole has been proposed as a marker for the performance in single ventricle circulations [142, 146], and therefore would require specific consideration in any modelling analysis.

Unrestricted communication between the left and right atria was modelled by adopting a low linear resistance between the two chambers as seen in Fig-

ures 5.1 and 5.1 and Table 5.1. The Equation for flow determined by linear resistance is given later in Equation (5.8).

The valves are modelled as ideal diodes such that there is no flow when the pressure gradient across the valve is reversed against the direction of flow. Therefore tricuspid regurgitation is not modelled by this study in which the effect of varying the geometrical configurations was the focus of interest. This was achieved by the use of a Heaviside function H as shown in Equation (5.5). A linear resistance was adopted where the pressure drop ΔP is proportional to the flow Q with the constant of proportionality being the resistance R (5.6).

$$H(\Delta P) = \begin{cases} 1 & \Delta P \geq 0 \\ 0 & \Delta P < 0 \end{cases} \quad (5.5)$$

$$Q = H(\Delta P) \cdot \frac{\Delta P}{R} \quad (5.6)$$

Different values for this linear resistance were assigned for the tricuspid and pulmonary valves and can be found in Table 5.1.

Vasculature

For the non-cardiac compliant chambers the pressure was determined by assuming a constant compliance, so that given the volume V in the chamber the blood pressure P could be calculated as:

$$P = \frac{V}{C} \quad (5.7)$$

which can be seen in the electrical equivalence circuit diagrams (Figures 5.1 and 5.2). Therefore, with the pressures for every chamber known, the flows Q between them can then readily be determined, using a linear resistance similar to single Windkessel models:

$$Q = \frac{\Delta P}{R} \quad (5.8)$$

with the resistance value R representative of a specific segment of the total systemic vascular resistance used in a single Windkessel model. All parameter definitions and values for the vasculature components are given in Table 5.1. The characteristic compliance of the pulmonary circulation as labelled in Table 5.1 is that of the MPA compliant chamber. It is the addition of this compliant chamber that the present Norwood Procedure circulation models vary from those published, with negligible difference in results (see Section 5.3.1). This change was established to allow better comparison between the lumped Hybrid and Norwood models and more appropriate coupling in the multiscale model in Chapter 7. The equations modelling the complex resistances of the stent and the pulmonary arterial banding are replaced by a three dimensional computational fluid dynamical model in Chapter 6.

5.2.2 Specific Sub-Models

Norwood

To account for non-linear effects through the stent such as inertia and turbulence Shimizu *et al.* utilise the equation used in [85] which is derived empirically from computational fluid dynamic simulations of shunt flow [5]:

$$\Delta P = \frac{k_1 Q + k_2 Q^2}{D^4} \quad (5.9)$$

where D is the diameter of the shunt and has a Poiseuille relationship. The constants k_1 and k_2 are defined in Table 5.1. The linear component k_1 denotes the effect of pure viscous effects, while the quadratic component k_2 denotes the convective acceleration. As seen from Figure 5.1, this equation was deployed in three separate configurations: a mBT shunt (from the additional compliant chamber representing the pulmonary trunk to the pulmonary artery chamber in the present study), and an open and valved Sano shunt direct from the ventricle to the pulmonary artery chamber.

The issue of reversed flow through the shunt required special consideration. As will be discussed below the volumes determine the pressures which then determine the flows. In the case of the shunt, a quadratic equation must be solved to determine Q . Between the two known pressure values (P_1, P_2) is resistance due to the shunt and the characteristic pulmonary resistance R_{pc} . With the two resistances in series, using the quadratic formula the stent flow is calculated as:

$$Q = -\frac{k_1 + R_{pc}D^4}{2k_2} \pm \sqrt{\left(\frac{k_1 + R_{pc}D^4}{2k_2}\right)^2 + \frac{\Delta PD^4}{k_2}} \quad (5.10)$$

where ΔP is positive and defined as $P_1 - P_2$. The selection of the positive or negative root depends on the direction of flow i.e. the sign of ΔP . In order to maintain the definition of positive flow away from the heart, and $\Delta P = P_1 - P_2$, such that $Q = 0$ when $\Delta P = 0$, Q was subsequently defined as:

$$Q = \begin{cases} -\frac{k_1 + R_{pc}D^4}{2k_2} + \sqrt{\left(\frac{k_1 + R_{pc}D^4}{2k_2}\right)^2 + \frac{\Delta PD^4}{k_2}} & \Delta P \geq 0 \\ +\frac{k_1 + R_{pc}D^4}{2k_2} - \sqrt{\left(\frac{k_1 + R_{pc}D^4}{2k_2}\right)^2 - \frac{\Delta PD^4}{k_2}} & \Delta P < 0 \end{cases} \quad (5.11)$$

This was implemented within the code as:

$$Q = \text{sgn}(\Delta P) \left(\frac{k_1 + R_{pc}D^4}{2k_2} + \sqrt{\left(\frac{k_1 + R_{pc}D^4}{2k_2}\right)^2 + \left| \frac{\Delta PD^4}{k_2} \right|} \right) \quad (5.12)$$

Appropriate calculation of backflow ($Q < 0$) was essential, particularly as retrograde flow through the PDA in diastole is a prominent feature of the Hybrid circulation which is discussed in the following section.

Hybrid

For modelling the post-Hybrid circulation, Equation (5.11) was also adopted as the stenting of the PDA is effectively maintaining a naturally occurring shunt.

Although this formula has been used for modelling both mBT (SA-PA connection) and Sano (RV-PA connection) configurations of the Norwood procedure [85, 86], this is the first use of this equation for stented ductal flow [144]. Using available data from a pre-stage II repair Hybrid test patient (see Chapter 2), who received an 8 mm stent and 3 mm PAB, it was found that in this configuration ($d = 3$ mm, $D = 8$ mm), the modelled ratio of the pressure drop across the stent (ΔP) to flow through it (Q) was greater than the clinical data i.e. the resistance was too high.

The model output was then matched to the clinical data by using a shunt diameter of 12 mm. Thus the stent diameter D used in (5.11) was determined by scaling the input stent diameter, \widehat{D} such that:

$$D = 1.5 \cdot \widehat{D} \quad (5.13)$$

To the author's knowledge, no existing model provided an indicative value for the resistance found in pulmonary banding within the context of a HLHS circulation. Therefore, pressure profiles from the same catheterization data used above determined an appropriate reference value. As can be seen from Figure 5.2, there are two resistive elements: the pulmonary banding and the characteristic resistance.

The characteristic resistance was fixed at the value found in the literature [85, 86, 91]. To determine the reference value for the banding resistance $\widehat{R}_{\text{band}}$ an averaged pressure drop δP was calculated from the difference between the mean pressure in the MPA and distal to the PAB. This was then combined with typical pulmonary perfusion values \widehat{Q}_p derived from [86], to initially define total pulmonary resistance \widehat{R}_{pul} cf. (5.8):

$$\widehat{R}_{\text{pul}} = \frac{\delta P}{\widehat{Q}_p} \quad (5.14)$$

The value of \widehat{R}_{pul} was calculated as 3 mmHg \cdot s/ml. The reference value for the banding resistance was then simply $\widehat{R}_{\text{band}} = \widehat{R}_{\text{pul}} - R_{cp}$. To allow this resis-

tance to vary with the external diameter of PAB (d), a Poiseuille relationship, as seen in Equation (5.11), was adopted so that the resistance was inversely proportional to fourth power of the diameter. Therefore, since the reference value was derived from a patient who received a 3 mm external banding the banding resistance R_{band} was determined by:

$$R_{\text{band}} = \widehat{R}_{\text{band}} \cdot \left(\frac{3}{d}\right)^4 \quad (5.15)$$

The specification of *external* banding diameter is a key distinction. Previous publications modelling the Hybrid Procedure in multiscale modelling [83, 84, 127] simply refer to banding diameter, without making this clinically essential distinction. The banding diameter for the 3D model of the Hybrid Procedure in the present study in fact refer to the *internal* luminal banded diameter.

5.2.3 Implementation and Protocols

Conservation of Flow

The hydraulic equivalent of Kirchoff's First Law is the conservation of flow. This is the intuitive law that the change in volume of a compliant chamber must equal the difference of the flow in and out of that specific chamber. This leads to the differential equation:

$$\frac{dV}{dt} = \sum Q_{\text{in}} - Q_{\text{out}} \quad (5.16)$$

where Q_{in} and Q_{out} , the flow in and out of each cardiac chamber respectively, are determined at each instantaneous time point. By summing all the individual differential equations for each compliant chamber it is shown that:

$$\frac{dV_T}{dt} = 0 \quad (5.17)$$

where V_T is the total stressed blood volume defined as the sum of the volume in the right ventricle, left and right atria, main pulmonary artery and both systemic and pulmonary arteries and veins:

$$V_T = V_{RV} + V_{RA} + V_{LA} + V_{MPA} + V_{SA} + V_{SV} + V_{PA} + V_{PV} \quad (5.18)$$

thus the total stressed blood volume is constant and this is employed as an input parameter, alongside the dimensions of the shunt (D), band (d) and ductal stent (also denoted D), to the respective models.

5.2.4 Numerical Time Integration

The differential equations above can be solved using many numerical approximations to solve an equation of the form $\frac{d\mathbf{x}}{dt} = f(\mathbf{x}, t)$ with the forward Euler's approach the simplest method which can determine the next term $\mathbf{x}^{[n+1]}$ based on the current solution $\mathbf{x}^{[n]}$. Euler's forward method determines the next time step as:

$$\mathbf{x}^{[n+1]} = \mathbf{x}^{[n]} + \Delta t \cdot f(\mathbf{x}^{[n]}, t_n) \quad (5.19)$$

To write this explicitly for one of the chambers, for example the right ventricle, the equation becomes:

$$V_{RV}^{[n+1]} = V_{RV}^{[n]} + \Delta t \cdot (Q_{tv} - Q_{pv}) \quad (5.20)$$

where the subscripts tv and pv denote the tricuspid and pulmonary valves respectively, n is the current time point, $n + 1$ is the succeeding time point, and Δt is the difference between the two time points, the time step.

Using the equations in Section 5.2.1 with a known volume (e.g. the initial solution at $t = 0$) the pressure can then be determined (e.g. (5.7)) from which the flow rates are calculated for that time step (e.g. (5.8)). Thus knowing the flow rates $Q_{in} - Q_{out}$ for each chamber the volume for the next time-step is

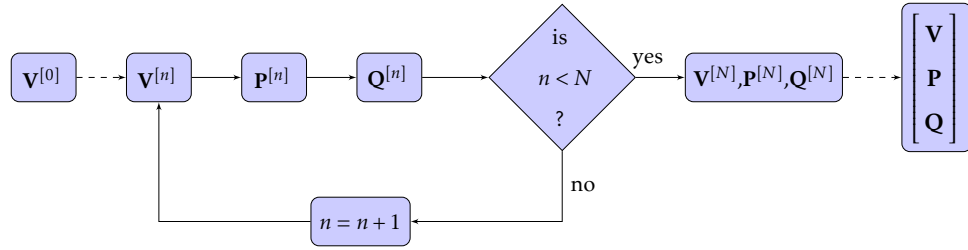


FIGURE 5.3: Time step process from initial volume vector input to determine final volume, pressure and flow vectors

determined by (5.19). Figure 5.3 illustrates the process in a flow chart starting with the initial conditions $\mathbf{V}^{[0]}$ as input into the iterative process, with the final solution vector $[\mathbf{V} \ \mathbf{P} \ \mathbf{Q}]^T$ the output. This method is valid provided that Δt is sufficiently small. In the lumped parameter modelling results presented in this chapter, a time step of 1×10^{-5} was necessary. Evidence of this instability can be observed in Section 7.2.1 where the time step is reduced by a factor of ten.

An explicit numerical time integration method, although prone to instability unless the time step is small, was selected for consistency throughout modelling methodologies to permit valid comparisons. This will be commented on further in Chapter 7. Similar simulations were performed with other other explicit methods, and an implicit method could have been adopted. This would have permitted a more stable solution with a larger time step, but may have increased computational complexity and it would have required iterating between the current time step value, n , and guesses for the next time step, $n + 1$, multiple times before determining the solution at the next time point. This was also dependent on having a function describing all state variables (pressure/flow) which is not the case in the work presented in Chapter 7.

By defining the input parameters of total stressed blood volume V_T , and the physical constraints (d, D) , the state equations above were solved simultaneously upon using the Forward Euler's method. Initially V_T was distributed appropriately between the compliant chambers and a sufficient number of heart cycles were simulated to ensure periodic convergence. All simulations

were carried out by user defined *.m files using the software package MATLAB (MathWorks Inc., Natick, MA) which can be found in Appendix D.

5.2.5 Model Protocols

To allow a valid comparison between the different configurations, the methodology used by Shimizu *et al.* [86] was adopted. This involved varying the total stressed blood volume to match the mean MPA pressure. The reference value used was taken from the 4 mm Blalock-Taußig model configuration with $V_T = 80$ ml. The mean MPA pressure used for matching was 58.514 mmHg as found in the results below.

To simulate different configurations of the Hybrid Procedure the external diameters of the PAB and stent were incrementally increased by 0.5 mm from 2.5 to 4 mm, and by 1 mm from 7 to 10 mm (initially) respectively.

Following the results and analysis of matching the mean MPA pressure, the study was repeated by matching the cardiac output at various levels. A range of cardiac outputs that would cover a spread of potential cardiac scenarios was adopted: 0.5, 1.0, 1.5, 2.0, 3.0 l/min. The cardiac output of 1.73 l/min from the reference configuration of 3 mm external banding and 8 mm stent for the fixed mean MPA pressure data was also included. This allows insight into the performance of the possible hybrid configurations of limited ventricular capabilities.

As this is a generalised non-specific HLHS patient, it is difficult to apply a generic body surface area (BSA) to allow a suitable scaling to allow comparison of the results with published clinical outcomes. Specifically for hybrid patients, the limited published BSA data range from 0.18 to 0.25 m² (mean 0.213 m²) [147], which is lower than the typical HLHS patient (typically a Norwood Procedure candidate) of 0.33 m² [85], although this reference does not match the Norwood results published by Li *et al.* [147]. This could be as a result of the use of the Hybrid Procedure for high-risk HLHS patients. With

limited available published data on BSA for HLHS, the generic value of 0.3 m^2 given in [91] is a reasonable value to compare cardiac index (cardiac output divided by BSA), the conventionally published outcome. This range of values however, leads to the cardiac output from the model being scaled by a value anywhere from 3 to 5 to allow comparisons with published cardiac index values. Therefore direct comparison to the values published in the literature for Hybrid (2.6 l/min/m^2 [147]) and general HLHS patients (6.18 l/min/m^2 [85]; 4.2 [148]; $\approx 10 \text{ l/min/m}^2$ [149]) is not ideal. Using the BSA value of 0.33 m^2 this cardiac output results in a cardiac index of 5.24 l/min/m^2 which matches those of a standard HLH patient.

Finally, the effect of an occluded ductal stent was investigated for all configurations of the Hybrid (maintaining both mean MPA pressure and a range of cardiac outputs). The full range of ductal stent diameters was 4 mm to 10 mm, again in 1 mm steps.

The matching of the total stressed blood volume to the constant mean MPA pressure and cardiac outputs was achieved using the Method of False Position. This is a numerical technique that “guesses” two initial total stressed blood volumes that provide outcome values greater and less than the targeted value (e.g. cardiac output of 1.73 l/min), and iterates until the V_T which matches the haemodynamical outcome is determined within a sufficient tolerance.

5.2.6 Calculation of Arterial and Venous Saturation and Oxygen Delivery

To determine the oxygen saturations and delivery associated with the circulation there are several parameters that need to be defined. Firstly the maximal oxygen carrying capacity of blood, \widehat{O}_2 , is determined using the maximum amount of oxygen carried per gram of haemoglobin ($1.34 \text{ ml O}_2/\text{g}$) and the

haemoglobin concentration (165.2 g/l) [85]:

$$\begin{aligned}\widehat{O}_2 &= 1.34 \times 16.52 \\ &= 22.14 \frac{\text{ml O}_2}{\text{l}}\end{aligned}\quad (5.21)$$

Dissolved oxygen in the blood is neglected in this calculation, although clinically this can effect the pulmonary vascular resistance which decreases with increased oxygen levels. As the binding of oxygen to the haemoglobin in the blood rarely 100% efficient, the oxygen content in the pulmonary vein, $C_{\text{pv}}\text{O}_2$, (fully oxygenated) is determined by multiplying the oxygen carrying capacity by the (assumed constant) pulmonary vein saturation $S_{\text{pv}}\text{O}_2$ of 98% [124]:

$$\begin{aligned}C_{\text{pv}}\text{O}_2 &= S_{\text{pv}}\text{O}_2 \times \widehat{O}_2 \\ &= 0.98 \times 22.14 \\ &= 21.69 \text{ ml O}_2 / (\text{l m}^2)\end{aligned}\quad (5.22)$$

To determine the oxygen delivery and the arterial and venous saturations we must define three balancing equations. Equation (5.23) balances the flow of oxygen into the pulmonary veins with the flow of oxygen going into the lungs in addition to the uptake of oxygen during respiration ($S\dot{V}\text{O}_2$). Similarly Equation (5.24) balances the oxygen content returning to the heart with the oxygen content supplied to the body minus the oxygen consumption by the body. Finally Equation (5.25) applies the steady-state condition for oxygen mass conservation where the oxygen uptake in the lungs is equal to the oxygen consumption of the body. The oxygen consumption rate of 185 ml O₂/min/ m² is adopted from the literature [150]:

$$Q_p \cdot C_{\text{pv}}\text{O}_2 = Q_p \cdot C_{\text{a}}\text{O}_2 + S\dot{V}\text{O}_2 \cdot \text{BSA} \quad (5.23)$$

$$Q_s \cdot C_{\text{v}}\text{O}_2 = Q_s \cdot C_{\text{a}}\text{O}_2 - C\dot{V}\text{O}_2 \cdot \text{BSA} \quad (5.24)$$

$$C\dot{V}\text{O}_2 = S\dot{V}\text{O}_2 \quad (5.25)$$

Upon rearranging Equation (5.23) and substituting Equation (5.25) the arterial oxygen content can be calculated from Equation (5.26):

$$C_aO_2 = C_{rv}O_2 - \frac{C\dot{V}O_2 \cdot BSA}{Q_p} \quad (5.26)$$

The oxygen delivery is then determined by multiplying the arterial oxygen content by the systemic flow rate, normalised by the body surface area:

$$\begin{aligned} DO_2 &= \frac{Q_s}{BSA} \cdot C_aO_2 \\ &= \frac{Q_s}{BSA} \left(C_{rv}O_2 - \frac{C\dot{V}O_2 \cdot BSA}{Q_p} \right) \\ &= \frac{Q_s}{0.33} \left(21.69 - \frac{61.05}{Q_p} \right) \end{aligned} \quad (5.27)$$

The arterial and venous saturations are calculated by dividing the arterial and venous oxygen content respectively by the oxygen carrying capacity of the blood:

$$S_aO_2 = \frac{C_aO_2}{\overline{O_2}} \quad (5.28)$$

$$S_vO_2 = \frac{C_vO_2}{\overline{O_2}} \quad (5.29)$$

where S_vO_2 is calculated from Equation (5.24).

This derivation was adapted from the work presented by Bove *et al.* [124]. In the following sections where a direct comparison is made to the results of Shimizu *et al.* the oxygen saturation and delivery calculations use the following constants: Haemoglobin concentration of 160 g/l, body surface area of 0.2 m² and pulmonary vein saturation of 97% [86]. This accounts for any perceived discrepancies in adapted model and subsequent Hybrid model results with the results from the direct reproduction.

5.2.7 Circulatory Parameters

Throughout the present study, all circulatory parameters (listed in Table 5.1) are kept constant i.e. are fixed. This is to maintain a valid haemodynamical comparison and to permit the investigation of changing the dimensions of the banding and stent diameters, in addition to assessing the methodological approaches regarding the varying of total stressed blood volume. This limitation of the current study is discussed further in Section 5.4.

5.3 Outcomes

The results of the simulations of the models outlined above are now presented. First identical reproduction followed by the adapted Norwood models are compared with the original work [86]. Following this, an analysis of the haemodynamical and ventricular performance of the Hybrid Procedure under different configurations is performed. The clinical implications of these results are then discussed. Finally, the optimal configuration of the Hybrid circulation is compared with the optimal Norwood configurations given by Shimizu *et al.* [86].

5.3.1 Norwood Circulation

The conclusions from the original publication regarding the Norwood configurations by Shimizu *et al.* [86] were:

"[The] use of the valved or non-valved [Sano] shunt eliminated pulmonary over-circulation which was observed when using the systemic to pulmonary artery shunt (modified BlalockTaufsig shunt). Although the valved [Sano] shunt improved pulmonary blood supply and consequently increased pulmonary artery flow and oxygen saturation compared to the non-valved [Sano] shunt, the non-valved [Sano] shunt improved ventricular energetics in spite of the presence of PA to RV regurgitation."

Upon reviewing the results, as suggested by the analysis presented within the article, the optimal configurations are 3.5 mm for the mBT shunt, 5 mm for the valved and 6 mm for the non-valved Sano Shunt. These configurations are used for comparison between the direct reproduction analysis and the adaptation method, which separates the systemic compliance to include an additional compliant chamber representing the neo-aorta. The neo-aortic compliance is given an identical value to the main pulmonary artery compliance in the Hybrid model, defined in Table 5.1 as characteristic pulmonary compliance, since the neo-aorta is reconstructed from the pulmonary trunk.

Direct Reproduction

Table 5.2 shows the reproduced results, the published results and the percentage difference for the three optimal configurations. As can be seen from the table, results correlate well, and all outcomes are within 3% at worst, with the difference in the majority of outcomes negligible. In the original publication, the results were rounded, in the most cases, to three significant figures. It was also established, through personal communication, that the *Simulink* toolbox for Matlab was utilised in the original study, while in our research all simulations were manually coded. These factors may account for the marginal discrepancies. Therefore, it was with confidence that this model was adapted to include the additional compliant chamber, resulting in a simplification of its execution, and later leading to the construction of the post-Hybrid circulation model.

Adapted Norwood Circulation

In adding the additional compliant chamber (the value of which is subtracted from the original compliance value of the systemic arteries to maintain total compliance [86, 144]) there are slight variations in results. These are more prominent in the BT shunt configuration, likely due to the fact that Sano shunt bypasses the additional chamber, with simulated blood flow passing directly from the right ventricle to the pulmonary artery chamber. The total stressed

TABLE 5.2: Direct comparison between reproduction of Shimizu *et al.* and published results [86]. *RVEDV*: Right Ventricle End Diastolic Volume; *PVA*: Pressure-Volume Area

	Blalock-Taussig			Non-valved Sano			Valved Sano		
	<i>D</i> = 3.5 mm			<i>D</i> = 6 mm			<i>D</i> = 5 mm		
	Adapted	Reproduced	% Difference	Adapted	Reproduced	% Difference	Adapted	Reproduced	% Difference
Systolic Systemic Pressure (mmHg)	87.58	87.00	0.67	76.53	76.20	0.44	77.24	77.00	0.31
Diastolic Systemic Pressure (mmHg)	45.28	45.00	0.63	52.15	51.80	0.67	52.14	51.90	0.47
Mean Systemic Pressure (mmHg)	59.08	58.70	0.65	59.06	58.70	0.62	59.06	58.70	0.62
Mean Pulmonary Pressure (mmHg)	13.86	13.80	0.43	12.73	12.60	1.04	12.11	11.90	1.78
Cardiac Output (l/min)	1.88	1.86	0.83	1.82	1.81	0.68	2.21	2.19	1.10
Pulmonary Flow (l/min)	1.05	1.04	0.54	0.99	0.98	0.56	0.91	0.90	0.94
Systemic Flow (l/min)	0.83	0.82	1.19	0.84	0.83	0.86	0.83	0.83	0.44
Pulmonary-Systemic Flow Ratio	1.26	1.26	0.01	1.18	1.18	-0.24	1.09	1.09	-0.02
Diastolic Run-Off (l/min)	-0.69	-0.69	-0.09						
Diastolic Regurgitation (l/min)							-0.47	-0.47	0.49
Systemic Oxygen Saturation (%)	80.50	80.40	0.12	79.49	79.30	0.24	78.00	77.80	0.26
Venous Oxygen Saturation (%)	59.70	59.50	0.33	58.87	58.50	0.64	57.30	56.90	0.70
Total Stressed Blood Volume (ml)	75.10	75.10	0.00	69.20	69.20	0.00	71.40	71.40	0.00
RVEDV (ml)	23.41	23.30	0.48	20.76	20.60	0.76	22.66	22.40	1.14
Stroke Work (mmHg · ml)	916.58	905.00	1.28	721.90	704.00	2.54	850.27	829.00	2.57
Systolic PVA (mmHg · ml)	1165.51	1157.00	0.74	858.17	843.00	1.80	966.96	949.00	1.89
Mechanical Efficiency (%)	78.64	78.20	0.56	84.12	83.50	0.74	87.93	87.40	0.61

TABLE 5.3: Comparison between adapted Norwood model and reproduced results of Shimizu *et al.*[86]. *RVEDV*: Right Ventricle End Diastolic Volume; *PVA*: Pressure-Volume Area

	Blalock-Taussig			Non-valved Sano			Valved Sano		
	<i>D</i> = 3.5 mm			<i>D</i> = 6 mm			<i>D</i> = 5 mm		
	<i>Adapted</i>	<i>Reproduced</i>	% <i>Difference</i>	<i>Adapted</i>	<i>Reproduced</i>	% <i>Difference</i>	<i>Adapted</i>	<i>Reproduced</i>	% <i>Difference</i>
Systolic Systemic Pressure (mmHg)	80.91	87.27	-7.29	72.47	76.53	-5.30	73.16	77.24	-5.28
Diastolic Systemic Pressure (mmHg)	45.52	45.29	0.50	52.25	52.15	0.19	52.31	52.14	0.31
Mean Systemic Pressure (mmHg)	58.54	59.15	-1.03	58.70	59.06	-0.62	58.77	59.06	-0.49
Mean Pulmonary Pressure (mmHg)	13.34	13.88	-3.84	12.18	12.73	-4.36	11.59	12.11	-4.29
Cardiac Output (l/min)	1.86	1.88	-0.76	1.81	1.82	-0.75	2.20	2.21	-0.68
Pulmonary Flow (l/min)	1.04	1.05	-0.49	0.98	0.99	-0.81	0.90	0.91	-0.84
Systemic Flow (l/min)	0.82	0.83	-1.10	0.83	0.84	-0.70	0.83	0.83	-0.57
Pulmonary-Systemic Flow Ratio	1.27	1.26	0.62	1.18	1.18	-0.11	1.09	1.09	-0.28
Diastolic Run-Off (l/min)	-0.51	-0.69	-25.22						
Diastolic Regurgitation (l/min)							-0.47	-0.47	-0.62
Arterial Oxygen Saturation (%)	80.42	80.51	-0.10	79.35	79.49	-0.18	77.84	78.00	-0.21
Venous Oxygen Saturation (%)	59.43	59.74	-0.52	58.58	58.87	-0.49	57.02	57.30	-0.49
Total Stressed Blood Volume (ml)	75.10	75.10	-0.00	69.20	69.20	-0.00	71.40	71.40	-0.00
RVEDV (ml)	23.60	23.50	0.40	20.73	20.76	-0.15	22.61	22.66	-0.23
Stroke Work (mmHg · ml)	831.53	931.42	-10.72	678.09	721.90	-6.07	801.40	850.27	-5.75
Systolic PVA (mmHg · ml)	1099.67	1185.47	-7.24	819.78	858.17	-4.47	922.94	966.96	-4.55
Mechanical Efficiency (%)	75.62	78.57	-3.76	82.72	84.12	-1.67	86.83	87.93	-1.25

blood volume is matched to the published value in the original paper, and upon viewing that the mean MPA varies (which is controlled at 58.7 mmHg), V_T could be adjusted to maintain it as specified in the original methodology. However, the purpose of Table 5.3 is to illustrate the effect solely of the inclusion of an additional compliant chamber, separated from one of the existing chambers, therefore identical stressed blood volumes were used.

To avoid the complexity of the full Norwood models, which require special consideration to determine flow through the mBT shunt depending on whether the valve is open or not, the flow was considered from the systemic artery chamber for the present adapted model. This is opposed to originating from an additional systemic node between the MPA and the systemic artery chambers. This vastly reduces the complexity of the code, improves its efficiency, and accounts for the slight variation between the direct reproduction and adapted models.

The most notable differences across all configurations is the decrease in stroke work and pressure-volume area (PVA). The decreases in stroke work of between 4.5% and 11% represent an absolute drop of between 100 and 40 mmHg · ml for each configuration. The differences of the all remaining outcomes from the Sano shunt models are approximately within 5%, with many have less than one percentage point of a discrepancy.

Specifically for the mBT shunt, there is over a 6 mmHg (7.3 %) drop in systolic MPA pressure. It is this difference that accounts for the only outcome with a discrepancy greater than 11%: The diastolic run-off to the pulmonary system (i.e. the stealing of systemic flow) is reduced by 25%. As the peak systolic pressure is lower there is less of a pressure difference across the stent in diastole, thus reducing the pulmonary flow during diastole. This discrepancy, as described above, is the only substantial disparity as a consequence of the simplification to the calculation of stent flow.

Upon comparing the differences, only the stroke work, PVA and systolic MPA pressures incur noteworthy changes, all of which are reductions. There-

fore there was no evidence to raise concerns over the adjustment. Variations from the published model can be negated by fixing the mean MPA pressure and varying the stressed blood volume accordingly to match.

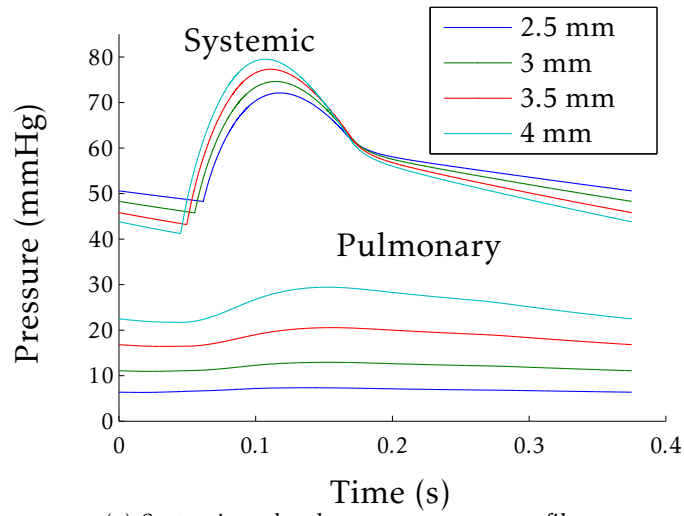
5.3.2 Hybrid Circulation

Effect of PAB diameter

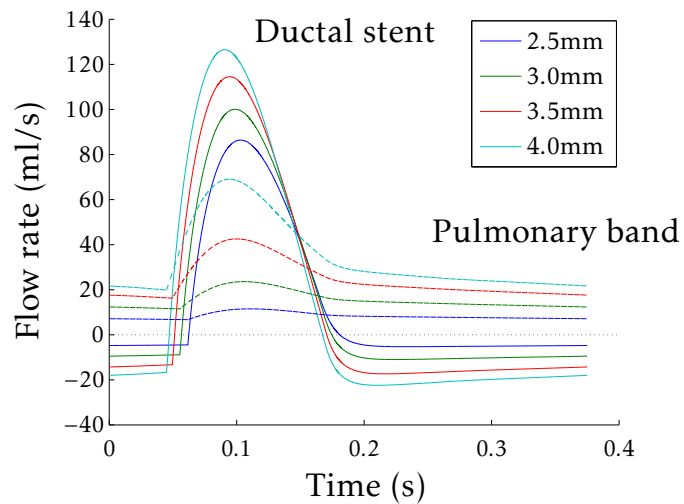
The haemodynamic results of the simulations with a ductal stent diameter of 8mm are summarised in Table 5.4, while the pressure and flow profiles for all band diameters with an 8 mm stent diameter as well as the pressure-volume loops are presented in Figure 5.4. Decrease in ductal stent diameter over the range 10 to 7 mm had a negligible haemodynamic effect. Hence, the results of the reference stent diameter is selected for presentation and discussion of the effect of varying internal PAB diameter. The case of a restrictive ductal stent will be discussed in the following section for a specified band diameter of 3 mm.

To validate the above assertion, the effect of varying the stent diameter from 7 to 10 mm is now surmised: The reduction of ductal stent diameter reduced systemic systolic pressure from 77 mmHg with a 10 mm stent to 72 mmHg with a 7 mm stent (PAB = 3 mm). The greatest systemic systolic pressure variation as a result of stent diameter occurred at the loosest banding of 4 mm, yet only varied by 7.5 mmHg. The increase in ventricular stroke work as ductal diameter is reduced for the reference PAB of 3 mm was 781.9 to 790 mmHg · ml, while for the 4 mm banding was from 1346.4 to 1370.1 mmHg · ml. Following from this, the cardiac output varied negligibly as the ductal diameter was restricted from 10 mm to 7 mm (less than 0.03 l/min). Little improvement to systemic oxygen delivery, DO_2 , was demonstrated (365.50 to 368.94 ml O_2 /min/m²).

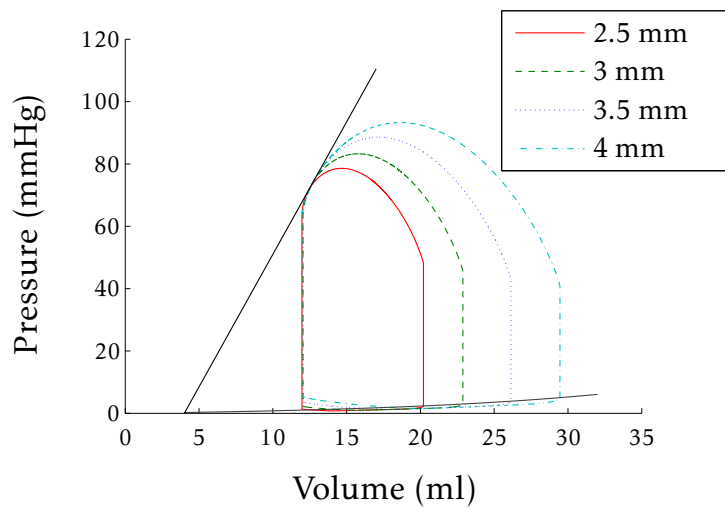
An increase in PAB diameter from 2.5 to 4 mm was associated with an increased $Q_p : Q_s$ (0.61 to 2.66), predominantly as a result of an increase in



(a) Systemic and pulmonary pressure profiles



(b) Systemic and pulmonary flow profiles



(c) Pressure-Volume loop

FIGURE 5.4: Hemodynamical profiles and pressure-volume loop of simulation with 8 mm ductal stent diameter, varying band diameter and fixed mean MPA pressure of 58.5 mmHg

TABLE 5.4: Hemodynamical data for Hybrid Circulation with varying pulmonary arterial banding and fixed ductal stent of 8 mm and mean MPA pressure of 58.51 mmHg

Band Diameter (mm)	2.5	3.0	3.5	4.0
Systolic MPA Pressure (mmHg)	78.55	83.21	88.52	93.19
Diastolic MPA Pressure (mmHg)	48.24	45.67	43.01	40.93
Mean MPA Pressure (mmHg)	58.51	58.51	58.51	58.51
Systolic Systemic Pressure (mmHg)	72.10	74.62	77.31	79.51
Diastolic Systemic Pressure (mmHg)	48.27	45.77	43.21	41.22
Mean Systemic Pressure (mmHg)	57.45	57.10	56.72	56.40
Mean Pulmonary Pressure (mmHg)	7.09	12.42	19.25	26.63
Cardiac Output (l/min)	1.32	1.73	2.25	2.80
Pulmonary Flow (l/min)	0.50	0.93	1.47	2.03
Systemic Flow (l/min)	0.82	0.80	0.79	0.77
Pulmonary-Systemic Flow Ratio	0.61	1.16	1.87	2.66
Stent Backflow (l/min)	-0.20	-0.40	-0.61	-0.78
Systemic Oxygen Saturation (%)	42.91	68.36	79.22	84.44
Venous Oxygen Saturation (%)	9.13	34.03	44.13	48.42
Systemic Oxygen delivery (ml O₂/min/m²)	234.97	368.39	417.61	433.67
Total Stressed Blood Volume (ml)	65.87	72.50	81.56	92.09
RVEDV (ml)	20.21	22.88	26.13	29.46
Stroke Work (mmHg·dotml)	576.29	786.48	1062.22	1360.08
Systolic pva (mmHg·dotml)	843.69	1059.60	1339.10	1638.19
Mechanical Efficiency (%)	68.31	74.22	79.32	83.02

pulmonary flow (0.5 to 2 l/min). In comparison, the systemic perfusion was slightly reduced (0.82 to 0.77 l/min). The decrease in resistance to pulmonary flow also resulted in increased diastolic stent backflow (-0.2 to -0.78 l/min) so almost all of the substantial increase in cardiac output (1.3 to 2.8 l/min) entered the pulmonary circulation. This is reflected in the increase in ventricular stroke work required to maintain the mean systemic MPA pressure (576 to 1360 mmHg · ml - see pressure-volume loop of the single ventricle in Figure 5.4(c)).

As both the systemic diastolic pressure decreased (48.3 to 41.2 mmHg) and systolic pressure increased (72.1 to 79.5 mmHg) when applying looser bands, the pulse pressure in the systemic arteries notably increased (23.8 to 38.3 mmHg). This is seen in the full pressure profiles shown in Figure 5.4(a). Mean pulmonary artery pressure (distal to banding site) increased with larger banding diameter from 7.09 to 26.63 mmHg for an external banding of 2.5 mm to 4.0 mm. Arterial and venous saturations also increased, SaO₂ from 43% to 84% and SvO₂ from 9% to 48% with decreasing pulmonary resistance from looser banding. The jumps in systemic oxygen delivery (235-to-368-to-418-to-434 l/min; 2.5-to-4 mm) show that decreasing the pulmonary banding impairs the oxygen delivery, while continual reduction of pulmonary resistance slows the rate of increase in oxygen delivery.

In order to maintain the mean MPA pressure and facilitate the increase in cardiac output, the stressed blood volume must increase from 65.87 to 92.09 ml as the external banding diameter increases from 2.5 to 4 mm. This methodology, which allows the increase of cardiac output, is the main reason for the increase of oxygen delivery. If we consider the oxygen delivery per litre per minute of cardiac output or normalised by stroke work we see that the most efficient, optimal outcome in both cases is the 3 mm banding as given in Table 5.5.

The tightness of PAB had the expected influence on the $Q_p : Q_s$ ratio as found in clinical experience (Figure 5.5(a)). The results of this work verify the

TABLE 5.5: Normalised systemic oxygen delivery

	2.5 mm	3.0 mm	3.5 mm	4.0 mm
O₂ delivery	234.97	368.39	417.61	433.67
O₂ delivery normalised by cardiac output	178.01	212.94	185.60	154.88
O₂ delivery normalised by stroke work	0.41	0.47	0.39	0.32

clinical observation that this variability is driven by the pulmonary circulation rather than the systemic when the mean main pulmonary artery pressure is maintained at 58.5 mmHg. Despite increased cardiac output with larger banding, the systemic supply decreases (see Figure 5.5(b)) which can be attributed to the increase in diastolic backflow through the stented ductus. The consequence of this is the compromised diastolic systemic flow could impact retrograde aortic arch supply to the brain and the coronary arteries, the latter of which is predominantly perfused in diastole [151]. The diastolic MPA pressure reduces as the pulmonary band is widened further highlighting this concern as shown in Figure 5.5(d). Another conclusion from this investigation is that the PAB does not have a significant effect on the systolic systemic perfusion, but by reducing the resistance to flow into the pulmonary circulation, it results in greater diastolic steal.

The increase in pulmonary flow, as would be expected, increased both the arterial and venous saturation levels as the greater flow to the lungs results in greater oxygenation of the blood. The increase in oxygenation comes at a greater cost and this must be balanced in identifying the optimal banding. The exposure to elevated pulmonary artery pressure distal to the banding resulting from looser bands increases the risk of pulmonary vascular disease [152, 153].

The results demonstrate that, in this model, the systemic haemodynamics distal to the stent vary little with pulmonary banding or stent diameter when the mean MPA pressure is maintained. This would suggest looking at the clinical options available to alter the systemic vascular resistance, such as through administration of vasodilators, or altering the blood volume with

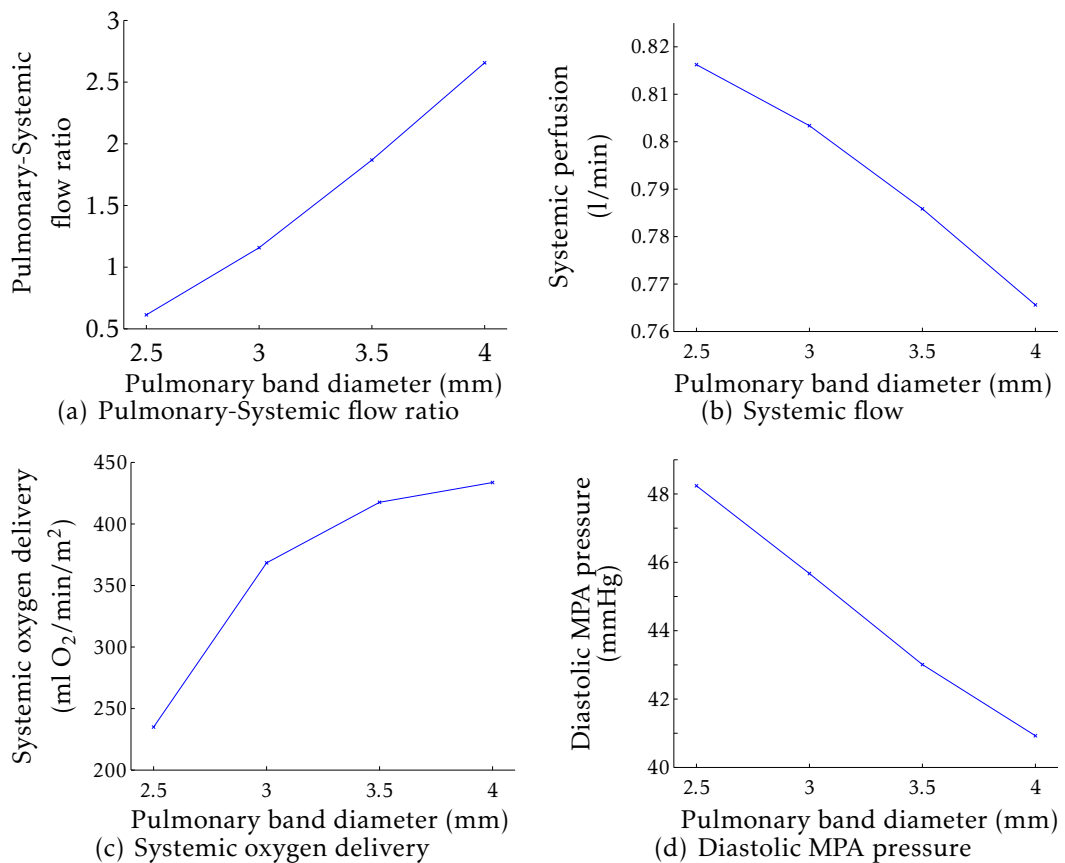


FIGURE 5.5: Hemodynamical outcomes of simulation with varying pulmonary arterial banding, fixed 8 mm ductal stent diameter and constant mean MPA pressure of 58.5 mmHg

diuretics. This could be simulated within the current model, provided appropriate values for the resistance constants could be determined. As the focus was on patient-specific modelling, and there was no quantitative relationship between the lumped resistances and pharmacological agents, this investigation was not performed. Additionally, the contractility of the ventricle could be altered clinically by the administration of pharmaceutical agents such as catecholamines. This can be simulated by adjusting the parameter A_{RV} , the gradient of the maximum elastance line as seen in Figure 5.4(c). In both cases, the overwhelming quantity of additional data and analysis that would have been required from these investigations was outside the scope of this research, which was addressed the question of optimising the surgical configuration of the Hybrid Procedure.

The configuration that resulted in the optimal haemodynamics of the hybrid circulation was an external PAB of 3 mm diameter and a stented ductus arteriosus of 8 mm or greater (as there was no distinguishable benefits to an expanded stent). See Table 5.4 for the full list of hemodynamical outcomes as well as those presented in Table 5.5. This conclusion was reached as there is only a slight drop in ventricular demand and negligible effect in all other outcomes with an enlarged stent. The risk of rupture or other clinical complications of over-stretching the ductus was considered too high. Due to the broad anatomical variation found within this cohort of patients, these results suggest that the stent should aim to maintain the maximal ductal diameter unless the patient presents with a restricted ductus.

Autonomic responses would most likely cause the mean MPA pressure to vary rather than increasing the cardiac output, as this methodology does, which would reduce the ventricular demands. The results warrant caution over loose pulmonary banding due to the general increases in the ventricular demand observed. The myocardial supply is also threatened as a result of the reduced systemic diastolic pressure and increased diastolic steal. This may compromise patients dependent on retrograde aortic flow for myocardial and cerebral supply. The band diameter that was most efficient at oxygen delivery was the 3 mm exterior banding.

Effect of Ductal Stent Occulsion

When restricting the ductal stent significant haemodynamical effects are found beyond the critical value of 7 mm. For the restricted duct discussion, the results for a controlled cardiac output of 1.73 l/min and PAB of 3 mm are given in Table 5.6. This effect was seen across all configurations, and cardiac outputs, thus the analysis is succinctly presented by this case. Restricted ductal patency significantly reduced systemic supply (0.8 to 0.73 l/min, 7 to 4 mm), increased $Q_p : Q_s$ (1.17 to 1.36) and ventricular workload increased (797 to 910 mmHg · ml) to overcome the greater resistance. Figure 5.6 illustrates the effect of ductal stent diameter decrease, emphasising the deterioration point

TABLE 5.6: Hemodynamical data for Hybrid Circulation with varying ductal stent diameter and fixed pulmonary banding of 3mm and cardiac output of 1.73 l/min

Stent Diameter (mm)	4.0	5.0	6.0	7.0	8.0	9.0	10.0
Systolic MPA Pressure (mmHg)	104.42	94.76	88.86	85.26	83.02	81.59	80.66
Diastolic MPA Pressure (mmHg)	42.41	44.13	44.95	45.35	45.57	45.69	45.77
Mean MPA Pressure (mmHg)	63.07	60.72	59.48	58.77	58.37	58.14	57.99
Systolic Systemic Pressure (mmHg)	61.87	66.89	70.34	72.76	74.46	75.65	76.47
Diastolic Systemic Pressure (mmHg)	43.68	44.70	45.24	45.51	45.66	45.75	45.81
Mean Systemic Pressure (mmHg)	52.68	54.78	55.94	56.59	56.98	57.21	57.36
Systolic Pulmonary Pressure (mmHg)	15.60	14.56	13.97	13.65	13.46	13.35	13.28
Diastolic Pulmonary Pressure (mmHg)	11.69	11.46	11.35	11.29	11.26	11.24	11.23
Mean Pulmonary Pressure (mmHg)	13.63	13.00	12.67	12.49	12.39	12.33	12.30
Cardiac Output (l/min)	1.73	1.73	1.73	1.73	1.73	1.73	1.73
Pulmonary Flow (l/min)	1.00	0.96	0.95	0.93	0.93	0.92	0.92
Systemic Flow (l/min)	0.73	0.77	0.79	0.80	0.80	0.81	0.81
Pulmonary-Systemic Flow Ratio	1.36	1.26	1.20	1.17	1.16	1.15	1.14
Stent Backflow (l/min)	-0.26	-0.32	-0.36	-0.39	-0.40	-0.41	-0.41
Systemic Oxygen Saturation (%)	70.37	69.38	68.82	68.49	68.29	68.18	68.10
Venous Oxygen Saturation (%)	32.70	33.40	33.70	33.82	33.89	33.93	33.95
Systemic Oxygen delivery (ml O ₂ /min/m ²)	345.62	356.71	362.49	365.50	367.25	368.29	368.94
Total Stressed Blood Volume (ml)	76.69	74.34	73.17	72.60	72.33	72.19	72.12
RVEDV (ml)	25.48	24.11	23.38	23.02	22.84	22.74	22.69
Stroke Work (mmHg · ml)	910.21	855.28	819.57	796.99	783.01	774.08	678.29
Systolic PVA (mmHg · ml)	1394.45	1222.50	1130.70	1081.65	1054.86	1039.36	1029.96
Mechanical Efficiency (%)	65.27	69.96	72.48	73.68	74.23	74.48	74.59

at 7 mm. Table 5.6 also highlights the decrease in mechanical efficiency and the increase in the oxygen requirement of the heart as represented by the PVA increase. This concurs with the clinical experience where stenotic stents or resistance at ductal level is associated with adverse clinical outcome [25, 154].

Once above the threshold for an unrestrictive stent (7mm), lowering the resistance further (increasing diameter up to 10 mm) has no substantial effect, even with varying PAB diameter. This shows that with a non-restrictive stent, the resistance in the peripheral circulation dominates, and a larger stent has no beneficial effect.

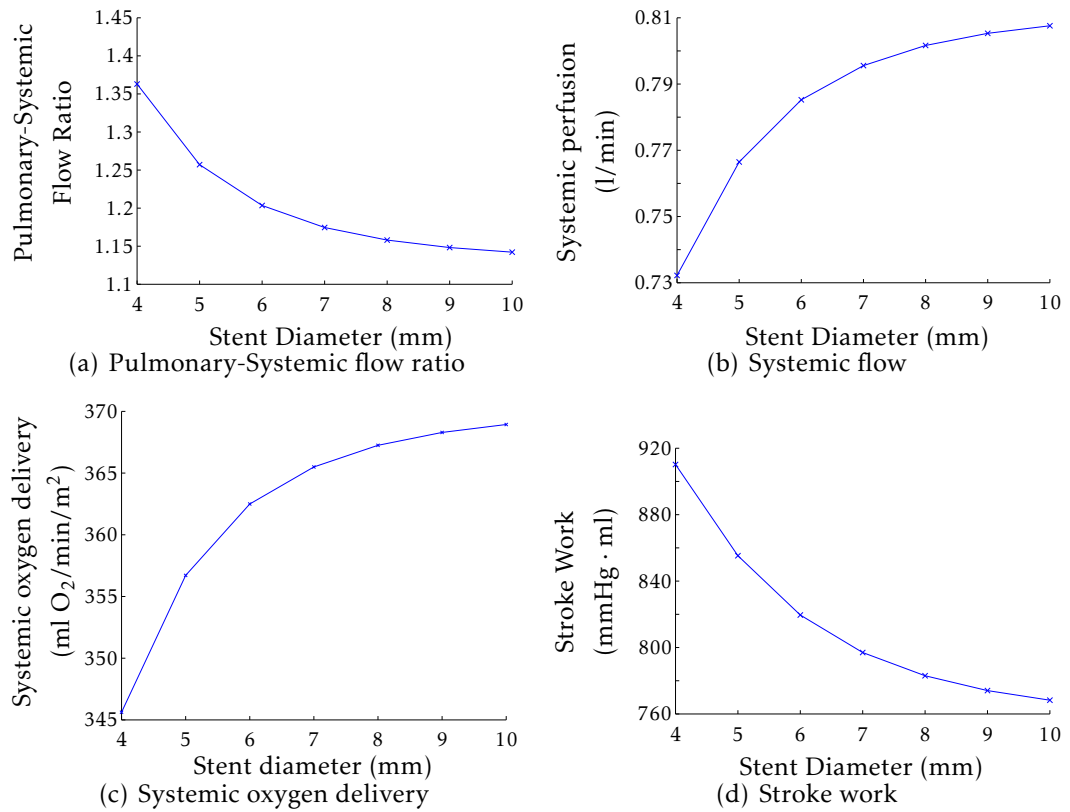


FIGURE 5.6: Hemodynamical outcomes of simulation with 3 mm pulmonary arterial banding, fixed cardiac output of 1.73 l/min and varying ductal stent diameter

This study was able to determine the effect of a restrictive stent which can often be difficult to acutely identify clinically. The increased ventricular demand in the short-term is likely to lead to impaired long-term ventricular function. Therefore, the lower ventricular demands for the reduced cardiac output could be masking the subtle onset of stent occlusion when investigated invasively or by Doppler.

Ventricular Demands

One of the consequences of the matching of the mean MPA pressure for all configurations, as in the study by Shimizu *et al.* [86], is the infinite potential for increasing ventricular workload by increasing total stressed blood volume. As can be seen in Figure 5.4(c), the stroke work (area of the pressure-volume loop) is increased to accommodate the increase in cardiac output and enforced maintenance of mean MPA pressure at 58.51 mmHg.

The assumption that the body will continue to maintain the mean MPA pressure when faced with different circulation configurations is not entirely physiologically realistic; it is a necessary over-simplification of the response of the body to a complex condition such as hypoplastic left heart syndrome. The heart is limited with respect to the stroke work and cardiac output the single ventricle can generate. This was the motivation behind the novel specified cardiac output analysis in the section below.

Potentially the most illuminating result of the simulation is with respect to the myocardial oxygen demand. In the case of aortic atresia, as modelled in this study of HLHS repaired with the Hybrid Procedure, coronary perfusion is supplied via retrograde flow in the aortic arch. As the demands on the ventricle increase, the supply of oxygenated blood to the the ventricle must also be increased. However, as can be seen in Table 5.4 and Figure 5.5(d), the diastolic pressure distal to the ductus decreases with looser banding, while the ventricular demand increases. This raises concerns over the cardiac performance of the patient as myocardial demand is not satisfied by the implied decrease in oxygen supply from reduced coronary perfusion in the otherwise superior configurations. This result would promote extreme caution in ensuring a sufficiently tight banding, otherwise the ventricular demand will increase, which combined with impaired coronary perfusion, would lead to ventricular dysfunction.

Regulated Cardiac Output

The analysis of the Hybrid circulation simulations with a regulated cardiac output shows that for the range of valid clinical outcomes of the model, the 3 mm banding is optimal, with 3.5 mm suitable for larger babies with greater cardiac output. This matches what is found in clinical practice [28].

The results from the controlled cardiac output simulations for a Hybrid configuration of 3 mm PAB and 8 mm ductal stent are listed in Table 5.7. The trends found in varying PAB in the previous section were similar for all cardiac

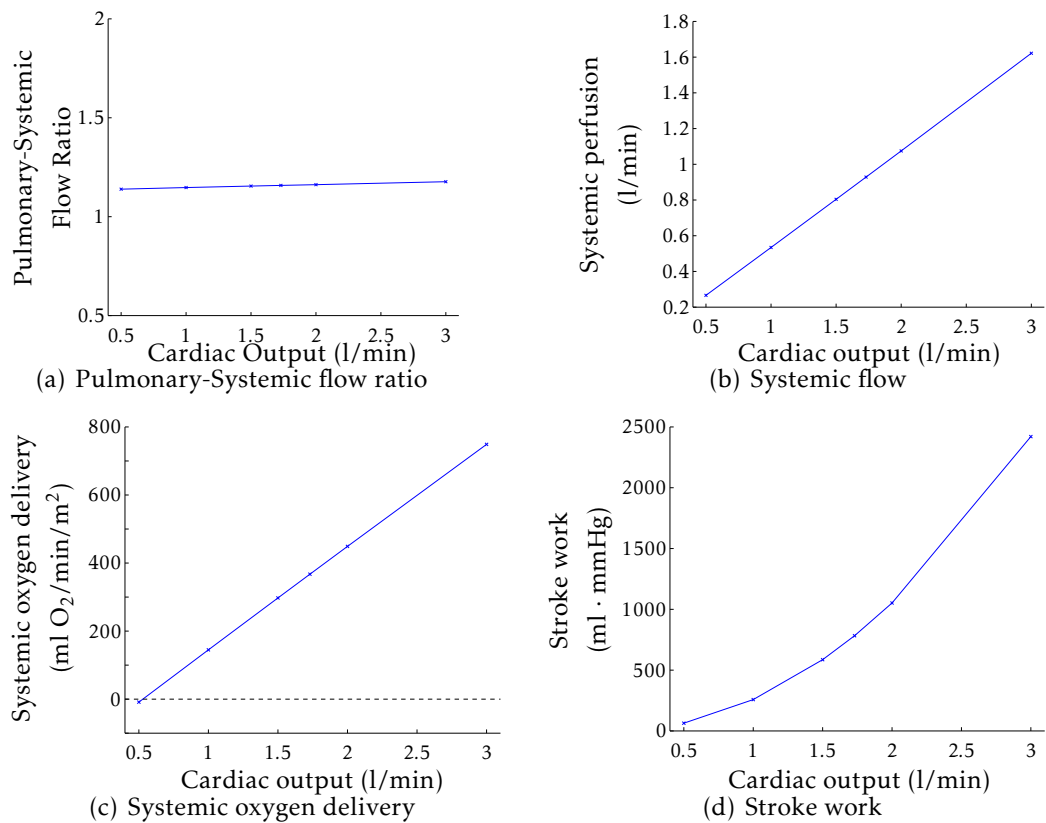


FIGURE 5.7: Hemodynamical outcomes of simulation with 3 mm pulmonary arterial banding and 8 mm ductal stent diameter varying cardiac output

outputs simulated with the exception of systemic oxygen delivery. As PAB is increased systemic flow decreases as found when varying the banding while maintaining mean MPA pressure (see Figure 5.5). The increase in PAB has a greater effect as cardiac output is increased.

It is found, from Figure 5.7(c), that the tighter banding produces better results for lower cardiac outputs and that effect is reversed for larger cardiac outputs. This very much supports the clinical assertion that lower birth weight patients should receive a tighter banding, however raises concerns over the future performance with growth. As no variation of the circulatory constants was able to be investigated to account for growth due to the scale of this task, it is cited as a precaution and a suggestion for future work.

Targeting predefined cardiac output values has no discernible effect on $Q_p : Q_s$ (Figure 5.7(a)). It is controlled by the external banding diameter (see

Figure 5.5(a)). From looking at the selected results presented in Table 5.7, we see that unphysiological results are obtained from the two extreme cardiac output values. Due to the ability of the model to mathematically match the desired output (mean MPA/cardiac output) by adjusting the total stressed blood volume, unphysiological results may be obtained, as in this case. This is best illustrated by the extremely high and low MPA pressures and the stroke work outcome. When compared with the range of results for the Norwood circulation, stroke work has some unrealistically high values (C.O. = 3 l/min) and concerning low values (C.O. = 0.5, 1 l/min). Figure 5.8(a) visualises these unphysiological results. Figure 5.8 best illustrates the conclusion that this model is only appropriate for the cardiac output range of 1 to 2 l/min. The haemodynamical data outwith this range is unphysiological, particularly so for the MPA (see Table 5.7).

Figure 5.8 also correlates well with clinical practice. Assuming that larger babies produce a larger cardiac output, this validates the practice that 3 mm PAB diameters are set for lower birth weight patients, while larger birth weights receive a 3.5 mm PA banding. We can see from the figure that the 3 mm banding best spans the physiological systemic perfusion rate for low-to-normal birth weights, with the 3.5 mm banding best spanning the normal-to-high range (where cardiac output is considered a surrogate for birth weight). A clinically relevant conclusion from this study is that tighter PABs maintain systemic perfusion at lower cardiac outputs.

One outcome that requires explanation is the negative oxygenation values for a lower cardiac outputs, which is an obvious unphysiological result. Upon reviewing the calculation found in Equation (5.29), this can be accounted for as a result of the the arterial oxygen supply being reduced as pulmonary flow decreases (see Equation (5.28)) and the systemic flow increasing, while the whole body oxygen consumption rate remains constant, which would obviously change with limited cardiac supply. This highlights another model simplification which is inappropriate in the extreme cases.

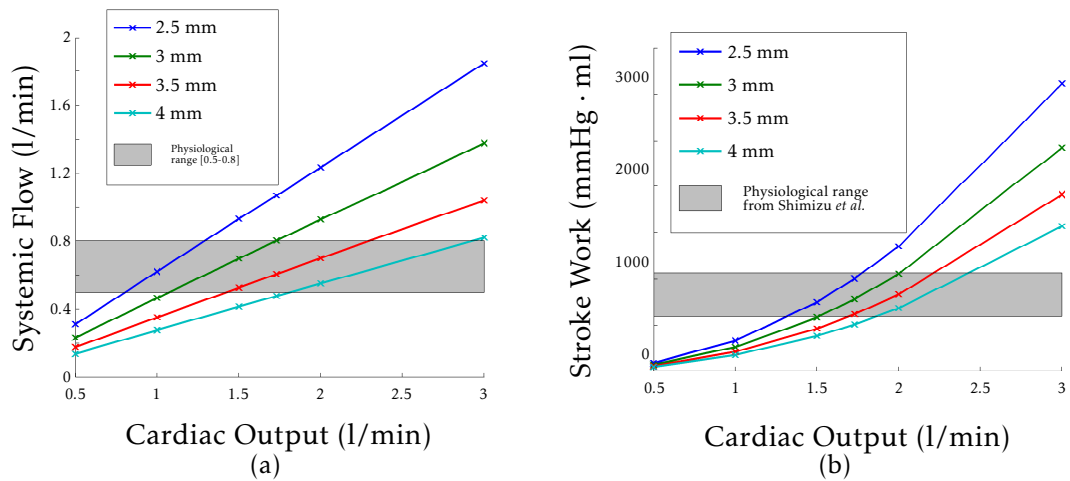


FIGURE 5.8: Haemodynamical outcomes with physiological reference regions as cardiac output is increased for different banding diameters

Total Stressed Blood Volume

As defined in the methodology of these simulations, the total stressed blood volume must be varied significantly to maintain either the mean MPA pressure, or cardiac output, to permit valid comparisons. This parameter is under-scrutinised in the literature, but as it is the main input parameter as described in the Methods section, it is vital. From current clinical perspective, there is no physiological measurement or observation that would supply an indicative value for future work such as patient specific circulation models. The total stressed blood volume can be considered as a lumped initial condition parameter, which then stabilises to periodically stable solution. Discussion of initial conditions for lumped circulation models for the modelling of repairs of HLHS are limited in the literature.

Current protocols dictate that this value must change to arrive at the desired clinical constraint, in this case the mean MPA pressure and specified cardiac output. It is stressed, however, that a fuller clinical context for this parameter is an essential step forward in cardiovascular, particularly patient-specific, modelling. Determining a clinically accepted range for this parame-

TABLE 5.7: Hemodynamical data for Hybrid Circulation with varying cardiac output for 3 mm banding and 8 mm ductal stent

Cardiac output (l/min)	0.5	1.0	1.5	1.73	2.0	3.0
Systolic MPA Pressure (mmHg)	22.95	46.77	71.40	83.02	96.92	151.36
Diastolic MPA Pressure (mmHg)	13.01	26.10	39.36	45.57	52.97	82.10
Mean MPA Pressure (mmHg)	16.51	33.27	50.36	58.37	67.93	105.36
Systolic Systemic Pressure (mmHg)	22.00	43.48	64.71	74.46	85.95	129.65
Diastolic Systemic Pressure (mmHg)	13.02	26.13	39.44	45.66	53.09	82.35
Mean Systemic Pressure (mmHg)	16.37	32.76	49.29	56.98	66.11	101.56
Mean Pulmonary Pressure (mmHg)	3.32	6.81	10.54	12.39	14.69	25.03
Pulmonary Flow (l/min)	0.27	0.53	0.80	0.93	1.07	1.62
Systemic Flow (l/min)	0.23	0.47	0.70	0.80	0.93	1.38
Pulmonary-Systemic Flow Ratio	1.14	1.15	1.15	1.16	1.16	1.18
Stent Backflow (l/min)	-0.12	-0.24	-0.35	-0.40	-0.46	-0.67
Systemic Oxygen Saturation (%)	-5.58	46.38	63.69	68.29	72.34	80.99
Venous Oxygen Saturation (%)	-123.56	-12.83	24.08	33.89	42.53	60.98
Systemic Oxygen Delivery (ml O ₂ /min/m ²)	-8.75	144.90	297.43	367.25	448.96	748.77
Total Stressed Blood Volume (ml)	23.48	42.02	62.23	72.33	85.03	143.46
RVEDV (ml)	9.37	14.79	20.28	22.84	25.86	37.41
Stroke Work (mmHg · ml)	63.75	257.83	585.98	783.01	1052.16	2420.52
Systolic PVA (mmHg · ml)	83.52	342.82	786.22	1054.86	1424.59	3352.58
Mechanical Efficiency (%)	76.32	75.21	74.53	74.23	73.86	72.20

ter is important, and is likely to depend on the number of compliant chambers used in the circulatory model.

Table 5.8 shows the change in haemodynamical results as the total stressed blood volume is varied between 60 and 90 ml. There is a clear trend that when the total stressed blood volume is increased, all other outcomes increase linearly with the exception of mean PA pressure (which decreases linearly) and with the pulmonary-systemic flow ratio which remains constant. The analysis of linearity will be addressed in greater depth in the coupled model analysis to avoid repetition of similar analysis and can be found in Section 7.3.2. A statistical analysis of linear trend will be presented.

TABLE 5.8: Hemodynamical data of the Hybrid Procedure ($d = 3\text{mm}, D = 8\text{mm}$) as total stressed blood volume is varied

Total Stressed Blood Volume (ml)	60.0	70.0	72.5	75.0	80.0	90.0
Systolic MPA Pressure (mmHg)	68.77	80.38	83.21	86.01	91.51	102.14
Diastolic MPA Pressure (mmHg)	37.96	44.16	45.67	47.16	50.09	55.74
Mean MPA Pressure (mmHg)	48.55	56.56	58.51	60.43	64.21	71.51
Systolic Systemic Pressure (mmHg)	62.48	72.27	74.62	76.95	81.50	90.22
Diastolic Systemic Pressure (mmHg)	38.03	44.25	45.77	47.26	50.20	55.88
Mean Systemic Pressure (mmHg)	47.54	55.24	57.10	58.94	62.56	69.52
Systolic Pulmonary Pressure (mmHg)	11.03	13.01	13.49	13.98	14.95	16.87
Diastolic Pulmonary Pressure (mmHg)	9.22	10.88	11.29	11.70	12.52	14.15
Mean Pulmonary Pressure (mmHg)	10.14	11.97	12.42	12.87	13.78	15.58
Cardiac Output (l/min)	1.45	1.68	1.73	1.79	1.90	2.10
Pulmonary Flow (l/min)	0.78	0.90	0.93	0.96	1.02	1.13
Systemic Flow (l/min)	0.67	0.78	0.80	0.83	0.88	0.97
Pulmonary-Systemic Flow Ratio	1.15	1.16	1.16	1.16	1.16	1.16
Stent Backflow (l/min)	-0.34	-0.39	-0.40	-0.41	-0.44	-0.48
Systemic Oxygen Saturation (%)	62.44	67.37	68.36	69.27	70.91	73.58
Venous Oxygen Saturation (%)	21.40	31.91	34.03	35.98	39.48	45.16
Systemic Oxygen Delivery (ml O ₂ /min/m ²)	281.45	351.53	368.38	384.98	417.37	479.09
RVEDV (ml)	19.70	22.26	22.88	23.49	24.69	26.99
Stroke Work (mmHg · ml)	545.07	736.03	786.47	837.85	943.14	1162.24
Systolic PVA (mmHg · ml)	730.66	990.66	1059.60	1129.95	1274.47	1576.72
Mechanical Efficiency (%)	74.60	74.30	74.22	74.15	74.00	73.71

As stated in [155] ‘*Elevation of [Systemic Vascular Resistance] to maintain blood pressure in the face of decreasing systemic cardiac output is a highly preserved cardiovascular reflex*’. Due to the nature of the model, this phenomenon is not accounted for. It would be extremely difficult to simulate, particularly with the ambiguity of the clinical representation of total stressed blood volume, as if this were not fixed the results could be engineered to produce any desired outcome when changing the systemic vascular resistance. There is currently no justification for the varying of the input parameter of total stressed blood volume other than fixing one of the model outcomes (e.g. mean MPA pressure) in order to compare models.

This is currently a necessary limitation, as without it, no simulations would be possible. It was a result of this parameter being presented openly by Shimizu *et al.* that enabled the reproduction and appreciation of how lumped circulation models do, and can, function [86]. Figure 5.9 illustrates the difference in using the reference stressed blood volume of 80 ml (in blue) in all configurations versus the value adjusted to maintain mean systemic (MPA in our model) pressure (in red). The subfigures are a reproduction of Figure 4 from the original publication.

The variation of total stressed blood volume will be addressed again in the multi-scale model presented in the following chapter. Currently the literature is ambiguous as to the methodology employed when using three dimensional CFD models with a lumped circulation model used for adaptive boundary conditions. The lumped circulation model could help provide an appropriate total stressed blood volume value to use to maintain a physiological outcome e.g. mean MPA pressure. This would require a relationship between the two contrasting band definitions adopted and is discussed in detail in Section 7.3.3.

5.3.3 Hybrid vs. Norwood Comparison

In maintaining the mean MPA pressure for the Hybrid configuration at the same pressure as the three optimal Norwood configuration, a comparison can

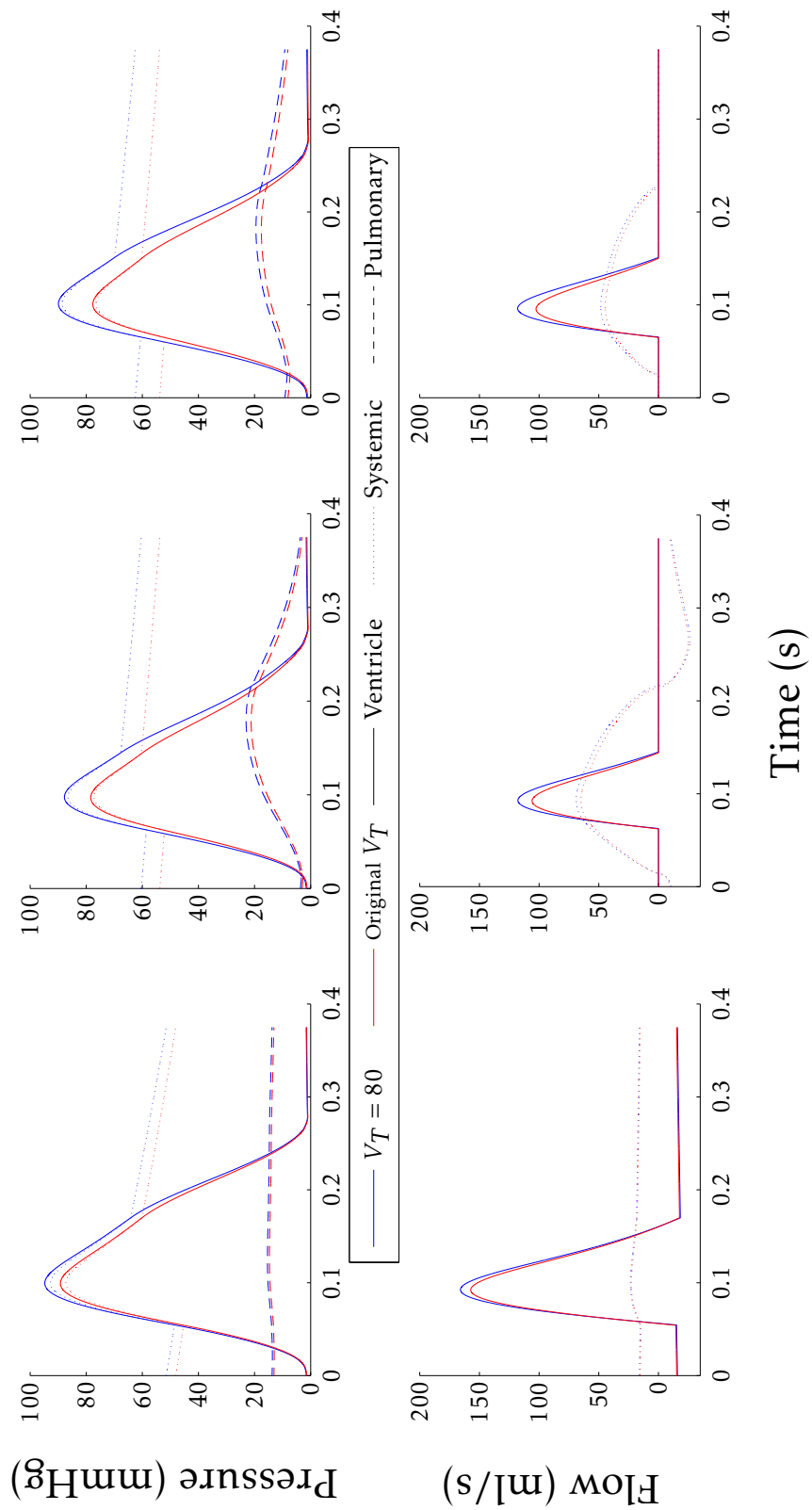


FIGURE 5.9: Fixed stressed blood volume in comparison to varied stressed blood volume as published by Shimizu *et al.* for optimal configuration of each model type [86]; Left: 3.5mm Blalock-Taussig Shunt; Middle: 6mm non-valved Sano Shunt; Right: 5mm valved Sano Shunt

TABLE 5.9: Hemodynamical data comparing the optimal Hybrid configuration versus optimal configurations of the Norwood Procedure

	Hybrid	Blalock-Taussig	Non-valved Sano	Valved Sano
	$d = 3 \text{ mm}, D = 8 \text{ mm}$	$D = 3.5 \text{ mm}$	$D = 6 \text{ mm}$	$D = 5 \text{ mm}$
Systolic MPA Pressure (mmHg)	83.22	80.88	72.84	72.25
Diastolic MPA Pressure (mmHg)	45.68	45.50	52.08	52.08
Mean MPA Pressure (mmHg)	58.51	58.51	58.51	58.51
Systolic Pulmonary Pressure (mmHg)	13.50	14.53	20.99	17.39
Diastolic Pulmonary Pressure (mmHg)	11.29	12.99	2.76	7.28
Mean Pulmonary Pressure (mmHg)	12.42	13.83	11.97	12.60
Cardiac Output (l/min)	1.73	1.86	2.19	1.80
Pulmonary Flow (l/min)	0.93	1.04	0.90	0.98
Systemic Flow (l/min)	0.80	0.82	0.83	0.83
Pulmonary-Systemic Flow Ratio	1.16	1.27	1.09	1.18
Stent Backflow (l/min)	-0.40	-0.51	-0.47	0.00
Systemic Oxygen Saturation (%)	68.36	71.50	67.29	69.73
Venous Oxygen Saturation (%)	34.04	37.93	33.87	36.45
Systemic Oxygen Delivery (ml O ₂ /min/m ²)	368.47	394.03	372.52	387.62
Total Stressed Blood Volume (ml)	72.51	75.06	71.09	68.99
RVEDV (ml)	22.88	23.59	22.53	20.68
Stroke Work (mmHg · ml)	786.70	830.83	795.16	674.28
Systolic PVA (mmHg · ml)	1059.92	1098.71	915.47	814.95
Mechanical Efficiency (%)	74.22	75.62	86.86	82.74

be made. It is essential to reiterate that to utilise mathematical models for comparisons, certain parameters must be controlled. For example, the comparisons between the surgery techniques presented here for the case of fixed mean MPA pressure, could be repeated at multiple alternative values to the 58.5 mmHg adopted. Again, for each pressure value that could be fixed, multiple shunt diameters can be simulated. For the Hybrid Procedure, each shunt diameter could be simulated while varying the pulmonary artery banding diameter also. This illuminates the wide range of investigations that are possible with modelling and this study has had to be specifically focussed when presenting the results given the volume generated.

Using the optimal configurations presented by Shimizu *et al.* [86] and the optimal configuration of the Hybrid from the analysis above, direct comparisons can be made. The haemodynamical results of the four alternative treatment options are presented side by side in Table 5.9.

There is higher systolic systemic pressure and lower pulmonary artery pressure resulting in the reduced diastolic pulmonary perfusion (stent backflow) in the Hybrid configuration. The reduced diastolic MPA pressure of the Hybrid, although comparing favourably to the mBT shunt (H: 45.68 mmHg; mBT: 45.50 mmHg) is lower than the 52.08 mmHg of both Sano variants. As discussed above, this will improve the coronary perfusion during diastole.

While the systemic perfusion of the Hybrid (0.80 l/min) is slightly reduced compared to all Norwood variants (0.82-0.83 l/min), the pulmonary perfusion (0.93 l/min) sits comfortably within the range of Norwood results (0.90-1.04 l/min). The $Q_p : Q_s$ ratio of the Hybrid, 1.16, is again comparable to the other configurations.

The stroke work required to match the Norwood mean MPA pressure for the Hybrid Procedure (786.70 ml · mmHg) compares favourably to that required for the Norwood configurations (674.28-830.83 ml · mmHg). However the main concern in the Hybrid configuration (and the BT Norwood) is that the myocardial demand (systolic PVA) is increased and the mechanical efficiency (stroke work/systolic PVA) is reduced by over 10% when compared to the Sano variants of the Norwood Procedure. This increase in the ventricular workload for both the Hybrid and BT Norwood is accompanied by a reduced diastolic MPA pressure affecting the coronary supply, which would compound each other leading to ventricular dysfunction. The above can be illustrated by referring to the pressure-volume loops presented in Figure 5.10. In varying the cardiac parameters, simulating the administration of various pharmaceutical treatment options, it is possible that the efficiency may be improved. This is also an option for all Norwood variants.

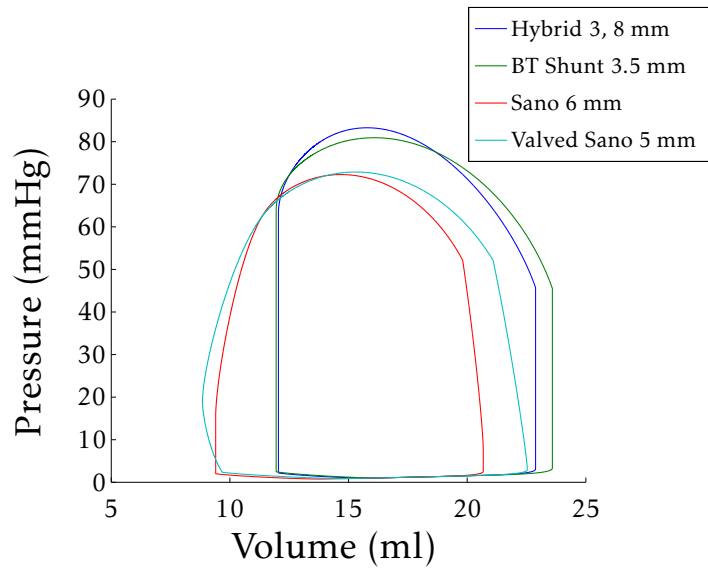


FIGURE 5.10: Pressure-Volume loops of the optimal Hybrid configuration and optimal configurations of the Norwood procedure

The only other non-favourable outcome of the Hybrid Procedure is the reduced oxygen delivery. This can, however, be explained by the decrease in systemic flow (0.8 versus 0.82-0.83 l/min) combined with a systemic arterial saturation level (68.36%) at the lower end of the range found in the Norwood results (67.29-71.50%).

Overall, the Hybrid Procedure results in very comparable haemodynamical outcomes with an inferred improvement in myocardial supply (as a result of the higher systolic systemic pressure, lower PA pressure and reduced diastolic stent backflow). The compromise of the Hybrid Procedure is the increased myocardial demand (increased systolic PVA) and the reduced oxygen delivery. The less invasive nature of the Hybrid (delaying the need for surgery involving cardiopulmonary bypass) must also be considered when comparing the two methods. The Hybrid utilises the natural vasculature and delays the need for aortic arch reconstruction, allowing the opportunity of ventricular growth, physiological stabilisation and even biventricular repair.

5.4 Summary and Conclusions

After outlining the multi-compartmental Windkessel approach used, the Norwood circulation models were validated against the results of Shimizu *et al.* and then adapted. The Hybrid model was investigated in detail, followed by a comparison with the adapted Norwood circulation models.

In this model increasing PAB diameter, or stent diameter less than 7 mm, substantially increased single ventricle workload and reduced systemic perfusion and diastolic pressure. This may compromise myocardial oxygen demand-supply, particularly in the setting of retrograde dependent coronary perfusion.

Caution must be exercised in the use of mathematical models. The nature of these models, and the number of parameters involved means that it is necessary to maintain certain parameters. In this study, all circulatory constants were not altered, which of course would respond to, and compensate for, different haemodynamic situations by changing in a complex, non-linear manner which as yet are not well understood. How the total stressed blood volume changes in different circumstances requires greater clarification, otherwise it will continue to be altered so that the desired outcome is reached and will continue to lead to non-physiological results, or worse, falsely engineered results and conclusions. This is illustrated by the analysis of varying the total stressed blood volume for a specific configuration and the range of outcomes observed.

The physiological changes in circulatory resistive and compliant parameters is not currently accounted for by our model. This can be changed medically through pharmacological agents, but a relationship describing how these parameters change with such interventions is required. The contractility of the ventricle can also be altered by the administration of pharmaceutical agents such as catecholamines. This could be simulated by adjusting the parameter A_{RV} , the gradient of the maximum elastance of the single right ventricle as seen in Figure 5.4(c). This adjustment may be used to investigate haemody-

namical outcomes in ventricular dysfunction. Of course, how the total stressed blood volume must vary (if at all) with these changes must be investigated further.

The optimal Hybrid Procedure results in comparable haemodynamical outcomes compared to the respective optimals for the mBT, valved and non-valved Sano shunt variants of the Norwood Procedure. The Hybrid Procedure results suggest improved myocardial supply compared to the Norwood.

The advantage of mathematical modelling is that, given a sufficiently descriptive equation, parameter or methodology, many physiologically different circumstances can be simulated. The consequence of this is the overwhelming volume of data it can produce (specifically for the 0D modelling) and the additional time it can take to simulate. Certain clinical circumstances would be of interest to investigate such as tricuspid regurgitation, the effect of a restrictive ASD, variation in heart rate, the effect of pharmacological agents on the contractility of the ventricle or on the systemic and pulmonary vascular resistances. The majority of these cases could be simulated by varying a single parameter, or adapting an equation. However, if the focus of the investigation is considered, each case would need to be repeated for every band and stent diameter, and at multiple total stressed blood volumes. Not only would the number of configurations being compared become overwhelming, but the review, analysis and presentation of the results would become disjointed and/or repetitive. Optimisation would then become exceedingly difficult as various effects could compound or negate each other.

Additionally, the quantification of how parameters change e.g. the systemic/pulmonary resistance with vasodilators/restrictors and nitric oxygen respectively is unclear. Therefore, the pulmonary vascular resistance could be halved or doubled, but without further clinical study, this would inevitably end up a numerical exercise and lose its clinical significance, particularly with the goal of predictive modelling to assist with treatment plans.

The intended direction for the modelling of the Hybrid Procedure, is toward patient-specific modelling. This should involve determining the circulatory constants (i.e. patient-specific values for the parameters listed in Table 5.1) to match clinical acquired pressure and flow profiles. The circulation parameters could also be adjusted to account for growth, but this requires greater clinical study through long-term observation.

Chapter 6

Patient-Specific Three Dimensional Modelling

In this chapter, we now discuss the work associated with the patient-specific three dimensional modelling. Firstly the available raw data and necessary compromises of the different stages involved in making a patient-specific geometry are considered, followed by an explanation of the steps involved in using the geometry created for CFD investigation. The patient-specific 3D Computational Fluid Dynamics Modelling involves 3 stages: Constructing a patient-specific 3D geometry/volume; Meshing this volume for use in a CFD package; and importing the mesh into the a CFD package and, as discussed in Chapter 3, supplying appropriate boundary conditions. How the original or default geometry was manipulated to simulate a “virtual surgery”, specifically altering the band dimensions, is then explained. This process is summarised in Figure 6.1, a flow chart showing the step-by-step process in generating patient-specific models. Finally the results of steady state CFD modelling using both clinically derived and clinically idealised data are presented.

6.1 Available Patient Data

As one of the key objectives of this research is modelling with patient specificity, it was essential to have appropriate imaging of the relevant anatomy. Appropriate forms of imaging would be either magnetic resonance imaging

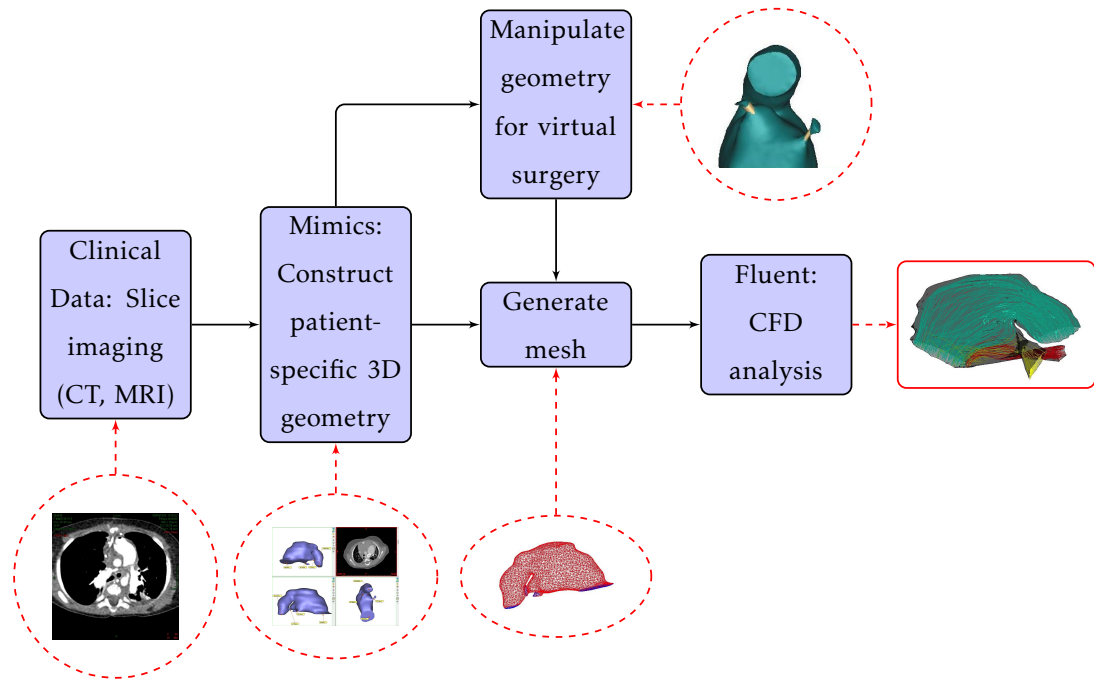


FIGURE 6.1: Summary flow chart of three dimensional patient-specific modelling

(MRI), or computed tomography imaging (CT) as both are a form of slice imaging with the slice resolution known. This means that the 2D images can be “stacked” together to produce a 3D geometry. Figure 4.3(b) illustrates one of many slices from a CT scan. Appropriate imaging has not been undertaken in all HLHS patients to date at our collaborators institution, and it is this reason, combined with the initial desire for a complete set of available clinical data, that there has only been the one test patient presented.

As a brief outline, in order to construct a patient-specific three dimensional geometry we must start with slice scan images (MRI/CT scans). By identifying the surgical region on multiple parallel stacked 2D images, with the distance between slices known, it is possible to construct a 3D volume using appropriate software. As stated in Section 4.5 the geometrical data available for model construction was in the DICOM format. However, it is not routine clinical practice to obtain MRI or CT scans at various stages throughout the course of treatment due to additional risk sedation brings, which helps reduce any motion artefact on the images. Therefore imaging investigations appropriate

for 3D geometry construction are only carried out where there is additional clinical motivation, such as neurological complications.

The availability of appropriate imaging investigations is extremely limited and this type of research is intended to support the notion that quality imaging of HLHS patients at early stages is advantageous despite mooted risks. If different “virtual surgeries” could be performed on pre-procedural scans, it is possible that the modelling could help predict the best clinical treatment plan. In order to achieve this, experience in the modelling processes, particularly with respect to patient-specific clinical data, has to be established, and our initial experience is outlined throughout this thesis.

Of the 17 identified patients who underwent Hybrid (11) or Norwood procedures for a Hypoplastic Left Heart related diagnosis, 7 patients did not undergo medical imaging of the heart (2 Hybrid). Of the remaining 10, only one patient underwent a pre-surgical scan of the chest, which in theory could be used in a predictive model. This patient also had a post procedural chest scan which again, in theory, could have been used to validate a predictive model; an ideal candidate for future study once the protocols are established. Both image sets were captured using CT. Four additional patients had post-stage I, pre-final repair scans of the cardiac anatomy, one of which was a Norwood (CT) and of the three Hybrid patients only one underwent MRI.

The quality of images available from MRI due to the underlying physics, allows for greater contrast of soft tissue types whose hydrogen atoms in their water content align and re-align differently under varied magnetic fields. MRI surpasses the contrast that can be obtained from CT in terms of the ability to visualise the vasculature and contrast agents, which are almost essential for CT, which further supports the use of MRI. The main difficulty with the MRI scan obtained of the hybrid patient was that there were only a limited number of slices, and at a relatively large interval (1.5 mm apart) for the size of the structures being reconstructed. Hence the available MRI scan was consid-

ered an inappropriate when better case study candidates existed with more appropriate resolution.

As the initial aim was to investigate altering the tightness of the banding in a patient-specific Hybrid anatomy, to reduce the unknown effect of how the application of bilateral banding effected the presurgical geometry of the anatomy, only post-hybrid, pre-final repair scans were considered. Excluding the MRI scan for the reasons above, this left three candidates for initial investigations, including the patient for whom a pre-hybrid CT scan existed. The candidate chosen, Patient A, was selected due to the relative ease of determining the vasculature of the surgical region (contrast media was most discernible), and the fewest possible outlets of the surgical region, reducing the complexity and number of future parameters necessary for implementing the coupled multiscale model, the end goal of this research. The available clinical data for 3D geometry construction, and the selection process of the selected patient is summarised in Figure 6.2. Remote access of the cohort of HLHS patients' scans (identified by hospital I.D. number) was secured for use out-with hospital premises. This was achieved thanks to the cooperation of the Radiology Department Royal Hospital for Sick Children, Glasgow, who ensured patient anonymity during the export process.

6.2 Construction of Patient-Specific Geometry

Following investigations into generation of a 3D model from medical imaging (see Section 3.3), the most widely used commercial software was MIMICS (Materialise Biomedical R & D, Leuven, Belgium). MIMICS is capable of reading in the scan data from CT and MRIs in their raw DICOM format. This means that all spacial coordinates are automatically interpreted and allows the axial slices to be reinterpreted to produce similar images in the transverse and sagittal planes. Access to MIMICS ver. 12 was already available, and all 3D geometry work in this project was achieved using this version. Figure 6.3 shows the layout of the MIMICS interface with the axial view (top right) the original

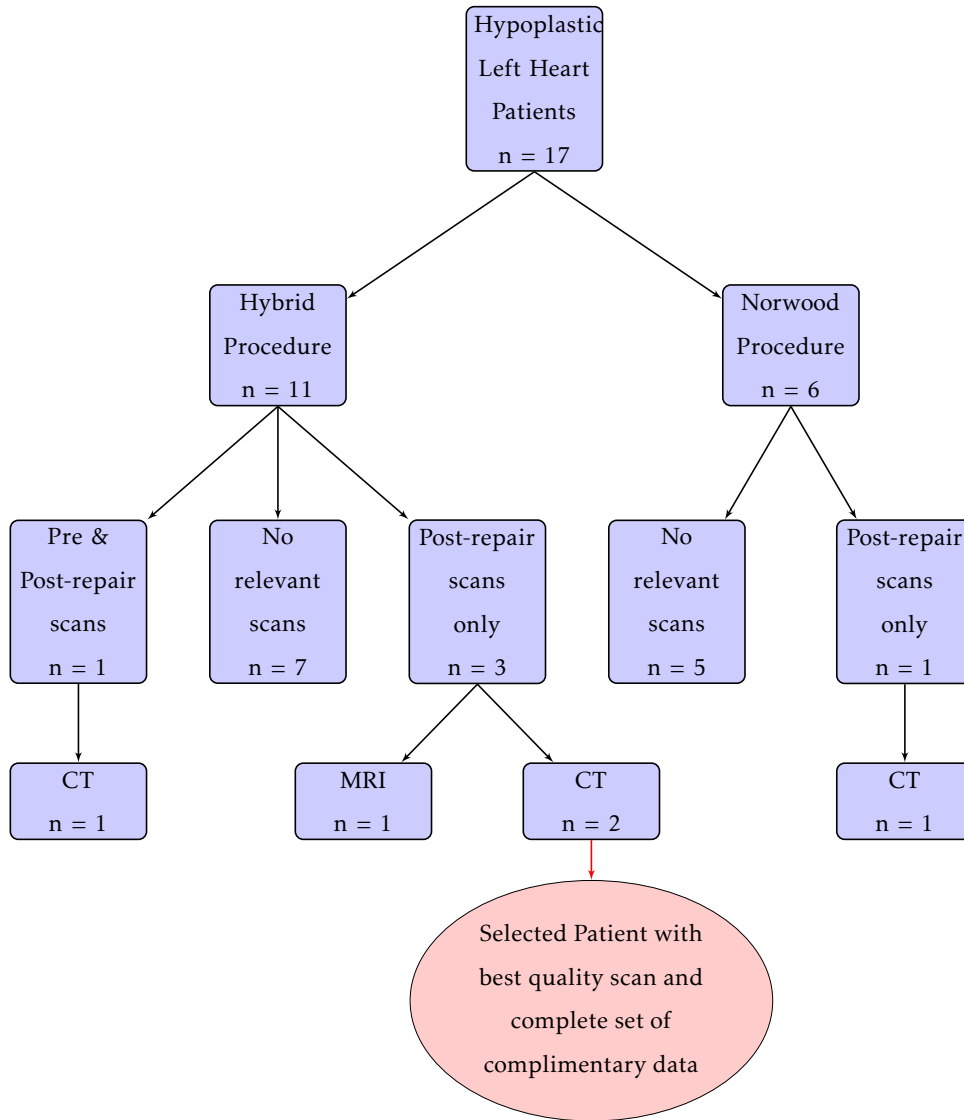


FIGURE 6.2: Flow chart of patient identification for patient-specific modelling

scan, and the coronal (top left) and sagittal (bottom left) planes derived from the spatial coordinates. The bottom right window shows the identified volumes in 3D and is vital in visualising the work carried out described in this section.

Once a suitable patient had been selected (see previous section), an anonymised CT data set was received in DICOM form from our clinical partners of a patient that had undergone the Hybrid Procedure. This choice was motivated by the notion that it was more appropriate to edit a correct geometry rather than try to reproduce one from a pre-procedural scan. Initially the built-in threshold-

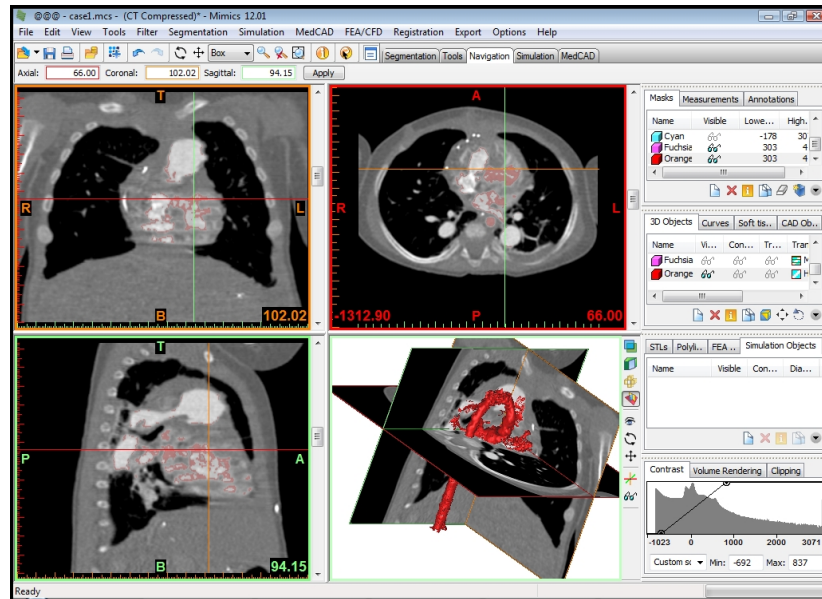


FIGURE 6.3: Screenshot of MIMICS interface with 4 window setup: Top left - Coronal plane; Top right - Axial plane; Bottom left - Sagittal plane; Bottom right - 3D view

ing features (selecting areas based on the intensity of greyscale), were utilised in an attempt to construct the desired volume. It was soon found that automatic identification of the specific vessels required was inappropriate. There were many factors contributing to this including: poor contrast of image, motion artefact and the resolution versus the size of the vessels of interest. Therefore, it was found that the anatomy was too complex, and the quality of the scan too poor to use the automatic tools, hence the appropriate vessels were manually identified, slice by slice.

The result of the manual constructed geometry of the patient-specific surgical region is best presented illustratively. Figure 6.4 shows what is constructed when identifying the region of interest, slice by slice, using the raw data from the on-site CT scanner where the scan is non-gated although does make use of a contrast agent, with slice spacings of 0.6 mm, which is not optimal given that the diameters of banded vessels will be below 3 mm. It is clear that manual correction is necessary. This was carried out by the author and verified by an expert in the field. The geometry was then smoothed to compensate for the rough shape, another consequence of manual construction, and clean inlet and outlet surfaces created. The patient studied had the following clinical di-

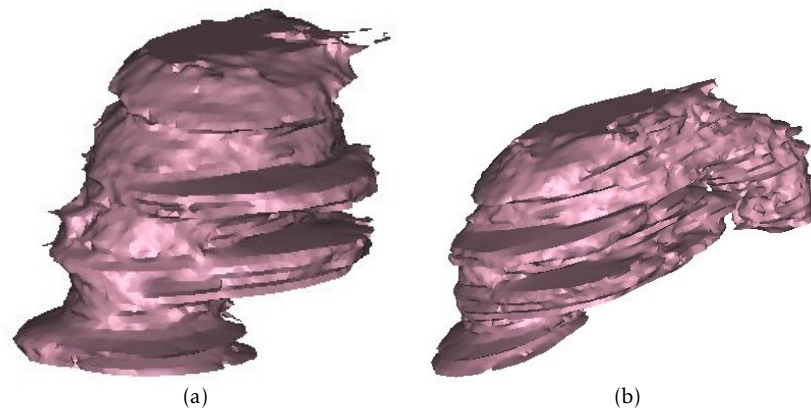
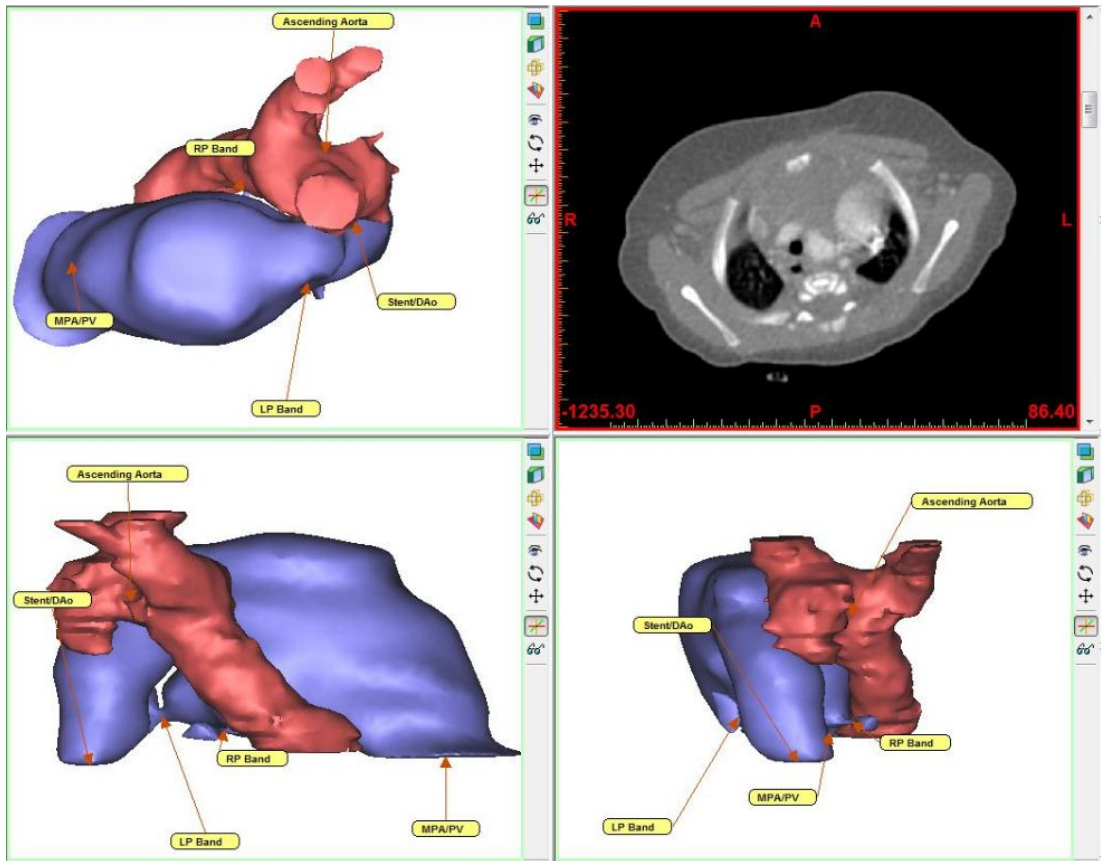


FIGURE 6.4: Manually constructed patient-specific geometry before manual correction and smoothing

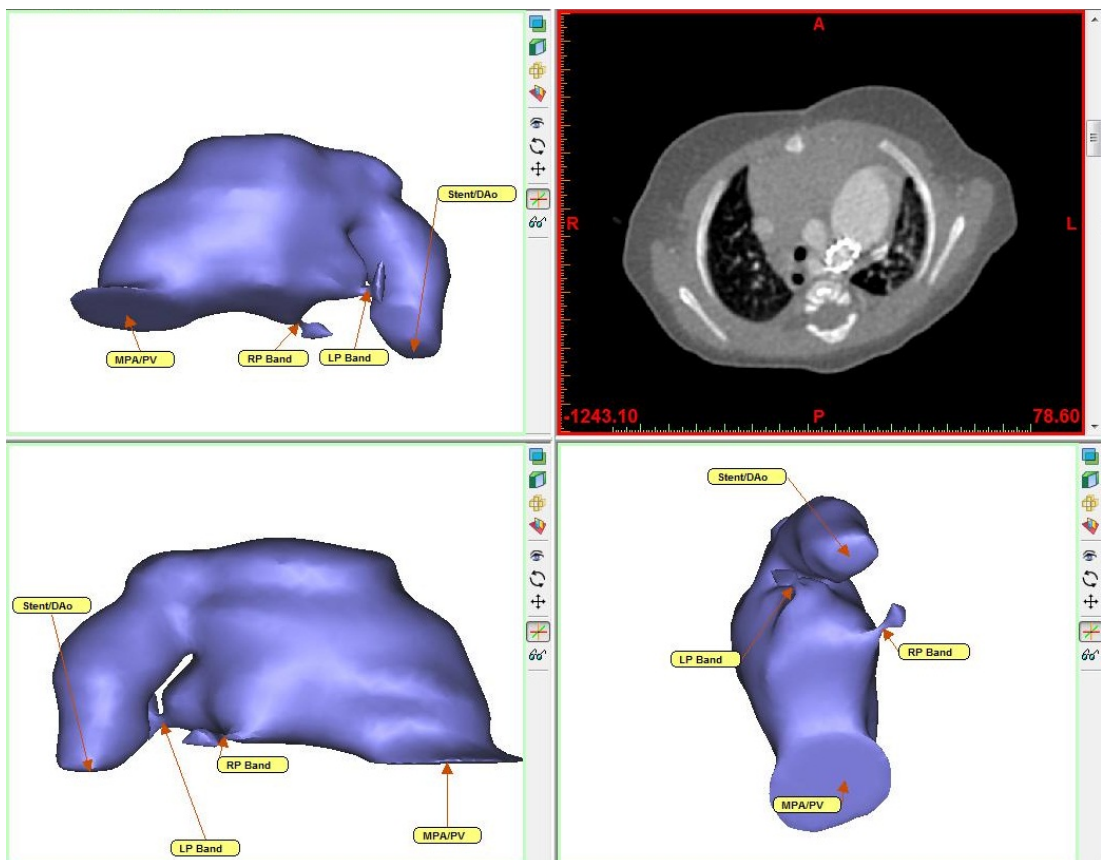
agnosis: Single outlet ventriculoarterial connection via pulmonary trunk (aortic atresia); ASVD with hypoplastic left ventricle; Therefore all cardiac supply was via the main pulmonary artery, with all systemic supply fully dependent on ductal flow, while coronary perfusion was by retrograde flow in the aortic arch. Therefore, for modelling purposes, the connection between the PDA and the aortic arch was not necessary, and in fact would lead to additional boundary conditions, which results in further complications and an increase in necessary parameters.

The connection between the duct and aorta was not abundantly clear from the scan, and so to avoid additional complications and computational cost, the region of interest was truncated at the duct proximal to its connection with the aorta. Figure 6.5(a) shows the (uncorrected) aorta alongside the the generated volume of the pulmonary artery structures. The final configuration, referred to as the default Hybrid configuration throughout this study, is shown in Figure 6.5(b).

It is worth noting that the internal banded diameter measured from the geometry created using the best interpretation of the CT scans possible, was significantly smaller than the external band diameter applied. This patient had received 3.0 mm bilateral bands. This highlights several vital issues: Insufficient resolution; Inappropriately gated scans resulting in motion artefact,



(a) Additional ascending aorta



(b) Main structures

FIGURE 6.5: Manually constructed patient-specific geometry

which in this case had duplicate branch pulmonary arteries due to its movement which was captured twice by the scan; the distinction between the reduced internal luminal area available for flow through the banded branch PAs and the original area based on the diameter of the externally applied banding.

At this stage, the author would like to acknowledge the compromises in the protocols adopted in geometry construction. Although the geometry matches that seen in other imaging modalities, it fails to capture the large amount of vessel movement as mentioned above. As technology improves, the imaging techniques for geometry construction will improve, and the user input and fixed shape simplifications will be removed. Figure 6.6 shows the difference between the geometry in systole and diastole from stills of a cine-angiogram taken of the patient this case study is based on. It provides a suitable 2D image with which to validate the shape, while the full video emphasises the motion. Fluid-Structure Interaction is proposed as the best hope of overcoming the lack of motion consideration, but due to limited initial experience within the field, limited resources and the focus of this project in assessing the application of patient-specific modelling within current clinical protocols, the compromises at this stage were noted and accepted.

6.3 Patient-Specific Geometry to Computational Fluid Dynamics

In order to use the anatomical shape constructed above for computational fluid dynamical studies, the entire volume needed to be meshed. This means splitting the volume into lots of smaller control volumes which are sufficiently small and appropriately shaped for the Navier-Stokes equations to be solved within that and neighbouring regions (see Section 3.3). This is achieved by placing nodes within this volume which are then the vertices of all these smaller volumes.

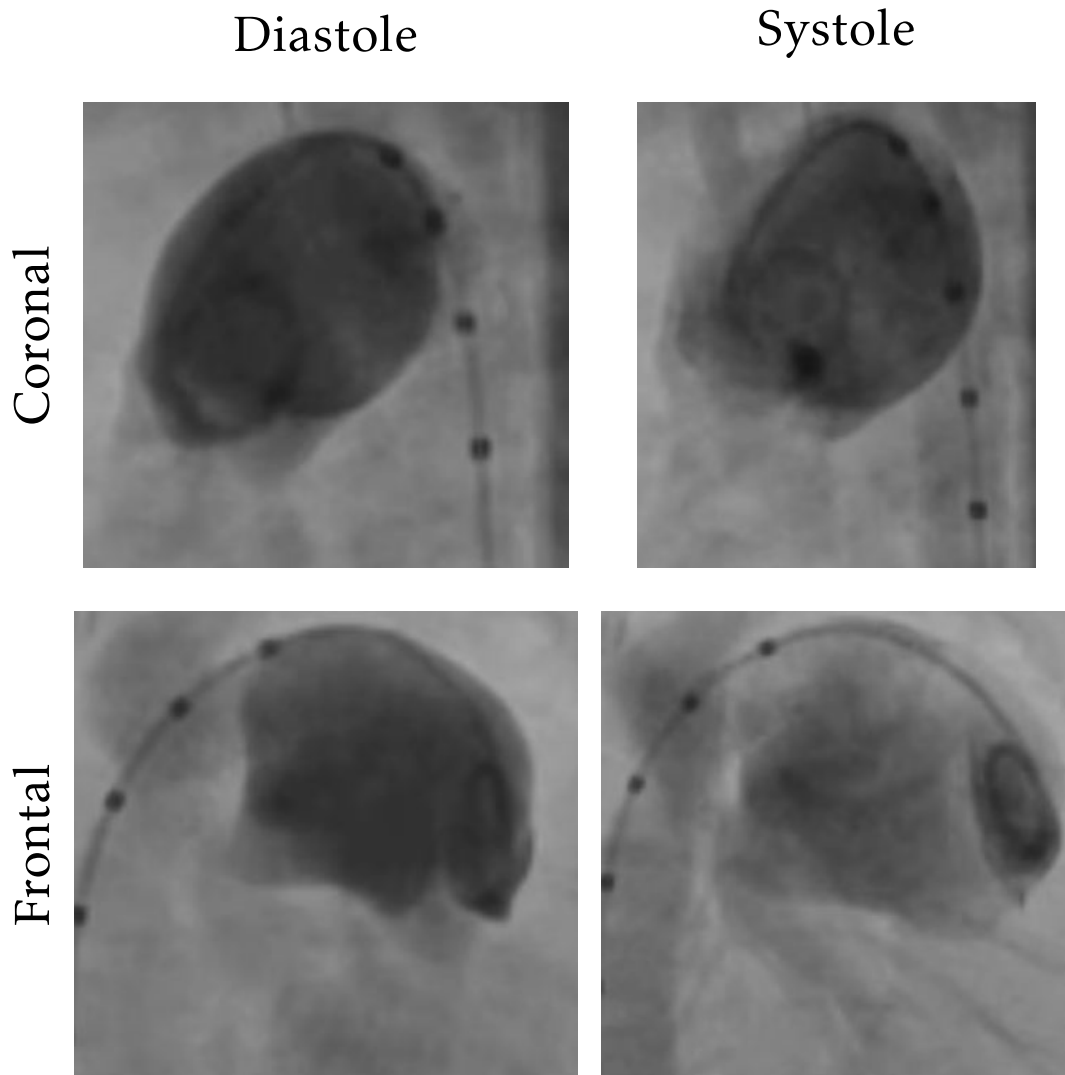


FIGURE 6.6: Patient-Specific geometry captured by angiogram to validate the virtual reconstruction and demonstrate the movement between systole and diastole

MIMICS ver. 12 includes an automated mesh generator which was used to generate a surface mesh. This means that nodes were only created on the outer surface of the geometry. As a consequence, only faces, and not control volumes were created. MIMICS automatically uses triangular as opposed to quadrilateral faces which in general, means a better quality mesh is generated for unconventional and awkwardly shaped geometries as found in physiological applications. Separate surfaces could be identified so that the wall and the inlets and outlets of the volume could be characterised separately when applying boundary condition types in the next stage of the mesh generation.

Several built-in functions of the commercial software package were adopted in the surface meshing process, including quality preserving triangle reduction. The surface meshes generated within the automated features of the meshing subpackage, 3-matic, were accepted as appropriate for this study. It was then possible to export the generated meshes in *.msh format for importation into the preprocessing software GAMBIT (Fluent, Inc., Lebanon, NH, USA). GAMBIT was able to generate a volume mesh based on the imported surface mesh, by defining the interval spacing between the internal nodes, applying them to align with the surface mesh. A default interval spacing of 1 was used with all physiological models for discretization. The number of nodes and 4-node tetrahedral cells (control volumes) for the default volume generated were 25,987 and 122,436 respectively (see Table 6.1). The choice of interval spacing was adopted following introductory CFD investigations, and a node count comparison with similar investigations published in the literature [81–83] where previous mesh analysis had been carried out.

Volume discretisation is important as it has a large impact on various modelling considerations. The finer the mesh is (i.e. the more nodes there are) the longer it takes for the solution to be determined due to the increased calculations necessary. However, if the mesh is too coarse, it will fail to capture the correct fluid dynamical outcomes by oversimplifying the internal geometry and result in discrepancies with finer meshes. The finer meshes are assumed to be the most accurate. Therefore it is a trade-off between the desired accuracy and computational expense, which reflects the length of time taken to determine a solution.

Following the volumetric mesh generation the pre-identified regions on the surface were defined with the appropriate boundary condition type: wall, pressure inlet, and pressure outlet; or wall, mass flow inlet, and outflow. The mesh was then exported as a complete *.msh file for use in a commercial software package FLUENT ver. 13.0 (Fluent, Inc., Lebanon, NH, USA) which was used throughout the project.

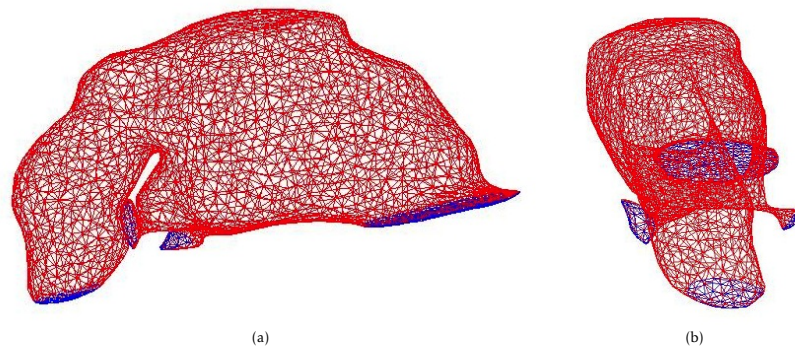


FIGURE 6.7: Surface mesh produced for patient-specific geometry

Figure 6.7 displays the surface mesh of the final anatomy imported into GAMBIT, with the image taken from Fluent following importation in to the software. Due to the nature of a full volume mesh and the density of all nodes within the geometry, no visual representation is provided.

Meshing of anatomical structures is a notoriously difficult process, and benefits from experience. In the present work we relied heavily on the adopted commercial resources with regard to node selection based upon contemporary work in the biomedical engineering literature. We matched current practice where possible, but recognise that there may be considerable room for improvement in this practice. The number of nodes adopted by other groups for similar anatomical regions following mesh analysis were comparable with those used in this research [81–83].

6.4 Simulating “*Virtual Surgeries*”

The concept of *virtual surgeries* is not new in the literature (see Section 3.4). The motivation behind such research, as stated previously, is to determine the effect of changing the geometry of the surgical region and determine what effect (local or global) that has on the outcomes of interest.

In the context of this research project, the major surgical effect that is to be simulated is that of varying band tightness as has already been modelled in

our lumped parameter circulation model (see Section 5.3.2). After attending a Mimics and 3-matic Innovation course at University of Sheffield, new features available on updated versions of Mimics were able to be sampled. There are many new tools which are useful in manipulating the 3D geometry, as the software improvements have been driven by improved cardiovascular modelling, such as the morphing functionality and improved centreline features. However, without access to the updated software, a different approach was necessary, which in fact allowed for greater specificity over the dimension of internal luminal area of the altered banding sites.

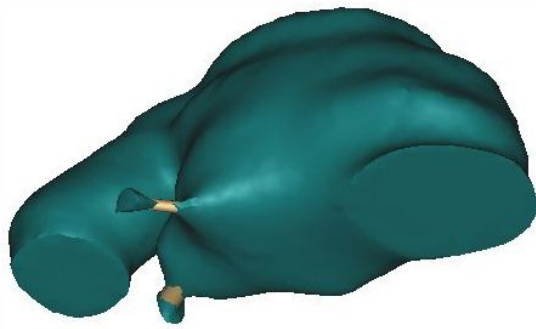
A feature that was already available within Mimics ver. 12 was the ability to include simple geometric shapes. Therefore, cylinders, of precisely known diameter, were generated, and their spatial position manipulated such that they overlapped the banded region. This therefore constructed a patient-specific geometry where the internal banding diameter was precisely known. This is shown pictorially in Figure 6.8. It is conceded that perfectly cylindrical banded lumens, are not physiologically accurate, but were considered a close enough approximation within the context of this methodology.

By merging the raw geometry from the scans discussed in section 6.2 with the cylinders into one volume, a surface mesh was generated in the same manner as in Section 6.3. The same steps were then taken to produce the full volumetric mesh. Using this technique, 7 patient-specific meshed geometries were produced mimicking a “virtual surgery”: the default, straight-from-scan geometry and 6 symmetrically bilateral banded geometries with internal banding diameters of 1.5 mm to 4 mm in 0.5 mm intervals. These meshes were then used for the remainder of the patient-specific CFD work set out in the remainder of this thesis. Table 6.1 lists the numbers of nodes and 4-node tetrahedral cells for the mesh of each geometry used.

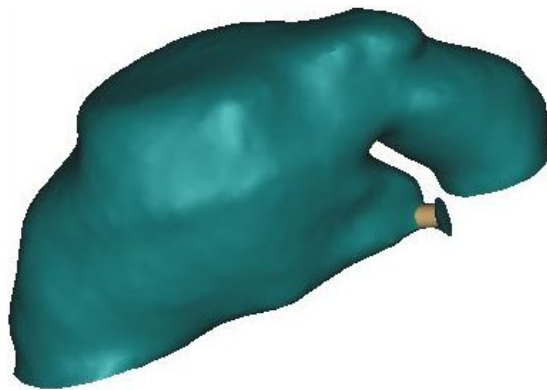
Without better understanding of the similarity or otherwise of downstream vasculature from the left and right pulmonary branches respectively, and the difficulties in producing a patient-specific mesh from a patients scan, the band-



(a)



(b)



(c)

FIGURE 6.8: Virtual surgeries simulated by overlapping of cylinders of known diameter to control internal band diameter

TABLE 6.1: Summary of meshes generated for banding diameters simulated

Model Banding	# of Nodes	# of 4-node Tetrahedral Cells
default	25,987	122,436
1.5	27,171	128,547
2.0	27,068	128,103
2.5	27,109	128,119
3.0	27,695	131,391
3.5	27,471	130,150
4.0	27,797	131,980

ing applied was symmetric. As pulmonary flow in a healthy patient favours the right lung, with appropriately balanced boundary conditions, the effect of unbalanced bilateral pulmonary banding may be worth consideration in future work.

6.5 Steady State Computational Fluid Dynamics

Initial investigations on mean parameters were carried out on the geometries created. Using steady state conditions, Fluent 13.0 (Fluent Inc., Lebanon, NH, USA) was used to import the respective meshes and carry out two different forms of analysis. These were based on the valid combinations of boundary conditions for the inlets and outlets of the surgical region: Defining the mean pressure at each inlet/outlet to determine the volumetric flow rates; and defining the volumetric flow rate at the inlet and the flow distribution to each outlet. As is conventional in the literature, and typical for the larger arteries, blood was assumed to behave as a Newtonian fluid, as the shear stresses necessary to reach non-Newtonian behaviour (where the viscosity varies with shear stress) is not reached. The material properties of blood adopted were defined as used by Migliavacca *et al.* [82]: Density $\rho = 1060\text{Kg/m}^3$; Viscosity $\mu = 0.005\text{Kg m}^{-1}\text{s}^{-1}$.

In order to use the meshes generated in GAMBIT in their native dimensions, when imported into Fluent they had to be scaled appropriately. Despite being in the correct dimensions from Mimics/3-matic, when imported into Gambit and then exported for use in Fluent, the dimensions were changed from millimeters to meters. Therefore upon importation of the mesh into Fluent, the grid was scaled by 0.001 in all axes to correct. The units were also updated to allow intuitive input values. For pressure the predefined Torricelli (torr), which is the approximately the equivalent of 1 millimeter of mercury (mmHg) was used. The SI unit for pressure is the Pascal (Pa) where 1 torr = 133.32 Pa. For volumetric flow rate the units of litres per minute (l/min) were defined. The SI unit for volumetric flow rate is metres cubed per second (m^3/s) where 1 l/min = $1.6667 \times 10^{-5} \text{ m}^3/\text{s}$. The two alternative compatible set-ups for boundary condition that were available (specify the flow rate at the inlet and flow distribution between outlets to determine the pressure at each inlet/outlet; and specify the pressure at the open boundaries to determine the flow rates and distributions) are investigated in the following sections.

The first-order upwind method was selected for method of solving the Navier-Stokes equations over the spacial discretization of the patient-specific geometry. This determined the quantities at cell faces by assuming that the cell-center values of pressure or velocity represent a cell-average value and hold throughout the entire cell. The face quantities are identical to the cell quantities. Thus when first-order upwind method is selected, the face value is set equal to the cell-center value in the upstream cell. Further details are available in the Fluent User Manual.

6.5.1 Mean Pressure Drop from Specified Flows

By using the same flow rates specified for the fixed cardiac output analysis of the lumped circulation model (see Section 5.3.2), and controlling the mean proportion of flow, the pressure drop between each outlet (left pulmonary artery, right pulmonary artery, stented ductus arteriosus) and the inlet (main

pulmonary artery) was calculated using the parameters specified above. To specify the volumetric flow rate, a boundary condition of mass flow rate within the Fluent boundary types was selected. Pseudo mass flow rate units were specified in l/min by converting from the SI units of Kg/s using the constant density of blood 1060Kg/m^3 ; $1\text{ l/min} = 0.0177\text{ Kg/s}$. Without evidence to the contrary, a $Q_p : Q_s$ ratio of one was enforced, while equal left and right pulmonary distribution was assumed. This was achieved by selecting the out-flow boundary type with flow weightings of 0.5, 0.25 and 0.25 for the stented ductus arteriosus, left pulmonary artery and right pulmonary artery outlets respectively.

The results are collated in Table 6.2 showing the pressure drop from the main pulmonary artery inflow to the ductal systemic outlet (ΔP_s) and average pulmonary outlet (ΔP_p) respectively for cardiac outputs of 0.5, 1, 1.5, 1.73, 2 and 3 for each banding configuration to obtain the specified flow ratio.

The trends observed reflect those anticipated: that as the banding loosens, the pulmonary pressure drop decreases (shown in Figure 6.9) with virtually no change in systemic pressure drop; and that as the the cardiac input increases, the increase in pulmonary pressure drop is substantial while the systemic pressure drop marginally increases. This result supports the claim that the stented PDA is non-restrictive as clinical outcome requires.

Pressure drop data observed clinically from a catheterisation procedure of the same patient whose specific geometry was virtually altered was available for comparison. However, as alluded to in Section 4.5, there were a number of available profiles that, according to their clinical description, could match the inlet and outlet faces. There were two profiles for the main pulmonary artery resulting in mean pressures of 54.48 and 56.83 mmHg. Therefore when compared with the 3 potential systemic pressure outlet alternatives and the two post band pulmonary pressure values it resulted in patient-specific clinical ranges for ΔP_s and ΔP_p of (0.38-9.03) and (43.25-51.16) mmHg respectively. However, the “Descending Aorta” mean pressure value which corresponds to

TABLE 6.2: Mean Systemic and Pulmonary Pressure drops of different banding diameters for a range of fixed Cardiac Outputs using steady state analysis

	c.o.=0.5 l/min		c.o.=1.0 l/min		c.o.=1.5 l/min	
	<i>Systemic</i>	<i>Pulmonary</i>	<i>Systemic</i>	<i>Pulmonary</i>	<i>Systemic</i>	<i>Pulmonary</i>
default	0.035503	11.9025	0.10458	43.2345	0.20304	95.6381
1.5 mm	0.035155	7.9178	0.1037	25.1769	0.20181	50.4286
2 mm	0.035196	3.2622	0.10391	10.2886	0.2023	20.7312
2.5 mm	0.035233	1.5795	0.1039	4.9509	0.20214	10.0442
3 mm	0.035247	0.72393	0.1041	2.1754	0.20271	4.26
3.5 mm	0.035028	0.67659	0.10346	2.1406	0.20143	4.3967
4 mm	0.034969	0.35086	0.10342	1.0443	0.20144	2.0256

	c.o.=1.73 l/min		c.o.=2.0 l/min		c.o.=3.0 l/min	
	<i>Systemic</i>	<i>Pulmonary</i>	<i>Systemic</i>	<i>Pulmonary</i>	<i>Systemic</i>	<i>Pulmonary</i>
default	0.25742	126.2444	0.32838	167.4133	0.65218	370.6684
1.5 mm	0.25609	64.711	0.3268	83.2954	0.6505	170.0132
2 mm	0.25675	26.6698	0.32767	34.4981	0.65244	72.2736
2.5 mm	0.2565	12.9612	0.3273	16.8594	0.65153	35.5429
3 mm	0.25728	5.4288	0.32834	6.9669	0.65376	14.1787
3.5 mm	0.25566	5.6961	0.32629	7.4815	0.64984	16.0164
4 mm	0.2557	2.5647	0.32638	3.269	0.65016	6.5069

the most physiological pressure drop range is 54.10 mmHg, resulting in a unrestrictive stent (as clinical investigation verified) meaning a more plausible physiological range for systemic pressure drop would be (0.38, 2.73 mmHg). The shaded region in Figure 6.9 represents the clinical pulmonary pressure drop range. Table 6.3 lists the values found for each location from determining the mean value of the ensemble pressure profiles generated using the methods previously described in Chapter 4.

Even before comparison with clinical data, it is clear that some configurations result in unphysiological results. From these results, the only config-

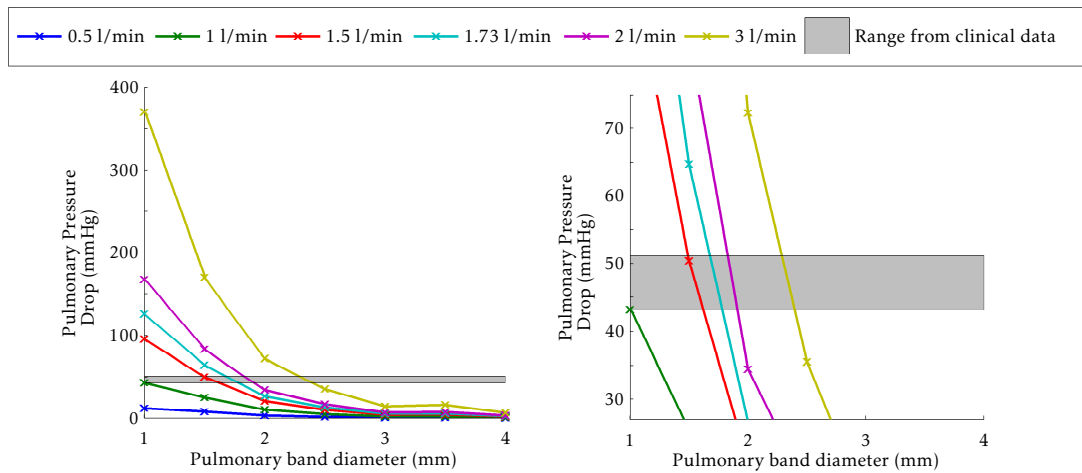


FIGURE 6.9: Pulmonary pressure drop vs band diameter for defined range of cardiac outputs with clinical range indicated from patient-specific data (see Table 6.4.) *default geometry given numerical value of 1 for graphical display purposes

TABLE 6.3: Mean pressure values derived from patient-specific catheterisation procedure for appropriately labeled clinical profiles

Location	Mean Pressure (mmHg)
Main Pulmonary Artery	54.48
	56.83
Descending Aorta	47.13
	50.77
	54.10
Post Band Pulmonary Artery	5.67
	11.23

uration that falls within the patient-specific clinical range for ΔP_p is the 1.5 mm internal diameter banding at a cardiac output of 1.5 l/min which results in a pulmonary pressure drop of 50.43 and a ductal pressure drop of 0.20. This is a feasible result, but since no accurate cardiac output was measured, it cannot be compared with the clinical results. Although this is a high cardiac output for a patient with a small body surface area, it is still a physiologically acceptable result. For a small child with impaired cardiac function, there is no

TABLE 6.4: Pressure configurations used for steady state analysis of cardiac output and flow distribution of patient-specific geometries

Configuration	Main Pulmonary Artery	Descending Aorta	Post Band Pulmonary Artery
A	54.48	54.10	5.67
B	54.48	54.10	11.23
C	56.83	54.10	5.67
D	56.83	54.10	11.23

configuration that gives a physiological pressure drop at the cardiac output of 0.5 l/min. An even tighter banding would be necessary as indicated by these results.

6.5.2 Flow Rates from Clinically Derived Pressures

Following the fixed cardiac output investigations to determine the mean pressure drop of each patient-specific hybrid configuration, the flow rates calculated from defined mean pressure values was determined, applying the three dimensional geometries to the second available set of compatible boundary conditions. Using only the mean pressure value of 54.10 for the outflow towards the distal end of the stent, four pressure configurations of the clinical pressures from Table 6.5 were tested as listed in Table 6.4.

As for the case with the fixed cardiac output and controlled $Q_p : Q_s$, the results presented in Table 6.5 are collated from the full results, combining the left and right pulmonary outflow.

From the results, it is observed that when the pressure drop across the stent is specified, the banding diameter has virtually no effect on the virtually constant systemic perfusion (Q_s) as represented in Figure 6.10(b). Also the variation of post band mean pulmonary pressure has no discernible effect on Q_s , and it is the change in MPA pressure that causes the two distinct values.

TABLE 6.5: Steady state analysis of cardiac output and flow distribution for varying band diameter geometries using mean pressure boundary configurations listed in Table 6.4

	<i>Configuration A</i>				<i>Configuration B</i>			
	c.o. (l/min)	Q_s (l/min)	Q_p (l/min)	$Q_p:Q_s$	c.o. (l/min)	Q_s (l/min)	Q_p (l/min)	$Q_p:Q_s$
Default	1.3893	0.86736	0.52194	0.60175	1.3578	0.86781	0.48997	0.56461
1.5 mm	1.5928	0.86861	0.72422	0.83377	1.5439	0.868	0.67587	0.77865
2 mm	2.0898	0.87412	1.2157	1.3908	2.0102	0.87304	1.1372	1.3025
2.5 mm	2.6518	0.88142	1.7704	2.0086	2.5377	0.87997	1.6577	1.8838
3 mm	3.827	0.90012	2.9269	3.2516	3.6434	0.89859	2.7448	3.0546
3.5 mm	3.6305	0.89618	2.7343	3.0511	3.4588	0.89425	2.5646	2.8678
4 mm	5.3866	0.89943	4.4872	4.989	5.1061	0.90022	4.2059	4.6721
	<i>Configuration C</i>				<i>Configuration D</i>			
	c.o. (l/min)	Q_s (l/min)	Q_p (l/min)	$Q_p:Q_s$	c.o. (l/min)	Q_s (l/min)	Q_p (l/min)	$Q_p:Q_s$
Default	3.027	2.4935	0.53359	0.214	2.9955	2.4931	0.50239	0.20152
1.5 mm	3.2332	2.4922	0.74103	0.29734	3.1852	2.4915	0.69367	0.27841
2 mm	3.7365	2.4959	1.2405	0.49703	3.6923	2.4956	1.1968	0.47956
2.5 mm	4.3087	2.5027	1.806	0.72165	4.1969	2.501	1.6959	0.67807
3 mm	5.5184	2.537	2.9814	1.1752	5.3368	2.533	2.8038	1.1069
3.5 mm	5.3095	2.5256	2.7839	1.1023	5.141	2.5224	2.6186	1.0381
4 mm	7.1491	2.5663	4.5829	1.7858	6.8678	2.5605	4.3073	1.6823

The variation of post band mean pulmonary pressure, despite almost doubling from 5.67 mmHg to 11.23 mmHg, only subtly reduces the pulmonary supply for all banding configurations.

As would be anticipated, the main effect of loosening the bands is to increase the pulmonary flow and as a consequence of Q_p increasing with Q_s constant, the increase in $Q_p : Q_s$ ratio is proportional to the increase in pulmonary flow. Of course, in clinical experience, and as simulated by the lumped circulation model, in varying the band diameter, the pressure drop would change and hence this is an obvious limitation of the steady state, fixed pressure drop analysis. It does however give some insightful conclusions. By considering plausible values for the cardiac output it shows that only the mean MPA pres-

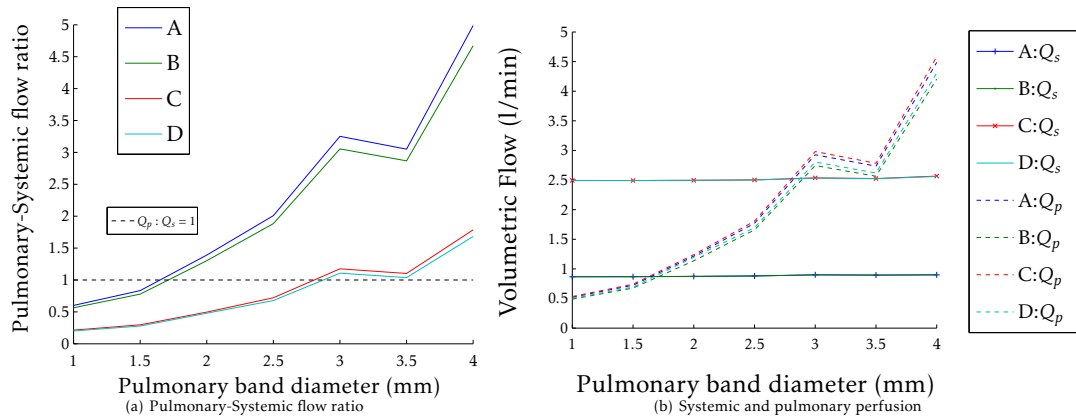


FIGURE 6.10: Steady state analysis of fixed pressure configurations for varying band diameter.
 * default geometry given numerical value of 1 for graphical display purposes

sure which results in realistic values is 54.48 mmHg, limiting the configuration set-up choice to A or B. The main conflicting results from this analysis is that the banding configuration that results in the most appropriate $Q_p : Q_s$ ratio around 1 is between 2.5 mm and 3.5 mm (Figure 6.10(a)), but this produces a cardiac output range that is stretching that of clinical expectancy with the high values of 2.5 to 3.6 l/min. The configurations that give plausible cardiac output (although could be deemed high depending on the body surface area considered) are the unmodified geometry up to the 2 mm specified internal banding, but the pulmonary flow is low enough to cause great concerns over the oxygen supply to the body if these results were observed.

The increase in pulmonary flow, and $Q_p : Q_s$ follows a linear pattern with the increased internal band diameter, with the exception of the 3.5 mm banded geometry. This is potentially caused by the alignment of the superimposed cylinders over the banded regions for this specific geometry having a restrictive effect. All alignment was done to fit within the pre-existing shape and this same effect is marginally observable in the fixed cardiac output and specified flow distribution analysis above.

6.5.3 Comments on Transient Simulations, Desired Outcomes and Appropriate Boundary Conditions

Although clinical outcomes can be reproduced, and useful conclusions drawn from the steady state analysis, this type of analysis is still rather limiting. Controlling the the cardiac output and the mean pressures in this manner does not truly reflect the cardiovascular system as a whole since it is incapable of reflecting the change in pressures and cardiac output that the physical alteration of the surgical region would cause. It is worth remembering that the mean pressures used are based on results from a catheterisation procedure from a 3.0 mm external banding diameter.

The reason that steady state analysis was chosen, was that although the imposition of pressure or flow profiles would have been possible, the output of this type of analysis would not have been clinically relevant. The desired outcome of the CFD analysis is to determine what effect the change in geometry has on the haemodynamics. By imposing transient boundary conditions one would be controlling the results obtained, and comparison would be difficult without varying them. Unless it was known how each pressure profile varied with banding diameter, no sensible flow profiles could be achieved, and the inverse true for specifying flow profiles. In each case, a profile of one outcome is only obtaining based on the other, neglecting, or over-riding the influence of the geometry. Only outcomes from within the surgical region would be available for investigation, such as velocity profiles or shear stresses through the banded region.

Therefore, what is necessary to fully characterise what is happening both locally in the surgical region and globally throughout the entire cardiovascular tree is to define adaptable boundary conditions. This requires specifying values for the inlet/outlet (either flow or pressure) that vary with what is happening throughout the whole circulation and can change during the cardiac cycle. This can be achieved, as mentioned in Chapter 3, by coupling the lumped cir-

ulation model from Chapter 5 with the CFD results presented in this chapter, and is described and discussed in Chapter 7.

6.6 Summary of Three Dimensional Approach

The advantage of the approach adopted in this thesis in the construction and modelling of the Hybrid Procedure was that it build upon the available resources and methodologies in the literature to quickly implement patient-specific modelling to a standard matching that found in the leading publications. In using available commercial software for geometry construction, mesh generation and determining a numerical solution to the Navier-Stokes equations, this research was accelerated to its final level from a novice beginning.

The quality of the geometry in this case was limited by several factors, constrained by the historical nature of the data. The availability of suitable imaging of the post-Hybrid anatomy was limited, especially when looking for cases that had pre-operative imaging with which to compare. This limited data is illustrated in Figure 6.2. Another limitation was the manual need for interpretation, an additional step which was required due to the resolution and contrast of the raw image files. The effect of this limitation can be seen in Figure 6.4. This resulted in a smoothed diastolic based geometry, and of course had rigid walls, neglecting the vessel wall motion.

In future patient-specific models, greater focus will be required around the meshing of the boundary layer (fluid close to the vessel wall), particularly in regions as constricted as the pulmonary artery banding sites. This will, however, lead to additional processing time in the generation of the mesh and will increase the node count of the mesh resulting in greater computational expense.

When considering whether turbulence (resulting in energy losses and a disruption of the smooth velocity field within the region of interest) is an

important factor, the non-dimensional Reynolds Number (Re) is crucial. By non-dimensionalising the full Navier-Stokes equations, see Equation (3.7), by scaling by a characterised length and velocity, it can be shown that:

$$\begin{cases} \frac{\partial \mathbf{u}'}{\partial t'} + (\mathbf{u}' \cdot \nabla') \mathbf{u}' - \frac{1}{Re} \nabla'^2 \mathbf{u}' + \nabla' P' = 0 \\ \nabla' \cdot \mathbf{u}' = 0 \end{cases} \quad (6.1)$$

where the Reynolds number for a diameter D , typical velocity v , density ρ , dynamic viscosity μ and assuming a circular cross section, flow Q is defined as:

$$Re = \frac{D\rho v}{\mu} = \frac{4\rho Q}{\mu\pi D} \quad (6.2)$$

Turbulent flow occurs for $Re > 4000$, with transitional flow (between laminar and turbulent) for $2100 < Re < 4000$ [156].

After analysing the projected Reynolds numbers for steady state analysis using a mean instantaneous flow rate, it was observed that transitional flow may occur in the narrower bandings at the higher cardiac outputs. The more extreme combinations (smaller banding and higher flow rate) suggested turbulent flow would occur.

In the case of transient flow (presented in the next chapter), there is a stronger likelihood of transitional and turbulent flow. This is due to the pulsatile nature of the flow, in which the blood will be accelerating and decelerating, particularly in the ductal region where both flow (and pressure gradient) reversal occurs.

This study, following leading publications in the literature (which have been cited frequently throughout) assumed laminar flow and is a limitation of the study. This assumption reduced the complexity of the simulations and

was to allow comparison of the use of patient-specific geometries with the idealised geometries found in the literature as discussed in Section 7.4. Given the likelihood of transitional and turbulent flow in certain regions, this is a limitation of the present and other cited studies that must be acknowledged.

Chapter 7

Coupled Multiscale Modelling

7.1 Introduction

Following the success in modelling the Hybrid circulation in Chapter 5 and the patient-specific geometry used in Chapter 6, the two were coupled together as discussed in Section 3.4. The generic lumped circulation model was used due to the issues raised in utilising clinical data in Chapter 4 as opposed to a patient-specific variation. Computing and time limitations also dictated this decision, with the analysis focussed on varying the geometry and total stressed blood volume adopted, rather than varying circulatory parameters in the coupled lumped model. A fuller analysis (e.g. sensitivity analysis) of a patient-specific lumped circulation model would be best studied initially on the stand alone lumped circulation model. The sheer magnitude of data that would be produced in such a study was too vast to be considered in the context of this thesis.

In this chapter the coupling methods are detailed, and an alteration to the the LCM is justified. The protocols of the study are outlined followed by a presentation of the results which are then analysed and discussed with both a clinical and methodological interpretation.

Finally, the fully coupled models are compared to the 0D lumped circulation model. The differences between, and interpretation of *internal* vs. *external*

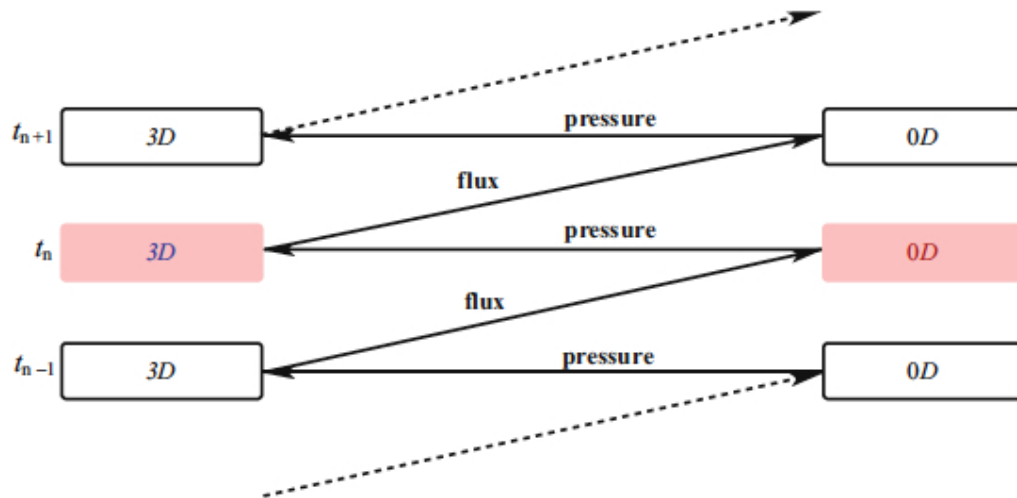


FIGURE 7.1: Explicit coupling of the 0D and 3D models as reproduced reproduced from Janela, Moura and Sequeira [157]

pulmonary arterial banding diameters is addressed by matching the 0D model to the outcomes of the coupled model.

7.2 Methods

The methods described in Migliavacca *et al.* [82] and Quarteroni, Ragni and Veneziani [121], a slightly modified lumped circulation model described in Chapter 5, and the three dimensional modelling described in Chapter 6 are used and coupled in the multiscale model. This is achieved by assuming continuity of the mean pressure and flow rate at each interface. Pressure boundary conditions are supplied to the 3D model, which then calculates the the flow at that time point. Thus all dependent variables for the n^{th} time point are known, and using the explicit Euler's Method, as in Section 5.2.4, all dependent variables excluding the flow rate at each boundary of the 3D control region can be determined for the succeeding time step. The calculated pressures are then used to update the pressure boundary conditions to determine the flow rate at the $n+1$ level. This is best illustrated with the assistance of the diagram shown in Figure 7.1. This diagram is reproduced from Janela, Moura and Sequeira [157] which is a simplified version of Figure 8 in the study by

Quarteroni, Ragni and Veneziani [121]. The coupling conditions are defined mathematically by equations (7.1) and (7.2).

$$\left\{ \begin{array}{l} Q_b = \int_{\Gamma_b} \frac{\dot{m}_b}{\rho} dA \quad \forall b \text{ upstream} \\ Q_b = - \int_{\Gamma_b} \frac{\dot{m}_b}{\rho} dA \quad \forall b \text{ downstream} \end{array} \right. \quad (7.1)$$

$$P_{3D,i} = P_{0D} \quad \forall i \text{ on } b \quad (7.2)$$

The notation above is defined as follows: b denotes an interface boundary, \dot{m}_b is the mass flow rate of the three dimensional boundary surface and i is a face of the three dimensional boundary surface (see Section 3.3). The interface conditions ensure the continuity of the mean pressure and flow rate between the two submodels. The approach adopted results in defective boundary conditions for Equation (3.7) since they require point-wise boundary conditions. This is one of the difficulties of using the multiscale approach, as the pressure distribution is unavoidably simplified in a non-physiological manner, and information regarding the velocity profiles on the artificial boundaries must be disregarded. This technique has proved to be a good approximation for blood flow simulations [118, 157] and captures the clinically relevant outcomes well.

In coupling the two submodels, the characteristic resistances of the pulmonary and systemic circulations were replaced, as well as the equations describing the resistance through the PABs and ductal stent by the 3D submodel. Thus the pressure interface conditions were at the nodes in the circuit representing the appropriate compliant cardiac chambers. This replacement is illustrated in Figure 7.2. The coupling was achieved by writing a user defined function for ANSYS Fluent (ver. 13.0). This used the C coding language, in addition to predefined Fluent macros to allow the integration of the mass flow rate over the surface area (see Equation 7.1) and a uniform pressure distribution (see Equation 7.2). The full code is presented in Appendix C. It also hard coded all algebraic equations determining the pressures and flows from the

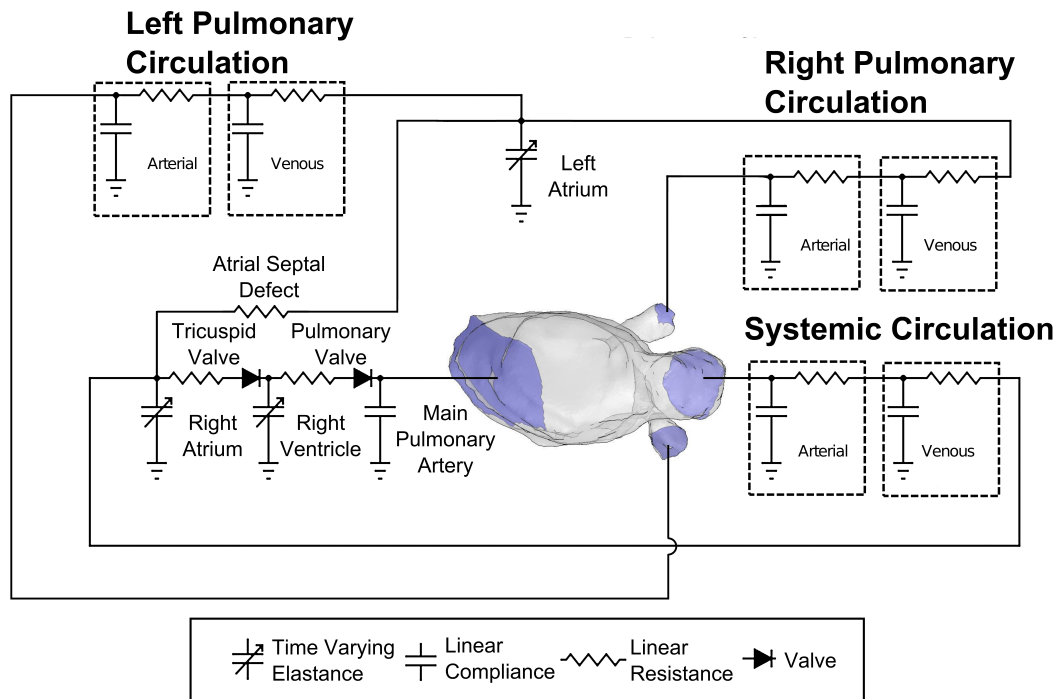


FIGURE 7.2: Circuit diagram representing the removal of 0D components which is replaced by the 3D submodel in the multiscale model.

volume variables, as well as solving the differential equations for the volume variables using the Explicit Forward Euler's Method. The user-defined function solving the lumped circulation model was built into Fluent as proposed in similar studies [82, 118]. This permitted a fully coupled solution at each time step, allowing a single execution of the solver.

Due to the coupling of the two submodels, what formerly was a complete set of differential equations for all state variables, introduced forcing terms based on the velocity (flow) solution from the 3D submodel. A more accurate explicit method, such as Runge-Kutta-Fehlberg method, which was investigated in Matlab, could have possibly adopted, but would have increased the complexity of the simulation. More complex code and additional temporary variables would have been required, which would have increased the execution time. It may have been possible that the reduction in the number of calculations per cardiac cycle due to the increased time step may have cancelled this out. In this study, we adopted the established technique published in the literature [81–83, 118].

An additional option available in numerical time integration is to use an implicit method. This increases the stability of the solution, and permits a larger time step. Although coupled multiscale models using implicit time integration methods are available in the literature, the requirement of potentially multiple sets of iterations to determine the solution of the 3D submodel per time step was deemed too costly given the resources available within this study [158]. The advantage of an implicit method is greater stability in the solution, particularly when backflow is present. Based on a study comparing explicit, implicit, and semi-implicit methods, the semi-implicit approach seemed the optimal choice. It provided a more stable, yet cost-effective solution. The explicit approach was less costly but proved to be less stable with a lower convergence rate that slightly increased the overall cost [158]. The semi-implicit method uses an explicit method for the 3D submodel, while using the considerably more computationally expensive implicit for the 0D model.

As can be seen in the code presented in Appendix C, the output of the model was written to a *.txt file which was later imported into Matlab for analysis and interpretation. During code testing and validation, Fluent generated output was compared to the *.txt output (e.g. ductal stent flow) to verify the code execution and appropriate scaling. All variables collected from, and passed back to Fluent were by necessity in SI units (Pascals, m, s), while the lumped circulation calculations were determined using base units of mmHg and l/min and so required appropriate scaling as observed in Appendix C.

7.2.1 Alteration of Valve Model

The time integration step size used in Chapter 5 (1×10^{-5} s) was sufficiently small to successfully solve the differential equations described given the use of the Heaviside function to replicate the effect of the valves. The value used as a typical heart rate of 160 beats/min in this study results in a cardiac cycle length of 0.375 s. Using the above time step size results in 37,500 calculations per cardiac cycle. Given the zero dimensional nature of the lumped circula-

tion model, this was not a concern, and did not practically impact the computational cost and time of producing a solution. However, when progressing to solve the coupled model problem, this became a huge obstacle. At each time step, the Fluent solver had to iterate a sufficient number of times (a maximum of 20 iterations) to determine an appropriately converged solution (within a statistical significance of 5%) of the 3D domain for that time point. Therefore, given the extra computational cost (manifesting as computational time) of determining the solution of the 3D region, it was necessary to increase the time integration step size.

The lumped circulation model was used to investigate the increasing of the time step size. The value 1×10^{-4} s adopted by Migliavacca *et al.* [81, 82], was the targeted value. Figure 7.3 shows the results of using this time step value for the LCM as described in Chapter 5 for the larger (solid) and smaller (dashed) time steps. What was found was that the time step was too large to appropriately capture the opening and closing of the valves. The variations in pressure and flow were such that when attempting to open (close) the valve, the resulting change in the next time step caused the valve to close (open), which consequentially resulted in the re-opening (-closing) in the following time step. This outcome motivated a review of the valve model adopted.

Initially, the linear valve model was adopted, as there was no apparent justification for the use of the more complex non-linear quadratic model as used by Migliavacca *et al.* [82, 85]. As outlined in Chapter 5, the least complex approach was the linear valve representation adopted, and was validated by the results published by Shimizu *et al.* [86]. Given the need to increase the time integration step size, the non-linear valve model was revisited, motivated by the evidence in the literature. The alternating nature of valvular flow identified in the linear model at the larger time step was a concern that needed addressed with regard to the implementation of the submodel coupling. It was found that the non-linear valve model did not break down for the 1×10^{-4} s time step. Figure 7.4 shows the minor differences in the profiles of certain key variables between the successful linear implementation ($\Delta t = 1 \times 10^{-5}$ s) and the

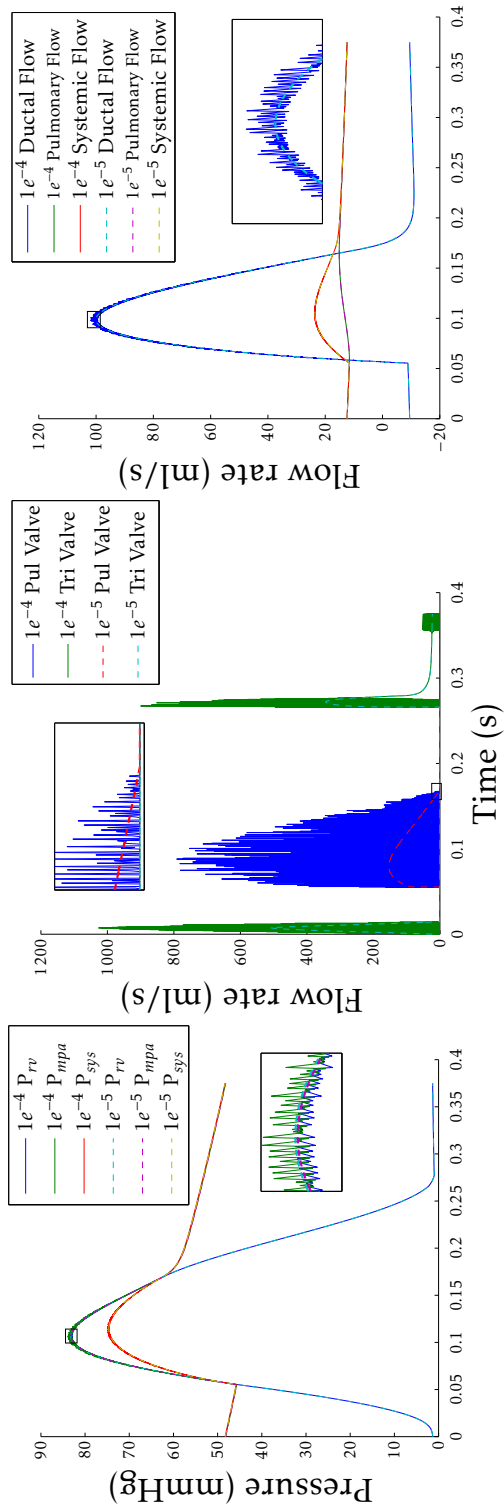


FIGURE 7.3: $\Delta t = 1 \times 10^{-4}$ (solid) versus $\Delta t = 1 \times 10^{-5}$ (dashed) time steps for pressures (left) valvular flows (middle) and systemic and pulmonary flows (right)

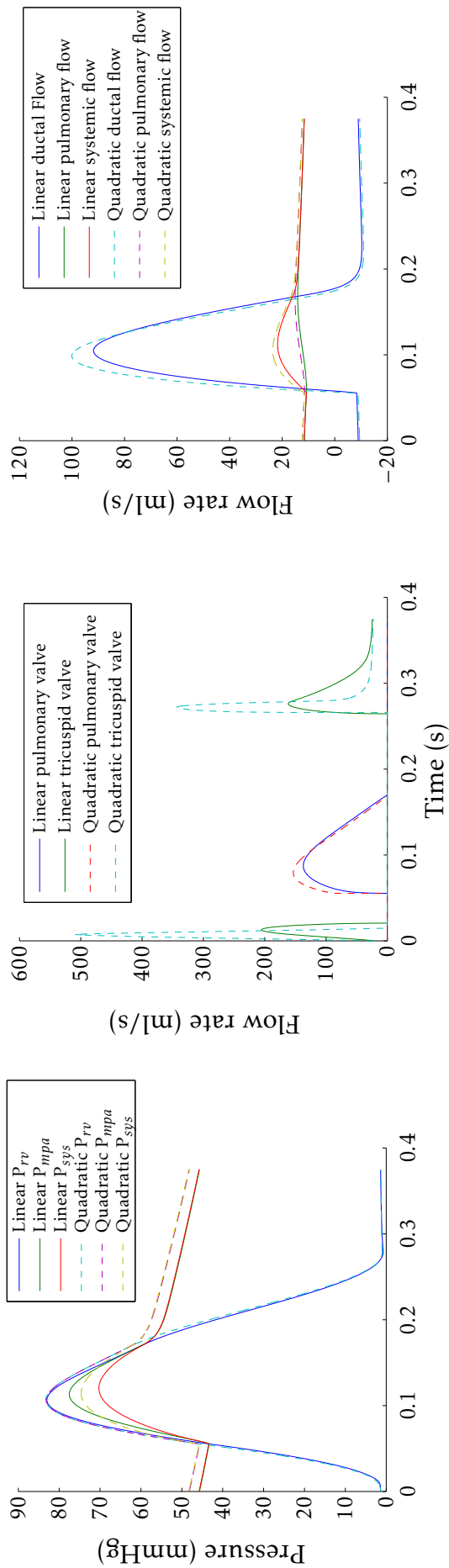


FIGURE 7.4: Linear valve model (solid) versus quadratic valve (dashed) model for pressures (left) valvular flows (middle) and systemic and pulmonary flows (right)

non-linear valvular resistance model at the larger time step ($\Delta t = 1 \times 10^{-4}$ s). This alteration reduced the number iterations required to simulate a cardiac cycle by a factor of ten. Given that it still took approximately 30 hours of processing time, using a serial processing of the Strathclyde University High Performance Computer, to simulate four cardiac cycles this was a drastic improvement. If this alteration had not been made, it would have taken 75 hours to simulate only one complete cardiac cycle. This outcome is an important step in the justification of selecting a valve model, and validates the selection of this valvular resistance model for any future research of this nature.

Table 7.1 illustrates the negligible differences between both models at each Δt with respect to the clinically relevant haemodynamical outcomes.

7.2.2 Adjustment of Pulmonary Branch of Lumped Circulation Model

As well as the alteration of the valvular resistance model, the lumped circulation model required an additional adjustment. In the LCM from Chapter 5 there was a single pulmonary branch, however, with the 3D region, the pulmonary circuit was split into its left and right components. Therefore the values of the arterial and venous pulmonary compliances and resistances had to be recalculated.

Using the electric circuit analogy, the pulmonary branch is split into two parallel paths. Therefore, given the assumption of an equal split of the flow (i.e. current) while maintaining the same pressure magnitude (i.e. voltage), the resistance was doubled while the compliance was halved. If R_{eq} is the equivalent single resistor, while R_1 and R_2 are the two new resistors in parallel they are related by:

$$\frac{1}{R_{eq}} = \frac{1}{R_1} + \frac{1}{R_2}$$

TABLE 7.1: Haemodynamical results of linear and quadratic/orifice valve models for $\Delta t = 1 \times 10^{-4}$ and 1×10^{-5} s

	Linear 1×10^{-5}		Linear 1×10^{-4}		Non-Linear 1×10^{-4}		% Difference	
	Value	% Difference	Value	% Difference	Value	% Difference	Value	% Difference
Systolic MPA Pressure (mmHg)	83.21		83.94	-0.73	77.52	-8.88	5.70	6.84
Diastolic MPA Pressure (mmHg)	45.67		45.69	-0.02	43.32	-0.05	2.35	5.14
Mean MPA Pressure (mmHg)	58.51		58.55	-0.04	55.09	-0.07	3.42	5.84
Systolic Systemic Pressure (mmHg)	74.62		74.97	-0.35	70.28	-0.47	4.34	5.82
Diastolic Systemic Pressure (mmHg)	45.77		45.79	-0.02	43.41	-0.05	2.36	5.15
Mean Systemic Pressure (mmHg)	57.10		57.14	-0.04	53.88	-0.06	3.22	5.64
Systolic Pulmonary Pressure (mmHg)	13.49		13.51	-0.01	13.09	-0.08	0.40	3.00
Diastolic Pulmonary Pressure (mmHg)	11.29		11.29	-0.00	10.97	-0.03	0.31	2.77
Mean Pulmonary Pressure (mmHg)	12.42		12.43	-0.01	12.08	-0.05	0.34	2.76
Cardiac Output (l/min)	1.73		1.74	-0.00	1.62	-0.08	0.11	6.58
Pulmonary Flow (l/min)	0.93		0.93	-0.00	0.87	-0.08	0.06	6.67
Systemic Flow (l/min)	0.80		0.80	-0.00	0.75	-0.08	0.05	6.48
Pulmonary-Systemic Flow Ratio	1.16		1.16	-0.00	1.16	-0.00	0.00	0.21
Stent Backflow (l/min)	-0.40		-0.41	0.01	-0.38	-1.77	-0.03	6.30
Systemic Oxygen Saturation (%)	78.45		78.47	-0.01	77.13	-0.02	1.33	1.69
Venous Oxygen Saturation (%)	56.97		57.00	-0.03	54.16	-0.05	2.81	4.94
Systemic Oxygen Delivery (ml O ₂ /min/m ²)	351.76		352.16	-0.40	318.30	-0.11	33.46	9.51
Total Stressed Blood Volume (ml)	72.50		72.50	-0.00	72.50	-0.00	-0.00	-0.00
RVEDV (ml)	22.88		22.88	-0.00	21.86	-0.01	1.02	4.44
Stroke Work (mmHg · ml)	786.47		785.76	0.71	734.62	0.09	51.85	6.59
Systolic PVA (mmHg · ml)	1059.60		1058.41	1.19	987.58	0.11	72.02	6.80
Mechanical Efficiency (%)	74.22		74.24	-0.02	74.39	-0.02	-0.16	-0.22

If we assume $R_1 = R_2 = R^*$, then we can show:

$$\frac{1}{R_{eq}} = \frac{2}{R^*}$$

which rearranges to determine the left and right branch resistance R^* as a function of the original and equivalent combined pulmonary resistance R_{eq} :

$$R^* = 2R_{eq}$$

For the compliant chamber it is assumed that the original chamber volume V_0 (i.e. charge) is split equally to each pulmonary branch and so the left and right chamber volumes V_1 are halved i.e. $V_0 = 2V_1$. Given that the pressure is to remain constant, using Equation (5.7), it can be shown:

$$\frac{V_0}{C_{eq}} = \frac{V_1}{C^*}$$

substituting for V_0 gives

$$\frac{2V_1}{C_{eq}} = \frac{V_1}{C^*}$$

Simplifying and solving for C^* allows us to determine the new compliance value as a function of the original and equivalent combined pulmonary compliance C_{eq} :

$$C^* = \frac{C_{eq}}{2}$$

Table 7.2 lists the differences in values used for the single pulmonary branch lumped circulation model compared with the left and right branched pulmonary circuit used in the coupled multiscale modelling.

TABLE 7.2: Parameter values of pulmonary components used in the stand alone lumped circulation model versus altered coupled lumped circulation model

	Combined Pulmonary Branch	
	Stand alone LCM	Split Left and Right Pulmonary Branches Coupled LCM
Pulmonary Arterial Resistance, R_a (mmHg · s/ml)	0.63	1.26
Pulmonary Venous Resistance, R_v (mmHg · s/ml)	0.011	0.022
Pulmonary Arterial Capacitance, C_a (ml/mmHg)	0.31	0.155
Pulmonary Venous Capacitance, C_v (ml/mmHg)	0.89	0.445

7.2.3 Cardiac Cycle Repetition

Four cardiac cycles were simulated to allow periodic convergence and stability of the solution. Four cycles were chosen given the evidence in the literature [82], acceptable computational time and sufficient convergence of key profiles. Figure 7.5 illustrates a range of output profiles demonstrating the level of convergence. The top row illustrates the continuous profile, while the bottom row has each cardiac cycle superimposed on top of one another.

The initial values of the cardiac chamber volumes for the multi-scale model were based on the lumped circulation model values for the reference configuration of 3 mm (external) branch pulmonary arterial banding and an 8 mm stent. Therefore to best illustrate the convergence effect, the 3 mm internal 3D submodel was chosen. Given the results from the stand alone 3D model, it would be expected that the 3 mm geometry would require greater convergence from the reference values. This indeed proved to be the case, and comparison between the stand alone LCM and the fully coupled models will be presented in Section 7.3.3.

In all outcomes, clear periodic convergence is observed. Of all profiles, on first glance, the systemic venous pressure does not appear sufficiently converged. However, upon looking at the range of pressure values of between 2.8 and 4.2 mmHg, this did not warrant the extra costs of simulating additional heart beats. The difference from beat 3 to 4 was deemed clinically negligible,

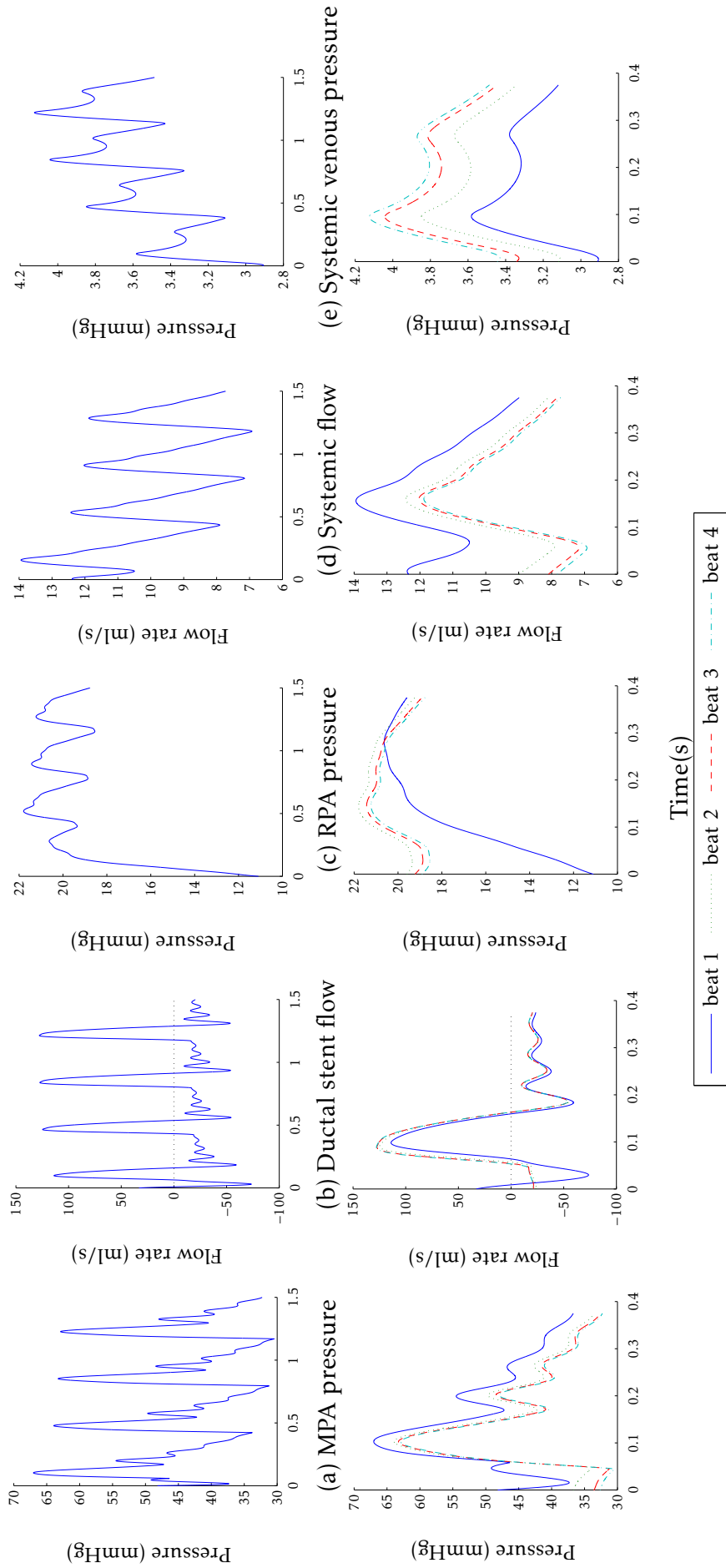


FIGURE 7.5: Continuous (top) and beat-by-beat (bottom) profiles of (a) MPA pressure (b) Stent flow (c) Right PA pressure (d) Systemic perfusion (e) Systemic venous pressure for the coupled multi-scale model using the 3 mm geometry

with this conclusion supported by the good convergence of clinically important profiles (e.g. ductal stent flow).

The oscillations observed in Figure 7.5 will be commented on fully in the results presented below, following the definition of the study protocols.

7.2.4 Protocols

In Chapter 5 as the computational cost of matching a specified outcome (e.g. mean MPA pressure, cardiac output) by varying the total stressed blood volume was low, the methodology was able to be adopted. However, it took simulating several cardiac cycles, for multiple “guesses” of V_T (between four and ten) to determine the desired outcome using the False Position Method. This was not plausible for the coupled multiscale model given that one cardiac cycle at a single stressed blood volume took approximately 7.5 hours. Therefore, two alternative protocols were adopted.

The first was to vary the geometry used while maintaining the total stressed blood volume. The set of geometries used in Chapter 6 were re-used: the unaltered geometry determined from the clinical data (*default*), and superimposed cylinders representing controlled intraluminal dimensions of 1.5 to 4 mm in 0.5 mm increments. The fixed stressed blood volume was set at 72.5 ml, based on the initial reference configuration used in the 0D model ($d = 3$ mm; $D = 8$ mm; mean MPA pressure = 58.5 mmHg) from Chapter 5.

As the False Position Method matching of the mean MPA pressure or cardiac output was not feasible given the computational constraints, a valid clinical comparison between geometries had to be selected. Without any indication for varying the total stressed blood volume with the 3D geometry to match a defined clinical outcome, this was deemed the most clinically appropriate. This further illustrates the need to define the clinical interpretation and significance of this modelling parameter hence the second protocol.

The second protocol was to use a single 3D geometry and vary the stressed blood volume, as studied in Section 5.3.2 for the lumped circulation model. The 2 mm internal banding geometry was selected for this investigation. This choice was supported by evidence in the literature [83] and the results of the first protocol which will be presented below. The range of total stressed blood volumes is listed below:

$$V_T = \{60, 70, 72.5, 75, 80, 90\}$$

Despite many publications using the presently adopted coupled multiscale methodology, definition of the methods used in relation to this essential parameter (or initial conditions) is often omitted [81–83, 85, 118]. Therefore the identification and transparent discussion of this vital parameter, with regard to the methods adopted throughout this area of research, is one of the main points of interest of this study.

It is essential that full transparency, and acknowledgement of all limitations for computational cardiac modelling are identified up-front in order that this work be deemed clinically relevant. By omission of the details of this step in the current methods in the literature, this area of research is generally considered to be of little clinical significance, hence clinicians may feel justified in receiving the impression that you can “*get out whatever you want out depending on whatever you put in*”. Our hope is that in our transparency regarding the synthetic and arbitrary nature of this parameter, further clinical context and physiologically appropriate values may be determined in the future.

7.3 Outcomes

Following the investigations described above, the results and their implications are now discussed. The first protocol of varying the band diameter while maintaining the total stressed blood volume is presented and is considered as the most natural clinical implementation, without an objective method for adjusting V_T to permit valid comparison. A retrospective study of the stand-

alone lumped circulation model for fixed V_T and a varied band diameter d (with a fixed ductal stent diameter $D = 8$ mm) was carried out and comparisons are made below.

The more methodological investigation of the total stressed blood volume is then openly discussed, with the intention of bringing to light the need to fully comprehend this vital input parameter. The author feels that this parameter has not had the investigation it deserves, with this lack of transparency creating a barrier to progress in obtaining truly patient-specific models, as opposed to the idealised models (particularly related to the lumped circulation submodels) found in the literature. This has been discovered as a result of the current investigations, and without the relevant clinical data to perform sufficient studies, the clinical definition of the total stressed blood volume is proposed as a challenge for this research field to appropriately define.

Finally, a comparison between the coupled and stand-alone LCM model is analysed. This was investigated by determining the (external) band diameter that matched the calculated mean MPA pressure and cardiac outputs respectively from the fully coupled model. This was achieved using the False Position Method as described in Chapter 5 for matching V_T to the desired mean MPA pressure/cardiac output. The same total stressed blood volume of 72.5 was used, as adopted by the initial multiscale investigation.

7.3.1 Varying Band Diameter

The full haemodynamical results of varying the 3D geometry while maintaining the same lumped circulation parameters and input total stressed blood volume are presented in Table 7.3. This is for a total stressed blood volume of 72.5 ml.

Given the methodologies adopted in Chapter 5 of varying V_T to maintain the mean MPA pressure and cardiac output respectively, we first discuss their results with respect to other relevant outcomes. The mean MPA pressure drops

TABLE 7.3: Multiscale model results for fixed total stressed blood volume, constant circulatory constants and differing geometries with varying internal PAB diameter

Band Diameter (mm)	Default	1.5	2.0	2.5	3.0	3.5	4.0
Systolic MPA Pressure (mmHg)	75.86	74.46	71.04	67.82	62.76	63.40	58.48
Diastolic MPA Pressure (mmHg)	46.94	48.56	42.42	37.05	30.15	30.86	26.04
Mean MPA Pressure (mmHg)	59.27	58.60	53.41	48.81	42.56	43.27	38.27
Systolic Systemic Pressure (mmHg)	63.70	63.36	58.80	54.73	49.17	49.83	45.28
Diastolic Systemic Pressure (mmHg)	47.61	48.91	42.53	37.04	30.09	30.82	26.04
Mean Systemic Pressure (mmHg)	56.01	55.82	50.31	45.48	39.09	39.80	34.93
Mean Left Pulmonary Pressure (mmHg)	9.71	9.73	13.08	16.17	24.16	23.15	26.39
Mean Right Pulmonary Pressure (mmHg)	9.31	10.04	14.75	18.66	19.99	19.95	23.98
Cardiac Output (l/min)	1.64	1.54	1.80	2.02	2.32	2.28	2.52
Left Pulmonary Flow (l/min)	0.28	0.35	0.50	0.63	0.98	0.94	1.08
Right Pulmonary Flow (l/min)	0.25	0.37	0.57	0.75	0.79	0.79	0.97
Pulmonary Flow (l/min)	0.52	0.72	1.07	1.37	1.77	1.73	2.04
Systemic Flow (l/min)	1.07	0.82	0.73	0.65	0.54	0.55	0.48
Pulmonary-Systemic Flow Ratio	0.49	0.88	1.47	2.12	3.27	3.12	4.28
Stent Backflow (l/min)	-0.35	-0.45	-0.64	-0.80	-0.98	-0.96	-1.04
Arterial Oxygen Saturation (%)	45.46	59.74	72.22	77.91	82.45	82.05	84.49
Venous Oxygen Saturation (%)	19.72	26.22	34.35	35.29	31.67	32.30	26.65
Systemic Oxygen Delivery (ml O ₂ /min/m ²)	326.77	329.70	352.77	338.21	300.37	305.14	270.24
RVEDV (ml)	21.59	20.88	21.81	22.61	23.65	23.53	24.31
Ejection Fraction (%)	0.47	0.46	0.52	0.56	0.61	0.61	0.65
Stroke Work (mmHg · ml)	756.03	703.37	782.87	842.74	907.25	900.73	940.88
Systolic PVA (mmHg · ml)	981.90	922.41	962.98	991.51	1017.18	1014.82	1025.94
Mechanical Efficiency (%)	77.00	76.25	81.30	84.99	89.19	88.76	91.71

from 58.6 to 38.3 mmHg as the internal band diameter is increased from 1.5 to 4.0 mm, while the cardiac output increases from 1.54 to 2.52 l/min over the same range. Following the conclusions drawn from Chapter 5 we can see that as there is no increase in V_T there is no compensation for the decrease in pulmonary resistance. This results in the increase in cardiac output as there is less resistance to the supply of blood to both the systemic and the pulmonary circulations. The increase in cardiac output is diverted, as one would anticipate, to the pulmonary arteries (Q_p increases from 0.72 to 2.04 l/min), while the systemic perfusion decreases (0.82 to 0.48 l/min) mainly due to increased diastolic steal (-0.45 to -1.04 l/min). This effect can be observed in Figure 7.6.

As there is no mechanism for the pressure in the circulation to increase while the total stressed blood volume is constant, unlike in Section 5.3.2, we

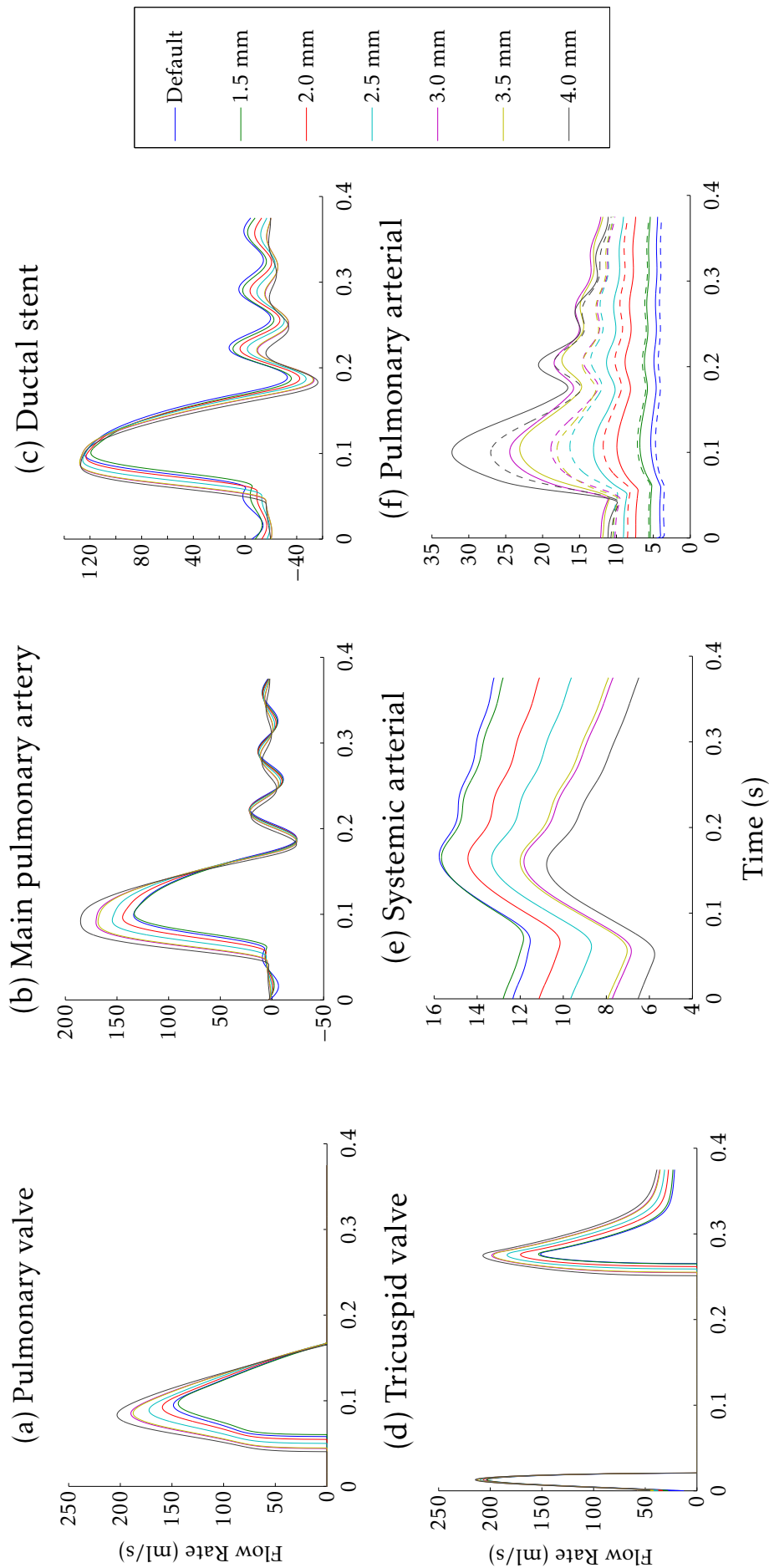


FIGURE 7.6: Flow profiles as 3D geometry is varied

see all systemic pressures drop, while the pressure in the pulmonary circuit increases as the exposure to the higher ventricle generated pressure is increased with larger banding. These trends are visible in Figure 7.7, which displays the pressure profiles at various locations throughout the circuit for each pulmonary band diameter (including the unaltered 'Default Geometry').

It is also clear from Table 7.3 that the systolic and diastolic pressures for the systemic sites decrease and pulmonary sites increase as the wider bands are used. The mean systemic pressure (post-stent) drops from 55.8 to 34.9 mmHg while the mean left pulmonary artery pressure (post-banding) increases from 9.7 to 26.4 mmHg. Of clinical concern, is the drop in diastolic MPA pressure. This falls from 48.56 to 26.04 mmHg, which raises concerns over the coronary supply to the single ventricle which is predominantly perfused in diastole. The coronary supply has been modelled on a generic hybrid geometry with a similar methodology [83] but the conclusions of this outcome were not published until recently [84]. Their simulations demonstrated that the coronary supply from a 1.5 mm band diameter to a 3.5 mm diameter dropped from 0.076 to 0.044 l/min while the coronary mean pressure dropped from 71.0 to 43.0 mmHg.

Overall, the results between the generic geometry and this study's patient-specific study correlate well. This will be discussed in greater detail below in Section 7.4.

Assuming that the fixing of V_T does not invalidate any clinical comparisons, as suggested by the literature cited, there are certain key trends to observe in varying the band diameter. These trends, including the increase in cardiac output and decrease in systemic perfusion are depicted in Figure 7.8. Additionally we see that $Q_p : Q_s$ ratio increases from 0.88 to 4.28 with this dramatic increase following from the increase in Q_p and decrease in Q_s (Figure 7.8 (c)) mentioned above.

The stroke work increases from 703 to 940 mmHgl · ml demonstrating an increased ventricular workload as the band is expanded. This is better illus-

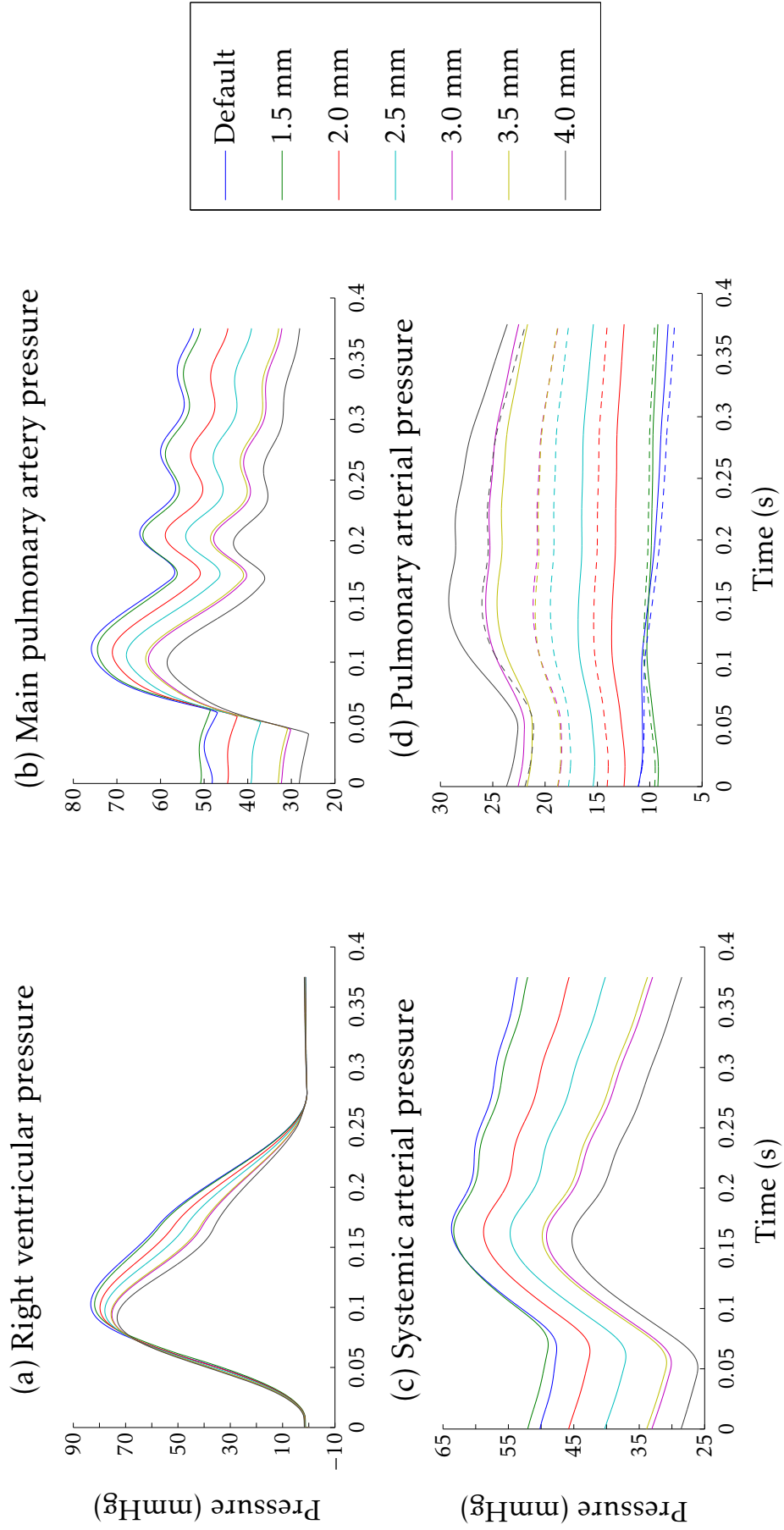


FIGURE 7.7: Pressure profiles as 3D geometry is varied

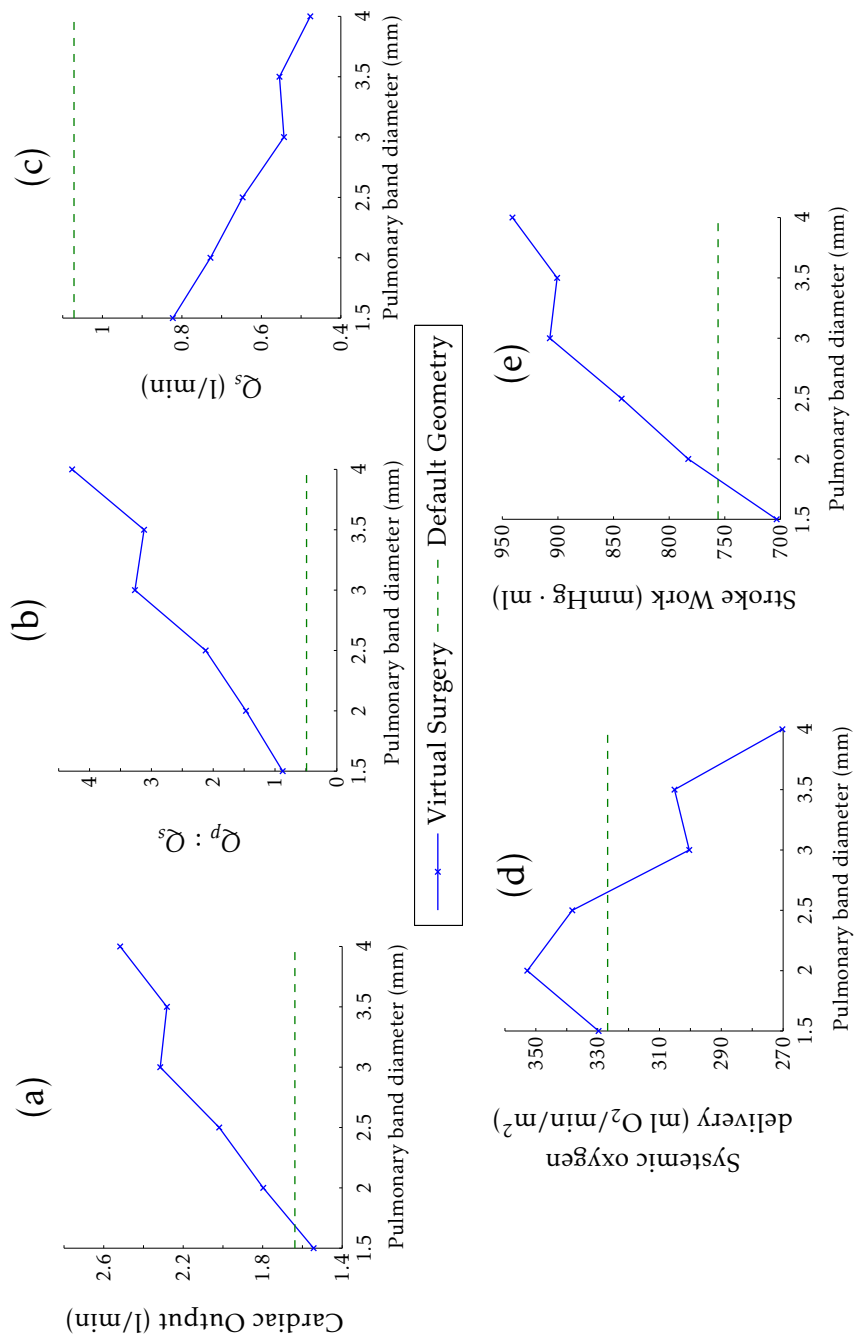


FIGURE 7.8: Internal pulmonary artery banding diameter versus (a) Cardiac Output (b) Pulmonary-to-Systemic Flow Ratio (c) Systemic Flow (d) Systemic Oxygen Delivery (e) Stroke Work

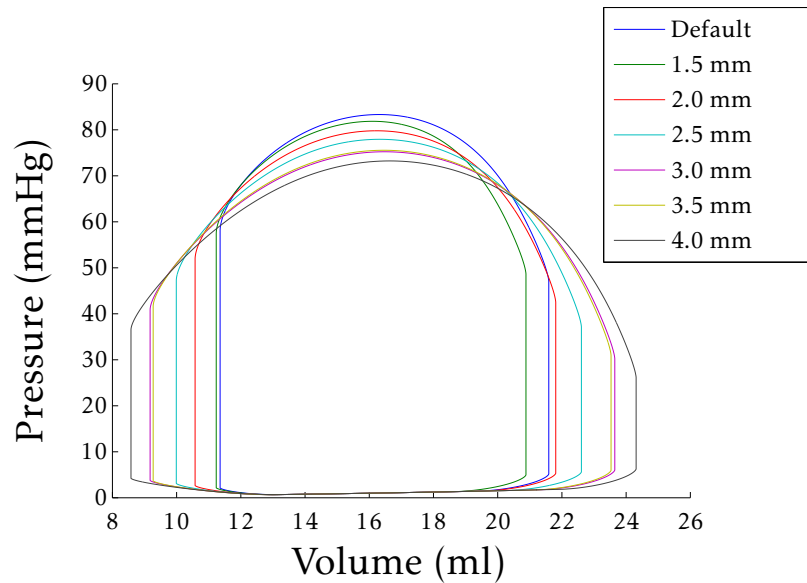


FIGURE 7.9: Pressure-volume loops for varying internal pulmonary band diameter

trated by the pressure-volume loops presented in Figure 7.9. This graph identifies the reason for the stroke work increasing: As the banding is increased, both the end systolic and end diastolic volume widen thus the area of the P-V loop increasing despite the decrease in maximum pressure. This also illustrates, given that the heart rate is constant, the cardiac output increasing. Despite this increase, both the ejection fraction (51.5 to 64.7 %) and mechanical efficiency of the ventricle improve with increasing PAB diameter (1.5 to 4 mm).

There are contraindicating trends observed for important outcomes that require optimisation (e.g. increasing the PAB diameter increases the mechanical ejection fraction and cardiac output while decreasing the systemic oxygen delivery, above 2 mm banding, and coronary perfusion). Thus a holistic view to the haemodynamics must be taken to conclude what the optimal banding diameter is. It is clear that too wide a band has a detrimental effect on the haemodynamics, while too tight a banding results in poor oxygen delivery and poorer ventricular efficiency. Upon reviewing the data published in Table 7.3 again, focusing on what has been highlighted above, it would be inappropriate (and unphysiological) to select a diameter above 2 mm. Both the 1.5 and 2 mm banding give the most physiologically beneficial results, with the 2 mm offering the maximal systemic oxygen delivery.

The systemic arterial oxygen saturation increases from 72.22 to 84.49% yet does not compensate for the lower systemic flow for larger pulmonary banding where the systemic oxygen delivery drops from 352.77 to 270.24 ml O₂/min/m² (2 to 4 mm). As can be seen in Table 7.3, illustrated in Figure 7.8 (d), the systemic oxygen delivery (one of the primary haemodynamical outcomes) is greatest with a 2 mm band at 352.77 ml O₂/min/m². This is a critical observation as supplying oxygen to the body is the primary purpose of the cardiovascular system, and so it is found that by tightening the bands, and reducing the diastolic steal from the systemic circuit, the O₂ delivery counter-intuitively increases until a critical value is reached. This value was observed, given our resolution of 0.5 mm steps to be around the 2 mm internal banded diameter. If you continue to tighten beyond this critical point, the pulmonary flow and consequently systemic arterial saturation decrease to a point where the increase in Q_s is ineffective. When the band is tightened beyond 2 mm to 1.5 mm the systemic oxygen delivery decreases to 329.70 ml O₂/min. These results, and therefore conclusions, do not consider autonomic regulation responses which could lead to differing conclusions.

This study would support the selection of the 2 mm internal PAB diameter, with a leaning to support a tighter band than looser band if faced with any uncertainty. The haemodynamical outcomes of the 1.5 mm banding versus the 2.5 mm are superior (decreased stroke work, better pulmonary-systemic flow balance, higher diastolic MPA pressure for coronary perfusion). These are the exact concerns that would be expected from clinical experience regarding identifying the optimal banding diameter, with the consequences of over or under tightening the bands observed in the simulation results. The results are also supported by the conclusions of the generalised geometry of the Hybrid Procedure found in the literature [83, 84, 127] where 2 mm internal banding diameter was also identified as optimal.

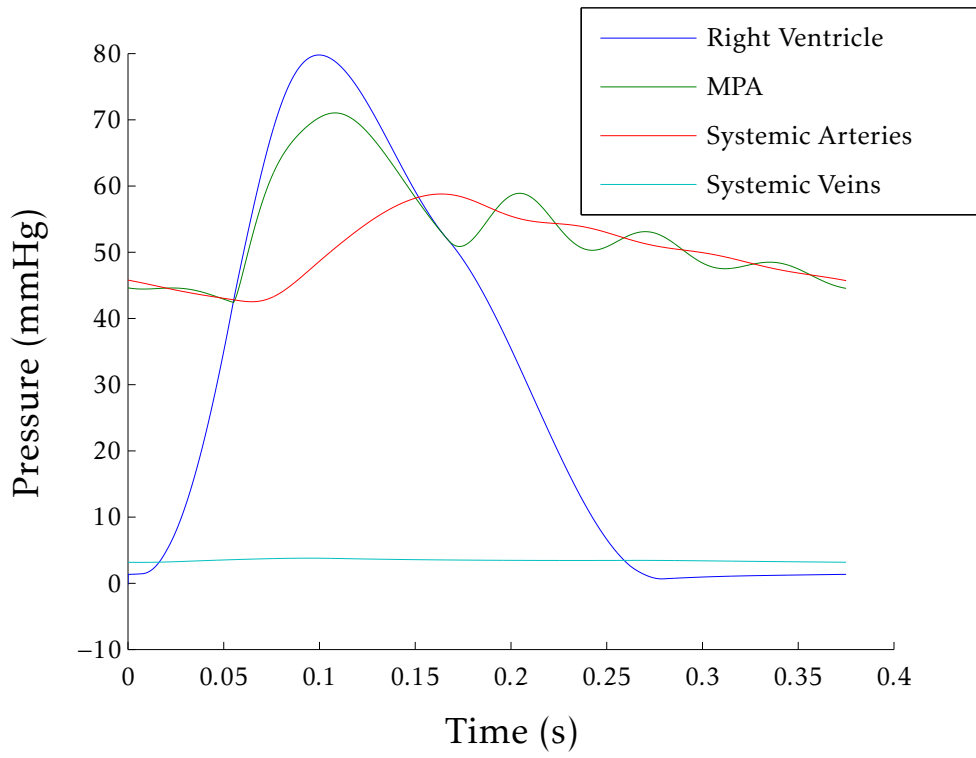
The sensitivity of the outcome of systemic oxygen delivery on BSA and the other relevant parameters (see Equation (5.27)) further highlights the need for patient specificity. Patient-specific parameters of body surface area, as well as

the pulmonary venous saturation and the required whole body oxygen consumption rate would produce more meaningful data for an individual patient. Patient-specific lumped circulatory constants (including those used to calculate clinical outcomes as just described) are vital to the relevance this modelling methodology has in the clinical setting, leading to a future of predictive, non-invasive patient-specific virtual surgeries.

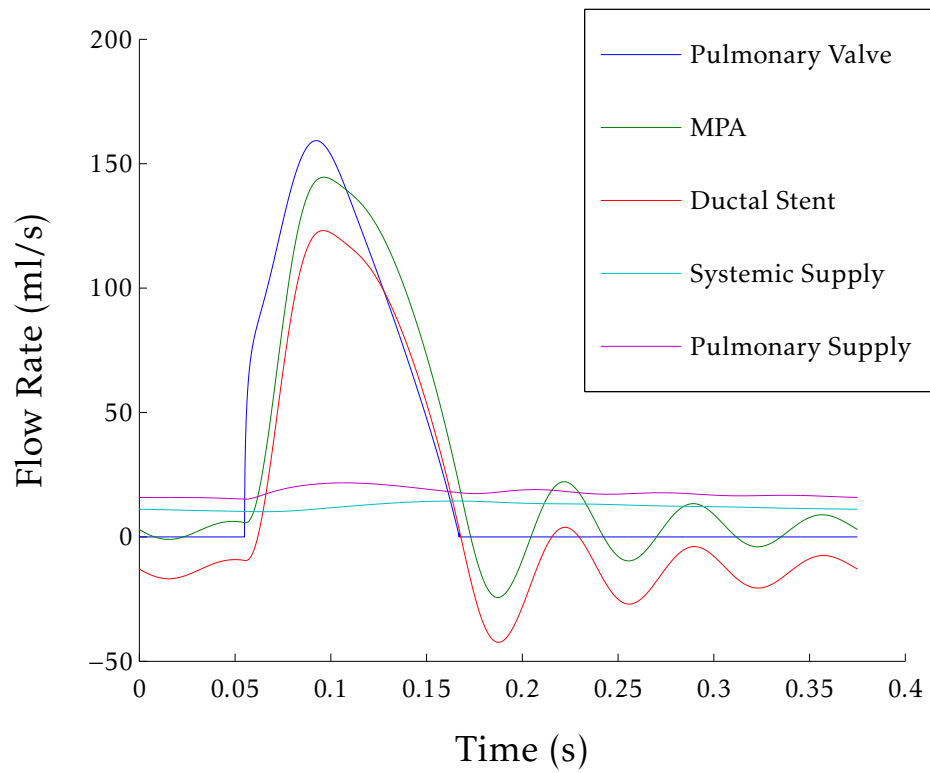
Geometric Influences

There are two observations noted from the results that must now be addressed, although they do not have any significant effect on the final clinical conclusions and recommendations: The discrepancy in trends observed for the clinical outcomes of the 3.5 mm geometry (see Figure 7.8) and the oscillations observed in the clinical profiles (see Figures 7.6 and 7.7). A comment on the default geometry will also be included when discussing the nonconformity of the general trend for the 3.5 mm geometry.

In adopting rigid walls i.e. the walls not being elastic, there is no absorption or release of energy by the vessel walls into the system as found in situ. The consequence of this is that there are the oscillations observed in the pressure and flow profiles of the artificial faces of the 3D region. From Figure 7.10 we can see that the oscillations are absorbed by the compliant chambers downstream. The results we produced match those of the original Norwood study from Laganá et al. [81] while the oscillations have been omitted from the later publication [82]. Following correspondence between the author of this study and those cited above, it was established that by the introduction of additional compliant chambers and presenting the profiles from those slightly further down the cardiovascular tree, the final published results were more clinically appealing. This approach was not adopted by our study, with the intent that future modelling would involve patient-specific lumped circulation models. One proposition would be that the location of each catheter derived pressure profile would dictate the number and location of compliant chambers.



(a) Pressure Progression



(b) Flow Progression

FIGURE 7.10: Absorbtion of reflection oscillations

It was also established that the oscillations are a reflection of the wave of propagating blood from the artificial boundaries, and as a result are more prominent in the systemic system, when pulmonary investigations (e.g. Fontan surgery) are not impacted the same way. The inclusion of fluid-structure interactions would address this observation with great potential to assess the impact of rigidity of the banding and stented ductus, as well as better assessing the energy requirements as the vessel utilises the contractile force in diastole. While the profiles suffer from this aberration, the clinical results are not adversely affected to any significant degree. Further developments in the accuracy of the modelling will lead to greater confidence in assessing the impact of the factors mentioned above. An increase in complexity of the model requires further parameters to be appropriately defined at greater computational expense, therefore the work presented here, gives great insight at an affordable cost.

As was the case in Chapter 6, the results of the 3.5 mm banding do not fit with the trend observed and described above. It does not counter the general trend of increasing band diameter (from 1.5 through 3 mm), and is an isolated occurrence. As previously stated, it is believed this unexpected improvement is a result of the geometric manipulation and was anticipated, given the analysis of Chapter 6. This highlights additional areas that require further study with regard to patient-specific geometries, namely the impact of the angle of banding and the location of the artificial boundaries, particularly with respect to the post banding branch pulmonary arteries.

Finally the default geometry is considered. The default geometry was the unaltered post-intervention patient-specific anatomy of the Hybrid Procedure. As discussed in Chapter 6, there is a requirement for user interpretation of the scans, particularly at the resolution of the original scan. It is therefore interesting to observe the results in comparison to the virtual surgeries undertaken.

In most haemodynamical and ventricular energetic outcomes, the results from the default geometry appear to fall between the 1.5 and 2 mm geome-

tries. This is the case for the systemic pressures, cardiac output, ejection fraction, stroke work and mechanical efficiency. The default geometry results in a systemic oxygen delivery of 326.77 ml O₂/min/m² (vs 352.77 ml O₂/min/m² of the 2 mm geometry).

This suggests, given the assumptions based into the calculation of systemic oxygen delivery (see Section 5.2.6), that the systemic perfusion dictates good oxygen delivery, and that pulmonary under-circulation is well tolerated. It is always to be remembered that the autonomic responses are not included and may need to be modelled before any clinically impacting conclusions regarding tighter banding is proposed.

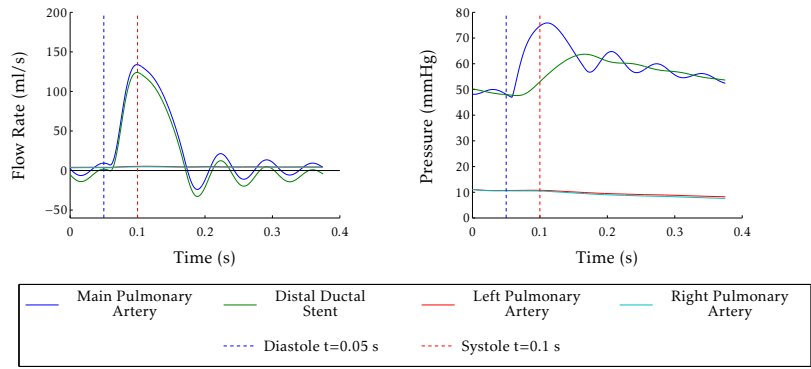
Visualisation of Results

In the following pages, a visual representation of the simulation results are presented. The full pressure and flow profiles for all artificial boundaries are given (top left and top right respectively), with a diastolic and systolic time point indicated on each. The diastolic time point was selected at $t = 0.05$ s, while the systolic time point was at $t = 0.1$ s. The normal velocity (second row) and pressure (bottom row) contours from the 3D geometry are displayed for the diastolic (left) and systolic (right) time points.

Pathlines (the path taken by a massless particle in the calculated flow configuration) that exit the region via the ductal stent, left and right pulmonary arteries are illustrated, visualising the source of flow distribution at diastole (middle left) and systole (middle right). The same colour-map is used for all velocities and likewise for pressures so that valid comparisons can be observed between geometries.

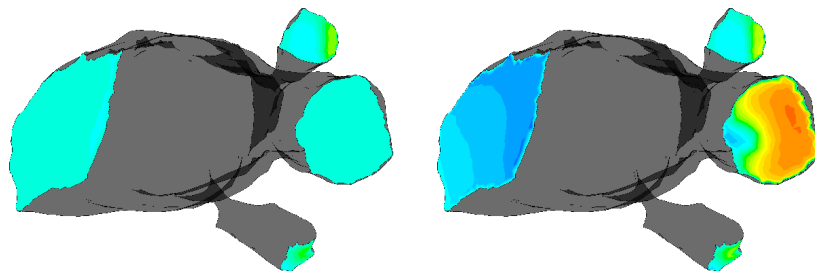
Legends are provided to indicate the colours of which surfaces the flow is headed towards for the pathline plots. The pathlines clearly show the antegrade flow through the branch pulmonary arteries with an element of retro-

grade flow through the ductal stent in diastole, while in systole the forward flow to the systemic and pulmonary circuits from the MPA is apparent.

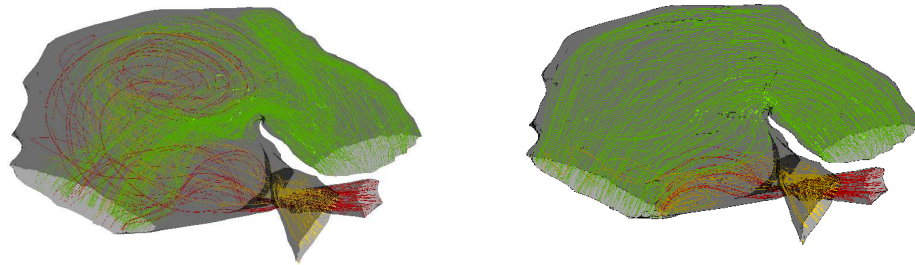
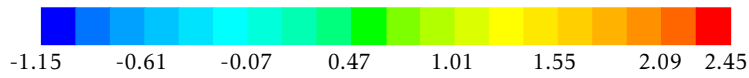


Diastole

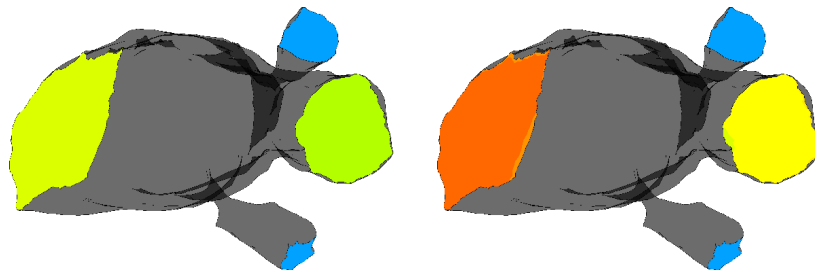
Systole



Normal Velocity (m/s)



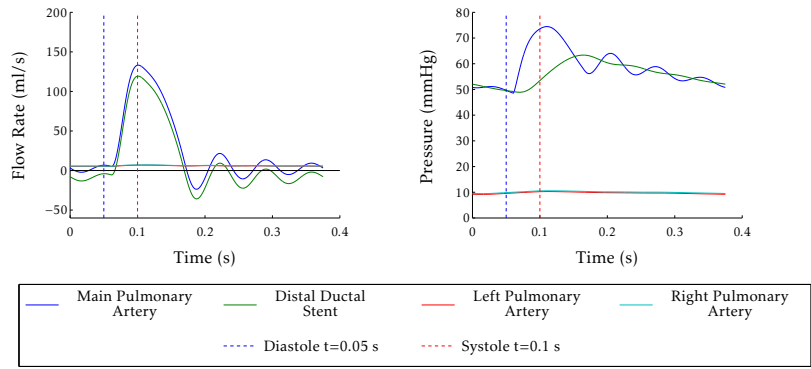
Pathlines



Pressure (mmHg)

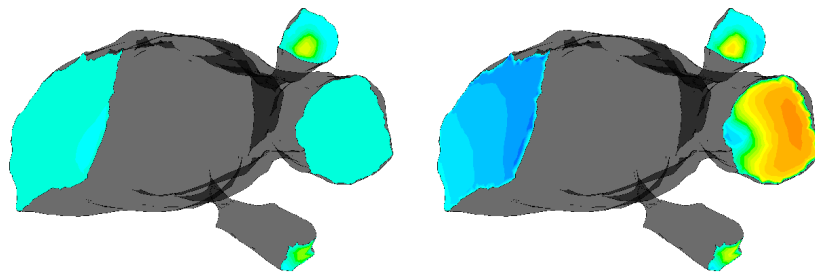


FIGURE 7.11: Visualisation of default internal band geometry results

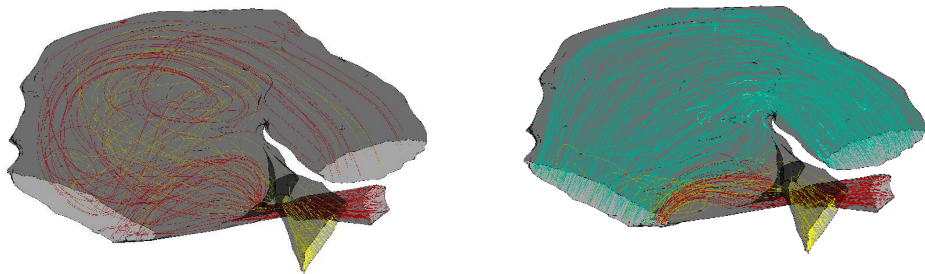
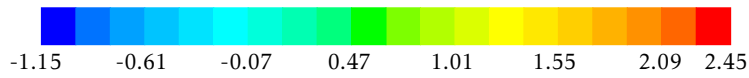


Diastole

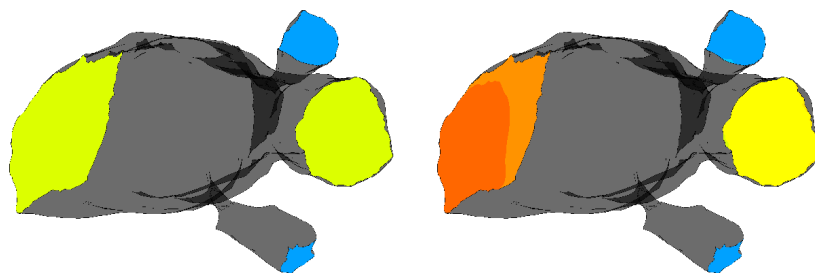
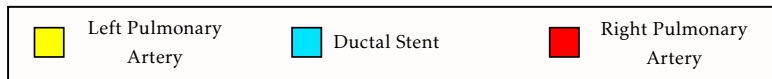
Systole



Normal Velocity (m/s)



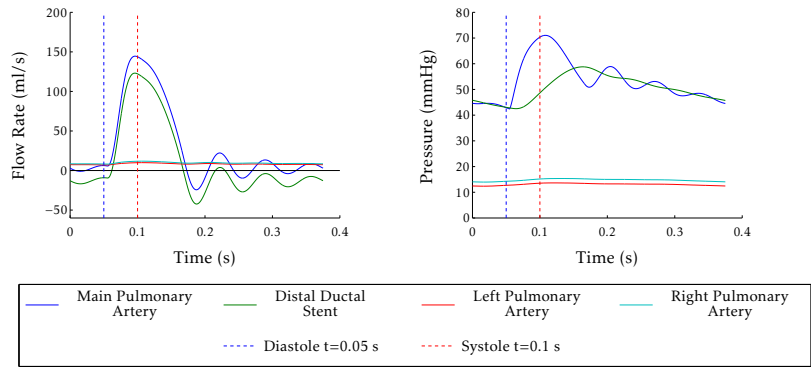
Pathlines



Pressure (mmHg)

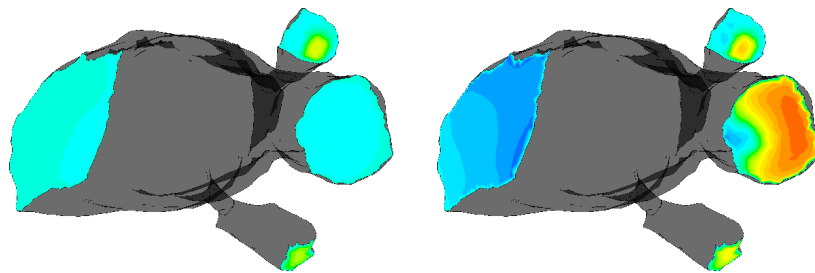


FIGURE 7.12: Visualisation of 1.5 mm internal band geometry results

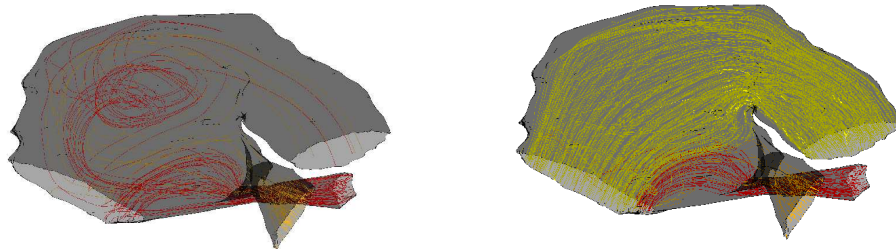
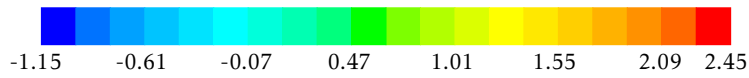


Diastole

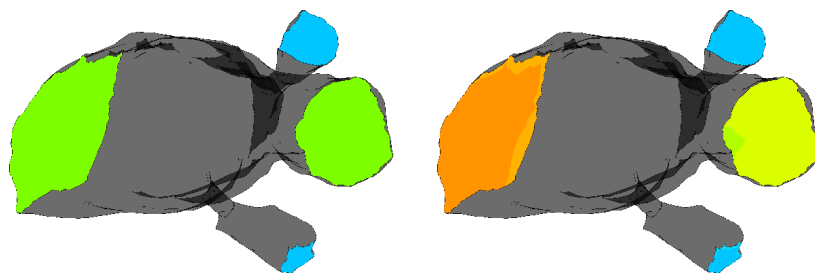
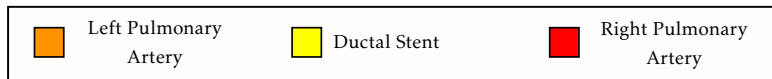
Systole



Normal Velocity (m/s)



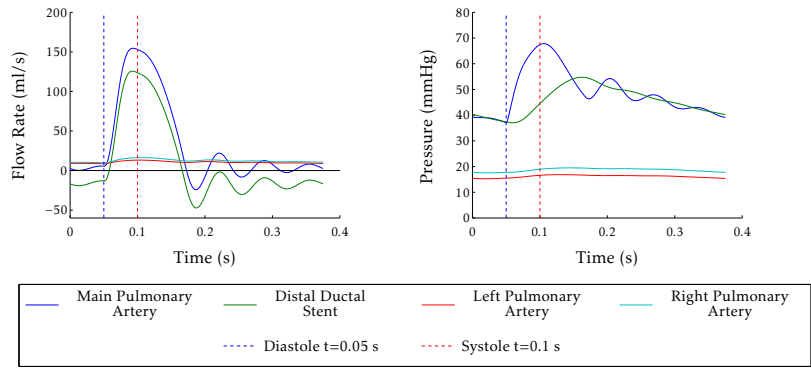
Pathlines



Pressure (mmHg)

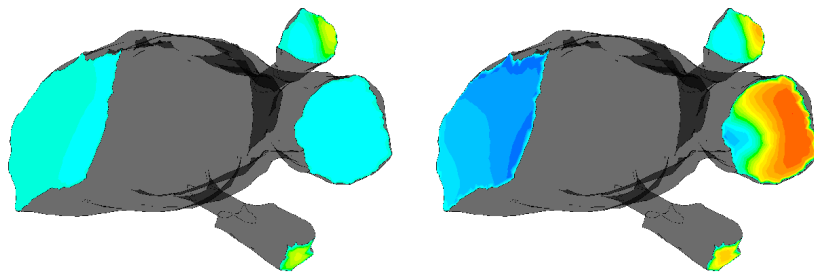


FIGURE 7.13: Visualisation of 2 mm internal band geometry results

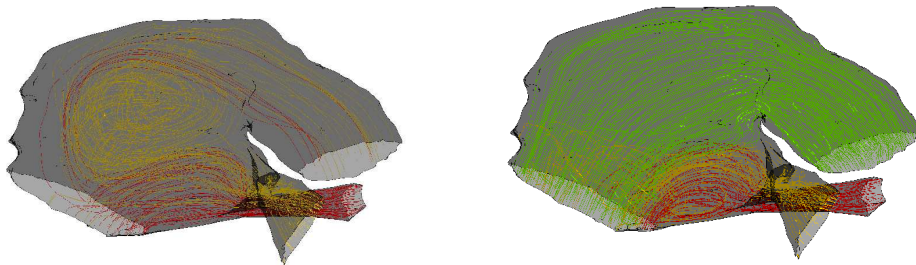
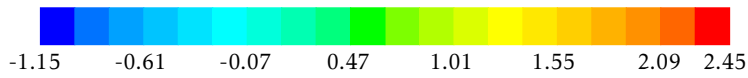


Diastole

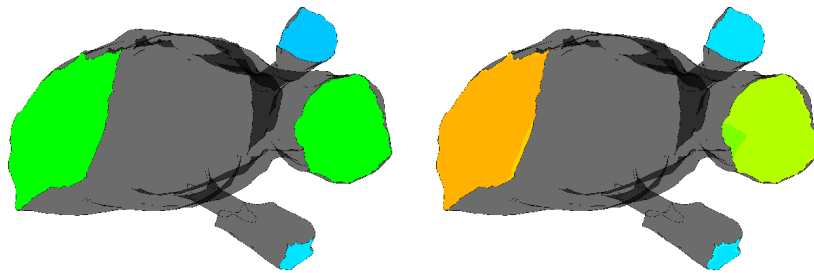
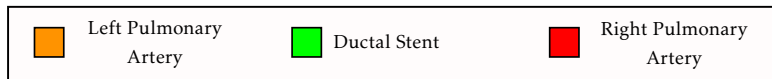
Systole



Normal Velocity (m/s)



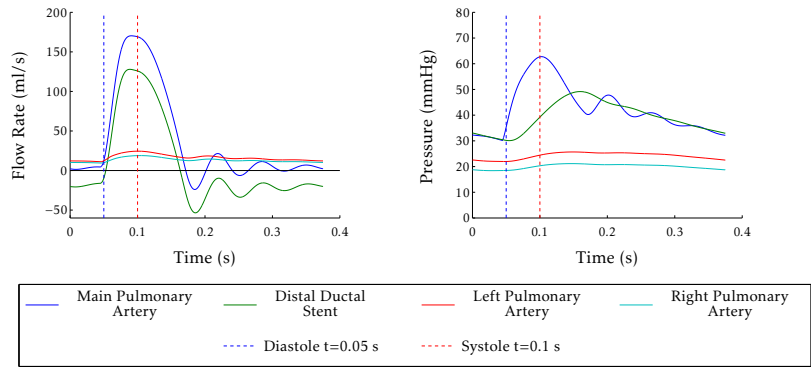
Pathlines



Pressure (mmHg)

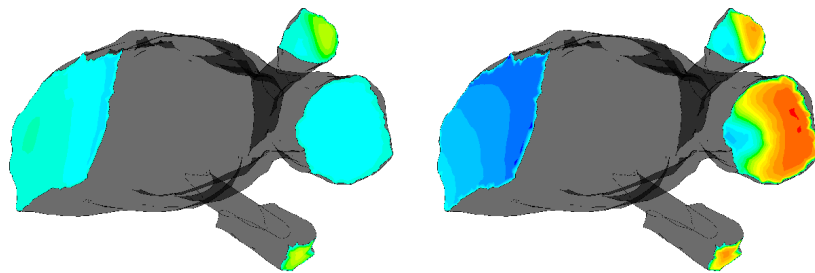


FIGURE 7.14: Visualisation of 2.5 mm internal band geometry results

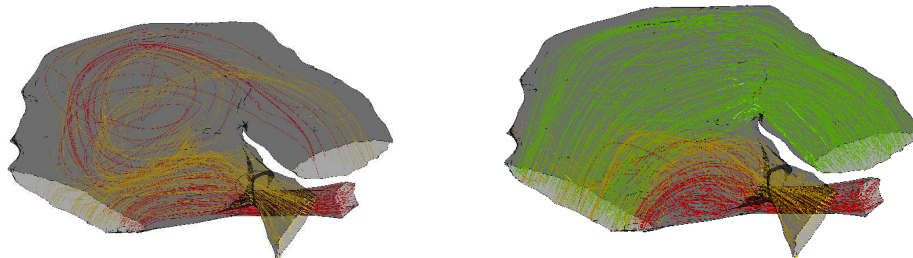
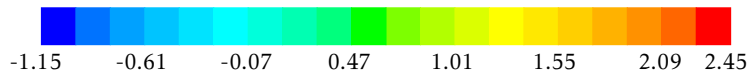


Diastole

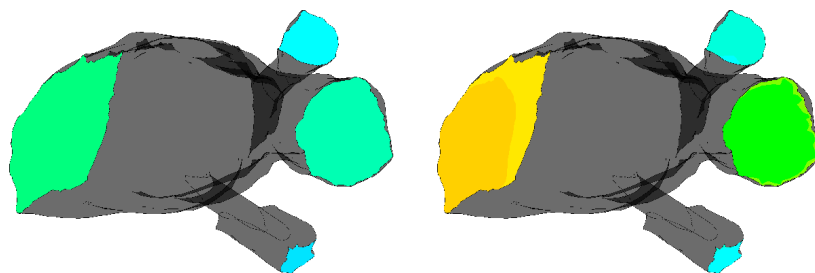
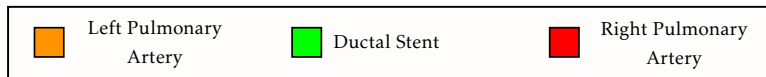
Systole



Normal Velocity (m/s)



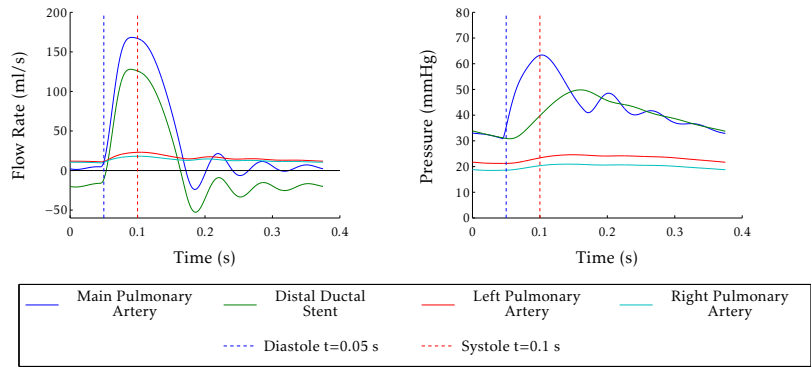
Pathlines



Pressure (mmHg)

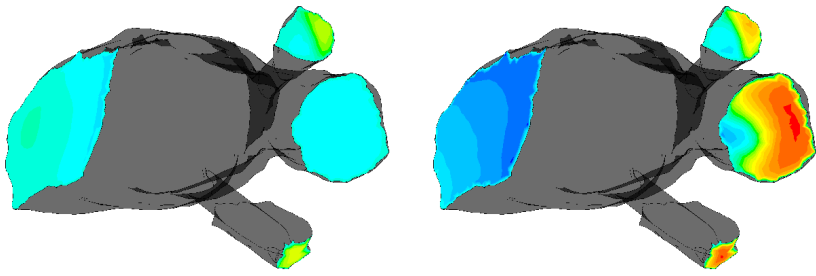


FIGURE 7.15: Visualisation of 3 mm internal band geometry results

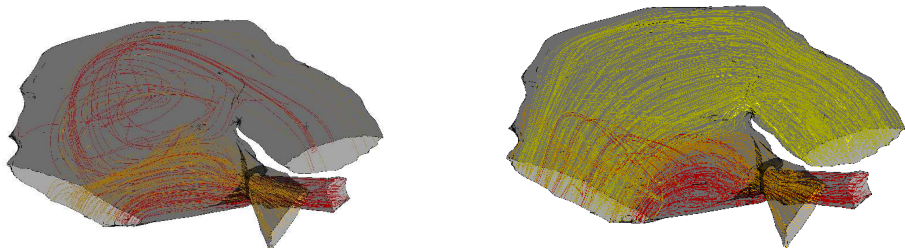
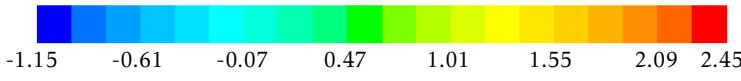


Diastole

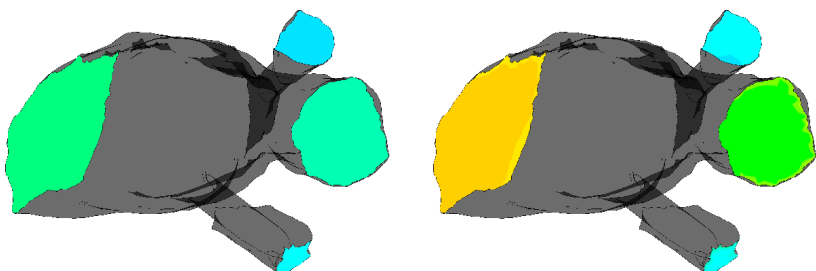
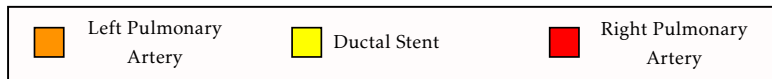
Systole



Normal Velocity (m/s)



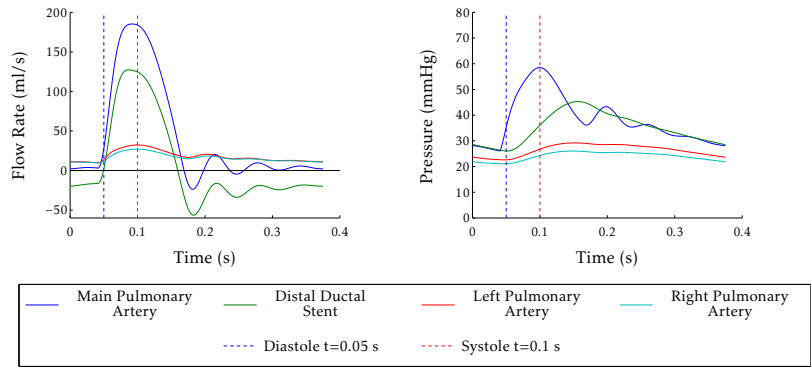
Pathlines



Pressure (mmHg)

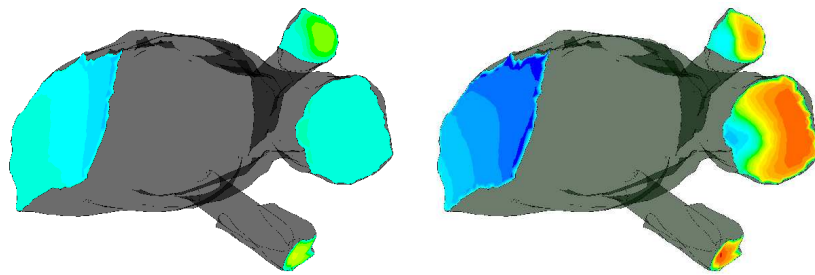


FIGURE 7.16: Visualisation of 3.5 mm internal band geometry results

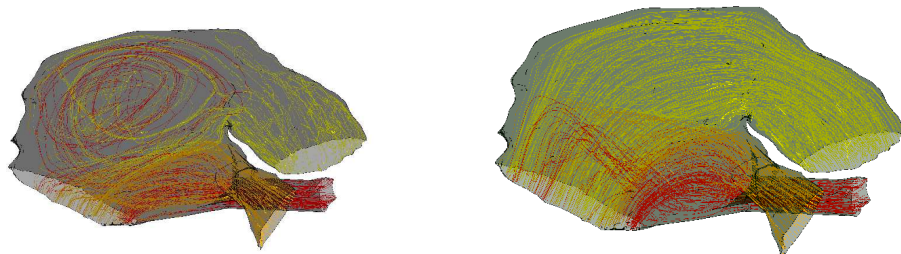
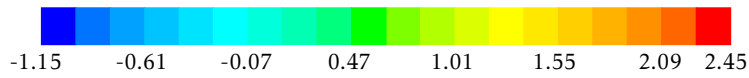


Diastole

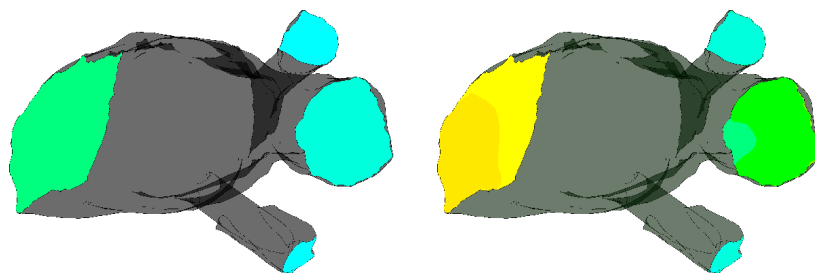
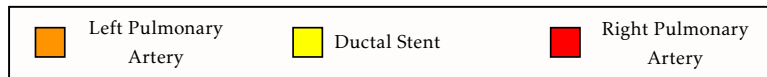
Systole



Normal Velocity (m/s)



Pathlines



Pressure (mmHg)

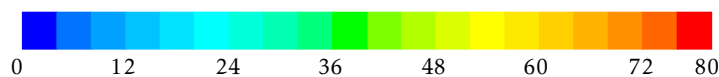


FIGURE 7.17: Visualisation of 4 mm internal band geometry results

7.3.2 Varying Total Stressed Blood Volume

In Chapter 5 the total stressed blood volume was varied to match both mean main pulmonary artery pressure, and cardiac output. In section 5.3.2 the effect of varying V_T while fixing the geometry was briefly investigated suggesting strong linear trends of most haemodynamical outcomes. Without any indication from previous studies from the literature, knowing that by varying the total stressed blood volume the outcomes could drastically change, it was concluded that to perform valid comparisons, V_T was fixed. An ad-hoc approach to changing the total stressed blood volume could lead to the impression that the simulations can produce any result desired.

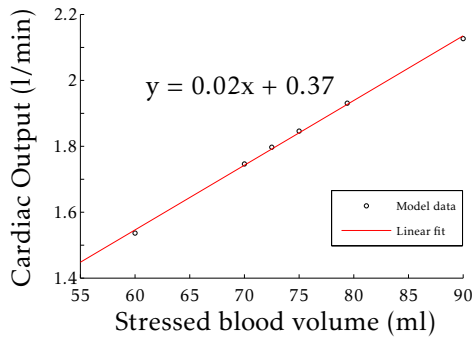
Table 7.4 shows the haemodynamical and ventricular energetics results from varying V_T using the optimal 2 mm geometry. Again, clear linear trends are observed, all positively correlated with the exception of $Q_p : Q_s$ and mechanical efficiency which decrease as V_T is increased. This is significantly different from the lumped circulation model where no variation in pulmonary-systemic flow ratio was observed.

Key outcomes, as displayed in Figure 7.8 for the varying of the geometry, are shown versus stressed blood volume. Figure 7.18 shows a scatter graph including the best fit straight line. Table 7.5 displays the gradient and intercept for each outcome, as well as the Pearson's Correlation Coefficient, where the closer to 1, the stronger the linear trend. Adopting the conventional 5% significance level, only the mechanical efficiency is not statistically significant at 0.9265, but this is accounted for by rounding errors as both the stroke work and systolic PVA hold a linear relationship with V_T .

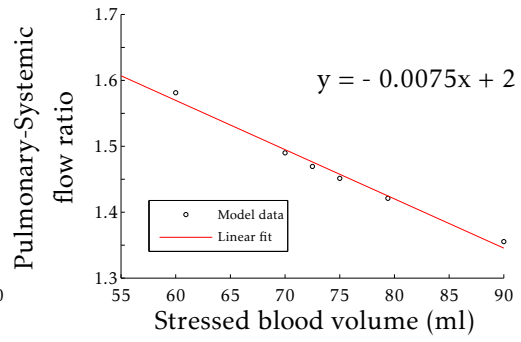
Theoretically, the total stressed blood volume could be optimised per geometry to determine the best results for a specific banding. Therefore, given the strong linearity between the haemodynamical outcomes, and the requirement for appropriate and clinically relevant patient-specific modelling, it is vital that this key input parameter be suitably defined. As it stands, there

TABLE 7.4: Multiscale model haemodynamical results for 2 mm internal PAB diameter geometry, constant circulatory constants and varying total stressed blood volume

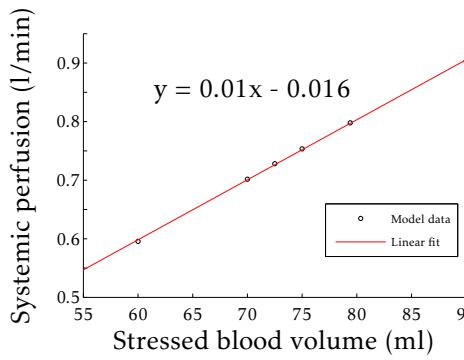
Total Stressed Blood Volume (ml)	60	70	72.5	75	80	90
Systolic MPA Pressure (mmHg)	57.50	68.35	71.04	73.70	78.37	89.39
Diastolic MPA Pressure (mmHg)	34.11	40.77	42.42	44.05	46.93	53.68
Mean MPA Pressure (mmHg)	43.39	51.42	53.41	55.37	58.81	66.93
Systolic Systemic Pressure (mmHg)	48.36	56.74	58.80	60.83	64.37	72.68
Diastolic Systemic Pressure (mmHg)	34.33	40.91	42.53	44.14	46.97	53.62
Mean Systemic Pressure (mmHg)	41.02	48.47	50.31	52.12	55.30	62.77
Systolic Left Pulmonary Pressure (mmHg)	11.79	13.28	13.64	14.00	14.62	16.08
Diastolic Left Pulmonary Pressure (mmHg)	10.66	12.03	12.37	12.70	13.28	14.64
Mean Left Pulmonary Pressure (mmHg)	11.27	12.72	13.08	13.43	14.04	15.48
Systolic Right Pulmonary Pressure (mmHg)	13.18	14.94	15.36	15.78	16.50	18.20
Diastolic Right Pulmonary Pressure (mmHg)	11.94	13.57	13.96	14.36	15.04	16.64
Mean Right Pulmonary Pressure (mmHg)	12.62	14.33	14.75	15.16	15.87	17.55
Cardiac Output (l/min)	1.54	1.75	1.80	1.85	1.93	2.13
Left Pulmonary Flow (l/min)	0.44	0.48	0.50	0.51	0.52	0.56
Right Pulmonary Flow (l/min)	0.50	0.56	0.57	0.59	0.61	0.66
Pulmonary Flow (l/min)	0.94	1.05	1.07	1.09	1.13	1.22
Systemic Flow (l/min)	0.60	0.70	0.73	0.75	0.80	0.90
Pulmonary-Systemic Flow Ratio	1.58	1.49	1.47	1.45	1.42	1.36
Stent Backflow (l/min)	-0.57	-0.62	-0.64	-0.65	-0.67	-0.72
Arterial Oxygen Saturation (%)	68.72	71.62	72.22	72.78	73.68	75.47
Venous Oxygen Saturation (%)	22.41	32.32	34.35	36.18	39.12	44.94
Systemic Oxygen Delivery (l/min)	274.53	337.13	352.77	367.86	394.38	457.33
RVEDV (ml)	18.86	21.23	21.81	22.38	23.37	25.70
Ejection Fraction (%)	0.51	0.51	0.52	0.52	0.52	0.52
Stroke Work (mmHg · ml)	541.91	731.91	782.87	834.24	927.78	1165.80
Systolic PVA (mmHg · ml)	655.06	897.40	962.98	1029.54	1151.47	1464.83
Mechanical Efficiency (%)	82.73	81.56	81.30	81.03	80.57	79.59



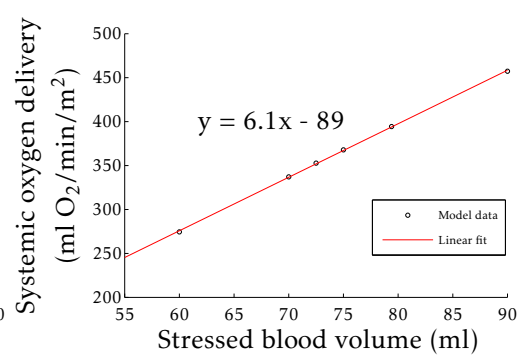
(a) Cardiac Output



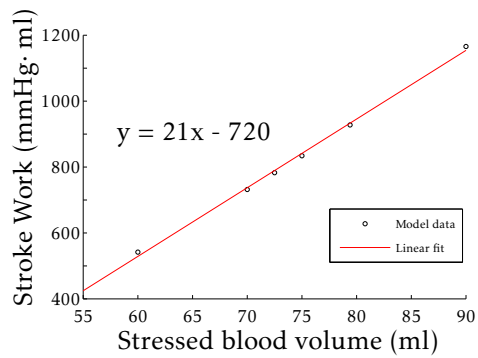
(b) Pulmonary-to-Systemic Flow Ratio



(c) Systemic Flow



(d) Systemic Oxygen Delivery



(e) Stroke Work

FIGURE 7.18: Analysis of linearity of haemodynamical outcomes as total stressed blood volume is varied

TABLE 7.5: Analysis of linearity of outcomes with respect to total stressed blood volume

Outcome	Gradient	Intercept	Pearson's Correlation r
Systolic MPA Pressure (mmHg)	1.06	-6.09	1.00
Diastolic MPA Pressure (mmHg)	0.65	-4.92	1.00
Mean MPA Pressure (mmHg)	0.78	-3.52	1.00
Systolic Systemic Pressure (mmHg)	0.81	-0.04	1.00
Diastolic Systemic Pressure (mmHg)	0.64	-4.13	1.00
Mean Systemic Pressure (mmHg)	0.72	-2.31	1.00
Systolic Left Pulmonary Pressure (mmHg)	0.14	3.26	1.00
Diastolic Left Pulmonary Pressure (mmHg)	0.13	2.73	1.00
Mean Left Pulmonary Pressure (mmHg)	0.14	2.91	1.00
Systolic Right Pulmonary Pressure (mmHg)	0.17	3.23	1.00
Diastolic Right Pulmonary Pressure (mmHg)	0.16	2.60	1.00
Mean Right Pulmonary Pressure (mmHg)	0.16	2.83	1.00
Cardiac Output (l/min)	0.02	0.37	1.00
Left Pulmonary Flow (l/min)	0.00	0.19	1.00
Right Pulmonary Flow (l/min)	0.01	0.19	1.00
Pulmonary Flow (l/min)	0.01	0.39	1.00
Systemic Flow (l/min)	0.01	-0.02	1.00
Pulmonary-Systemic Flow Ratio	-0.01	2.02	-0.99
Stent Backflow (l/min)	-0.01	-0.27	-1.00
Arterial Oxygen Saturation (%)	0.22	55.79	0.99
Venous Oxygen Saturation (%)	0.74	-20.46	0.99
Systemic Oxygen Delivery (l/min)	6.09	-89.47	1.00
Total Stressed Blood Volume (ml)	1.00	0.00	1.00
RVEDV (ml)	0.23	5.26	1.00
Stroke Work (mmHg · ml)	20.84	-721.48	1.00
Systolic PVA (mmHg · ml)	27.06	-988.43	1.00
Mechanical Efficiency (%)	-0.10	88.91	-1.00

is no identified definition or protocol to vary V_T other than that described in Chapter 5. Identifying an appropriate value (or range of values) from clinical measurements or determining how this parameter can validly be adjusted as the hybrid (or other procedures modelled using this methodology) configuration changes are two of many challenges that can not be neglected for this exciting conceptual work to gain clinical acceptance and therefore produce clinical impact.

For further comment on the significance of this parameter, please refer back to Section 5.3.2.

Figure 7.19 shows the effect of continually increasing V_T on the pressure-volume loop. As the total stressed blood volume is increased the area expands and shifts upwards and to the right. This could perhaps suggest considering the total stressed blood volume input as being defined partially upon cardiac function, however many avenues are yet to be explored.

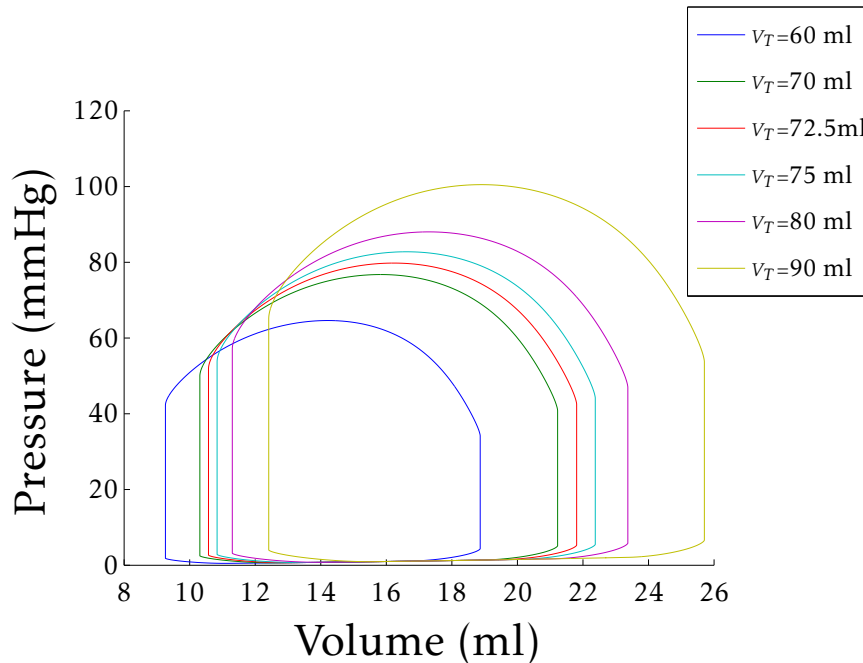


FIGURE 7.19: Pressure-Volume loops for varying total stressed blood volume with 2 mm geometry

TABLE 7.6: Equivalent external band diameter of lumped circulation model to match mean MPA pressure and cardiac output of each banding geometry

3D Diameter	0D Diameter to matching cardiac output	0D Diameter to matching MPA pressure
1.5 mm	2.67 mm	2.97 mm
2.0 mm	3.10 mm	3.40 mm
2.5 mm	3.47 mm	3.81 mm
3.0 mm	4.05 mm	4.55 mm
3.5 mm	3.98 mm	4.45 mm
4.0 mm	4.58 mm	5.37 mm
default	2.83 mm	2.92 mm

7.3.3 Zero Dimensional vs. Multiscale Modelling

The final analysis carried out was in comparing the stand alone LCM to the coupled multiscale model. The diameter of the stented ductus arteriosus of the three dimensional region was measured at 10 mm and this input was matched. Likewise the total stressed blood volume was fixed at 72.5 ml as in Section 7.3.1. The Method of False Position was adopted again, this time determining the input external band diameter (d) that matched both the mean MPA pressure and the cardiac output from the multiscale model.

Table 7.6 shows the equivalent external band diameter determined by the 0D model to match the mean MPA pressure and cardiac output of each simulated 3D geometry with known internal band diameter. The first comment is that in order to match the mean MPA pressure, a wider band was required with an increase of approximately 0.3 mm for the smaller bandings up to approximately 0.8 mm for the 4 mm band. The dimensional results, however, match anticipated observations well. The optimal internal banding diameter of 2 mm from the multiscale modelling match an external banding diameter of

between 3 and 3.5 mm, correlating well with clinical experience. Likewise, the acceptable performance from the 1.5 and 2.5 mm internal diameters matches up with ranges of 2.5 to 3 mm and 3.5 to 4 mm respectively.

This is a critical distinction regarding clinical interpretation. The findings of Young *et al.* [144], as discussed in Chapter 5, of a 3 mm optimal banding appear to disagree with the 2 mm banding suggested by the multiscale approach. This analysis clarifies that the two conclusions are effectively the same, with the loss of luminal area assumed to be a consequence of vessel wall thickness and redistribution. It is vital that the internal banding diameters of the three dimensional geometries are not mistakenly represented as the external banding diameter applied to a patient. Applying an external band of 1.5 to 2 mm diameter may result in complete pulmonary obstruction. It is cross-disciplinary issues such as this definition that this work has contributed to this particular field of research, focusing strongly on integrating the biomedical engineering theory with clinical protocols.

Table 7.7 directly compares the clinical outcomes of the fully coupled multiscale model and the stand alone lumped circulation model for both matched results. The matched mean MPA pressure of the LCM resulted in an increase in pulmonary pressures, stroke work, cardiac output, pulmonary perfusion (and consequentially $Q_p : Q_s$) and decrease in stent backflow and mechanical efficiency compared with the 2 mm multiscale model. The matched cardiac output also had reduced mechanical efficiency and stent backflow, however the pulmonary-systemic flow ratio decreased as a result of the increase in systemic and decrease in pulmonary perfusion. There was also a marked increase in MPA pressures. Both matched configurations had noticeably higher systemic systolic pressures, most likely a consequence of the artificial boundary of the multiscale model versus the generic compliant chamber of the LCM. Additionally, both matched configurations improved the systemic oxygen delivery from 347.88 to 369.36 and 369.91 ml O_2 /min/ m^2 respectively.

TABLE 7.7: Haemodynamical outcomes of fully coupled multiscale model versus the matched stand along lumped circulation models for matched mean MPA and cardiac output using the 2mm geometry

	Coupled Model	0D Model matching Mean MPA Pressure	0D Model Matching Cardiac Output
Band Diameter (mm)	2.00	3.40	3.10
Systolic MPA Pressure (mmHg)	71.04	77.86	80.31
Diastolic MPA Pressure (mmHg)	42.42	40.25	44.55
Mean MPA Pressure (mmHg)	53.41	53.41	57.08
Systolic Systemic Pressure (mmHg)	58.80	73.24	75.98
Diastolic Systemic Pressure (mmHg)	42.53	40.31	44.60
Mean Systemic Pressure (mmHg)	50.31	52.73	56.43
Systolic Pulmonary Pressure (mmHg)	14.50	17.68	14.40
Diastolic Pulmonary Pressure (mmHg)	13.17	14.37	12.08
Mean Pulmonary Pressure (mmHg)	13.91	16.10	13.29
Cardiac Output (l/min)	1.80	1.98	1.80
Pulmonary Flow (l/min)	1.07	1.24	1.00
Systemic Flow (l/min)	0.73	0.74	0.79
Pulmonary-Systemic Flow Ratio	1.47	1.68	1.27
Stent Backflow (l/min)	-0.64	-0.55	-0.45
Arterial Oxygen Saturation (%)	72.22	75.77	70.54
Venous Oxygen Saturation (%)	34.35	38.32	35.76
Systemic Oxygen Delivery (ml O₂/min/m²)	352.77	374.30	375.23
Total Stressed Blood Volume (ml)	72.50	72.50	72.50
Right Ventricle End Diastolic Volume (ml)	21.81	23.62	22.99
Stroke Work (ml · mmHg)	782.87	833.78	791.44
Systolic Pressure-Volume Area (ml · mmHg)	962.98	1057.87	1045.77
Mechanical Efficiency (%)	81.30	78.82	75.68

7.4 Patient-Specific vs. Generalised Geometry

We now consider the assertion made earlier that the patient-specific model presented in this thesis correlates well with published generic Hybrid geometries from the Modelling Of Congenital Hearts Alliance (MOCHA) [83, 84, 127]. In comparing the results of the patient-specific Hybrid modelling with these articles, key conclusions regarding the coupled multiscale modelling methodology are made highlighting conclusions with potentially critical implications within this field of research.

7.4.1 Comparison of Geometrical Data

Table 7.8 reproduces Table 1 from Baker *et al.* [84] using a generic Hybrid geometry. Additionally, the difference between the results published and the equivalent outcomes from the corresponding patient-specific geometries are given (see Table 7.3 for full results). The data used for comparison is that produced by using the specified geometries with the total stressed blood volume maintained at $V_T=72.5$ ml.

Figure 7.20 directly contrasts the idealised geometry (taken from Corsini *et al.* [83]) with the strikingly different patient-specific geometry constructed within this project. Although the orientations differ, and the generalised geometry incorporates the post-stent aortic anatomy as well as extended branch pulmonary arteries, the natural shape of the pulmonary trunk (inclusive of the stented ductus arteriosus) is distinctively different. Referring back to Figure 6.6, it is clear that the patient-specific geometry represents the anatomy for this specific patient well. Both images in Figure 7.20 represent the pathlines during systole for the 1.5 mm internal pulmonary artery banding diameter geometries.

Firstly, it should be noted that in the data presented by Baker *et al.* an oxygen consumption rate of 156.83 ml O_2 /min/m² is used [84]. Therefore for a

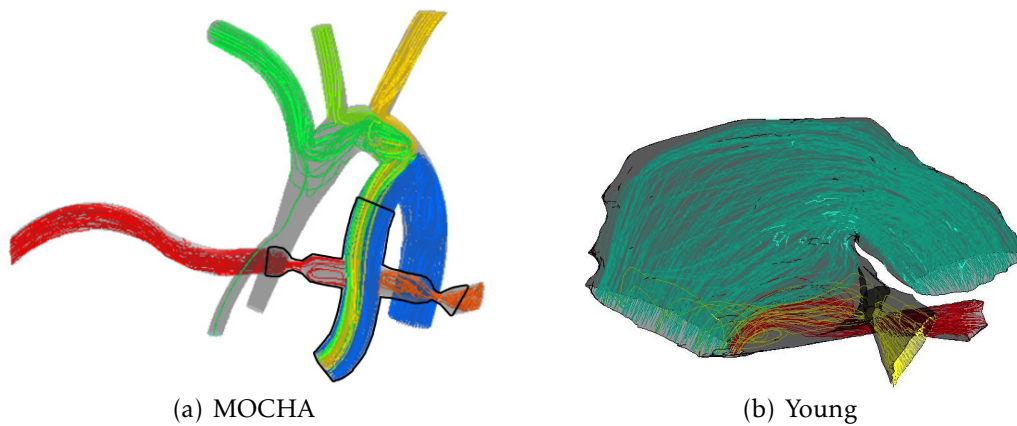


FIGURE 7.20: Comparison of published generic Hybrid geometry from the MOCHA collaborators [83] and patient-specific Hybrid geometry constructed for this study

valid comparison, this value was adjusted from the $185 \text{ ml O}_2/\text{min}/\text{m}^2$ used elsewhere in the present study and other publications [86, 150]. Analysing the table, good correlation with the presented results is observed with two noticeable exceptions: Stroke work and systemic oxygen delivery. As the discrepancy in the stroke work was so significant, and approximately two orders of magnitude greater than other differences, it was excluded from the calculation of the sum of all differences squared given as the final row of Table 7.8. As is readily seen, the difference in systemic oxygen delivery accounts for the majority of the remaining sum of squared errors (s.s.e.), this also becomes less pronounced as the band diameter is increased.

The majority of outcomes presented provide plausible and comparable values with the exception of those stated above. The mean pulmonary artery pressure in the patient-specific model (cited as Young) is negligible ranging between 2.48 and 0.45 mmHg greater than that presented by the MOCHA collaborators. However, the cardiac outputs published from the generic geometry modelling is between 0.25 and 0.47 l/min less in the present results. This is significant when the discrepancy in stroke work is discussed in the subsequent section.

TABLE 7.8: Comparison of MOCHA geometrical band diameter variation with idealised geometry and patient-specific geometry as presented in this research

	d=1.5 mm			d=2 mm			d=2.5 mm			d=3 mm			d=3.5 mm			
	Baker	Baker - Young	Baker	Baker - Young	Baker	Baker - Young	Baker	Baker - Young	Baker	Baker - Young	Baker	Baker - Young	Baker	Baker - Young	Baker	Baker - Young
Mean PA pressure (mmHg)	8.80	-1.09	13.30	-0.61	16.70	-0.72	19.60	-2.48	21.10	-0.45						
Pulmonary Flow (l/min)	0.70	-0.02	1.24	0.17	1.65	0.28	2.00	0.23	2.18	0.45						
Pulmonary-Systemic flow ratio	0.70	-0.18	1.40	-0.07	2.20	0.08	3.20	-0.07	3.80	0.68						
Cardiac Output (l/min)	1.79	0.25	2.14	0.34	2.40	0.38	2.62	0.30	2.75	0.47						
Ejection Fraction (%)	39.30	-6.90	46.10	-5.41	50.90	-4.91	55.00	-6.20	57.60	-3.01						
Mechanical Efficiency (%)	60	-16.3	67	-14.3	72	-13.0	76	-13.2	79	-9.8						
Stroke work (ml · mmHg)	1913.50	1210.13	2187.60	1404.73	2358.30	1515.56	3486.70	2579.45	2554.70	1653.97						
Arterial Oxygen Saturation (%)	43.40	6.25	53.10	9.06	52.60	7.76	48.80	7.03	46.40	4.09						
Venous Oxygen Saturation (%)	64.80	-0.76	79.20	3.05	83.80	2.83	86.30	1.48	87.30	2.82						
Systemic Oxygen Delivery (ml O ₂ /min/m ²)	471.20	109.34	475.20	103.26	421.70	70.21	361.20	52.21	335.20	21.03						
Summed Squared Difference		109.75		103.85		70.87		53.13		21.84						

TABLE 7.9: Comparison of MOCHA 2 mm idealised geometry and 2 mm patient-specific geometry for varying total stressed blood volumes

	Baker	Baker - Young $V_T=60$ ml	Baker - Young $V_T=75$ ml	Baker - Young $V_T=90$ ml
Mean PA pressure (mmHg)	13.30	1.35	-0.99	-3.21
Pulmonary perfusion (l/min)	1.24	0.30	0.15	0.02
Pulmonary-Systemic flow ratio	1.40	-0.18	-0.05	0.04
Cardiac output (l/min)	2.14	0.60	0.29	0.01
Ejection fraction	46.10	-4.81	-5.47	-5.61
Mechanical efficiency (%)	67	-15.7	-14.0	-12.6
Stroke work (ml · mmHg)	2187.60	1645.69	1353.36	1021.80
Arterial oxygen saturation (%)	53.10	19.18	7.51	0.08
Venous oxygen saturation (%)	79.20	6.03	2.58	0.30
Systemic oxygen delivery (ml O ₂ /min/m ²)	475.20	182.86	87.94	-2.91
Summed squared difference		184.03	88.47	7.10

7.4.2 Comparison of Methodologies

As alluded to earlier, there is no clear methodology presented by the MOCHA collaboration group in their previous publications with regards to the definition of the crucial initial conditions [81, 82, 84, 85]. This issue, addressed through the discussion of total stressed blood volume has been considered and transparently presented by Shimizu *et al.* in a lumped circulation model [86] and consequentially adopted in the present work [144].

Given the analysis of varying total stressed blood volume for the 2 mm patient-specific geometry in Section 7.3.2, it was decided to compare the published data of the 2 mm idealised geometry with the patient-specific 2 mm geometry while varying V_T . These results are presented in Table 7.9 for a subset of total stressed blood volumes simulated ($V_T = \{60, 75, 90\}$). As for the geometric comparison, the full haemodynamical results of varying the total stressed blood volume are presented in Table 7.4.

The results of this comparison clearly suggest that near identical results can be obtained from the equivalent patient-specific geometry solely by increasing V_T . By excluding the difference in stroke work (as above), the sum of squared

error is significantly reduced when V_T is increased from 60 ml (s.s.e.=184.03) to 90 ml (s.s.e.=7.10) demonstrating the ability to greatly alter the clinical findings of identical geometries through adjustment of this single parameter. As the outcomes follow a strong linear relationship (see Section 7.3.2) there is nothing to prevent varying this parameter to suit the desired outcome. It is this reason that this parameter *must* be clearly defined, or at least the methodology adopted clearly defined, when considering any work of this nature.

7.4.3 Stroke Work Discrepancy

Aside from the lack of clarity regarding the specification of initial conditions (addressed in this work through the parameter of total stressed blood volume V_T), the value of stroke work required for the Hybrid configurations as presented by MOCHA raise serious concerns.

The values presented for the final coupled multiscale patient-specific geometry model in this chapter correlate well with those found for the lumped circulation model presented here and published elsewhere [144] as discussed in Section 7.3.3. Also, this study's determination of stroke work for the Norwood variants as presented by Shimizu *et al.*[86] were validated (see Section 5.3.1) and found comparable with the adaptation representing the post-Hybrid Procedure circulation (see Section 5.3.3).

Upon additional investigations, the physiological validity of the generic Hybrid models published by MOCHA require further considerations. In all Hybrid related MOCHA publications, limited haemodynamical data is presented, specifically no systemic pressures are presented. The closest observed data relating to determining the validity of the stroke work of the Hybrid simulations is Figure 3 from Hsia *et al.* [127], reproduced here in Figure 7.21.

From Figure 7.21 we see that the peak systolic pressure in the single ventricle reaches 160 mmHg. From observed clinical data (see Chapter 4), clinical experience, and a stringent literature search for published systolic systemic

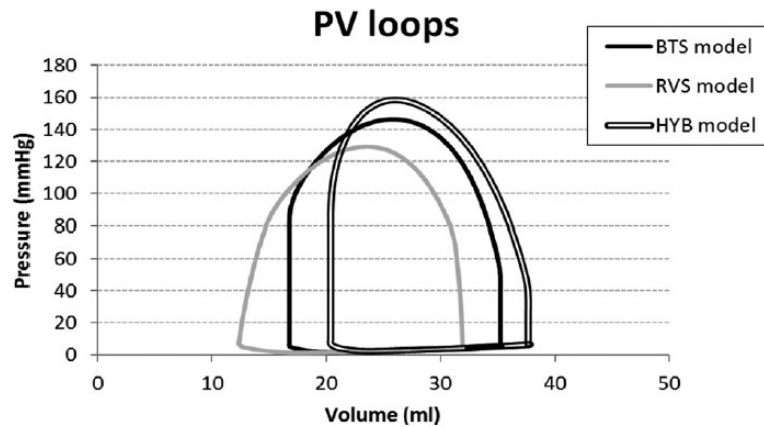


FIGURE 7.21: Figure 3 from Hsia *et al.* showing pressure-volume loop for mBT shunt (BTS), Sano shunt (RVS) and Hybrid (HYB) repairs [127]

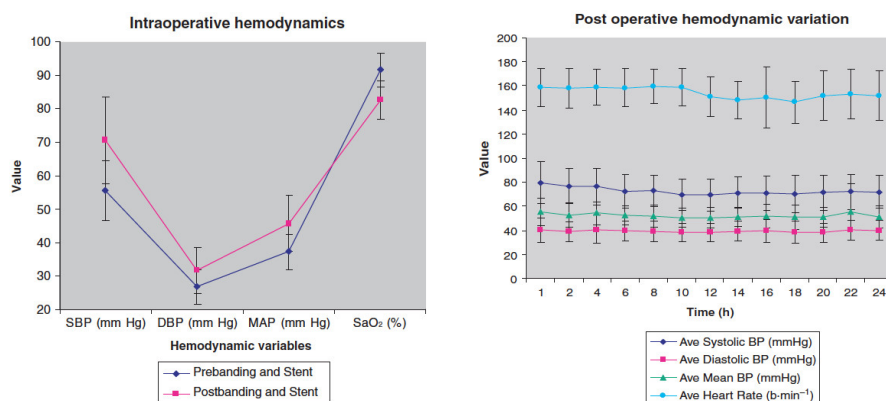
pressures following the hybrid procedure it was concluded that this value is unphysiological.

The highest ventricular pressure from the catheterisation data gathered from the same patient from which the geometry was constructed is under 100 mmHg. From an extensive review of the clinical literature, the highest (mean) systemic systolic pressure following the Hybrid Procedure was 76 mmHg (with a published range of 60-92 mmHg) [147]. Table 7.10 displays the systemic systolic pressure data from four publications in addition to the patient-specific clinical data gathered both before and after the procedure. Figure 7.22 shows graphs taken from Naguib *et al.* [159] and Honjo and Caldarone [160], which displays similar results, and while no numbers were quoted, the relevant graphs showing the outcomes of interest can be readily interpreted.

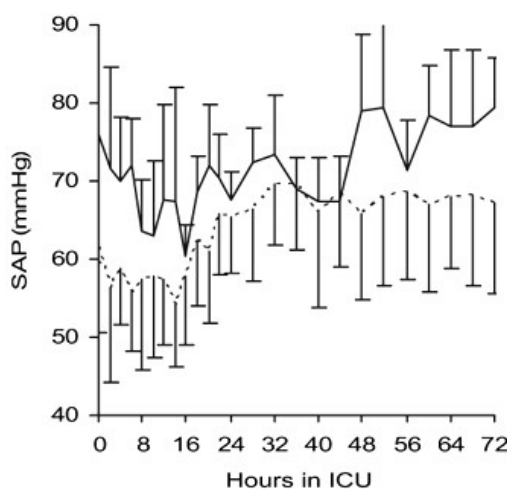
The peak systolic ventricular pressures, as well as systemic arterial pressures, from the results presented in this thesis clearly match the published clinical data observed in Table 7.10. The outcomes suggested by the solitary pressure-volume loop presented by Hsia *et al.* in conjunction with the grossly elevated stroke work values raise serious questions regarding their clinical validity. The fact that other haemodynamical outcomes are physiologically realistic raises additional concerns over the methodology adopted. Therefore it is imperative, for this approach of modelling to be of benefit to clinical practice,

TABLE 7.10: Review of clinical publications presenting systolic systemic pressures for Hybrid patients. Pressures presented as mean \pm standard deviation or indicative values

Authors	Pressure Source Reference	Pre-Hybrid/Intraoperative Pressure (mmHg)	Post-Hybrid Pressure (mmHg)
Li <i>et al.</i> [147]	Systemic Arterial Pressure	56 \pm 3	76 \pm 16
Koziol <i>et al.</i> [161]	Arterial Blood Pressure	65 \pm 12.7	69 \pm 13.7
Naguib <i>et al.</i> [159]	Systemic Blood Pressure	< 72 mmHg See Figure 7.22(a)	< 80 mmHg See Figure 7.22(a)
Honjo <i>et al.</i> [160]	Systemic Arterial Pressure		< 80 mmHg See Figure 7.22(b)
Yorkhill Hybrid Specific Patient	Right Ventricular Pressure		< 91 mmHg



(a) Naguib *et al.* [159]



(b) Honjo and Caldarone [160]

FIGURE 7.22: Systolic systemic pressure data from the literature

that the methodology adopted for initial conditions, or alternatively a practical definition of total stressed blood volume, is clearly justified and defined.

Given that intra-operative hypotension is a common concern in hybrid patients [161], the suspicion surrounding the Hybrid simulation results presented by MOCHA is justified. Looking at the pressure-volume loop for the 2 mm Hybrid simulation in Figure 7.21 it is clear to see why there is such a large discrepancy between the MOCHA results in contrast to the results presented in this thesis. The stroke work outcome in this study was determined using the *polyarea* function in Matlab using the ventricular pressure and volume vector output from the model as seen in Appendix D and is therefore presented with confidence in its reliability.

7.5 Summary

The work presented in this chapter signifies an important step in integrating established methods in multiscale modelling with clinically derived patient-specificity. In adopting a patient-specific geometry it has been demonstrated that sliced medical imaging can be used to test hypothetical test surgical configurations by altering the patient-specific geometry in a virtual surgery approach.

In simulating increasing band diameter it was shown, as was anticipated from clinical experience, certain haemodynamical trends existed. In increasing the band diameter the pulmonary perfusion increased while the systemic perfusion decreased mainly due to greater diastolic backflow through the stent for larger bands. Consequentially the $Q_p : Q_s$ ratio increased as did the stroke work, although it resulted in greater mechanical efficiency. The diastolic MPA pressure also notably dropped with wider banding raising concerns over coronary perfusion in this situation. One of the key outcomes of interest was the systemic oxygen delivery, which was improved from 1.5 to 2 mm internal banding, but decreased as the band diameter was increased above 2 mm.

Given the optimal systemic oxygen delivery as well as factoring other key outcomes such as pulmonary-systemic flow ratio, systemic pressures and mechanical efficiency, the 2 mm banding geometry resulted in the best haemodynamical and ventricular performance. The systemic oxygen delivery was 352.77 ml O₂/min/m², with a cardiac output of 1.8 l/min and a $Q_p : Q_s$ of 1.47. This conclusion correlates well with other studies of generic anatomies published in the literature [83, 84, 127].

The total stressed blood volume, a key input parameter in executing any simulation was transparently investigated. It was felt that this parameter had failed to be properly identified and discussed and as yet, has no clinical interpretation or means for defining an appropriate value. It was observed that most outcomes follow a strong linear trend and increase as V_T is increased. It is imperative, for clinically meaningful studies and for future simulations to have patient-specific clinical impact, that this parameter is better understood and defined. This has been highlighted further by certain unphysiological results published in the literature, while no method of defining initial conditions has been formally presented.

The internal diameter simulated in the multiscale approach is often quoted as the banding diameter. However, clinically speaking, a banding diameter would refer to an external banding. This distinction is vital in interpreting the results of computational simulations and could lead to confusion for clinicians, who would know that a 2 mm band is too tight. In comparing the zero-dimensional model with the multiscale model, we demonstrated that there is good correlation between the sets of results. The external banding diameters required for good performance of the Hybrid determined by the multiscale model (internal banding diameters of 1.5 to 2.5 mm) fall within the current common clinical range of diameters (2.5 to 4 mm).

One issue identified with the methodology adopted, given the high pressure pulsatility of a pseudo-systemic circuit, is that the assumption of rigid walls results in wave reflection generated oscillations. This did not have any

obvious impact on the clinical outcomes of the analysis. However, to truly gauge the energy efficiencies of the circuit, future work needs to determine how influential these effects are by modelling the fluid-structure interactions (FSI). This would potentially improve the efficiency calculations by accounting for the stored energy in the distending of the arteries which help absorb the pulsatility of the blood supply and transform it to steady flow, similar to the Windkessel analogy. The increase of complexity in modelling FSI is marked, therefore it is important to determine whether the simplification of rigid walls is suitably accurate or not. This would also open the door to determining the effect of a rigid band and/or stent within an elastic wall model.

Chapter 8

Discussion, Limitations and Future Work

In this thesis, the goal of patient-specific modelling of the Hybrid Procedure for the treatment of Hypoplastic Left Heart Syndrome has been addressed. This has incorporated a wide area of interest including lumped circulation modelling, three dimensional computational fluid dynamical modelling, coupled multiscale modelling. Significantly, the format and quality of the available clinical data has also been assessed.

In addition to the discussion and summaries throughout the body of this work, specifically the conclusions of each chapter, this chapter reflects on those outcomes. The original objectives are used to lead the concluding discussions of this research throughout the present chapter.

The interconnected nature of the various elements of the research throughout this project is presented in the flow chart in Figure 8.1.

8.1 Clinical Data and Patient-Specific Modelling

- *Assess the available clinical data and applicability for use in patient-specific modelling of the Hybrid Procedure.*

The first objective of this research (see Chapter 1) was to assess what medical data was available with which to generate patient-specific mathematical mod-

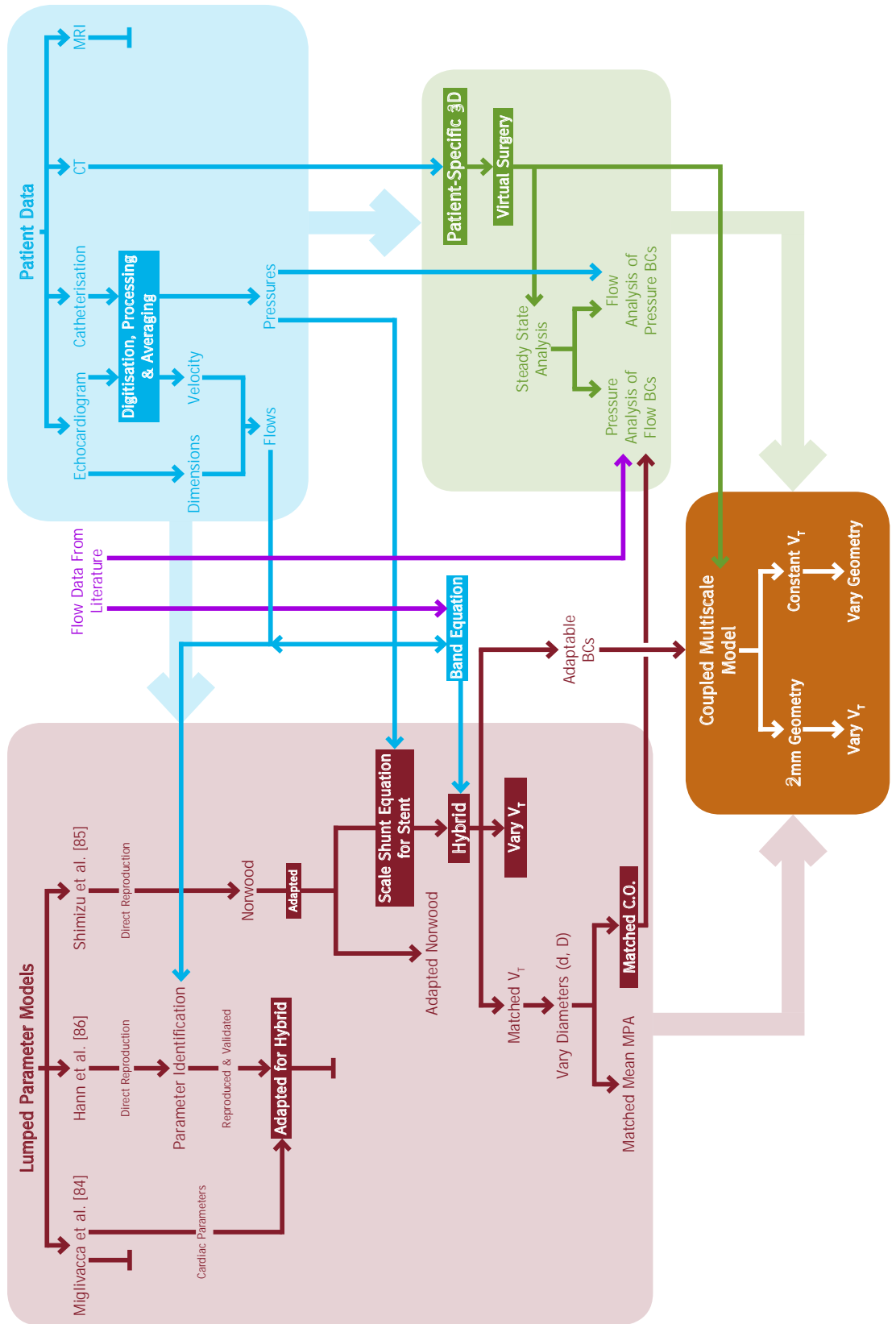


FIGURE 8.1: Flow chart outlining the work undertaken throughout the investigation of mathematical modelling of the Hybrid Procedure for the treatment of hypoplastic left heart syndrome

els of the Hybrid Procedure. After a significant investigation on location at the Royal Hospital for Sick Children, Yorkhill, Glasgow, there were many conclusions including the usability of Doppler ultrasound for velocity measurements and the superfluous digitisation steps that were required for this study.

Chapters 4 and 6 outlined the available clinical data, and many of the limitations and obstacles found in using data from routine clinical practice. What was apparent throughout this research, is that there is a mismatch in priority of the form of data collected for clinical and modelling/engineering purposes. The raw data, although often digitised at source, was not available in that format, which resulted in the labourious digitisation process outlined in Section 4.4. It is recommended for future research, that this information be stored digitally ready for use in modelling or other forms of analysis. Automatic averaging capabilities would also be recommended, with a convention set as to whether normalised or absolute time averaging methods are used.

In looking at time averaging techniques, and integrating this data with other available clinical scans (e.g. echocardiograms, CT and MRI) that there was sometimes significant disparities in the haemodynamical state of the patient. This is illustrated in Figure 4.12(a) where the profiles are coloured by heart rate and the scaled velocities (approximated from echocardiogram data) are substantially different from that of the pressure data. There is even a disparity observed within the available pressure data observed in Figure 4.12(b).

The recommendation following this investigation would be to have a more consistent and complete collection of haemodynamical data as close as possible to being simultaneous. This would include imaging, flow and pressure data.

The quality and consistency of data collected in current clinical practice, although appropriate for diagnostic purposes, is difficult for use in the types of patient-specific modelling investigated in this study. It is of utmost importance not to expose the patient to any unnecessary risk, however by stronger collaboration between cardiac surgeons, cardiologists, echocardiographers, anaes-

thetists, radiologists, biomedical engineers and administrators this ideal approach is possible. The complexity of HLHS is highlighted by the sheer number of different specialists involved, especially when factoring in potential predictive modelling.

8.2 Reproduction of Literature Models and Creation of Hybrid Model

- *Reproduce relevant mathematical models from the literature and construct equivalent models for the Hybrid Procedure.*

The second objective was achieved in the latter stages of the present work. Significant effort was expended in attempting to reproduce the LCM Norwood model published by Migliavacca *et al.* [85] which was later coupled to an idealised 3D geometry in a multiscale model [82]. However, due to a lack of transparency with what was later identified as the initial conditions, this model was not successfully reproduced. This incomplete transparency was also the case with related models representing the foetal and univentricular circulation models by the same authors [88, 89].

Following this setback, an adult model first published by Smith *et al.* was successfully reproduced [137]. This model was selected due to the later work involving the identification of patient-specific parameters, which will be discussed in the next section [87].

The publication of the Norwood model by Shimizu *et al.* [86] which was a simplified adaptation of the Migliavacca model that included initial conditions, was successfully reproduced. Validation of the results was presented in Section 5.3.1. This was used as a foundation for modelling the post-Hybrid circulation for different diameters of ductal stenting and PAB.

A successful model of the post-Hybrid Procedure circulation was produced following two novel steps. The first was to use an empirically derived equation

for synthetic shunt flow (via 3D CFD [5]) and scale the diameter to match the clinically observed pressure drop across the ductus as seen in Equation (5.13). This was achieved simulating the model with the same banding diameter as stated in the clinical case notes (3 mm for the specific patient used throughout this study - see Section 5.2.2) and matching the stent diameter to the relevant clinical pressure data as seen in Figure 8.1.

The second novel step was to construct an equation for pulmonary artery banding resistance that varied with the diameter. A Poiseuille relationship, as observed in the stent/shunt flow equation, was adopted. This relationship was used to scale a reference PAB resistance which was constructed from the acquired pressure data and the use of typical flow values published in the literature. The value of reference banding resistance was found to be 3 mmHg · s/ml and the banding resistance was determined using Equation (5.15). These critical steps in the construction of this unique lumped circulation model of the post-Hybrid circulation are discussed in full in Section 5.2.2 [144, 162].

Additionally there was the unique analysis of comparing configurations at a defined cardiac output (see Section 5.3.2). This allowed a comparison of various bandings at a fixed cardiac supply, and the opportunity to assess a fixed configuration (stent and band diameters) at various levels of cardiac output. It was observed that the trends in varying the band diameter at a fixed cardiac output were similar to those when maintaining the mean MPA pressure, the method of comparison adopted from the literature. It was also concluded that when varying the controlled cardiac output, that the model supported the current clinical practice of using the tighter banding of 3 mm for small to medium sized patients and a larger 3.5 mm band diameter for larger patients. This is adopting a linear relationship between cardiac output and body surface area/birth weight.

The final unique analysis undertaken on the LCM was of varying the total stressed blood volume. This showed that the haemodynamical outcomes

could be controlled by varying the initial conditions. It is essential that this parameter has greater clinical relevance and understanding.

The next step in creating a multiscale patient-specific Hybrid model was the construction of patient-specific 3D geometry of a Hybrid repair and a steady state CFD analysis. The geometry was generated using the clinically available CT scans and despite the issues in using clinical data outlined in Chapter 6 and reinforced in the previous section, an accurate representation of the Hybrid anatomy, as validated by an expert radiologist, was constructed. Again, the patient data collected through routine clinical practice was used to determine suitable boundary conditions for pressure, and typical flow values adopted guided by available data in the literature. The geometry was adapted in a virtual surgery allowing an analysis of varying PAB diameters.

Finally, a multiscale Hybrid model with the patient-specific geometry was constructed. Band diameter and total stressed blood volume variation were analysed. The results of band diameter variation demonstrated that the 2 mm internal band diameter was the optimal configuration, providing the greatest systemic oxygen delivery at the lowest ventricular demand. This correlated well with an idealised Hybrid geometry published in the literature [83, 84, 127]. However, this research highlighted a point of interest regarding the published ventricular workload and systolic systemic pressures and was outlined in great detail in Section 7.4. The novel analysis of varying total stressed blood volume again highlighted the dependency of the results on this parameter, emphasising the need for stricter clinically based protocols in the definition of initial conditions. This is a vital area of investigation for future work in this field of research.

8.3 Fully Patient-Specific Models

- *Implement full patient specificity for all aspects of mathematical models produced (lumped parameters and geometrical representation of the surgical region).*

The third thesis objective was partially met. Unfortunately, mainly due to the disjointed clinical data available, patient-specific lumped parameters were not successfully identified. It was with this goal in mind that the work by Smith and Hann *et al.* was reproduced [87, 137]. The model was adapted for the Hybrid Procedure, cardiac parameters identified from the literature, and parameter identification using the patient-specific data was attempted. Due to the issues of disjointed data, ambiguous location labelling and no clear method of standardising processing of the data, the output included unphysiological negative values.

A key objective for the future is for full patient specificity for all parameters used. The same modelling group discussed presently have publications, based on porcine data, identifying cardiac parameters [92], that look promising in terms of achieving specificity. What is required is greater collaboration between biomedical engineers and clinical partners. One proposal would be to have a consistent protocol to measure pressure profiles at specific and consistent points of the cardiovascular tree which would then be the location of the pseudo-compartments in the electric analogy. If this could be coordinated with other procedures that would gather flow and geometrical imaging data at the same time, or as close as possible to an identical haemodynamic state, then patient-specific parameter identification may be closer than it currently is.

In order for this approach to be facilitated, and adopted as routine clinical practice, a comprehensive cost-benefit analysis would be required. This should assess both the health and economical impact of obtaining all the relevant clinical data at the beginning of the treatment planning, and the benefit of being able to predict the best outcome for the patient. The predictive capabilities of models will be discussed in the following section.

This research was successful in reproducing a patient-specific geometry. However, the quality of the scan data was restrictive, as was the incomplete set of available data needed for full patient specificity. As medical imaging improves so will the 3D geometry generation. The next step for the future would

be to implement fluid-structure interactions with suitable patient-specific parameters to define the elastic qualities of the vascular walls.

8.4 Predictive Modelling

- *Assess the predictive capabilities of patient-specific modelling by comparing the predictions of the modelled post-surgical data built from pre-surgical data, with the actually observed clinical outcomes.*

Unfortunately this objective was not achieved. This was ultimately due to lack of coordinated data, and would require the collaboration and procedural change outlined in the previous section. What is unclear is how any pre-surgical parameters would alter post-repair and therefore a blinded trial would be necessary. This would compare a fully patient-specific post-procedure model that would be validated to observed clinical outcome, with a predictive model based on pre-procedure imaging and data.

This is an exciting prospect, with additional scope to model long-term growth, and so with longer term observation, it could be possible to optimise the repair for not just the short or medium term. Currently there are too many questions related to growth and factors that have not been accounted for such as autonomic feedback, or the physical growth of structures as considered by Figueroa *et al.* [131].

8.5 Key Outcomes

The key outcomes and conclusions of this research are summarised below:

- Routine clinical data is not currently suitable for use in patient-specific cardiac modelling for the applications adopted in this research
- A new use of an equation for flow through a shunt was adapted to describe ductal stent flow

- Clinical data was used in the derivation of an equation for pulmonary artery banding resistance that varied with the diameter
- A lumped circulation model of the Hybrid Procedure was successfully generated and published [144]
- A patient-specific geometry was successfully constructed and adapted to mimic virtual surgery
- A coupled multiscale model of the Hybrid Procedure was successfully created combining the LCM and 3D models
- A key distinction between **internal** and **external** banding diameter was made, and assessed comparing LCM and coupled simulations
- The significance of initial conditions or definition of total stressed blood volume is vital for future work
- Improved imaging is necessary for better spatial and temporal resolution in 3D geometry construction
- The optimal configuration for oxygen delivery and ventricular demands is an internal band of 2 mm which corresponds to an external band of 3 mm
- Multidisciplinary cooperation is essential for future work, particularly for patient-specific and predictive modelling

Appendix A

Additional Mathematical Comments

A.1 One Dimensional Models

Starting with the full Navier-Stokes equations, certain assumptions can be made which result in the simplification of the equations that result in the one dimensional model.

The Navier-Stokes equations were given in Equation (3.7) and are repeated below:

$$\begin{cases} \rho \frac{\partial \mathbf{u}}{\partial t} + \rho (\mathbf{u} \cdot \nabla) \mathbf{u} - \mu \nabla^2 \mathbf{u} + \nabla P = 0 \\ \nabla \cdot \mathbf{u} = 0 \end{cases} \quad (\text{A.1})$$

The first step is to consider the geometry of the vasculature in cylindrical polar coordinates, which is a reasonable first approximation. This replaces the Cartesian x and y components and describes that plane by the distance from the centre r and the angle of rotation θ from the line of reference ($\theta = 0$), while the axis along the centre of the cylinder z is the as in Cartesian coordinates.

By considering the incompressible axisymmetric Navier-Stokes equations (where there is no tangential velocity and no dependency on θ , Equation A.1 can be written as below [163].

$$\left\{ \begin{array}{l} \rho \left(\frac{\partial u_z}{\partial t} + u_z \frac{\partial u_z}{\partial z} + u_r \frac{\partial u_z}{\partial r} \right) + \frac{\partial p}{\partial z} = \mu \left(\frac{1}{r} \frac{\partial}{\partial r} \left(r \frac{\partial u_z}{\partial r} \right) + \frac{\partial u_z}{\partial t} \right) \\ \frac{\partial u_z}{\partial z} + \frac{1}{r} \frac{\partial (r u_r)}{\partial r} = 0 \end{array} \right. \quad (\text{A.2})$$

By integrating over each cross sectional area of the pipe $A(z, t)$ and introducing some new parameters these equations are then represented by Equation (A.3) over the length of the cylinder from $z = 0$ to $z = l$.

$$\left\{ \begin{array}{l} \frac{\partial A}{\partial t} + \frac{\partial Q}{\partial z} = 0 \\ \frac{\partial Q}{\partial t} + \frac{\partial}{\partial z} \left(\frac{\alpha Q^2}{A} \right) + \frac{A}{\rho} \frac{\partial P}{\partial z} = -K_R \frac{Q}{A} \end{array} \right. \quad (\text{A.3})$$

The parameter K_R is an assumed constant related to the resistance due to viscosity which is dependent on the assumed velocity profile boundary condition. The variable Q is flow as defined in Equation (4.1), and α is the Coriolis coefficient, a momentum-flux correction term, defined below [46, 120].

$$\alpha = A \left(\int_A u_z^2 d\sigma \right) \left(\int_A u_z d\sigma \right)^{-2} \quad (\text{A.4})$$

By assuming a reference area A_0 at rest, a Pressure-Area relationship for the vessel, using the parameter $\beta = \frac{\sqrt{\pi} h E}{(1-\sigma^2)}$ is often used as presented by Milisic and Quarteroni [46]. The constant h , E and σ are the wall thickness, Youngs Modulus and Poisson ratio respectively.

$$P(A) = \frac{\beta}{A_0} \left(\sqrt{A} - \sqrt{A_0} \right) \quad (\text{A.5})$$

Using this relationship and the chain rule for partial differentiation, and defining the mean velocity as $\bar{u} = \frac{Q}{A}$, Equation A.3 can be rewritten as below.

$$\left\{ \begin{array}{l} \frac{\partial P}{\partial t} + \frac{\beta}{2A_0^{3/2}} \frac{\partial Q}{\partial z} = 0 \\ \frac{\partial Q}{\partial t} + 2\alpha\bar{u} \frac{\partial Q}{\partial z} + \left(\frac{A}{\rho} - \alpha\bar{u}^2 \frac{\beta}{2A_0^{3/2}} \right) \frac{\partial P}{\partial z} = -K_R \frac{Q}{A} \end{array} \right. \quad (\text{A.6})$$

By then linearising around A_0 and $\bar{u} = 0$, for small variations in A and u , neglecting the small second order terms of A and u , Equation (A.6) becomes Equation (A.6). This is a reasonable step as it results in the reproduction of most of the essential features of the blood flow for the whole systemic tree.

$$\left\{ \begin{array}{l} \frac{\partial P}{\partial t} + \frac{\beta}{2A_0^{3/2}} \frac{\partial Q}{\partial z} = 0 \\ \frac{\partial Q}{\partial t} + \frac{A_0}{\rho} \frac{\partial P}{\partial z} = -\frac{K_R}{A_0} Q \end{array} \right. \quad (\text{A.7})$$

By setting $C = l \frac{2A_0^{3/2}}{\beta}$, $R = -l \frac{\rho K_R}{A_0^2}$ and $L = l \frac{\rho}{A_0}$, and integrating along the z axis from $z = 0$ to $z = l$ we obtain an identical expression to the 0D governing equations presented in Equations (3.1) and (3.3) when recalling Equation (5.7) for a constant C .

In the cardiovascular system, waves are smooth and propagate rapidly with wave speeds of between 1.5 and 10 m/s. The length of a single ‘tube’ inside the cardiovascular tree can vary between a few millimeters up to 10 cm in an adult. This is even less in the neonate. Thus two inlet and outlet values of the tube can be very close for a sufficiently small time delay, justifying why the averaged quantities are suitable.

By assuming that Equation (A.7) holds for all x along the systemic network, and that it can be replaced by an infinite number of elementary circuits 0D circuits of length δx . Thus it can be proven that as you add more and more 0D

elements, the solution will tend to the 1D model. See Milisic and Quarteroni for the mathematical proof [46].

Thus 1D modelling, versus the lumped 0D modelling adopted in this thesis has the capability of representing wave propagation (and reflection) throughout the cardiovascular tree. Therefore, phenomenon such as wave interference as observed in Section 4.5. The difficulty in using these models would be to define values such as Youngs Modulus, vessel wall thickness, and lengths of segments of the vascular tree, particularly in the case of Hypoplastic Left Heart Syndrome.

Appendix B

Caldicott Guardian Approval



Application for Caldicott Guardian approval for use of patient identifiable data (PID)

Audit / Project Title

Insight into potential computational model of the Hybrid Procedure for patients diagnosed with Hypoplastic Left Heart Syndrome.

Details of individual / organisation requesting data

Internal: Paediatric Cardiology Unit, NHS Greater Glasgow, Yorkhill Division. Medical contact: Mr Mark Danton. e: markdanton@nhs.net

External: Mr. Andrew Young and Prof. Terry Gourlay, University of Strathclyde, Bioengineering, 106 Rotten Row, Wolfson Building, Glasgow G4 0NW. e: andrew.g.young@strath.ac.uk; terry.gourlay@strath.ac.uk t:0141 548 2005; Prof. Sean McKee, University of Strathclyde, Mathematics and Statistics, Livingstone Tower, 26 Richmond Street, Glasgow G1 1XH. e: s.mckee@strath.ac.uk t: 01415483671

Purpose for which data are to be used

Access to relevant patient's data will be used solely to determine what patient records are available so that their applicability, and interpretation for use within a computation model, can be assessed.

Which identifiable data items are required?

Forename Surname DoB Age Sex Address
Post code Clinical Information Other (please provide further details below)

Please justify why each identifiable data item is required

An audit of patient records of patients who have been diagnosed with hypoplastic left heart syndrome is requested so that we may see how best pressure measurements and scans (e.g. echocardiogram, MRI and angiogram) can be used in a potential tool to assist surgical decision making within current diagnostic and treatment procedures.

Who will have access to this information?

Internal: Mr Mark Danton, NHS Greater Glasgow, Yorkhill Division. e: markdanton@nhs.net

External: Mr. Andrew Young and Prof. Terry Gourlay, University of Strathclyde, Bioengineering, 106 Rotten Row, Wolfson Building, Glasgow G4 0NW. e: andrew.g.young@strath.ac.uk; terry.gourlay@strath.ac.uk t:0141 548 2005; Prof. Sean McKee, University of Strathclyde, Mathematics and Statistics, Livingstone Tower, 26 Richmond Street, Glasgow G1 1XH. e: s.mckee@strath.ac.uk t: 01415483671

Storage and use of personal data during the audit/project

Will you be undertaking any of the following activities at any stage (including in the identification of potential participants)? (Tick as appropriate)

- Access to medical records
- Electronic transfer by magnetic or optical media, email or computer networks
- Sharing of personal data with other organisations
- Publication of data that might allow identification of individuals
- Use of audio/visual recording devices
- Storage of personal identifiable data on any of the following:
 - Manual files, including x-rays
 - NHS Computers
 - Home or other personal computers
 - University computer
 - Private company computer
 - Laptop computers

Additional Information:

The Laptop to be used is owned by Strathclyde and is registered to Andrew Young. It is password protected and will only be used for interpretation and analysis of any data. This will be the sole external access point of any data used away from its source. The majority of access to records will be on site at the Paediatric Cardiology Unit, Yorkhill where access of external individuals will be supervised.

Full research ethics submission will be submitted pending the initial audit to determine feasibility.

Please list your organisation's Data Protection Registration Number
(if external to NHSGGC)

Z5964973

Person responsible for the requested data

Name Andrew Young

Job Title Research Student

Signature: *Andrew Young* Date: 11/2/10

Note:

- Please provide copies of any other relevant supporting documentation (e.g. ethics approval, patient information leaflet etc.)
- Appendix A details the Caldicott Principles

The release of data as described above is: **approved / ~~not approved~~** 18/02/10

Caldicott Guardian *A Brown* Date: 18/02/10

Caldicott principles

Principle 1 - Justify the purpose(s)

Every proposed use or transfer of patient-identifiable information within or from an organisation should be clearly defined and scrutinised, with continuing uses regularly reviewed, by an appropriate guardian.

Principle 2 - Don't use patient-identifiable information unless it is absolutely necessary

Patient-identifiable information items should not be used unless there is no alternative.

Principle 3 - Use the minimum necessary patient-identifiable information

Where use of patient-identifiable information is considered to be essential, each individual item of information should be justified with the aim of reducing identifiability.

Principle 4 - Access to patient-identifiable information should be on a strict need-to-know basis

Only those individuals who need access to patient-identifiable information should have access to it, and they should only have access to the information items that they need to see.

Principle 5 - Everyone should be aware of their responsibilities

Action should be taken to ensure that those handling patient-identifiable information - both clinical and non-clinical staff - are made fully aware of their responsibilities and obligations to respect patient confidentiality.

Principle 6 - Understand and comply with the law

Every use of patient-identifiable information must be lawful. Someone in each organisation should be responsible for ensuring that the organisation complies with legal requirements.

Caldicott Guardian for NHS Greater Glasgow & Clyde

Richard Copland
Director of Health, Information & Technology
Greater Glasgow & Clyde NHS Board
Dalian House
P O Box 15329
350 St. Vincent Street
Glasgow G3 8 YZ

All queries in the first instance should be made to:

Isobel Brown, Information Governance Manager
Tel: 0141 211 1790 or E-Mail: isobel.brown@ggc.scot.nhs.uk

Appendix C

Fluent Coupling Code

```
#include 'udf.h'
#include 'stdio.h'
#include 'myfuncs.h' /* Include Functions: heaviside ,square ,activeV ,activeA */

/* PARAMETER DEFINITION */
#define rho 1060.0
#define Erv 8.5
#define Era 7.35
#define Ela 7.35
#define Arv 0.9
#define Ara 0.17
#define Ala 0.17
#define Brv 0.062
#define Bra 0.484
#define Bla 0.484
#define v0rv 4.0
#define v0ra 1.0
#define v0la 1.0
#define Rpvalve 0.0004
#define Rtvalve 0.00004
#define Rasd 0.001
#define Rsa 3.83
#define Rsv 0.083
#define Rpa 1.26
#define Rpv 0.022
#define Csa 0.44296
#define Csv 4.39
#define Clpa 0.155
#define Clpv 0.445
#define Crpa 0.155
#define Crpv 0.445
#define Tc 0.375
#define Tesrv 0.136
#define k1 57.6
#define k2 18.7
#define Tesra 0.056
#define Tesla 0.056
#define Cmpa 0.06118

/* VVARIABLE DEFINITION */
real VRV0,VMPA0,VSA0,VSV0,VLPA0,VRPA0,VLPV0,VRPV0,VRA0,VLA0; /* Volume n level */
real VRV1,VMPA1,VSA1,VSV1,VLPA1,VRPA1,VLPV1,VRPV1,VRA1,VLA1; /* Volume n+1 level */
real Qst,Qmpa,Qlp,Qrp; /* Measured Flow */
real Prv ,Pra ,Pla ,Pmpa ,Psa ,Psv ,Plpa ,Prpa ,Plpv ,Prpv ,Ppul ,Psys; /* Pressure Variables*/
real Qpvalv ,Qs1 ,Qtvalv ,Qasd ,Qs2 ,Qs3 ,Qlp2 ,Qlp3 ,Qrp2 ,Qrp3; /* Flow Variables */
real t ,t1 ,tt ,ta ,dt; /* Time Variables */
real h1,h2,h3,h4,h5,h6; /* Local Heaviside Variables */
```

```

real v1,v2,v3,pedrv1,pesrv1,pedra1,pesra1,pedla1,pesla1,pedrv2,pesrv2,pedra2,pesra2,pedla2,pesla2,AV,ALA,ARA; /*
    Cardiac Chamber Local Variables */

/* MANUALLY SET SURFACE ID */
int IDa = 6; /* Main Pulmonary Artery */
int IDb = 5; /* Ductal Stent */
int IDc = 4; /* Left Pulmonary Artery */
int IDd = 3; /* Right Pulmonary Artery */

/* ADDITIONAL FLUENT SPECIFIC DEFINITIONS */
char fname[22]='two.Fdata.txt'; /* Output *.txt file name */
Domain *domain;
Thread *thread1;
Thread *thread2;
Thread *thread3;
Thread *thread4;
face_t f;
FILE *fp;

/* INITIAL SET UP OF SOLUTION: init. Executed on loading following steady state initiation */
DEFINE_EXECUTE_ON_LOADING(init,lib)
{
domain=Get_Domain(1);
thread1 = Lookup_Thread(domain,IDa);
thread2 = Lookup_Thread(domain,IDb);
thread3 = Lookup_Thread(domain,IDc);
thread4 = Lookup_Thread(domain,IDd);
fp = fopen(fname,'w');

/* N=0 */
/* Initial Volume Values */
VRV0=18.8459;
VMPA0=2.7301;
VSA0=20.2858;
VSV0=13.9594;
VLPA0=1.9311;
VRPA0=2.1815;
VLPV0=0.6931;
VRPV0=0.7006;
VRA0=5.5933;
VLA0=5.5791;
/* Initial Time Values */
t=0.0;
t1=0.0;
dt=0.0001;
/* Initial Pressure Values */
Pmpa=VMPA0/Cmpa;
Psa=VSA0/Csa;
Psv=VSV0/Csv;
Plpa=VLPA0/Clpa;
Prpa=VRPA0/Crpa;
Plpv=VLPV0/Clpv;
Prpv=VRPV0/Crpv;

/* Cardiac Chamber Calculations */
AV=activeV(t1,Tc,Tesrv);
ARA=activeA(t1,Tc,Tesra);
ALA=activeA(t1,Tc,Tesla);

v1 = VRV1-v0rv;
pedrv1 = Arv*(exp(Brv*v1)-1.0);
pesrv1 = Erv*v1;
pedrv2 = pedrv1*(1-AV);
pesrv2 = AV*pesrv1;
Prv = pedrv2 + pesrv2;

```

```

v2 = VRA1-v0ra;
pedra1 = Ara*(exp(Bra*v2)-1.0);
pesra1 = Era*v2;
pedra2 = pedra1*(1-ARA);
pesra2 = ALA*pesra1;
Pra = pedra2 + pesra2;

v3 = VLA1-v0la;
pedla1 = Ala*(exp(Bla*v3)-1.0);
pesla1 = Ela*v3;
pedla2 = pedla1*(1-ALA);
pesla2 = ALA*pesla1;
Pla = pedla2 + pesla2;

/* Initial Flow Values from 3D Geometry */
Qmpa=0.0; /* Zero variable */
begin_f_loop(f,thread1)
{
    Qmpa+= F_FLUX(f,thread1); /* integrate mass flux over surface */
}
end_f_loop(f,thread1)
Qmpa=-((1e6)*Qmpa/rho); /* divide by density to obtain volumetric flow and scale units from m3 to ml */
/* (Negative value for MPA due to normal direction of surface in Fluent) */

Qst=0.0;
begin_f_loop(f,thread2)
{
    Qst+= F_FLUX(f,thread2);
}
end_f_loop(f,thread2)
Qst=1e6*Qst/rho;

Qlp=0.0;
begin_f_loop(f,thread3)
{
    Qlp+= F_FLUX(f,thread3);
}
end_f_loop(f,thread3)
Qlp=1e6*Qlp/rho;

Qrp=0.0;
begin_f_loop(f,thread4)
{
    Qrp+= F_FLUX(f,thread4);
}
end_f_loop(f,thread4)
Qrp=1e6*Qrp/rho;

/* Valvular Flow Calculations */
h3 = heaviside(Pra - Prv);
h4 = heaviside(Prv - Pmpa);
h5 = h3*(Pra - Prv)/Rtvalve;
h6 = h4*(Prv - Pmpa)/Rpvalve;
Qtvalv = sqrt(h5);
Qpvalv = sqrt(h6);
/* Remaining Linear Flow Calculations */
Qasd = (Pla - Pra)/Rasd;
Qs2 = (Psa-Psv)/Rsa;
Qs3 = (Psv-Pra)/Rsv;
Qlp2 = (Plpa-Plpv)/Rpa;
Qlp3 = (Plpv-Pla)/Rpv;
Qrp2 = (Prpa-Prpv)/Rpa;
Qrp3 = (Prpv-Pra)/Rpv;

/* Print headers for tab delimited output text file */

```



```

VLPA0 = VLPA1;
VLPV0 = VLPV1;
VRPA0 = VRPA1;
VRPV0 = VRPV1;
VRA0 = VRA1;
VLA0 = VLA1;
}

/* EXPLICIT COUPLING CODE AT EACH TIME POINT: couple */
DEFINE_EXECUTE_AT_END(couple)
{
domain=Get.Domain(1);
thread1 = Lookup.Thread(domain, IDa);
thread2 = Lookup.Thread(domain, IDb);
thread3 = Lookup.Thread(domain, IDc);
thread4 = Lookup.Thread(domain, IDd);

/* Calculate N Flow Variables */
t=CURRENT.TIME;
dt=CURRENT.TIMESTEP;

Qmpa=0.0;
begin_f_loop(f, thread1)
{
    Qmpa+= F.FLUX(f, thread1);
}
end_f_loop(f, thread1)
Qmpa=-1e6*Qmpa/rho;

Qst=0.0;
begin_f_loop(f, thread2)
{
    Qst+= F.FLUX(f, thread2);
}
end_f_loop(f, thread2)
Qst=1e6*Qst/rho;

Qlp=0.0;
begin_f_loop(f, thread3)
{
    Qlp+= F.FLUX(f, thread3);
}
end_f_loop(f, thread3)
Qlp=1e6*Qlp/rho;

Qrp=0.0;
begin_f_loop(f, thread4)
{
    Qrp+= F.FLUX(f, thread4);
}
end_f_loop(f, thread4)
Qrp=1e6*Qrp/rho;

h3 = heaviside(Pra - Prv);
h4 = heaviside(Prv - Pmpa);
h5 = h3*(Pra - Prv)/Rtvalve;
h6 = h4*(Prv - Pmpa)/Rpvalve;
Qtvalv = sqrt(h5);
Qpvalv = sqrt(h6);
Qasd = (Pla - Pra)/Rasd;
Qs2 = (Psa-Psv)/Rsa;
Qs3 = (Psv-Pra)/Rsv;
Qlp2 = (Plpa-Plpv)/Rpa;
Qlp3 = (Plpv-Pla)/Rpv;
Qrp2 = (Prpa-Prpv)/Rpa;
Qrp3 = (Prpv-Pra)/Rpv;

```



```

VRPV0 = VRPV1;
VRA0 = VRA1;
VLA0 = VLA1;
}

/* Define Macro for Setting Pressure Profile on Surface in Pascals from mmHg */
DEFINE_PROFILE(mpa_pressure , thread1 , IDa)
{
    face_t f;
    begin_f_loop(f , thread1)
    {
        F_PROFILE(f , thread1 , IDa) = Pmpa*133.322;
    }
    end_f_loop(f , thread1)
}
DEFINE_PROFILE(systemic_pressure , thread2 , IDb)
{
    face_t f;
    begin_f_loop(f , thread2)
    {
        F_PROFILE(f , thread2 , IDb) = Psa*133.322;
    }
    end_f_loop(f , thread2)
}
DEFINE_PROFILE(left_pulmonary_pressure , thread3 , IDc)
{
    face_t f;
    begin_f_loop(f , thread3)
    {
        F_PROFILE(f , thread3 , IDc) = Plpa*133.322;
    }
    end_f_loop(f , thread3)
}
DEFINE_PROFILE(right_pulmonary_pressure , thread4 , IDd)
{
    face_t f;
    begin_f_loop(f , thread4)
    {
        F_PROFILE(f , thread4 , IDd) = Prpa*133.322;
    }
    end_f_loop(f , thread4)
}

/* Close/Finalise output text file upon closing Fluent */
DEFINE_EXECUTE_AT_EXIT(close)
{
    fclose(fp);
}

```

Additional Functions Header Code

```

#ifndef ADD_H_GUARD
#define ADD_H_GUARD

real heaviside(real x)
{
    real result;

    if( x > 0 )
    {

```

```

        result = 1.0;
    }
    else
    {
        result = 0.0;
    }
    return result;
}

real square(real x)
{
    real y;
    y= x*x;
    return y;
}

real activeV(real t,real t1,real t2)
{

    real N;
    real t3;
    real t4;
    real t5;
    real on;
    real e;
    real t6;
    real pi;
    N = floor(t/t1);
    t4=0.02*t1;
    t3 = t - N*t1 - t4;
    t5 = t3 - 2*t2;
    on = heaviside(t3)-heaviside(t5);
    pi = 3.14159265358979323846;
    t6 = t3*pi/t2;
    e = on*0.5*(1-cos(t6));
    return e;
}

real activeA(real t,real t1,real t2)
{

    real N;
    real e;
    real t6;
    real pi;
    real on;
    real t3;
    real t5;
    N = floor(t/t1);
    t3 = t - N*t1;
    t5 = t3 - 2*t2;
    on = heaviside(t3)-heaviside(t5);
    pi = 3.14159265358979323846;
    t6 = t3*pi/t2;
    e = on*0.5*(1-cos(t6));
    return e;
}

real dVdt(real t,real V[18])
{

    real out[10];
    real Pla,Plv,Psa,Psv,Pra,Prv,Ppa1,Ppa2,Ppv;
    real Qmvlv,Qavlv,Qs1,Qs2,Qtvlv,Qpvlv,Qp1,Qp2,Qp3;

```

```

Ped_la = P.Ala*(exp(P.Bla*(y(9)-P.v0la))-1);
Pes_la = P.Ela*(y(9) - P.v0la);
Pla = Ped_la + Active(t,P.Tes_la,P.Tc)*( Pes_la - Ped_la);

Ped_ra = P.Ara*(exp(P.Bra*(y(10)-P.v0ra))-1);
Pes_ra = P.Era*(y(10) - P.v0ra);
Pra = Ped_ra + Active(t,P.Tes_ra,P.Tc)*( Pes_ra - Ped_ra);

Ped_rv = P.Arv*(exp(P.Br*(y(2)-P.v0rv))-1);
Pes_rv = P.Erv*(y(2) - P.v0rv);
Prv = Ped_rv + Active(t,P.Tes_rv,P.Tc,1)*( Pes_rv - Ped_rv);

Ped_lv = P.Alv*(exp(P.Blv*(y(1)-P.v0lv))-1);
Pes_lv = P.El*(y(1) - P.v0lv);
Plv = Ped_lv + Active(t,P.Tes_lv,P.Tc,1)*( Pes_lv - Ped_lv);

Pao = y(3)/P.Cao;
Psa = y(4)/P.Csa;
Psv = y(5)/P.Csv;
Pmpa = y(6)/P.Cmpa;
Ppa = y(7)/P.Cpa;
Ppv = y(8)/P.Cpv;

Rmi = (1 - cos(y(11)))^2/(1 - cos(c.theta_max_mi))^2;
Rao = (1 - cos(y(13)))^2/(1 - cos(c.theta_max_ao))^2;
Rti = (1 - cos(y(15)))^2/(1 - cos(c.theta_max_ti))^2;
Rpo = (1 - cos(y(17)))^2/(1 - cos(c.theta_max_po))^2;

Qmvlv = sign(Pla-Plv)*c.CQmi*Rmi*sqrt(abs(Pla-Plv));
Qavlv = sign(Plv-Pao)*c.CQao*Rao*sqrt(abs(Plv-Pao));
Qtlv = sign(Pra-Prv)*c.CQti*Rti*sqrt(abs(Pra-Prv));
Qpvlv = sign(Prv-Pmpa)*c.CQpo*Rpo*sqrt(abs(Prv-Pmpa));

Qs1 = (Pao - Psa)/P.Rsc;
Qs2 = (Psa - Psv)/P.Rsa;
Qs3 = (Psv - Pra)/P.Rsv;
Qp1 = (Pmpa - Ppa)/P.Rpc;
Qp2 = (Ppa - Ppv)/P.Rpa;
Qp3 = (Ppv - Pla)/P.Rpv;

out[1]=Qmvlv-Qavlv;
out[2]=Qtlv-Qpvlv;
out[3]=Qavlv-Qs1;
out[4]=Qs1-Qs2;
out[5]=Qs2-Qs3;
out[6]=Qpvlv-Qp1;
out[7]=Qp1-Qp2;
out[8]=Qp2-Qp3;
out[9]=Qp3-Qmvlv;
out[10]=Qs3-Qtlv;
out[11]= V[12];
out[12] = c.Kpmi*(Pla - Plv)*cos(V[11]) - c.Kfmi*V[12];
out[13]=V[14];
out[14] = c.Kpao*(Plv - Psa)*cos(V[13]) - c.Kfao*V[14];
out[15]= V[16];
out[16] = c.Kpti*(Pra - Prv)*cos(V[15]) - c.Kfti*V[16];
out[17]= V[18];
out[18] = c.Kppo*(Prv - Pmpa)*cos(V[17]) - c.Kfpo*V[18];

}
#endif

```

Appendix D

Matlab *.m files

simulate.m

Function calculating all haemodynamical outcomes

```
function [t,v,a,c] = simulate(N,dt,vol,D,d,model, valve, varargin)

% N - number of cycles to simulate
% dt - timestep (s)
5 % vol - total stressed blood volume (ml)
% D - diameter of shunt (mm)
% d - diameter of band (mm); dummy value for Norwood models
% model - 1: hybrid; 2: non-valved shunt; 3: valved shunt; 4: blalock-taussig shunt
% valve - 1: linear; 2: quadratic/orifice
10
if model == 1
    D=D*1.5; % scale band diameter for hybrid
end

15 % parameter labels:
% _rv: right ventricle; _ra: right atrium; _la: left atrium
% mpa: main pulmonary artery; asd: atrial septal defect
% _s*: systemic; _p*: pulmonary
% _*c: characteristic; _*a: arterial; _*v: venous
20 % _pvalve: pulmonary valve; _tvalve: tricuspid valve; _band: pulmonary banding
% R_: resistance; C_: compliance
% Tes_: end systolic time; E_: maximum elastance; A_: , B_: , v0_:

% struct P containing constant parameters
25 P.HR=160; % heart rate (beats per min)
P.Tc=60/P.HR; % length of cardiac cycle (s)
P.k1=5.76e1; % shunt/stent flow parameter 1
P.k2=1.87e1; % shunt/stent flow parameter 2
P.Tes_rv=0.136; % time to end systole of right ventricle (s)
```

```

30 P.Tes_ra=0.056;
P.Tes_la=0.056;
P.Erv=8.5;
P.Era=7.35;
P.Ela=7.35;
35 P.Arv=0.9;
P.Ara=0.17;
P.Ala=0.17;
P.Brv=0.062;
P.Bra=0.484;
40 P.Bla=0.484;
P.v0rv=4;
P.v0ra=1;
P.v0la=1;
P.Rpvalve=0.0004;
45 P.Rtvalve=0.00004;
P.Rasd=0.001;
P.Rsc=0.2;
P.Rsa=3.83;
P.Rsv=0.083;
50 P.Rpc=0.028;
P.Rpa=0.63;
P.Rband=(3-P.Rpc)*3^4/d^4; % Poiseuille scaling
P.Rpv=0.011;
P.Cmpa=0.06118;
55 P.Csa=0.44296;
P.Cpa=0.31;
P.Csv=4.39;
P.Cpv=0.89;

60 P = parse_pv_pairs(P,varargin); % function to allow changing of specific parameters

T = 0:dt:N*P.Tc; % time vector for N cycles
I = round(P.Tc/dt)+1; % length of vector in cardiac cycle

65 % set initial volumes – distributed to produce convergent solution
V(1).Vrv = 1.5*vol/8;
V(1).Vmmpa = vol/8;
V(1).Vsa = 1.5*vol/8;
V(1).Vsv = vol/8;
70 V(1).Vpa = 0.5*vol/8;
V(1).Vpv = vol/8;
V(1).Vra = 0.75*vol/8;
V(1).Vla = 0.75*vol/8;

75 % determine initial algebraic parameters from volume
A(1) = algebraic(V(1),P,T(1),D,d);

% preallocate volume and algebraic variable structs

```

```

V(length(T))=struct('Vrv',[],'Vmpa',[],'Vsa',[],'Vsv',[],'Vpa',[],'Vpv',[],'Vra',[],'
    Vla',[]);
80 A(length(T))=struct('Prv',[],'Pra',[],'Pla',[],'Pmpa',[],'Psa',[],'Psv',[],...
    'Ppa',[],'Ppv',[],'Qs1',[],'Psys',[],'Qp1',[],'Ppu1',[],...
    'Qpvalve',[],'Qtvalve',[],'Qasd',[],'Qs2',[],'Qs3',[],'Qp2',[],'Qp3',[]);

n=1; % initiate cycle number n
85 while n<N
    % solve first cardiac cycle
    if n==1
    for i=2:I-1
        V(i) = dvdt(V(i-1),A(i-1),dt);
90     A(i) = algebraic(V(i),P,T(i),D,d,model,valve);
    end
    end

    n=n+1; % update cardiac cycle number

95     if n <= N
        for i=(n-1)*(I-1)+1:n*(I-1)
            V(i) = dvdt(V(i-1),A(i-1),dt);
            A(i) = algebraic(V(i),P,T(i),D,d,model,valve);
100        end
    end
end

% final calculation
105 i=N*(I-1)+1;
V(i) = dvdtN_hybrid(V(i-1),A(i-1),dt);
A(i) = algebraicN_hybrid(V(i),P,T(i),D,d);

j=round((N-1)*P.Tc/dt)+1; % index for start of final cardiac cycle
110 k=round(P.Tc/dt)+1; % index of end of first cardiac cycle

t=T(1:k); % output time vector 0 -> Tc
a=A(j:end); % output algebraic struct of final cardiac cycle
v=V(j:end); % output volume struct of final cardiac cycle
115 c=resultstable(t,v,a,d,D); % haemodynamic results

% solve differential equations subfunction
function V1 = dvdt(V0,A0,dt)

120     % V0 - current time step volumes
    % A0 - current time step pressures and flows
    % V1 - next time step volumes

    V1.Vrv = V0.Vrv + dt*(A0.Qtvalve - A0.Qpvalve);
125     V1.Vmpa = V0.Vmpa + dt*(A0.Qpvalve - A0.Qs1 - A0.Qp1);
    V1.Vsa = V0.Vsa + dt*(A0.Qs1 - A0.Qs2);

```

```

V1.Vsv = V0.Vsv + dt*(A0.Qs2 - A0.Qs3);
V1.Vpa = V0.Vpa + dt*(A0.Qp1 - A0.Qp2);
V1.Vpv = V0.Vpv + dt*(A0.Qp2 - A0.Qp3);
130 V1.Vra = V0.Vra + dt*(A0.Qs3 - A0.Qtvalve + A0.Qasd);
V1.Vla = V0.Vla + dt*(A0.Qp3 - A0.Qasd);
end

% solve algebraic equations subfunction
135 function A = algebraic(V,P,t,D,d,model, valve)

% right ventricle
Ped_rv = P.Arsv*(exp(P.Brsv*(V.Vrv-P.v0rv))-1);
Pes_rv = P.Erv*(V.Vrv - P.v0rv);
140 A.Prsv = Ped_rv + Active(t,P.Tes_rv,P.Tc,2)*(Pes_rv - Ped_rv);

% right atrium
Ped_ra = P.Ara*(exp(P.Bra*(V.Vra-P.v0ra))-1);
Pes_ra = P.Era*(V.Vra - P.v0ra);
145 A.Pra = Ped_ra + Active(t,P.Tes_ra,P.Tc,1)*(Pes_ra - Ped_ra);

% left atrium
Ped_la = P.Ala*(exp(P.Bla*(V.Vla-P.v0la))-1);
Pes_la = P.Ela*(V.Vla - P.v0la);
150 A.Pla = Ped_la + Active(t,P.Tes_la,P.Tc,1)*(Pes_la - Ped_la);

% systemic pressures
A.Pmpa = V.Vmpa/P.Cmpa;
A.Psa = V.Vsa/P.Csa;
155 A.Psv = V.Vsv/P.Csv;

% pulmonary pressures
A.Ppa = V.Vpa/P.Cpa;
A.Ppv = V.Vpv/P.Cpv;
160

switch model
case 1 % hybrid
A.Qs1 = sign(A.Pmpa-A.Psa)*(-(P.k1+P.Rsc*D^4)/(2*P.k2) + sqrt(abs(A.Pmpa-
A.Psa)*D^4/P.k2 + ((P.k1+P.Rsc*D^4)/(2*P.k2))^2));
A.Qp1 = (A.Pmpa - A.Ppa)/(P.Rband + P.Rpc);
165 A.Psys = A.Psa + A.Qs1*P.Rsc;
case 2 % non-valved sano
A.Qs1 = (A.Pmpa - A.Psa)/P.Rsc;
A.Qp1 = sign(A.Prsv-A.Ppa)*(-(P.Rpc*D^4 +P.k1)/(2*P.k2) + sqrt(abs(A.Prsv-A
.Ppa)*(D^4)/P.k2 + ((P.Rpc*D^4 +P.k1)/(2*P.k2))^2));
A.Psys = A.Psa + A.Qs1*P.Rsc/2;
170 case 3 % valved sano
A.Qs1 = (A.Pmpa - A.Psa)/P.Rsc;
A.Qp1 = -(P.Rpc*D^4 +P.k1)/(2*P.k2) + sqrt(heaviside(A.Prsv-A.Ppa)*((D^4)/
P.k2*(A.Prsv-A.Ppa)) + ((P.Rpc*D^4 +P.k1)/(2*P.k2))^2);

```

```

        A.Psys = A.Psa + A.Qs1*P.Rsc/2;
    case 4 % bt shunt
175         A.Qs1 = (A.Pmpa - A.Psa)/P.Rsc;
        A.Qp1 = sign(A.Pmpa-A.Ppa)*(-(P.k1+P.Rpc*D^4)/(2*P.k2) + sqrt(abs(A.Pmpa-
            A.Ppa)*D^4/P.k2 + ((P.k1+P.Rpc*D^4)/(2*P.k2))^2));
        A.Psys = A.Psa + A.Qs1*P.Rsc/2;
    end

180     A.Ppul = A.Ppa + A.Qp1*P.Rpc;

    % valvular + septal flow
    switch valve
        case 1
185             A.Qpvalve = heaviside(A.Prv - A.Pmpa)*(A.Prv - A.Pmpa)/P.Rpvalve;
            A.Qtvalve = heaviside(A.Pra - A.Prv)*(A.Pra - A.Prv)/(P.Rtvalve);
        case 2
            A.Qpvalve = heaviside(A.Prv - A.Pmpa)*sqrt((A.Prv - A.Pmpa)/P.Rpvalve);
            A.Qtvalve = heaviside(A.Pra - A.Prv)*sqrt((A.Pra - A.Prv)/P.Rtvalve);
190     end

        A.Qasd = (A.P1a - A.Pra)/P.Rasd;

    % systemic flow
195     A.Qs2 = (A.Psa - A.Psv)/P.Rsa;
        A.Qs3 = (A.Psv - A.Pra)/P.Rsv;

    % pulmonary flow
        A.Qp2 = (A.Ppa - A.Ppv)/P.Rpa;
200     A.Qp3 = (A.Ppv - A.P1a)/P.Rpv;
    end

    % cardiac activation subfunction
    function e = Active(t,Tes,Tc,C)
205     % t: time, Tes: end systolic time, Tc: cardiac cycle duration, C: chamber type
        % C, 1: atrium, 2: ventricle
        if C == 2
            DT=0.02*Tc; % delay onset of ventricular systole
        else
210             DT=0;
        end

        N=floor(t/Tc); % cardiac cycle number
        t1 = t-N.*Tc - DT; % translate to [0,Tc]
215     on = (heaviside(t1)-heaviside(t1-2*Tes)); % limit range
        e= on.*0.5.*(1-cos(t1*pi/Tes));
    end

    function out=resultstable(t,v,a,d,D)
220

```

```

% t – time vector input
% v – volume array input
% a – algebraic variables array input
    out=zeros(27,1); % preallocate output vector
225    out(1) = d; % banding diameter
        out(2) = D; % ductal stent diameter
        out(3) = max([a.Pmpa]); % systolic MPA pressure
        out(4) = min([a.Pmpa]); % diastolic MPA pressure
        out(5) = mean([a.Pmpa]); % mean MPA pressure
230    out(6) = max([a.Psys]); % systolic distal-stent/aortic pressure
        out(7) = min([a.Psys]); % diastolic distal-stent/aortic pressure
        out(8) = mean([a.Psys]); % mean distal-stent/aortic pressure
        out(9) = max([a.Ppul]); % systolic post-band/shunt PA pressure
        out(10) = min([a.Ppul]); % diastolic post-band/shunt PA pressure
235    out(11) = mean([a.Ppul]); % mean post-band/shunt PA pressure
        out(12) = trapz(t,[a.Qpvalv])*160/1000; % cardiac output (l/min)– forward flow
            through pulmonary valve
        Qp = trapz(t,[a.Qp1])*160/1000; % pulmonary flow (l/min)
        out(13) = Qp;
        Qs = trapz(t,[a.Qs1])*160/1000; % systemic flow (l/min)
240    out(14) = Qs;
        out(15) = Qp/Qs; % Qp:Qs ratio
        runoff=find([a.Qs1]<0); % identify backflow through stent
        out(16)=trapz(t(runoff),[a(runoff).Qs1])*160/1000; % stent backflow (l/min)
        saO2 = 100*(0.98*1.34*10*16.52 - 185*.33./Qp)/(1.34*10*16.52); % arterial oxygen
            saturation
245    out(20,i) = saO2;
        svO2 = 100*((0.98*1.34*10*16.52 - 185*.33./Qp) - 185*.33./Qs)/(1.34*10*16.52); %
            venous oxygen saturation
        out(21,i) = svO2;
        out(22,i)=(Qs/0.33)*(0.98*1.34*10*16.52-185*.33/Qp); % systemic oxygen delivery
        out(23) = sum(cell2mat(struct2cell(v(1)))); % total stressed blood volume
250    out(24) = max([v.Vrv]); % right ventricle end diastolic volume
        sw = polyarea([v.Vrv],[a.Prv]); % stroke work
        out(25) = sw;
        spva = syspva(v,a); % systolic pressure-volume area
        out(26) = spva;
255    out(27)= 100*sw/spva; % mechanical efficiency
end

% sub function calculating systolic pressure-volume area
function pva=syspva(V,A,P)
260
        bottom_right=max([V.Vrv]); % identify end diastolic volume
        i1=find([V.Vrv]==bottom_right,1,'first'); % find index of end diastole
        E=[A.Prv]./[V.Vrv]; % elastance vector
        Emax=find(E==max(E)); % index of maximum elastance
265    % bottom diastolic curve pressure and volume vectors
        v1=linspace(P.v0rv,bottom_right,101);

```

```

p1=P.ArV*(exp(P.BrV*(v1-P.v0rv))-1);
% end diastole to maximum elastance pressure and volume vectors
v2=[V(i1:Emax).Vrv];
270 p2=[A(i1:Emax).Prv];
% end systolic corner to zero pressure volume intercept
v3=linspace(V(Emax).Vrv,P.v0rv,100);
p3=A(Emax).Prv/(V(Emax).Vrv-P.v0rv)*(v3-P.v0rv);
% stitching of volume and pressure vectors
275 v=[v1,v2,v3];
p=[p1,p2,p3];
pva=polyarea(v,p); % calculation of systolic pressure-volume area
end

```

match_outcome.m

Function matching total stressed blood volume with specified haemodynamical outcome. Matching band diameter d is a variation of the code presented here.

```

function [t,vr,ar,cr,xr]=match_outcome(xl,xu,d,D,model,valve,n,F,maxerror,maxit)

% INPUT
% xl: lower stressed blood volume limit
5 % xu: upper stressed blood volume limit
% d: band diameter, D: stent diameter
% model: 1-hybrid, 2-non-valved sanq, 3-valved sanq, 4-bt shunt
% valve: 1-linear, 2-quadratic/oriface
% n: haemodynamical outcome matched (see simulate.m for identifier details)
10 % F: value to match outcome n
% maxerror: tolerance for matching outcome
% maxit: maximum number of iterations
% OUTPUT
% t: time vector
15 % vr: matched volume struct data
% ar: matched pressure and flow struct data
% cr: matched haemodynamical outcomes
% xr: required total stress blood volume to match specified haemodynamical outcome

20 [t,vl,al,cl,f1]=sim(xl,d,D,n); % initial lower guess
f1=f1-F; % initial lower difference
[t,vu,au,cu,fu]=sim(xu,d,D,n); % initial upper guess
fu=fu-F; % initial upper difference

25 % ensure positive difference with upper guess
while fu<0
    xu=1.1*xu; % increase upper limit

```

```

    [t,vu,au,cu,fu]=sim(xu,d,D,n);
    fu=fu-F;
30  end
    % ensure negative difference with lower guess
    while f1>0
        x1=0.75*x1; % decrease lower limit
        [t,v1,a1,c1,f1]=sim(x1,d,D,n);
35  f1=f1-F;
    end

count = 0; % iteration counter
fr = fu; % to force entry into while loop
40 xr = xu; % require starting value in loop below

    while (abs(fr) > maxerror) && (count < maxit)
        count = count + 1;

45  xr = xu - fu*(xu-x1)/(fu-f1); % estimate volume for matched solution
        [t,vr,ar,cr,fr]=sim(xr,d,D,n); % solve at estimated volume
        fr=fr-F; % test estimate against desired matching value

        test = f1 * fr; % form test product

50  if test == 0
            fr = 0; % root is at xr
        elseif test < 0 % update upper limit
            xu = xr;
55  fu = fr; % root is below xr
            vu = vr;
            au = ar;
            cu = cr;
        else % update lower limit
60  x1 = xr;
            f1 = fr; % root is above xr
            v1 = vr;
            a1 = ar;
            c1 = cr;
65  end
    end

end

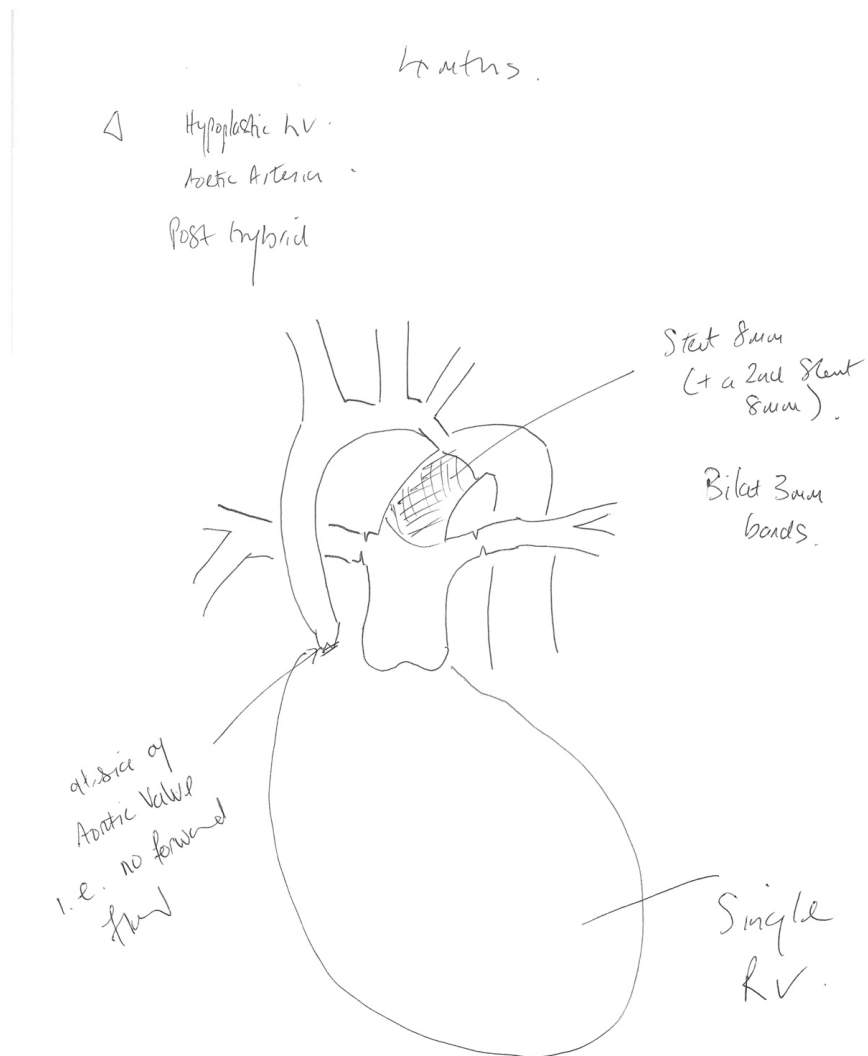
70 function [t,v,a,c,f]=sim(vol,d,D,model,valve,n)
    [t,v,a,c]=simulate(15,1e-5,vol,D,d,model,valve);
    f=c(n);
end

```

Appendix E

Patient-Specific Catheterisation

Data





GE Medical Systems
Information Technologies

Royal Hospital for Sick Children
Glasgow

Patient Information

Patient Name
Study Date 07/06/2011
MRN
Date of Birth 13/01/2011
Age 4 Months
Gender Female
Race
Height 58.00 cm (1'11")
Weight 5.00 kg (11 lbs)
BSA 0.27 M2

Patient History

LAI, Azyg continuation to RIVC, Hepatics to RA PVs to LA, AVSD, Hypoplastic LV, Ao atresia, Hyybrid

Procedures

Entry	Procedure
LFV 4F	Diagnostic L and R heart cath
RFA 4F	

Staff

Duty	Name
Consultant Cardiologist	
Assisting Physician	
Anaesthetist	
Cardiac Physiologist	
Nurse	
Nurse	
Nurse	
Radiographer	

Radiology Contrast

Site	RV	MPA	RPA	PA	PA	Arch	AzygV	Duct
Volume	8	10	5	5	5	4	3	8
Rate	8	15	Hand	Hand	Hand	Hand	Hand	15
	Frontal							
LAO								
RAO	30							
Cran/Caud								
	Lateral							
LAO	60	80	90	90	90	90	90	90
RAO								
Cran/Caud								

Screening Time: 18:14mins
 Total Dosage: 5545 mGycm²
 Total Contrast: 48ml(Omnipaque 350)
 Start Time: 13:30 End Time: 15:43 Total time: 133mins

Study Date: 07/06/2011
Admission ID: N/A



GE Medical Systems
Information Technologies

Royal Hospital for Sick Children
Glasgow

2

Pressure Summary (mmHg)

Time	Site	Sys	Dias	End	Mean	A Wave	V Wave	Max dp/dt	HR
2:21PM	ART	44	34	0	38	0	0	0	99
2:21PM	FA	56	42	0	50	0	0	0	100
2:21PM	ARCH	43	33	0	38	0	0	0	100
2:22PM	ARCH	43	32	0	37	0	0	0	99
2:22PM	DSAO	79	33	0	54	0	0	0	99
2:23PM	PA	86	32	0	56	0	0	0	99
2:23PM	PA	86	32	0	55	0	0	0	99
2:23PM	DSAO	71	32	0	50	0	0	0	99
2:25PM	LV	83	0	8	0	0	0	702	97

Post-Angio

Time	Site	Sys	Dias	End	Mean	A Wave	V Wave	Max dp/dt	HR
2:30PM	AO	88	31	0	56	0	0	0	94

Post-Angio

Time	Site	Sys	Dias	End	Mean	A Wave	V Wave	Max dp/dt	HR
2:39PM	RPA	14	11	0	12	0	0	0	94

Post-Angio

Time	Site	Sys	Dias	End	Mean	A Wave	V Wave	Max dp/dt	HR
3:00PM	RPA	54	29	0	41	0	0	0	87
3:04PM	LA	0	0	0	6	7	7	0	86
3:04PM	RPA			0	-427	0	0	0	86
3:04PM	FA	46	24	0	34	0	0	0	86
3:05PM	LA	0	0	0	6	7	7	0	85
3:05PM	RA	0	0	0	6	7	7	0	85

Study Date: 07/06/2011
Admission ID: N/A



GE Medical Systems
Information Technologies

Royal Hospital for Sick Children
Glasgow

3

Event Log

Time	Summary	Comment
	Phase:	
1:30:22 PM		Patient arrived
1:59:32 PM		Drapes on
2:00:59 PM		Needle to skin
2:03:57 PM	12-Lead Print	
2:05:03 PM	5.2Fr (PSI 1200) MPA	
2:05:07 PM	4F MPA	
2:07:38 PM	4F UHF pig	
2:13:08 PM	4F 7cm Sheath Introducer	
2:13:13 PM	5F Avanti Introducer	
2:14:04 PM	SAT: FA ***%	
2:14:54 PM	.021x50cm Standard Guidewire	
2:19:01 PM	Heparin (IA) IA 250 units	
2:21:45 PM	ART : 44/34/38, HR = 99, II	
2:21:45 PM	Snapshot: ART : 44/34/38	
2:21:57 PM	FA : 56/42/50, HR = 100, II	
2:21:57 PM	ARCH : 43/33/38, HR = 100, II	
2:21:57 PM	Snapshot: FA : 56/42/50	
2:21:57 PM	Snapshot: ARCH : 43/33/38	
2:22:13 PM	ARCH : 43/32/37, HR = 99, II	
2:22:18 PM	Pullback from ARCH to DSAO	
2:22:19 PM	Snapshot: Pullback: ARCH to DSAO.	
2:22:20 PM	DSAO : 79/33/54, HR = 99, II	
2:23:33 PM	PA : 86/32/56, HR = 99, II	
2:23:33 PM	Snapshot: PA : 86/32/56	
2:23:38 PM	PA : 86/32/55, HR = 99, II	
2:23:43 PM	Pullback from PA to DSAO	
2:23:44 PM	Snapshot: Pullback: PA to DSAO.	
2:23:45 PM	DSAO : 71/32/50, HR = 99, II	
2:25:39 PM	LV : 83/0/8, Max dP/dt = 702, HR = 97, II	
2:25:39 PM	Snapshot: LV : 83/0/8	
2:29:51 PM		Phase
2:29:51 PM	Phase: Post-Angio	LV angio 8ml at 8ml/s
2:29:52 PM		Contrast
2:30:27 PM	Pullback: LV to AO.	
2:30:47 PM	AO : 88/31/56, HR = 94, II	
2:30:47 PM	Snapshot: AO : 88/31/56	
2:34:55 PM		Phase
2:34:55 PM	Phase: Post-Angio	MPA angio 10ml at 15ml/s
2:34:57 PM		Contrast
2:39:55 PM	RPA : 14/11/12, HR = 94, II	
2:39:55 PM	Snapshot: RPA : 14/11/12	
2:41:10 PM		Phase
2:41:10 PM	Phase: Post-Angio	RPA angio 5ml by hand
2:41:14 PM		Contrast
2:56:55 PM		Phase
2:56:55 PM	Phase: Post-Angio	MPA Angio 5mls Hand Injection
2:57:01 PM		Contrast
2:58:33 PM	Phase: Post-Angio	AO Angio 5mls Hand Injection
2:58:33 PM		Phase
2:58:41 PM		Contrast

Study Date: 07/06/2011
Admission ID: N/A



GE Medical Systems
Information Technologies

Royal Hospital for Sick Children
Glasgow

3:21PM	4F	Cordis	Special catheter	
--------	----	--------	------------------	--

Study Date: 07/06/2011
Admission ID: N/A

References

- [1] H. P. Gutgesell and D. S. Lim, "Hybrid palliation in hypoplastic left heart syndrome," *Current Opinions in Cardiology*, vol. 22, pp. 55–59, 2007.
- [2] R. G. Ohye, E. J. Devaney, J. C. Hirsch, and E. L. Bove, "The modified blalock-taussig shunt versus the right ventricle-to-pulmonary artery conduit for the norwood procedure," *Pediatric Cardiology*, vol. 28, pp. 122–125, 2007.
- [3] J. I. E. Hoffman and S. Kaplan, "The incidence of congenital heart disease," *Journal of the American College of Cardiology*, vol. 39, no. 12, pp. 1890–900, 2002.
- [4] J. A. Connor and R. Thiagarajan, "Hypoplastic left heart syndrome," *Orphanet Journal of Rare Diseases*, vol. 2, p. 23, 2007.
- [5] F. Migliavacca, R. Yates, G. Pennati, G. Dubini, R. Fumero, and M. R. de Leval, "Calculating blood flow from doppler measurements in the systemic-to-pulmonary artery shunt after the norwood operation: A method based on computational fluid dynamics," *Ultrasound in Medicine & Biology*, vol. 26, no. 2, pp. 209–219, 2000.
- [6] C. D. Morris, J. Outcalt, and V. D. Menashe, "Hypoplastic left heart syndrome: natural history in a geographically defined population," *Pediatrics*, vol. 85, pp. 977–983, 1990.
- [7] R. G. Ohye, L. A. Sleeper, L. Mahony, J. W. Newburger, G. D. Pearson, M. Lu, C. S. Goldberg, S. Tabbutt, P. C. Frommelt, N. S. Ghanayem, P. C. Laussen, J. F. Rhodes, A. B. Lewis, S. Mital, C. Ravishankar, I. A. Williams, C. Dunbar-Masterson, A. M. Atz, S. Colan, L. L. Minich, C. Pizarro, K. R. Kanter, J. Jagers, J. P. Jacobs, C. D. Krawczeski, N. Pike, B. W. McCrindle, L. Virzi, and J. W. Gaynor, "Comparison of shunt types in the norwood procedure for single-ventricle lesions," *New England Journal of Medicine*, vol. 362, no. 21, pp. 1980–1992, 2010.
- [8] J. A. Feinstein, D. W. Benson, A. M. Dubin, M. S. Cohen, D. M. Maxey, W. T. Mahle, E. Pahl, J. Villafae, A. B. Bhatt, L. F. Peng, B. A. Johnson, A. L. Marsden, C. J. Daniels, N. A. Rudd, C. A. Caldarone, K. A. Mussatto, D. L. Morales, D. D. Ivy, J. W. Gaynor, J. S. Tweddell, B. J. Deal, A. K. Furck, G. L. Rosenthal, R. G. Ohye, N. S. Ghanayem, J. P. Cheatham, W. Tworetzky, and G. R. Martin, "Hypoplastic left heart syndrome: Current considerations and expectations," *Journal of the American College of Cardiology*, vol. 59, no. 1, pp. S1 – S42, 2012.

- [9] C. I. Tchervenkov, J. P. Jacobs, P. M. Weinberg, V. D. Aiello, M. J. Béland, S. D. Colan, M. J. Elliott, R. C. Franklin, J. W. Gaynor, O. N. Krogmann, H. Kurosawa, B. Maruszewski, and G. Stellin, "The nomenclature, definition and classification of hypoplastic left heart syndrome," *Cardiology in the Young*, vol. 16, pp. 339–368, 2006.
- [10] N. T. Kouchoukos, E. H. Blackstone, D. B. Doty, F. L. Hanley, and R. B. Karp, "Aortic atresia and other forms of hypoplastic left heart physiology," in *Kirkin/Barratt-Boyes cardiac surgery* (K. NT, B. EH, D. DB, H. FL, and K. RB, eds.), vol. 2, pp. 1377–1400, Philadelphia: Churchill Livingstone, third ed., 2003.
- [11] G. Barber, J. Helton, B. Aglira, A. Chin, J. Murphy, J. Pigott, and W. Norwood, "The significance of tricuspid regurgitation in hypoplastic left-heart syndrome," *American Heart Journal*, vol. 116, no. 6, pp. 1563–1567, 1988.
- [12] S. Sano, K. Ishino, M. Kawada, and O. Honjo, "Right ventricle-pulmonary artery shunt in first-stage palliation of hypoplastic left heart syndrome," *Operative Techniques in Thoracic and Cardiovascular Surgery*, vol. 10, no. 2, pp. 141–151, 2005.
- [13] B. Alsoufi, J. Bennetts, S. Verma, and C. A. Caldarone, "New developments in the treatment of hypoplastic left heart syndrome," *Pediatrics*, vol. 119, no. 1, pp. 109–117, 2007.
- [14] D. J. DiBardino, D. B. McElhinney, A. C. Marshall, and E. A. Bacha, "A review of ductal stenting in hypoplastic left heart syndrome: Bridge to transplantation and hybrid stage i palliation," *Pediatric Cardiology*, vol. 29, pp. 251–257, 2008.
- [15] J. S. Tweddell, "The norwood procedure with an innominate artery-to-pulmonary artery shunt," *Operative Techniques in Thoracic and Cardiovascular Surgery*, vol. 10, no. 2, pp. 123–140, 2005.
- [16] W. I. Norwood, P. Lang, A. R. Castaneda, and D. N. Campbell, "Experience with operations for hypoplastic left heart syndrome," *Journal of Thoracic and Cardiovascular Surgery*, vol. 82, pp. 511–519, 1981.
- [17] S. Fuller, N. Ghanayem, P. Chai, J. Nigro, T. Kleisli, and S. Tabbutt, "Neonatal surgical reconstruction and peri-operative care for hypoplastic left heart syndrome: current strategies," *Cardiology in the Young*, vol. 21, no. S2, pp. 38–46, 2011.
- [18] W. T. Mahle, T. L. Spray, G. Wernovsky, J. W. Gaynor, and B. J. Clark III, "Survival after reconstructive surgery for hypoplastic left heart syndrome: A 15-year experience from a single institution," *Circulation*, vol. 102, no. 19, pp. III136–III141, 2000.
- [19] J. Tibballs, Y. Kawahira, B. G. Carter, S. Donath, C. Brizard, and J. Wilkinson, "Outcomes of surgical treatment of infants with hypoplastic left heart syndrome: An institutional experience 1983-2004," *Journal of Paediatrics and Child Health*, vol. 43, pp. 746–751, 2007.

- [20] J. L. Gibbs, C. Wren, K. G. Watterson, S. Hunter, and J. R. L. Hamilton, "Stenting of the arterial duct combined with banding of the pulmonary arteries and atrial septectomy or septostomy: A new approach to palliation for hypoplastic left heart syndrome," *British Heart Journal*, vol. 699, pp. 551–555, 1993.
- [21] T. Sakurai, H. Kado, T. Nakano, K. Hinokiyama, A. Shiose, M. Kajimoto, K. Joo, and Y. Ueda, "Early results of bilateral pulmonary artery banding for hypoplastic left heart syndrome," *European Journal of Cardio-Thoracic Surgery*, vol. 36, no. 6, pp. 973–979, 2009.
- [22] K. Kitahori, A. Murakami, T. Takaoka, S. Takamoto, and M. Ono, "Precise evaluation of bilateral pulmonary artery banding for initial palliation in high-risk hypoplastic left heart syndrome," *Journal of Thoracic and Cardiovascular Surgery*, vol. 140, no. 5, pp. 1084–1091, 2010.
- [23] A. F. Corno, "Pulmonary artery banding," *Swiss Medical Weekly*, vol. 135, no. 35-36, pp. 515–519, 2005.
- [24] I. Michel-Behnke, H. Akintuerk, I. Marquardt, M. Mueller, J. Thul, J. Bauer, K. J. Hagel, J. Kreuder, P. Vogt, and D. Schranz, "Stenting of the ductus arteriosus and banding of the pulmonary arteries: basis for various surgical strategies in newborns with multiple left heart obstructive lesions," *Heart*, vol. 89, no. 6, pp. 645–650, 2003.
- [25] M. Galantowicz, J. P. Cheatham, A. Phillips, C. L. Cua, T. M. Hoffman, S. L. Hill, and R. Rodeman, "Hybrid approach for hypoplastic left heart syndrome: Intermediate results after the learning curve," *The Annals of Thoracic Surgery*, vol. 85, pp. 2063–2071, 2008.
- [26] C. Apitz, R. Kaulitz, G. Ziemer, and M. Hofbeck, "Severe left ventricular hypoplasia in patients with unbalanced incomplete atrioventricular septal defect and pulmonary hypertension: Feasibility of biventricular repair," *Pediatric Cardiology*, vol. 30, pp. 70–73, 2009.
- [27] L. Grosse-Wortmann, T.-J. Yun, O. Al-Radi, S. Kim, M. Nii, K.-J. Lee, A. Redington, S.-J. Yoo, and G. van Arsdell, "Borderline hypoplasia of the left ventricle in neonates: Insights for decision-making from functional assessment with magnetic resonance imaging," *Journal of Thoracic and Cardiovascular Surgery*, vol. 136, no. 6, pp. 1429–1436, 2008.
- [28] H. Akintürk, I. Michel-Behnke, K. Valeske, M. Mueller, J. Thul, J. Bauer, K.-J. Hagel, and D. Schranz, "Hybrid transcatheter-surgical palliation: Basis for univentricular or biventricular repair: The giessen experience," *Pediatric Cardiology*, vol. 28, pp. 79–87, 2007.
- [29] A. Torres, "Classic norwood versus sano modification versus hybrid approach: necrotizing enterocolitis or no necrotizing enterocolitis?," *Pediatric Critical Care Medicine*, vol. 12, no. 1, pp. 109–110, 2011.
- [30] O. Honjo, L. N. Benson, H. E. Mewhort, D. Predescu, H. Holtby, G. S. V. Arsdell, and C. A. Caldarone, "Clinical outcomes, program evolution, and pulmonary artery growth in single ventricle palliation using hybrid and norwood palliative strategies," *The Annals of Thoracic Surgery*, vol. 87, no. 6, pp. 1885 – 1893, 2009.

- [31] W. Knirsch, R. Liamlahi, M. I. Hug, R. Hoop, M. von Rhein, O. Prtre, Ren17and Kretschmar, and B. Latal, "Mortality and neurodevelopmental outcome at 1 year of age comparing hybrid and norwood procedures," *European Journal of Cardio-Thoracic Surgery*, vol. 42, no. 1, pp. 33–39, 2012.
- [32] A. Carotti, "Postoperative neurodevelopmental outcome of patients with hypoplastic left heart complex: hybrid versus norwood strategy," *European Journal of Cardio-Thoracic Surgery*, vol. 42, no. 1, pp. 40–41, 2012.
- [33] C. Pizarro, C. D. Derby, J. M. Baffa, K. A. Murdison, and W. A. Radtke, "Improving the outcome of high-risk neonates with hypoplastic left heart syndrome: hybrid procedure or conventional surgical palliation," *European Journal of Cardio-Thoracic Surgery*, vol. 33, no. 4, pp. 613–618, 2008.
- [34] N. Westerhof, J.-W. Lankhaar, and B. Westerhof, "The arterial windkessel," *Medical and Biological Engineering and Computing*, vol. 47, pp. 131–141, 2009.
- [35] O. Frank, "Die grundform des arteriellen pulses," *Zeitschrift fur Biologie*, vol. 37, pp. 483–526, 1899.
- [36] Y. Shi, P. Lawford, and R. Hose, "Review of zero-d and 1-d models of blood flow in the cardiovascular system," *Biomedical Engineering Online*, vol. 10, pp. 33+, 2011.
- [37] N. Westerhof, F. Bosman, C. J. D. Vries, and A. Noordergraaf, "Analog studies of the human systemic arterial tree," *Journal of Biomechanics*, vol. 2, no. 2, pp. 121 – 143, 1969.
- [38] G. Porenta, D. Young, and T. Rogge, "A finite-element model of blood-flow in arteries including taper, branches, and obstructions," *Journal of Biomechanical Engineering - Transactions of the ASME*, vol. 108, no. 2, pp. 161–167, 1986.
- [39] E. Rooz, D. Young, and T. Rogge, "A finite-element simulation of pulsatile flow in flexible obstructed tubes," *Journal of Biomechanical Engineering - Transactions of the ASME*, vol. 104, no. 2, pp. 119–124, 1982.
- [40] J. Wan, B. Steele, S. A. Spicer, S. Strohsband, G. R. Feijoo, T. J. Hughes, and C. A. Taylor, "A one-dimensional finite element method for simulation-based medical planning for cardiovascular disease," *Computer Methods in Biomechanics and Biomedical Engineering*, vol. 5, no. 3, pp. 195–206, 2002.
- [41] B. Steele, J. Wan, J. Ku, T. Hughes, and C. Taylor, "In vivo validation of a one-dimensional finite-element method for predicting blood flow in cardiovascular bypass grafts," *Biomedical Engineering, IEEE Transactions on*, vol. 50, no. 6, pp. 649–656, 2003.
- [42] I. Surovtsova, "Effects of compliance mismatch on blood flow in an artery with endovascular prosthesis," *Journal of Biomechanics*, vol. 38, no. 10, pp. 2078 – 2086, 2005.

- [43] S. J. Sherwin, L. Formaggia, P. J., and V. Franke, "Computational modelling of 1d blood flow with variable mechanical properties and its application to the simulation of wave propagation in the human arterial system," *International Journal for Numerical Methods in Fluids*, vol. 43, no. 6-7, pp. 673–700, 2003.
- [44] G. Pontrelli and E. Rossoni, "Numerical modeling of the pressure wave propagation in the arterial flow," *International Journal for Numerical Methods in Fluids*, vol. 43, pp. 651–671, 2003.
- [45] K. Parker and C. Jones, "Forward and backward running waves in the arteries - analysis using the method of characteristics," *Journal of Biomechanical Engineering - Transactions of the ASME*, vol. 112, no. 3, pp. 322–326, 1990.
- [46] V. Milisic and A. Quarteroni, "Analysis of lumped parameter models for blood flow simulations and their relation with 1D models," *Mathematical Modelling and Numerical Analysis*, vol. 38, no. 4, pp. 613–632, 2004.
- [47] J. Levick, *An introduction to cardiovascular physiology*. Arnold ; Oxford University Press, London : New York :, 4th ed. ed., 2003.
- [48] J.-J. Li, *The arterial circulation: Physical principles and clinical applications*. Humana Press Inc., 2000.
- [49] N. Westerhof, G. Elzinga, and P. Sipkema, "An artificial arterial system for pumping hearts.," *Journal of Applied Physiology*, vol. 31, no. 5, pp. 776–781, 1971.
- [50] D. Burkhoff, J. Alexander, and J. Schipke, "Assessment of windkessel as a model of aortic input impedance," *American Journal of Physiology - Heart and Circulatory Physiology*, vol. 255, no. 4, pp. H742–H753, 1988.
- [51] H. Suga, K. Sagawa, and A. A. Shoukas, "Load independence of the instantaneous pressure-volume ratio of the canine left ventricle and effects of epinephrine and heart rate on the ratio," *Circulation Research*, vol. 32, no. 3, pp. 314–322, 1973.
- [52] H. Senzaki, C.-H. Chen, and D. A. Kass, "Single-beat estimation of end-systolic pressure-volume relation in humans: A new method with the potential for noninvasive application," *Circulation*, vol. 94, no. 10, pp. 2497–2506, 1996.
- [53] M. ek and E. Krause, "Numerical simulation of the blood flow in the human cardiovascular system," *Journal of Biomechanics*, vol. 29, no. 1, pp. 13 – 20, 1996.
- [54] J. Werner, D. Bohringer, and M. Hexamer, "Simulation and prediction of cardiotherapeutical phenomena from a pulsatile model coupled to the guyton circulatory model," *IEEE Transactions on Biomedical Engineering*, vol. 49, no. 5, pp. 430 –439, 2002.
- [55] H. Yaku, Y. Goto, S. Futaki, Y. Ohgoshi, O. Kawaguchi, and H. Suga, "Multicompartment model for mechanics and energetics of fibrillating ventricle," *American Journal of Physiology - Heart and Circulatory Physiology*, vol. 260, no. 1, pp. H292–H299, 1991.

- [56] P. Bovendeerd, P. Borsje, T. Arts, and F. van De Vosse, "Dependence of intramyocardial pressure and coronary flow on ventricular loading and contractility: A model study," *Annals of Biomedical Engineering*, vol. 34, pp. 1833–1845, 2006.
- [57] V. Diaz-Zuccarini and J. L. Fevre, "An energetically coherent lumped parameter model of the left ventricle specially developed for educational purposes," *Computers in Biology and Medicine*, vol. 37, no. 6, pp. 774 – 784, 2007.
- [58] S. Cavalcanti and L. Y. Di Marco, "Numerical simulation of the hemodynamic response to hemodialysis-induced hypovolemia," *Artificial Organs*, vol. 23, no. 12, pp. 1063–1073, 1999.
- [59] S. Cavalcanti, S. Cavani, A. Ciandrini, and G. Avanzolini, "Mathematical modeling of arterial pressure response to hemodialysis-induced hypovolemia," *Computers in Biology and Medicine*, vol. 36, no. 2, pp. 128 – 144, 2006.
- [60] Y. Shi, T. J. H. Yeo, and Y. Zhao, "Numerical simulation of a systemic flow test rig.," *American Society for Artificial Internal Organs Journal*, vol. 50, no. 1, pp. 54–64, 2004.
- [61] T. Korakianitis and Y. Shi, "A concentrated parameter model for the human cardiovascular system including heart valve dynamics and atrioventricular interaction," *Medical Engineering & Physics*, vol. 28, no. 7, pp. 613 – 628, 2006.
- [62] M. Ursino, A. Fiorenzi, and E. Belardinelli, "The role of pressure pulsatility in the carotid baroreflex control: A computer simulation study," *Computers in Biology and Medicine*, vol. 26, no. 4, pp. 297 – 314, 1996.
- [63] M. Ursino, "Interaction between carotid baroregulation and the pulsating heart: a mathematical model," *American Journal of Physiology - Heart and Circulatory Physiology*, vol. 275, no. 5, pp. H1733–H1747, 1998.
- [64] M. Ursino and E. Magosso, "Acute cardiovascular response to isocapnic hypoxia. i. a mathematical model," *American Journal of Physiology - Heart and Circulatory Physiology*, vol. 279, no. 1, pp. H149–H165, 2000.
- [65] M. Ursino and E. Magosso, "Acute cardiovascular response to isocapnic hypoxia. ii. model validation," *American Journal of Physiology - Heart and Circulatory Physiology*, vol. 279, no. 1, pp. H166–H175, 2000.
- [66] K. Lu, J. W. Clark, F. H. Ghorbel, D. L. Ware, and A. Bidani, "A human cardiopulmonary system model applied to the analysis of the valsalva maneuver," *American Journal of Physiology - Heart and Circulatory Physiology*, vol. 281, no. 6, pp. H2661–H2679, 2001.
- [67] J. F. Green and N. C. Miller, "A model describing the response of the circulatory system to acceleration stress," *Annals of Biomedical Engineering*, vol. 1, pp. 455–467, 1973.
- [68] C. A. Lodi and M. Ursino, "Hemodynamic effect of cerebral vasospasm in humans: A modeling study," *Annals of Biomedical Engineering*, vol. 27, pp. 257–273, 1999.

- [69] A. D. Jeays, P. V. Lawford, R. Gillott, P. A. Spencer, K. D. Bardhan, and D. R. Hose, "A framework for the modeling of gut blood flow regulation and postprandial hyperaemia," *World Journal of Gastroenterology*, vol. 13, no. 9, pp. 1393–1398, 2007.
- [70] A. J. M. Cornelissen, J. Dankelman, E. VanBavel, H. G. Stassen, and J. A. E. Spaan, "Myogenic reactivity and resistance distribution in the coronary arterial tree: a model study," *American Journal of Physiology - Heart and Circulatory Physiology*, vol. 278, no. 5, pp. H1490–H1499, 2000.
- [71] A. J. M. Cornelissen, J. Dankelman, E. VanBavel, and J. A. E. Spaan, "Balance between myogenic, flow-dependent, and metabolic flow control in coronary arterial tree: a model study," *American Journal of Physiology - Heart and Circulatory Physiology*, vol. 282, no. 6, pp. H2224–H2237, 2002.
- [72] K. Peterson, E. T. Ozawa, G. M. Pantalos, and M. K. Sharp, "Numerical simulation of the influence of gravity and posture on cardiac performance," *Annals of Biomedical Engineering*, vol. 30, pp. 247–259, 2002.
- [73] M. Ursino, "A mathematical model of the carotid baroregulation in pulsating conditions," *IEEE Transactions on Biomedical Engineering*, vol. 46, no. 4, pp. 382–392, 1999.
- [74] O. Barnea, T. Moore, S. Dubin, and D. Jaron, "Cardiac energy considerations during intraaortic balloon pumping," *IEEE Transactions on Biomedical Engineering*, vol. 37, no. 2, pp. 170–181, 1990.
- [75] C. Zervides, A. J. Narracott, P. V. Lawford, and D. R. Hose, "The role of venous valves in pressure shielding," *Biomedical Engineering Online*, vol. 7, 2008.
- [76] R. Beyar, M. J. Hausknecht, H. R. Halperin, F. C. Yin, and M. L. Weisfeldt, "Interaction between cardiac chambers and thoracic pressure in intact circulation," *American Journal of Physiology - Heart and Circulatory Physiology*, vol. 253, no. 5, pp. H1240–H1252, 1987.
- [77] M. F. Snyder and V. C. Rideout, "Computer simulation studies of the venous circulation," *IEEE Transactions on Biomedical Engineering*, vol. BME-16, no. 4, pp. 325–334, 1969.
- [78] J. Li, T. Cui, and G. Drzewiecki, "A nonlinear model of the arterial system incorporating a pressure-dependent compliance," *Biomedical Engineering, IEEE Transactions on*, vol. 37, no. 7, pp. 673–678, 1990.
- [79] A. Cappello, G. Gnudi, and C. Lamberti, "Identification of the 3-element windkessel model incorporating a pressure-dependent compliance," *Annals of Biomedical Engineering*, vol. 23, no. 2, pp. 164–177, 1995.
- [80] M. C. F. Geven, V. N. B. W. H. Aarnoudse, P. M. J. van den Berg, M. C. M. Rutten, N. H. J. Pijls, and F. N. van de Vosse, "A physiologically representative in vitro model of the coronary circulation," *Physiological Measurement*, vol. 25, no. 4, p. 891, 2004.

- [81] K. Laganà, R. Balossino, F. Migliavacca, G. Pennati, E. L. Bove, M. R. de Leval, and G. Dubini, “Multiscale modeling of the cardiovascular system: application to the study of pulmonary and coronary perfusions in the univentricular circulation,” *Journal of Biomechanics*, vol. 38, no. 5, pp. 1129 – 1141, 2005.
- [82] F. Migliavacca, R. Balossino, G. Pennati, G. Dubini, T.-Y. Hsia, M. R. de Leval, and E. L. Bove, “Multiscale modelling in biofluidynamics: Application to reconstructive paediatric cardiac surgery,” *Journal of Biomechanics*, vol. 39, pp. 1010–1020, 2006.
- [83] C. Corsini, D. Cosentino, G. Pennati, G. Dubini, T.-Y. Hsia, and F. Migliavacca, “Multiscale models of the hybrid palliation for hypoplastic left heart syndrome,” *Journal of Biomechanics*, vol. 44, no. 4, pp. 767 – 770, 2011.
- [84] C. E. Baker, C. Corsini, D. Cosentino, G. Dubini, G. Pennati, F. Migliavacca, and T.-Y. Hsia, “Effects of pulmonary artery banding and retrograde aortic arch obstruction on the hybrid palliation of hypoplastic left heart syndrome,” *The Journal of Thoracic and Cardiovascular Surgery*, pp. –, 2013.
- [85] F. Migliavacca, G. Pennati, G. Dubini, R. Fumero, R. Pietrabissa, G. Urceley, E. Bove, T. Hsia, and M. De Leval, “Modeling of the norwood circulation: effects of shunt size, vascular resistances, and heart rate,” *American Journal of Physiology - Heart and Circulatory Physiology*, vol. 280, no. 5, pp. H2076–H2086, 2001.
- [86] S. Shimizu, D. Une, T. Shishido, A. Kamiya, T. Kawada, S. Sano, and M. Sugimachi, “Norwood procedure with non-valved right ventricle to pulmonary artery shunt improves ventricular energetics despite the presence of diastolic regurgitation: a theoretical analysis,” *The Journal of Physiological Sciences*, vol. 61, pp. 457–465, 2011.
- [87] C. Hann, J. Chase, and G. Shaw, “Integral-based identification of patient specific parameters for a minimal cardiac model,” *Computer Methods and Programs in Biomedicine*, vol. 81, no. 2, pp. 181 – 192, 2006.
- [88] G. Pennati, F. Migliavacca, G. Dubini, R. Pietrabissa, and M. R. de Leval, “A mathematical model of circulation in the presence of the bidirectional cavopulmonary anastomosis in children with a univentricular heart,” *Medical Engineering & Physics*, vol. 19, no. 3, pp. 223 – 234, 1997.
- [89] G. Pennati, M. Bellotti, and R. Fumero, “Mathematical modelling of the human foetal cardiovascular system based on doppler ultrasound data,” *Medical Engineering & Physics*, vol. 19, no. 4, pp. 327 – 335, 1997.
- [90] J.-W. Lankhaar, F. Rvekamp, P. Steendijk, T. Faes, B. Westerhof, T. Kind, A. Vonk-Noordegraaf, and N. Westerhof, “Modeling the instantaneous pressure-volume relation of the left ventricle: A comparison of six models,” *Annals of Biomedical Engineering*, vol. 37, pp. 1710–1726, 2009.

- [91] A. Jalali and C. Nataraj, "A cycle-averaged model of hypoplastic left heart syndrome (hlhs)," in *Engineering in Medicine and Biology Society, EMBC, 2011 Annual International Conference of the IEEE*, pp. 190 – 194, 2011.
- [92] C. Hann, J. Revie, D. Stevenson, S. Heldmann, T. Desaive, C. Froissart, B. Lambermont, A. Ghuysen, P. Kolh, G. Shaw, and J. Chase, "Patient specific identification of the cardiac driver function in a cardiovascular system model," *Computer Methods and Programs in Biomedicine*, vol. 101, no. 2, pp. 201 – 207, 2011.
- [93] T. Heldt, E. Shim, R. Kamm, and R. Mark, "Computational modeling of cardiovascular response to orthostatic stress," *Journal of Applied Physiology*, vol. 92, no. 3, pp. 1239–1254, 2002.
- [94] G. Drzewiecki, J.-J. Wang, J. K. J. Li, J. Kedem, and H. Weiss, "Modeling of mechanical dysfunction in regional stunned myocardium of the left ventricle," *Biomedical Engineering, IEEE Transactions on*, vol. 43, no. 12, pp. 1151–1163, 1996.
- [95] M. Vollkron, H. Schima, L. Huber, and G. Wieselthaler, "Interaction of the cardiovascular system with an implanted rotary assist device: Simulation study with a refined computer model," *Artificial Organs*, vol. 26, no. 4, pp. 349–359, 2002.
- [96] D. McQueen, C. Peskin, and E. Yellin, "Fluid-dynamics of the mitral-valve - physiological-aspects of a mathematical model," *American Journal of Physiology*, vol. 242, no. 6, pp. 1095–1110, 1982.
- [97] H. Kitajima and A. P. Yoganathan, "Blood flow - the basics of the discipline," in *Ventricular function and blood flow in congenital heart disease* (M. A. Fogel, ed.), pp. 38–54, Malden, MA: Blackwell Publishing, 2005.
- [98] X. Y. Xu and M. W. Collins, "A review of the numerical analysis of blood flow in arterial bifurcations," *Proceedings of the Institution of Mechanical Engineers, Part H: Journal of Engineering in Medicine*, vol. 204, no. 4, pp. 205–216, 1990.
- [99] K. Perktold, H. Florian, and D. Hilbert, "Analysis of pulsatile blood flow: A carotid siphon model," *Journal of Biomedical Engineering*, vol. 9, no. 1, pp. 46 – 53, 1987.
- [100] K. Perktold and R. Peter, "Numerical 3d-simulation of pulsatile wall shear stress in an arterial t-bifurcation model," *Journal of Biomedical Engineering*, vol. 12, no. 1, pp. 2 – 12, 1990.
- [101] K. Perktold, R. Nerem, and R. Peter, "A numerical calculation of flow in a curved tube model of the left main coronary artery," *Journal of Biomechanics*, vol. 24, no. 3-4, pp. 175 – 189, 1991.
- [102] K. Perktold, M. Resch, and R. O. Peter, "Three-dimensional numerical analysis of pulsatile flow and wall shear stress in the carotid artery bifurcation," *Journal of Biomechanics*, vol. 24, no. 6, pp. 409 – 420, 1991.

- [103] S. D.A., "Image-based computational fluid dynamics modeling in realistic arterial geometries," *Annals of Biomedical Engineering*, vol. 30, no. 4, pp. 483–497, 2002.
- [104] C. A. Taylor, M. T. Draney, J. P. Ku, D. Parker, B. N. Steele, K. Wang, and C. K. Zarins, "Predictive medicine: Computational techniques in therapeutic decision-making," *Computer Aided Surgery*, vol. 4, no. 5, pp. 231–247, 1999.
- [105] D. Steinman and C. Taylor, "Flow imaging and computing: Large artery hemodynamics," *Annals of Biomedical Engineering*, vol. 33, no. 12, pp. 1704–1709, 2005.
- [106] A. O. Frank, P. W. Walsh, and J. E. Moore, "Computational fluid dynamics and stent design," *Artificial Organs*, vol. 26, no. 7, pp. 614–621, 2002.
- [107] K. H. Fraser, M. E. Taskin, B. P. Griffith, and Z. J. Wu, "The use of computational fluid dynamics in the development of ventricular assist devices," *Medical Engineering & Physics*, vol. 33, no. 3, pp. 263 – 280, 2011.
- [108] F. Liang, H. Taniguchi, and H. Liu, "A multi-scale computational method applied to the quantitative evaluation of the left ventricular function," *Computers in Biology and Medicine*, vol. 37, no. 5, pp. 700 – 715, 2007.
- [109] S. Khalafvand, E. Ng, and L. Zhong, "Cfd simulation of flow through heart: a perspective review," *Computer Methods in Biomechanics and Biomedical Engineering*, vol. 14, no. 1, pp. 113–132, 2011.
- [110] J. Waniewski, W. Kurowska, J. K. Mizerski, A. Trykozko, K. Nowiński, G. Brzezińska-Rajszyś, and A. Kościeszka, "The effects of graft geometry on the patency of a systemic-to-pulmonary shunt: A computational fluid dynamics study," *Artificial Organs*, vol. 29, no. 8, pp. 642–650, 2005.
- [111] M. R. de Leval, G. Dubini, F. Migliavacca, H. Jalali, G. Camporini, A. Redington, and R. Pietrabissa, "Use of computational fluid dynamics in the design of surgical procedures: application to the study of competitive flows in cavopulmonary connections," *Journal Thoracic and Cardiovascular Surgery*, vol. 111, no. 3, pp. 502–513, 1996.
- [112] A. L. Marsden, A. J. Bernstein, V. M. Reddy, S. C. Shadden, R. L. Spilker, F. P. Chan, C. A. Taylor, and J. A. Feinstein, "Evaluation of a novel y-shaped extracardiac fontan baffle using computational fluid dynamics," *The Journal of Thoracic and Cardiovascular Surgery*, vol. 137, no. 2, pp. 394 – 403.e2, 2009.
- [113] E. Bove, M. Leval, F. Migliavacca, R. Balossino, and G. Dubini, "Toward optimal hemodynamics: Computer modeling of the fontan circuit," *Pediatric Cardiology*, vol. 28, no. 6, pp. 477–481, 2007.
- [114] C. DeGroff, "Modeling the fontan circulation: Where we are and where we need to go," *Pediatric Cardiology*, vol. 29, no. 1, pp. 3–12, 2008.

- [115] G. Pennati, C. Corsini, D. Cosentino, T.-Y. Hsia, V. S. Luisi, G. Dubini, and F. Migliavacca, "Boundary conditions of patient-specific fluid dynamics modelling of cavopulmonary connections: possible adaptation of pulmonary resistances results in a critical issue for a virtual surgical planning," *Interface Focus*, vol. 1, no. 3, pp. 297–307, 2011.
- [116] I. E. Vignon-Clementel, C. A. Figueroa, K. E. Jansen, and C. A. Taylor, "Outflow boundary conditions for three-dimensional finite element modeling of blood flow and pressure in arteries," *Computer Methods in Applied Mechanics and Engineering*, vol. 195, no. 29-32, pp. 3776 – 3796, 2006.
- [117] K. Pekkan, D. d. Zlicourt, L. Ge, F. Sotiropoulos, D. Frakes, M. Fogel, and A. Yoganathan, "Physics-driven cfd modeling of complex anatomical cardiovascular flows-a tpc case study," *Annals of Biomedical Engineering*, vol. 33, no. 3, pp. 284–300, 2005.
- [118] K. Laganá;, G. Dubini, F. Migliavacca, R. Pietrabissa, G. Pennati, A. Veneziani, and A. Quarteroni, "Multiscale modelling as a tool to prescribe realistic boundary conditions for the study of surgical procedures.," *Biorheology*, vol. 39, no. 3-4, pp. 359–64, 2002.
- [119] L. Formaggia, F. Nobile, A. Quarteroni, and A. Veneziani, "Multiscale modelling of the circulatory system a preliminary analysis," in *Computing and Visualization in Science Germany*, vol. 2, pp. 75–83, 1999.
- [120] L. Formaggia, J. Gerbeau, F. Nobile, and A. Quarteroni, "On the coupling of 3d and 1d navier-stokes equations for flow problems in compliant vessels," *Computer Methods in Applied Mechanics and Engineering*, vol. 191, no. 6-7, pp. 561 – 582, 2001.
- [121] A. Quarteroni, S. Ragni, and A. Veneziani, "Coupling between lumped and distributed models for blood flow problems," *Computing and Visualization in Science*, vol. 4, pp. 111–124, 2001.
- [122] A. Quarteroni and A. Veneziani, "Analysis of a geometrical multiscale model based on the coupling of ode and pde for blood flow simulations," *Multiscale Modeling & Simulation*, vol. 1, no. 2, pp. 173–195, 2003.
- [123] M. Esmaily Moghadam, Y. Bazilevs, T.-Y. Hsia, I. Vignon-Clementel, and A. Marsden, "A comparison of outlet boundary treatments for prevention of backflow divergence with relevance to blood flow simulations," *Computational Mechanics*, vol. 48, no. 3, pp. 277–291, 2011.
- [124] E. L. Bove, F. Migliavacca, M. R. de Leval, R. Balossino, G. Pennati, T. R. Lloyd, S. Khambadkone, T.-Y. Hsia, and G. Dubini, "Use of mathematic modeling to compare and predict hemodynamic effects of the modified blalock-taussig and right ventricle-pulmonary artery shunts for hypoplastic left heart syndrome," *The Journal of Thoracic and Cardiovascular Surgery*, vol. 136, no. 2, pp. 312 – 320.e2, 2008.
- [125] H. J. Kim, I. E. Vignon-Clementel, C. A. Figueroa, J. F. LaDisa, K. E. Jansen, J. A. Feinstein, and C. A. Taylor, "On coupling a lumped parameter heart model and a three-dimensional finite element aorta model," *Annals of Biomedical Engineering*, vol. 37, no. 11, pp. 2153–2169, 2009.

- [126] F. V. Vosse, “Mathematical modelling of the cardiovascular system,” *Journal of Engineering Mathematics*, vol. 47, no. 3, pp. 175–183, 2003.
- [127] T.-Y. Hsia, D. Cosentino, C. Corsini, G. Pennati, G. Dubini, F. Migliavacca, and for the Modeling of Congenital Hearts Alliance (MOCHA) Investigators, “Use of mathematical modeling to compare and predict hemodynamic effects between hybrid and surgical norwood palliations for hypoplastic left heart syndrome,” *Circulation*, vol. 124, no. 11 suppl 1, pp. S204–S210, 2011.
- [128] G. Pennati, F. Migliavacca, G. Dubini, and E. L. Bove, “Modeling of systemic-to-pulmonary shunts in newborns with a univentricular circulation: State of the art and future directions,” *Progress in Pediatric Cardiology*, vol. 30, no. 1-2, pp. 23 – 29, 2010.
- [129] C. Taylor and C. Figueroa, “Patient-specific modeling of cardiovascular mechanics,” *Annual Review of Biomedical Engineering*, vol. 11, no. 1, pp. 109–134, 2009.
- [130] R. Spilker and C. Taylor, “Tuning multidomain hemodynamic simulations to match physiological measurements,” *Annals of Biomedical Engineering*, vol. 38, no. 8, pp. 2635–2648, 2010.
- [131] C. A. Figueroa, S. Baek, C. A. Taylor, and J. D. Humphrey, “A computational framework for fluid-solid-growth modeling in cardiovascular simulations,” *Computer Methods in Applied Mechanics and Engineering*, vol. 198, no. 45-46, pp. 3583 – 3602, 2009.
- [132] A. Baretta, C. Corsini, A. L. Marsden, I. E. Vignon-Clementel, T.-Y. Hsia, G. Dubini, F. Migliavacca, and G. Pennati, “Respiratory effects on hemodynamics in patient-specific cfd models of the fontan circulation under exercise conditions,” *European Journal of Mechanics - Bio-Fluids*, vol. 35, no. 0, pp. 61 – 69, 2012.
- [133] A. L. Marsden, J. A. Feinstein, and C. A. Taylor, “A computational framework for derivative-free optimization of cardiovascular geometries,” *Computer Methods in Applied Mechanics and Engineering*, vol. 197, no. 21-24, pp. 1890 – 1905, 2008.
- [134] M. Esmaily Moghadam, F. Migliavacca, E. Vignon-Clementel, Irene, T.-Y. Hsia, L. Marsden, Alison, and F. The Modeling Of Congenital Hearts Alliance (mocha) Investigators, “Optimization of shunt placement for the norwood surgery using multi-domain modeling.,” *Journal of Biomechanical Engineering*, vol. 134, no. 5, p. 051002, 2012.
- [135] A. Baretta, C. Corsini, W. Yang, I. Vignon-Clementel, E., A. Marsden, L., J. Feinstein, A., T.-Y. Hsia, G. Dubini, F. Migliavacca, G. Pennati, and M. Modeling Of Congenital Hearts Alliance Investigators, “Virtual surgeries in patients with congenital heart disease: a multi-scale modelling test case.,” *Philosophical Transactions A: Mathematical, Physical and Engineering Sciences*, vol. 369, no. 1954, pp. 4316–4330, 2011. Fondation Leducq.

- [136] E. Kung, A. Baretta, C. Baker, G. Arbia, G. Biglino, C. Corsini, S. Schievano, I. E. Vignon-Clementel, G. Dubini, G. Pennati, A. Taylor, A. Dorfman, A. M. Hlavacek, A. L. Marsden, T.-Y. Hsia, and F. Migliavacca, "Predictive modeling of the virtual hemi-fontan operation for second stage single ventricle palliation: Two patient-specific cases," *Journal of Biomechanics*, vol. 46, no. 2, pp. 423 – 429, 2013.
- [137] B. W. Smith, J. Chase, R. I. Nokes, G. M. Shaw, and G. Wake, "Minimal haemodynamic system model including ventricular interaction and valve dynamics," *Medical Engineering & Physics*, vol. 26, no. 2, pp. 131 – 139, 2004.
- [138] N. Xiao, J. D. Humphrey, and C. A. Figueroa, "Multi-scale computational model of three-dimensional hemodynamics within a deformable full-body arterial network," *Journal of Computational Physics*, vol. 244, pp. 22–40, 2013.
- [139] S. Ieng, J. Davies, J. Baksi, D. Francis, K. Parker, J. Mayet, and A. Hughes, "Evidence of a common reservoir pressure transmitted along the length of the aorta which is the predominate determinate of arterial pressure in humans," *Artery Research*, vol. 2, no. 3, p. 87, 2008.
- [140] J. Alastruey, A. W. Khir, K. S. Matthys, P. Segers, S. J. Sherwin, P. R. Verdonck, K. H. Parker, and J. Peir, "Pulse wave propagation in a model human arterial network: Assessment of 1-d visco-elastic simulations against in vitro measurements," *Journal of Biomechanics*, vol. 44, no. 12, pp. 2250 – 2258, 2011.
- [141] R. Sarnari, R. Y. Kamal, M. K. Friedberg, and N. H. Silverman, "Doppler assessment of the ratio of the systolic to diastolic duration in normal children: Relation to heart rate, age and body surface area," *Journal of the American Society of Echocardiography*, vol. 22, no. 8, pp. 928 – 932, 2009.
- [142] M. K. Friedberg and N. H. Silverman, "The systolic to diastolic duration ratio in children with hypoplastic left heart syndrome: A novel doppler index of right ventricular function," *Journal of the American Society of Echocardiography*, vol. 20, no. 6, pp. 749 – 755, 2007.
- [143] W. W. Nichols, M. F. O'Rourke, C. Hartley, and D. A. McDonald, *McDonald's blood flow in arteries : theoretical, experimental, and clinical principles / Wilmer W. Nichols, Michael F. O'Rourke ; with a contribution from Craig Hartley*. Arnold ; Oxford University Press, London : New York :, 4th ed. ed., 1998.
- [144] A. Young, T. Gourlay, S. McKee, and M. H. Danton, "Computational modelling to optimize the hybrid configuration for hypoplastic left heart syndrome," *European Journal of Cardio-Thoracic Surgery*, vol. 44, no. 4, pp. 664–672, 2013.
- [145] H. Piene, "Impedance matching between ventricle and load," *Annals of Biomedical Engineering*, vol. 12, pp. 191–207, 1984.

- [146] M. Friedberg, N. Silverman, R. Kamal, and R. Sarnari, "The systolic to diastolic duration ratio in children with normal cardiac function and its relation to heart rate, age and body surface area," *Heart Views*, vol. 10, no. 1, pp. 11–16, 2009.
- [147] J. Li, G. Zhang, L. Benson, H. Holtby, S. Cai, T. Humpl, G. S. V. Arsdell, A. N. Redington, and C. A. Caldarone, "Comparison of the profiles of postoperative systemic hemodynamics and oxygen transport in neonates after the hybrid or the norwood procedure: A pilot study," *Circulation*, vol. 116, pp. I179–I187, 2007.
- [148] S. Takabayashi, H. Kado, Y. Shiokawa, K. Fukae, and T. Nakano, "Comparison of hemodynamics between norwood procedure and systemic-to-pulmonary artery shunt for single right ventricle patients," *European Journal of Cardio-Thoracic Surgery*, vol. 27, no. 6, pp. 968–974, 2005.
- [149] J. Photiadis, N. Sinzobahamvya, C. Fink, M. Schneider, E. Schindler, A. M. Brecher, A. E. Urban, and B. Asfour, "Optimal pulmonary to systemic blood flow ratio for best hemodynamic status and outcome early after norwood operation," *European Journal of Cardio-Thoracic Surgery*, vol. 29, no. 4, pp. 551–556, 2006.
- [150] A. C. Chang, T. J. Kulik, P. R. Hickey, and D. L. Wessel, "Real-time gas-exchange measurement of oxygen consumption in neonates and infants after cardiac surgery," *Critical Care Medicine*, vol. 21, no. 9, pp. 1369–75, 1993.
- [151] K. O. Maher, C. Pizarro, S. S. Gidding, K. Januszewska, E. Malec, W. I. N. Jr, and J. D. Murphy, "Hemodynamic profile after the norwood procedure with right ventricle to pulmonary artery conduit," *Circulation*, vol. 108, pp. 782–784, 2003.
- [152] M. B. Mitchell, D. N. Campbell, M. M. Boucek, H. M. Sondheimer, K. C. Chan, D. D. Ivy, B. Pietra, and T. Mackenzie, "Mechanical limitation of pulmonary blood flow facilitates heart transplantation in older infants with hypoplastic left heart syndrome," *European Journal of Cardio-Thoracic Surgery*, vol. 23, no. 5, pp. 735–742, 2003.
- [153] J. Rychik, "Hypoplastic left heart syndrome: From in-utero diagnosis to school age," *Seminars in Fetal and Neonatal Medicine*, vol. 10, no. 6, pp. 553 – 566, 2005.
- [154] E. A. Bacha, S. Daves, J. Hardin, R. id Abdulla, J. Anderson, M. Kahana, P. Koenig, B. N. Mora, M. Gulecyuz, J. P. Starr, E. Alboliras, S. Sandhu, and Z. M. Hijazi, "Single-ventricle palliation for high-risk neonates: The emergence of an alternative hybrid stage i strategy," *The Journal of Thoracic and Cardiovascular Surgery*, vol. 131, no. 1, pp. 163 – 171.e2, 2006.
- [155] J. S. Tweddell, G. M. Hoffman, R. T. Fedderly, S. Berger, J. Thomas, John P., N. S. Ghanayem, M. W. Kessel, and S. B. Litwin, "Phenoxybenzamine improves systemic oxygen delivery after the norwood procedure," *The Annals of Thoracic Surgery*, vol. 67, no. 1, pp. 161–167, 1999.
- [156] R. J. Schuhmann, *Metallurgical Engineering Volume 1: Engineering Principles*. Addison-Wesley Publishing Company, 1st ed. ed., 1952.

- [157] J. a. Janela, A. Moura, and A. Sequeira, "A 3d non-newtonian fluid-structure interaction model for blood flow in arteries," *Journal of Computational and Applied Mathematics*, vol. 234, pp. 2783–2791, 2010.
- [158] M. E. Moghadam, I. E. Vignon-Clementel, R. Figliola, and A. L. Marsden, "A modular numerical method for implicit 0d/3d coupling in cardiovascular finite element simulations," *Journal of Computational Physics*, vol. 244, no. 0, pp. 63 – 79, 2013. Multi-scale Modeling and Simulation of Biological Systems.
- [159] A. N. Naguib, P. Winch, L. Schwartz, J. Isaacs, R. Rodeman, J. P. Cheatham, and M. Galantowicz, "Anesthetic management of the hybrid stage 1 procedure for hypoplastic left heart syndrome (hlhs)," *Pediatric Anesthesia*, vol. 20, no. 1, pp. 38–46, 2010.
- [160] O. Honjo and C. A. Caldarone, "Hybrid palliation for neonates with hypoplastic left heart syndrome: current strategies and outcomes.," *Korean Circulation Journal*, vol. 40, no. 3, pp. 103–11, 2010.
- [161] J. Koziol, R. Gertler, C. Manlhiot, B. McCrindle, H. Holtby, C. Caldarone, and K. Taylor, "The effect of intraoperative hypotension on the outcomes of initial hybrid palliation for single ventricle congenital heart disease: an historical cohort study," *Canadian Journal of Anesthesia/Journal canadien d'anesthsie*, vol. 60, no. 5, pp. 465–470, 2013.
- [162] A. Young, T. Gourlay, S. McKee, and M. H. Danton, "Computational modelling to optimize hybrid configuration for hypoplastic left heart syndrome," in *26th Annual Meeting of the European Association for Cardio-Thoracic Surgery (EACTS)*, (Barcelona, Spain), October 2012.
- [163] M. Olufsen, "A one-dimensional fluid dynamic model of the systemic arteries," in *Proceedings from mathematical modelling in medicine* (J. Ottesen and M. Danielsen, eds.), Roskilde Universitetsforlag, 1997.